

# **ACOUSTIC TRANSDUCTION – MATERIALS AND DEVICES**

**Period 1 January 2000 to 31 December 2000**

**Annual Report**

**VOLUME V**

**OFFICE OF NAVAL RESEARCH**

**Contract No: N00014-96-1-1173**

**APPROVED FOR PUBLIC RELEASE –  
DISTRIBUTION UNLIMITED**

**Reproduction in whole or in part is permitted for any  
purpose of the United States Government**

**Kenji Uchino**

**PENNSTATE**



**THE MATERIALS RESEARCH LABORATORY  
UNIVERSITY PARK, PA**

**20010817 079**

# REPORT DOCUMENTATION PAGE

Form Approved  
OMB No. 0704-0188

Public reporting burden for this collection of information is estimated to average 1 hour per response, including the time for reviewing instructions, searching existing data sources, gathering and maintaining the data needed, and completing and reviewing the collection of information. Send comments regarding this burden estimate or any other aspect of this collection of information, including suggestions for reducing this burden, to Washington Headquarters Services, Directorate for Information Operations and Reports, 1215 Jefferson Davis Highway, Suite 1204, Arlington, VA 22202-4302, and to the Office of Management and Budget, Paperwork Reduction Project (0704-0188), Washington, DC 20503.

1. AGENCY USE ONLY (Leave blank)		2. REPORT DATE 7/12/2001	3. REPORT TYPE AND DATES COVERED ANNUAL REPORT 01/01/2000--12/31/2000	
4. TITLE AND SUBTITLE ACOUSTIC TRANSDUCTION -- MATERIALS AND DEVICES			5. FUNDING NUMBERS ONR CONTRACT NO. N00014-96-1-11173	
6. AUTHOR(S) Materials Research Laboratory The Pennsylvania State University University Park, Pa 16802				
7. PERFORMING ORGANIZATION NAME(S) AND ADDRESS(ES)			8. PERFORMING ORGANIZATION REPORT NUMBER	
9. SPONSORING / MONITORING AGENCY NAME(S) AND ADDRESS(ES) Office of Naval Research      Office of Naval Research ONR 321SS      Regional Office Chicago Ballston Centre Tower One      536 S. Clark Str. RM 208 800 N. Quincy Street      Chicago IL 60605-1588 Arlington, VA 2217-5660			10. SPONSORING / MONITORING AGENCY REPORT NUMBER	
11. SUPPLEMENTARY NOTES				
12a. DISTRIBUTION / AVAILABILITY STATEMENT			12b. DISTRIBUTION CODE	
13. ABSTRACT (Maximum 200 words)  SEE FOLLOWING PAGE				
14. SUBJECT TERMS			15. NUMBER OF PAGES	
			16. PRICE CODE	
17. SECURITY CLASSIFICATION OF REPORT UNCLASSIFIED	18. SECURITY CLASSIFICATION OF THIS PAGE UNCLASSIFIED	19. SECURITY CLASSIFICATION OF ABSTRACT UNCLASSIFIED	20. LIMITATION OF ABSTRACT	

## GENERAL INSTRUCTIONS FOR COMPLETING SF 298

The Report Documentation Page (RDP) is used in announcing and cataloging reports. It is important that this information be consistent with the rest of the report, particularly the cover and title page. Instructions for filling in each block of the form follow. It is important to *stay within the lines* to meet *optical scanning requirements*.

**Block 1. Agency Use Only (Leave blank).**

**Block 2. Report Date.** Full publication date including day, month, and year, if available (e.g. 1 Jan 88). Must cite at least the year.

**Block 3. Type of Report and Dates Covered.** State whether report is interim, final, etc. If applicable, enter inclusive report dates (e.g. 10 Jun 87 - 30 Jun 88).

**Block 4. Title and Subtitle.** A title is taken from the part of the report that provides the most meaningful and complete information. When a report is prepared in more than one volume, repeat the primary title, add volume number, and include subtitle for the specific volume. On classified documents enter the title classification in parentheses.

**Block 5. Funding Numbers.** To include contract and grant numbers; may include program element number(s), project number(s), task number(s), and work unit number(s). Use the following labels:

C - Contract	PR - Project
G - Grant	TA - Task
PE - Program Element	WU - Work Unit Accession No.

**Block 6. Author(s).** Name(s) of person(s) responsible for writing the report, performing the research, or credited with the content of the report. If editor or compiler, this should follow the name(s).

**Block 7. Performing Organization Name(s) and Address(es).** Self-explanatory.

**Block 8. Performing Organization Report Number.** Enter the unique alphanumeric report number(s) assigned by the organization performing the report.

**Block 9. Sponsoring/Monitoring Agency Name(s) and Address(es).** Self-explanatory.

**Block 10. Sponsoring/Monitoring Agency Report Number.** (If known)

**Block 11. Supplementary Notes.** Enter information not included elsewhere such as: Prepared in cooperation with...; Trans. of...; To be published in.... When a report is revised, include a statement whether the new report supersedes or supplements the older report.

**Block 12a. Distribution/Availability Statement.** Denotes public availability or limitations. Cite any availability to the public. Enter additional limitations or special markings in all capitals (e.g. NOFORN, REL, ITAR).

DOD - See DoDD 5230.24, "Distribution Statements on Technical Documents."

DOE - See authorities.

NASA - See Handbook NHB 2200.2.

NTIS - Leave blank.

**Block 12b. Distribution Code.**

DOD - Leave blank.

DOE - Enter DOE distribution categories from the Standard Distribution for Unclassified Scientific and Technical Reports.

NASA - Leave blank.

NTIS - Leave blank.

**Block 13. Abstract.** Include a brief (Maximum 200 words) factual summary of the most significant information contained in the report.

**Block 14. Subject Terms.** Keywords or phrases identifying major subjects in the report.

**Block 15. Number of Pages.** Enter the total number of pages.

**Block 16. Price Code.** Enter appropriate price code (NTIS only).

**Blocks 17. - 19. Security Classifications.** Self-explanatory. Enter U.S. Security Classification in accordance with U.S. Security Regulations (i.e., UNCLASSIFIED). If form contains classified information, stamp classification on the top and bottom of the page.

**Block 20. Limitation of Abstract.** This block must be completed to assign a limitation to the abstract. Enter either UL (unlimited) or SAR (same as report). An entry in this block is necessary if the abstract is to be limited. If blank, the abstract is assumed to be unlimited.

## ABSTRACT

This report describes research performed over the period 1<sup>st</sup> January 2000 to 31<sup>st</sup> December 2000 on a MURI under Office of Naval Research contract N00014-96-1-1173 on the topic "Acoustic Transduction Materials and Devices". This program brings together researchers from the Materials Research Laboratory (MRL), the Applied Research Laboratory (ARL) and the Center for Acoustics and Vibrations (CAV) at the Pennsylvania State University. As has become customary over many years, research on the program is detailed in the technical appendices of published work, and only a brief narrative description connecting these studies is given in the text.

The program combines a far reaching exploration of the basic phenomena contributing to piezoelectric and electrostrictive response with the highly applied thrusts necessary to produce the "pay-off" in new applications relevant to Navy needs. Polarization vector tilting in the ferroelectric phase of perovskite structure crystals at compositions close to a morphotropic phase boundary (MPB) was first underscored on this program some four years ago, and is now widely accepted as one mode for exploiting the large intrinsic spontaneous strain in the ferroelectric to produce exceedingly strong anhysteretic piezoelectric response and very large electric field controlled elastic strain. New evidence for the importance of both spontaneous (monoclinic) and electric field induced tilting on the properties of both single and polycrystal MPB systems is presented in this report.

The puzzling phenomena associated with relaxor ferroelectric response have long been a topic of study in MRL, where the micro-polar region model and the application of Vogel/Fulcher to the dielectric slowing down were first applied. The current "pay-off" is in the greatly enhanced relaxor ferroelectric electrostrictive response from high electron energy irradiated polyvinylidene difluoride: trifluoroethylene (PVDF: TrFE) co-polymer discussed in this report. This development opens a new field of high strain, high energy density actuators with tremendous practical applicability. Now the possibility of engineering this response by chemical manipulation in the terpolymer systems without irradiation further enhances the exciting possibilities.

In composite structures, the early promise of the flextensional cymbal type actuators is now being fully realized and programs exploring large area cymbal transducer arrays are progressing very well, both at MRL/ARL and at NRL. The connection with CAV at Penn State is particularly important in keeping the MURI faculty aware of problems endemic to water as our host medium and the effects of turbulence in flow and the need for many types of acoustic noise control.

New designs of piezoelectric transformers and motors are demanding materials with lower loss levels under continuous high driving, and important progress is reported in separating and understanding the components of this loss and in designing new doping schemes for ceramics which enhance power capability almost tenfold. New piezoelectric micro-motor designs look particularly attractive and appear to offer significant advantages over electromagnetics for very small-scale applications. Thick and thin film studies for MEMS are progressing well and offering new insights into fatigue and switching behavior in the ferroelectrics.



# **ACOUSTIC TRANSDUCTION – MATERIALS AND DEVICES**

**Period 1 January 2000 to 31 December 2000**

**Annual Report**

**VOLUME V**

**OFFICE OF NAVAL RESEARCH  
Contract No: N00014-96-1-1173**

**APPROVED FOR PUBLIC RELEASE –  
DISTRIBUTION UNLIMITED**

**Reproduction in whole or in part is permitted for any  
purpose of the United States Government**

**Kenji Uchino**

## APPENDICES

### VOLUME I

#### GENERAL SUMMARY PAPERS

1. Uchino, K., Encyclopedia of Vibration, Partial Charge "Electrostrictive Materials", Academic Press, London (2000). [in press]
2. Uchino, K., and Y. Ito, Encyclopedia Smart Materials, J. Harvey, Edit., Partial Charge "Smart Ceramics: Transducers, Sensors and Actuators", John Wiley & Sons, New York (2000). [in press]
3. Wennu Ma, L.E. Cross, "Observation of the flexoelectric effect in relaxor PB ( $\text{Mg}_{1/3}\text{Nb}_{2/3}\text{O}_3$ ) ceramics", Applied Physics Letters. Volume #8 number 19 pp. 2920
4. R. Hatt and W. Cao, "Landau-Ginzburg Model for Antiferroelectric Phase Transition Based on Microscopic Symmetry", Phys. Rev. B, vol. 62, pp. 818-823 (2000).

#### 2.0 MATERIALS STUDIES

##### 2.1 Polycrystal Perovskite Ceramics

5. A.S. Bhalla, R. Guo, R. Roy, "The Perovskite Structure - A Review of Its Role in Ceramic Science and Technology, "Mat. Res. Innovat., 4(1), 3-26, (2000)
6. E.F. Alberta, R. Guo, L.E. Cross, A.S. Bhalla, "Structure-Property Diagrams of Ferroic Solid Solutions. Part I: Perovskite Ferroelectrics with Morphotropic Phase Boundaries," *Ferroelectrics Review*, 3, 1, (2001)
7. B. Noheda, J.A. Gonzalo, L.E. Cross, R. Guo, S-E. Park, D.E. Cox, G. Shirane, "Tetragonal-to-Monoclinic Phase Transition in a Ferroelectric Perovskite: the Structure of  $\text{PbZr}_{0.52}\text{Ti}_{0.48}\text{O}_3$ , "Phys. Rev. B, 61(13), 8687-8689, (2000)
8. B. Noheda, D.E. Cox, G. Shirane, R. Guo, B. Jones, L.E. Cross, "Stability of the monoclinic phase in the ferroelectric perovskite  $\text{PbZr}_{(1-x)}\text{Ti}_x\text{O}_3$ , "Los Alamos Natl. Lab., Prepr. Arch., Condens. Matter, 1-8, arXiv:cond-mat/0006152, (2000)
9. R. Guo, L.E. Cross, S-E. Park, B. Noheda, D.E. Cox, G. Shirane, "Origin of the high piezoelectric response in  $\text{PbZr}_{1-x}\text{Ti}_x\text{O}_3$ ," Phys. Rev. Letters, 84(23), 5423-5426, (2000)
10. W. Jiang and W. Cao, "Nonlinear Elastic Properties of Lead Zirconate Titanate Ceramics", J. Appl. Phys., vol. 88: 6684-6689 (2000).
11. Chen, Y. H., D. Viehland and K. Uchino, "Substituent Effects in  $0.65\text{Pb}(\text{Mg}_{1/3}\text{Nb}_{2/3})\text{O}_3$ - $0.35\text{PbTiO}_3$  Piezoelectric Ceramics" J. Electroceramics, 6, 13-20 (2001). (First Author Supervised by Candidate).
12. W.H. Jiang and W. Cao, "Intrinsic and Coupling-induced Elastic Nonlinearity of Lanthanum-doped Lead Magnesium Niobate-Lead Titanate Electrostrictive Ceramic", Appl. Phys. Lett., vol. 77, pp. 1387-1389 (2000).

## VOLUME II

### 2.0 MATERIALS STUDIES

#### 2.2 *Single Crystal Systems*

13. L.E. Cross, J. Fousek, "Engineering Multidomain Ferroic Samples", *Ferroelectrics*, 2001, Vol. 252, pp. 171-180.
14. Wada, Satoshi, Takaaki Tsurumi, Miour Osada, Masato Kakihana, Seung Eek Park, L.Eric Cross and Thomas R. Shrout. "Change of Macroscopic and Microscopic Symmetries in Relaxor PZN Single Crystal Under Bias Filed." Transactions of the Material Research Society of Japan, **25** (1). 281-284 (2000).
15. Wada, Satoshi, Takaaki Tsurumi, Miour Osada, Masato Kakihana, Seung Eek Park, L.Eric Cross and Thomas R. Shrout. "Dipolar Behavior in PZN Relaxor Single crystals under Bias Fields." Transactions of the Materials Research Society of Japan **25** (1), 281-284 (2000).
16. Belegundu, U., X. Du and K. Uchino, "Switching Current in  $\text{Pb}(\text{Zn}_{1/3}\text{Nb}_{2/3})\text{O}_3$ - $\text{PbTiO}_3$  Single Crystals," Symp. LL Proc., Mater. Res. Soc. Fall Mtg. '99, (LL.1.9, Boston, Nov. 29-Dec.3. 1999), Vol. **604**, 39-44 (2000).
17. Yu Lu, D.-Y. Jeong, Z. Y. Cheng, Q. M. Zhang, H. Luo, Z. Yin, and D. Viehland. Phase Transitional Behavior and Piezoelectric Properties of the orthorhombic Phase of PMN-PT Single Crystals. *Appl. Phys. Lett.* **78**, 3109 (2001).
18. Yu Lu, Z.-Y. Cheng, E. Park, S. F. Liu and Q. M. Zhang. Linear Electro-optic Effect of  $0.88\text{Pb}(\text{Zn}_{1/3}\text{Nb}_{2/3})-0.12\text{PbTiO}_3$  Single Crystal. *Jpn. J. Appl. Phys.* **39**, 141-145 (2000).
19. Y. Barad, Yu Lu, Z. Y. Cheng, S. E. Park, and Q. M. Zhang. Composition, Temperature, and Crystal Orientation Dependence of Linear Electro-optic Properties of PZN-PT Single Crystals. *Appl. Phys. Lett.* **77**, 1247-1249 (2000).
20. Y. Lu, Z.-Y. Cheng, Y. Barad, and Q. M. Zhang. Photoelastic Effects in the Tetragonal PZN-PT Single Crystals near the Morphotropic Phase Boundary. *J. Appl. Phys.* **89**, 5075 (2001).

#### 2.3 *High Strain Polymers*

21. Vivek Bharti, H. S. Xu, G. Shanthi, Q. M. Zhang, and Kuming Liang. Polarization and Structural Properties of High Energy Electron Irradiated P(VDF-TrFE) Copolymer Films. *J. Appl. Phys.* **87**, 452-461 (2000).
22. Haisheng Xu, G. Shanthi, V. Bharti, Q. M. Zhang, and T. Ramatowski. Structural, Conformational, and Polarization Changes of P(VDF-TrFE) Copolymer Induced by High Energy Electron Irradiation. *Macromolecules*, **33**, 4125-4131(2000).
23. Q. M. Zhang, Z. Y. Cheng, and Vivek Bharti. Relaxor Ferroelectric Behavior in High Energy Electron Irradiated P(VDF-TrFE) copolymers. *Appl. Phys.* **A70**, 307-312 (2000).
24. Vivek Bharti and Q. M. Zhang. Dielectric Study of Relaxor Ferroelectric P(VDF-TrFE) Copolymer System. *Phys. Rev. B.* **63**, 184103 (2001).
25. Z.Y. Cheng, Vivek Bharti, T.B. Xu, Hansheng Xu, T. Mai, and Q. M. Zhang. Electrostrictive P(VDF-TrFE) Copolymers. *Sensors and Actuators A-Phys.* **90**, 138-147 (2001)

26. Z. Y. Cheng, V. Bharti, T. Mai, T. B. Xu, Q. M. Zhang, K. Hamilton, T. Ramotowski, K. A. Wright, and R. Ting. Effect of High Energy Electron Irradiation on the Electromechanical Properties of Poly(vinylidene fluoride-trifluoroethylene) 50/50 and 65/35 Copolymers. *IEEE Trans. UFFC* **47**, 1296 (2000).
27. Vivek Bharti, Z.-Y. Cheng, T. Mai, Q. M. Zhang, T. Ramotowski, K. A. Wright. High Electromechanical Coupling Factor and Electrostrictive Strain over a Broad Frequency Range in Electrostrictive Poly(vinylidene fluoride-trifluoroethylene) Copolymer. *Japn. J. Appl. Phys.* **40**, 672 (2001).
28. Vivek Bharti, G. Shanthi, H. Xu, Q. M. Zhang, and K. Liang. Evolution of Transitional Behavior and Structure of Electron Irradiated P(VDF-TrFE) Copolymer Films. *Mater. Lett.* **47**, 107-111 (2001).
29. F. Xia, H. Xu, F. Fang, B. Razivi, Z. Y. Cheng, Yu Lu, Baoming Xu, and Q. M. Zhang. Thickness Dependence Behavior of Ferroelectric Switching in P(VDF-TrFE) Spin Cast Films. *Appl. Phys. Lett.* **78**, 1122 (2001).
30. Q. M. Zhang, H. S. Xu, Fei Fang, Z.-Y. Cheng, Xia Feng, and H. You. Observation of Critical Thickness of Crystallization in Spin Cast Ferroelectric Thin Films. *J. Appl. Phys.* **89**, 2613 (2001).
31. Shizhuo Yin, Q. M. Zhang, K.-W. Chung, R. Yang, Z. Y. Cheng, and Yu Lu. Investigation of the Electro-optic Properties of Electron-irradiated P(VDF-TrFE) Copolymer. *Opt. Eng.* **39**, 670-672 (2000).
32. Hai-Sheng Xu, Z.-Y. Cheng, Vivek Bharti, Shexi Wang, and Q. M. Zhang. All-Polymer Electromechanical Systems Consisting of Electrostrictive Poly(vinylidene fluoride-trifluoroethylene) and Conductive Polyaniline. *J. Appl. Poly. Sci.* **75**, 945-951 (2000).
33. H. Xu, Z.Y. Cheng, D. Olson, T. Mai, Q. M. Zhang, and G. Kavarnos. Ferroelectric and Electromechanical Properties of P(VDF-TrFE-CTFE) Terpolymer. *Appl. Phys. Lett.* **78**, 2360 (2001).

### 3.0 TRANSDUCER STUDIES

#### 3.1 *Composite Structures*

34. Uchino, K., "Piezoelectro Composites," Chap.5.24, *Comprehensive Composite Materials*, Elsevier Science, Oxford, UK (2000).
35. Tressler, J. and K. Uchino, "Piezoelectric Composite Sensors," Chap.5.22, *Comprehensive Composite Materials*, Elsevier Science, Oxford, UK (2000).

### VOLUME III

36. Meyer, R.J. Jr., A. Dogan, C. Yoon, S. Pilgrim and R.E. Newnham, "Displacement Amplification of Electroactive Materials Using the Cymbal Flexensional Transducer," *Sensors & Actuators A*, vol.87, pp. 157-162 (2001).
37. Dogan, A., K. Uchino and R. E. Newnham, "Flexensional Composite Transducers: Designing, Fabrication and Application," *Proc. NATO- Advanced Research Workshop: Piezoelectric Materials: Advance in Science, Technology and Applications*, (Predeal, Romania, May 24-27, 1999, Kluwer Academic Publ., p.357-374 (2000).

38. Zhang, J., A.C. Hladky-Hennion, W.J. Hughes, and R.E. Newnham, "Modeling and Underwater Characterization of Cymbal Transducers and Arrays," IEEE Transactions on Ultrasonics, Ferroelectrics, and Frequency Control, vol. 48 (2), pp. 560-568 (2001).
39. Zhang, J., W. J. Hughes, R. J. Meyer Jr., K. Uchino and R. E. Newnham, "Cymbal Array: A Broad Band Sound Projector," Ultrasonics 37, 523-529 (2000).
40. Zhang, J., A.C. Hladky-Hennion, W.J. Hughes, and R.E. Newnham, "A Miniature Class V flextensional cymbal transducer with directional beam pattern: The Double-Driver," Ultrasonics, vol. 39, pp. 91-95 (2001).
41. Meyer, R.J. Jr. and R.E. Newnham, "Flextensional transducers with Shape Memory Caps for Tunable Devices," Journal of Intelligent Materials Systems and Structures, vol. 11, pp. 199-205 (2001).
42. Meyer, R.J. Jr., S. Alkoy, J. Cochran, T. Ritter, and R.E. Newnham, "Pre-focused Lead Titanate > 25 MHz Single Element Transducers from Hollow Spheres," IEEE Transactions on Ultrasonics, Ferroelectrics, and Frequency Control, vol. 48 (2), pp. 488-493 (2001).
43. Y. Bai, Z.Y. Cheng, V. Bharti, H. S. Xu, and Q. M. Zhang. High Dielectric Constant Ceramic Powder Polymer Composites. Appl. Phys. Lett. 76, 3804-3806 (2000).
44. M.R. Shen and W. Cao, "Acoustic Bandgap Formation in a Periodic Structure with Multilayer Unit Cells", J. Phys. D: Applied Physics, vol. 33, pp. 1150-1154 (2000).
45. T.B. Xu, Z.-Y. Cheng, Q. M. Zhang, R. Baughman, C. Cui, A. Zakhidov, and J. Su. Fabrication and Characterization of 3-Dimensional Periodic Ferroelectric Polymer-Silica Opal Composites and Inverse Opal. J. Appl. Phys. 88(1), 405-409 (2000).

### 3.2 *Piezoelectric Transformers*

46. Uchino, K., B. Koc, P. Laoratanakul and A. Vazquez Carazo, "Piezoelectric Transformers -New Perspective--," Proc. 3<sup>rd</sup> Asian Mtg. Ferroelectrics, D1d.1, Hong Kong, Dec. 12-15 (2000).
47. Koc, B., and K. Uchino, "Disk Type Piezoelectric Transformer with Crescent Shape Input Electrodes," Proc. NATO- Advanced Research Workshop: Piezoelectric Materials: Advance in Science, Technology and Applications, (Predeal, Romania, May 24-27, 1999, Kluwer Academic Publ., p.375-382 (2000).

### 3.3 *High Power Level Materials*

48. Uchino, K. and S. Hirose, "Loss Mechanisms in Piezoelectrics: How to Measure Different Losses Separately," IEEE UFFC Transactions, 48, 307-321 (2001).
49. Uchino, K., and J. Zheng, Y. H. Chen, X. Du and S. Hirose, "Loss Mechanisms in Piezoelectrics and Resonance/ Antiresonance," Proc. 101st Annual Mtg. of Amer. Ceram. Soc., Symp. Electronic Ceramic Materials and Devices, (Indianapolis, April 25 - 28, 1999), p.79-100 (2000).
50. Uchino, K., J. Zheng, Y. H. Chen, X. Du, S. Hirose and S. Takahashi, "Loss Mechanisms in Piezoelectrics -Extrinsic and Intrinsic Losses--," Mater. Res. Soc. Fall Mtg. '99, (LL.1.6, Boston, Nov. 29-Dec.3, 1999), Vol. 604, 25-31 (2000).

51. Chen, Y. H., S. Hirose, D. Viehland and K. Uchino, "Doping Effects in  $\text{Pb}(\text{Mg}_{1/3}\text{Nb}_{2/3})\text{O}_3\text{-PbTiO}_3$  Ceramics for High Power Transduction Applications," Mater. Res. Soc. Fall Mtg. '99, (LL.5.8, Boston, Nov. 29-Dec.3, 1999), Vol. **604**, 215-220 (2000).
52. Chen, Y. H., S. Hirose, D. Viehland, S. Takahashi and K. Uchino, " Mn-Modified  $\text{Pb}(\text{Mg}_{1/3}\text{Nb}_{2/3})\text{O}_3\text{-PbTiO}_3$  Ceramics: Improved Mechanical Quality Factors for High-Power Transducer Applications," Jpn. J. Appl. Phys. **39**, 4843-4852 (2000).
53. Gao, Y. Y. H. Chen, J. Ryu, K. Uchino and D. Viehland, " Eu and Yb Substituent Effects on the Properties of  $\text{Pb}(\text{Zr}_{0.52}\text{Ti}_{0.48})\text{O}_3\text{-Pb}(\text{Mn}_{1/3}\text{Sb}_{2/3})\text{O}_3$  Ceramics: Development of a New High-Power Piezoelectric with Enhanced Vibrational Velocity," Jpn. J. Appl. Phys., **40**, 79-85 (2001).

## VOLUME IV

### 3.4 *Fluid Structure Interactions*

54. Lauchle, G. C., W. A. Kargus IV. Scaling of Turbulent Wall Pressure Fluctuations Downstream of a Rearward Facing Step. *J. Acoust. Soc. Am.* **107**: L1-L6 (2000).
55. Capone, D. E., G. C. Lauchle. Modeling the Unsteady Lift and Drag on a Finite-Length Cylinder in Cross Flow. *J. Fluids and Struct.* **14**: 799-817 (2000).
56. Gavin, J. R., G. C. Lauchle. Modeling the Space-Time Correlations in the Wake Region of a Turbulent Boundary Layer. *Proc. of the ASME Noise Control and Acoustics Division 2000*, NCA-Vol. 27, pp 227-241 (2000).
57. Gavin, J. R., G. C. Lauchle, M. L. Jonson. Prediction of Turbulence Ingestion Forces for Rotors with Arbitrary Rake and Skew. *Proc. of the ASME Noise Control and Acoustics Division 2000*. NCA-Vol. 27, pp 217-226 (2000).
58. Lauchle, G. C, D. K. McLaughlin. Review of: *Acoustics of Fluid Structure Interactions* by M. S. Howe in *Noise Control Eng. J.* **48**: 70-71 (2000).

## 4.0 ACTUATOR STUDIES

### 4.1 *Materials and Designs*

59. Koc, B. and K. Uchino, "Piezoelectric Ultrasonic Motors," Chap.6.34, Comprehensive Composite Materials, Elsevier Science, Oxford, UK (2000).
60. Uchino, K., "Recent Trend of Piezoelectric Actuator Developments -Material, Design and Drive Technique Related Issues--," Proc. Actuator 2000 (7<sup>th</sup> Int'l Conf. New Actuators, June 19-21, 2000), p.34-39 (2000).
61. Yao, K., K. Uchino, Y. Xu, S. Dong, and L. C. Lim, "Compact Piezoelectric Stacked Actuators for High Power Applications," IEEE Trans. UFFC, **47**, 819-825 (2000).
62. Liu, Rubin, L.e. Cross, Gareth Knowles, Bruce Bower, and Brookd Childers. " A Stackable Bonding-Free Flextensional Piezoelectirc Actuator" *Journal of Electroceramics* **4** (1), 201-206 92000)
63. A. E. Glazounov, Q. M. Zhang, C. Kim. Torsional Actuator Based on Mechanically Amplified Shear Piezoelectric Response. *Sensors and Actuators A* **79**, 22-30 (2000).

#### 4.2 Photostriction

64. Poosanaas, P., K. Tonooka and K. Uchino, "Photostrictive Actuators," J. Mechatronics **10**, 467-487 (2000).
65. Uchino, K., P. Poosanaas and K. Tonooka, "Photostrictive Actuators—New Perspective-," Proc. 3<sup>rd</sup> Asian Mtg. Ferroelectrics, C3p.105, Hong Kong, Dec. 12-15 (2000).
66. Uchino, K., P. Poosanaas and K. Tonooka, "Photostrictive Actuators—New Perspective-," Proc. 5<sup>th</sup> Euroconf. Appl. Polar Dielectrics, O-43, Jurmala, Latvia, Aug. 27-30 (2000).
67. Poosanaas, P., K. Tonooka, I. R. Abothu, S. Komarneni, and K. Uchino, "Influence of Composition and Dopant on Photostriction in Lanthanum-Modified Lead Zirconate Titanate Ceramics," J. Intelligent Mater. Systems and Structures **10**, 439-445 (2000). (
68. Poosanaas, P., Dogan, A., Prasadarao, A. V., Komarneni, S. and Uchino, K., "Effect of Ceramic Processing Methods on Photostrictive Ceramics", J. Advanced Performance Mater. **6**, 57-69 (1999).

### VOLUME V

#### 4.3 High Force Actuators

69. A. E. Glazounov, Q. M. Zhang, and C. Kim. Torsional Actuator and Stepper Motor Based on Piezoelectric  $d_{15}$  Shear Response. J. Intel. Mater. Syst. & Struct. **11**(6), 456-468 (2000).
70. Galante, T., J. Frank, J. Bernard, W. Chen, G.A. Lesieutre, and G.H. Koopmann, "A High-Force, High-Displacement Piezoelectric Inchworm Actuator," Journal of Intelligent Materials Systems and Structures, Vol. 10, No. 12, December, 2000, pp. 962-972.

#### 4.4 Piezoelectric Motors

71. Koc, B. and K. Uchino, "Piezoelectric Ultrasonic Motors," Chap.6.34, Comprehensive Composite Materials, Elsevier Science, Oxford, UK (2000).
72. Uchino, K., and B. Koc, "Compact Piezoelectric Ultrasonic Motors," Proc. NATO-Advanced Research Workshop: Piezoelectric Materials: Advance in Science, Technology and Applications, (Predeal, Romania, May 24-27, 1999, Kluwer Academic Publ., p.309-320 (2000).
73. Koc, B., J. F. Tressler and K. Uchino, "A Miniature Piezoelectric Rotary Motor Using Two Orthogonal Bending Modes of a Hollow Cylinder," Proc. Actuator 2000 (7<sup>th</sup> Int'l Conf. New Actuators, June 19-21, 2000), p.242-245 (2000).
74. Koc, B., J. F. Tressler and K. Uchino, "A Miniature Piezoelectric Rotary Motor Using Two Orthogonal Bending Modes of a Hollow Cylinder," Proc. Actuator 2000 (7<sup>th</sup> Int'l Conf. New Actuators, June 19-21, 2000), p.242-245 (2000).
75. Bouchilloux, P., B. Koc and K. Uchino, "New Concept for Resonant Longitudinal-Shear Ultrasonic Motor," Symp. LL Proc., Mater. Res. Soc. Fall Mtg. '99, (LL.2.10, Boston, Nov. 29-Dec.3, 1999), Vol. **604**, 71-78 (2000).

76. Koc. B., P. Bouchilloux, and K. Uchino, "Piezoelectric Micromotor Using A Metal-Ceramic Composite Structure," IEEE Trans. Ultrasonic, Ferroelectrics, and Frequency Control **47** (4), 836-843 (2000).
- 4.5 *Acoustic Absorbers*
77. Davis, C.L. and G.A. Lesieutre, "An Actively Tuned Solid State Vibration Absorber Using Capacitive Shunting of Piezoelectric Stiffness," Journal of Sound and Vibration, Vol. 232(3), 4 May 2000, pp. 601-617.
  78. Patricia L. Driesch, Hisao Iwata, Gary H. Koopmann, and Jeff Dosch. Nov. 2000. Development and evaluation of a surface acoustic intensity probe. Review of Scientific Instruments, 71 (11), pp. 1-6.
  79. W. Huang. G. H. Koopmann, S. J. Sharp, and W. Chen. April 2000. Enhanced Low Frequency Transmission Loss of Lightweight Trim Panels. Journal of Intelligent Material Systems and Structures, Volume 11, No 4.
  80. E.W. Constans, A.D. Belegundu, and G.H. Koopmann. 2000. Optimally Designed Shell Enclosures with Tuned Absorbers for Minimizing Sound Power. Optimization and Engineering, 1, 67-86, (an International Journal, Kluwer Publishers)

## VOLUME VI

### 5.0 MODELING AND CHARACTERIZATION

#### 5.1 *Design and Simulation*

81. K. Uchino, "Designing With Piezoelectric Devices" International Center for Actuators and Transducers, Materials Research Institute, The Pennsylvania State University, University Park, PA (2000)
82. W.K. Qi, and W. Cao, "Finite Element Study on 1-D Array Transducer Design", IEEE Transaction, Ultra. Ferro. and Frequency Control, vol. **47**, pp. 949-955 (2000).
83. T.A. Ritter, K. K. Shung, W. Cao and T. R. Shrout, "Electromechanical Properties of Thin Strip Piezoelectric Vibrators at High Frequency", J. Applied Phys, vol. **88**, pp. 394-397 (2000).
84. T.A. Ritter, K. K. Shung, W. Cao and T. R. Shrout, "Electromechanical Properties of Thin Strip Piezoelectric Vibrators at High Frequency", J. Applied Phys, vol. **88**, pp. 394-397 (2000).

#### 5.2 *Thick and Thin Films*

85. Kalpat, S., X. Du, I. R. Abothu, A. Akiba, H. Goto and K. Uchino, "Effect of Crystal Orientation on Dielectric Properties of Lead Zirconate Titanate Thin Films Prepared by Reactive RF-Sputtering," Jpn. J. Appl. Phys., **40**, 158-162 (2001).
86. Kalpat, S., X. Du, I. R. Abothu, A. Akiba, H. Goto, S. Trolrier-McKinstry and K. Uchino, "Dielectric Properties of Highly Oriented Lead Zirconate Titanate Thin Films Prepared by Reactive RF-Sputtering," Symp. LL Proc., Mater. Res. Soc. Fall Mtg. '99, (LL.1.3, Boston, Nov. 29-Dec.3, 1999), Vol. **604**, 3-8 (2000).
87. S. Trolrier-McKinstry, "Piezoelectric Films for MEMS Applications," J. Ceram. Soc. Jpn. **109** (5) S76-S79 (2001).



88. Jeong Hwan Park, Fei Xu, and Susan Trolier-McKinstry, "Dielectric and Piezoelectric Properties of Sol-Gel Derived Lead Magnesium Niobium Titanate Films with Different Textures," *J. Appl. Phys.* 89(1) 568 - 574 (2001).
89. Q. F. Zhou, E. Hong, R. Wolf, and S. Trolier-McKinstry, "Dielectric and Piezoelectric Properties of PZT 52/48 Thick Films with (100) and Random Crystallographic Orientation," *Ferroelectric Thin Films*, Vol 655 (2000).
90. L.-P. Wang, R. Wolf, Q. F. Zhou, S. Trolier-McKinstry and R. J. Davis, "Wet-etch patterning of lead zirconate titanate (PZT) thick films for microelectromechanical systems (MEMS) application," *Mat. Res. Soc. Symp.* Vol.657 (MEMS)

### 5.3 Domain Studies

91. Uchino, K., and H. Aburatani, "Field Induced Acoustic Emission in Ferroelectric Ceramics," *Proc. 101st Annual Mtg. of Amer. Ceram. Soc., Symp. Electronic Ceramic Materials and Devices*, SE-56, (Indianapolis, April 25 – 28, 1999), (2000).
92. J. Fousek<sup>ab</sup>, L.E. Cross<sup>b</sup>, "Engineering Multidomain Ferroic Samples, Dept of Physics and International Center for Piezoelectric Research, University of Technology, Liberec, 46117 Czech Republic and <sup>b</sup> Materials Research Laboratory, The Pennsylvania State University, University Park, PA 16802, USA. (June 2000)
93. J.H. Yin, and W. Cao, "Domain Configurations in Domain-Engineered  $0.955\text{Pb}(\text{Zn}_{1/3}\text{Nb}_{2/3})\text{O}_3$ - $0.045\text{PbTiO}_3$  Single Crystals", *J. Appl. Phys.*, vol. 87, pp. 7438-7441 (2000).
94. Rajeev Ahluwalia, "Computer Simulations of Domain Pattern Formation in Ferroelectrics", *AIP Conference Proceedings Series*, © 2001 American Institute of Physics, *Proceedings of the 2001 Workshop on Fundamental Physics of Ferroelectrics* Williamsburg, Va, 2001
95. R. Ahluwalia and W. Cao, "Influence of Dipolar Defects on Switching Behavior in Ferroelectrics", *Phys. Rev. B*, vol. 63, pp. 012103 (2000)
96. Uchino, K., and H. Aburatani, "Field Induced Acoustic Emission in Ferroelectric Ceramics," *Proc. 101st Annual Mtg. of Amer. Ceram. Soc., Symp. Electronic Ceramic Materials and Devices*, SE-56, (Indianapolis, April 25 – 28, 1999), (2000).

# **ACTUATOR STUDIES**

*High Force Actuators*

# **APPENDIX 69**

# Piezoelectric Stepper Motor with Direct Coupling Mechanism to Achieve High Efficiency and Precise Control of Motion

A. E. Glazounov, S. Wang, Q. M. Zhang, *Senior Member, IEEE*, and C. Kim

**Abstract**—The paper describes a piezoelectric motor that combines the merits of piezoelectric materials, such as high power density generated at electromechanical resonance, and a precise control of displacement. In the motor, standing shear wave is excited at the resonance in the piezoelectric tube, and it produces high-frequency torsional vibrations of the stator. The vibrations are converted into unidirectional rotation of a rotor by using a direct coupling mechanism between the stator and the rotor in which a clutch drives the rotor via locking it. The direct coupling makes it possible to transmit the whole power generated in the piezoelectric tube to the rotor, and thus achieve the high efficiency of the motor. It also allows combining two regimes of operation: continuous rotation and a stepwise motion within a 360° interval with a high resolution of angular displacement.

## I. INTRODUCTION

AMONG ACTUATOR materials, piezoelectric materials such as lead zirconate titanate (PZT) are distinguished by the possibility of the precise control of produced displacement and by a high power density that enables operation at high driving frequencies [1]. The applications that make use of these features include, for example, robotics [1], vibration and noise cancellation, and translation stages for optical systems and scanning tunneling microscopes [2], [3]. At the same time, the major demerit of PZT is that the piezoelectric strain is very small. Therefore, in order to convert a small strain into a large displacement, possible solutions include either a built-in amplification mechanism such as a “moonie” [4] or a tubular torsional actuator [5], or an accumulation of the displacement over many periods of the AC driving voltage such as with “inchworm” actuators [1] or ultrasonic motors [6].

Ultrasonic motors also take advantage of the high power density of PZT; and they operate at the electromechanical resonance of the piezoelectric element, which is built into the stator. The displacement is accumulated by convert-

ing the high frequency mechanical vibrations excited at the resonance into the motion of the rotor by using the frictional contact between the stator and the rotor [6]. However, the frictional contact limits the performance of the motor: the energy dissipation due to the friction reduces its efficiency, the torque that can be transmitted from the piezoelectric element is limited by the frictional force, and sliding of the rotor due to its inertia does not enable an instantaneous start-and-stop operation, and hence it is difficult to achieve a precise control over the displacement of the rotor.

This paper will describe a novel type of piezoelectric motor, in which the shortcoming related with the use of frictional contact is eliminated, and thus one fully employs the merits of piezoelectric materials, such as high-power density generated at electromechanical resonance and the precise control of displacement. This becomes possible due to the use of a direct coupling mechanism between the stator and rotor, in which the clutch drives the rotor via locking it. The direct coupling allows transmitting the whole power generated in PZT at the resonance to the rotor, because now there is no energy loss in the frictional contact, and the friction force does not limit the torque. Also, the locking mechanism allows smooth motion either in a continuous or stepwise fashion within a 360° interval with a precise control over angular positioning.

## II. TORSIONAL VIBRATIONS IN PIEZOELECTRIC TUBE

The core element of any piezoelectric motor is the piezoelectric element that excites high frequency vibrations at resonance in the stator, which are then converted into rotation of the rotor via transmission mechanism. In the motor described in this work, the piezoelectric element is made in the form of a tube, Fig. 1(a), which generates high frequency torsional vibrations. This tube was first introduced in [5] as a torsional actuator generating large angular displacement,  $\beta$ , from the amplified shear piezoelectric strain,  $S_5 = d_{15}E_1$ , where  $d_{15}$  is shear piezoelectric coefficient, and  $E_1$  is electric field. From the geometry of the tube, it was shown that, in the case of quasi-static response,  $\beta$  and  $S_5$  were related by [5]:

$$\beta = d_{15}E_1 \cdot L/R_{out}, \quad (1)$$

where the ratio between the length of the tube,  $L$ , and its radius,  $R_{out}$ , serves as a built-in amplification of the piezo-

Manuscript received November 18, 1999; accepted February 2, 2000. This work was supported by DARPA under the Order No. D752.

A. E. Glazounov is with the Institute for Ceramics in Mechanical Engineering, University of Karlsruhe, D-76131 Karlsruhe, Germany.

S. Wang and Q. M. Zhang are with the Materials Research Laboratory and Department of Electrical Engineering, The Pennsylvania State University, University Park, PA 16802 (e-mail: qxz1@psu.edu).

C. Kim is with the Naval Research Laboratory, Washington, DC 20375.

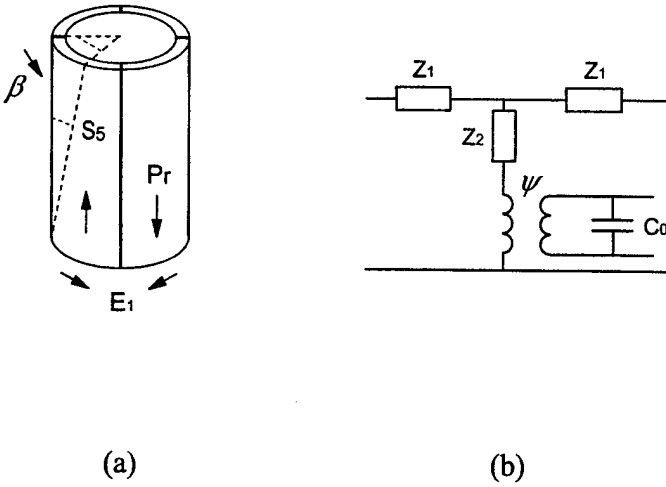


Fig. 1. (a) Piezoelectric ceramic segments are bonded together to form a tube using a conductive adhesive, which also act as electrodes to apply the driving electric field,  $E_1$ . Since the direction of the polarization,  $P_r$ , alternates between the adjacent segments, they exhibit a coherent shear piezoelectric strain  $S_5 = d_{15}E_1$ , and that results in a torsional deformation of the tube on an angle  $\beta$ . (b) Equivalent circuit for torsional vibrations of the tube.

electric strain. This expression was confirmed experimentally in [5], [7]. Similarly, it was shown that the blocking torque developed by the tube in the static regime is given by [8]:

$$T = \frac{A_s R_{out}}{s_{44}^E} \cdot d_{15} E_1, \quad (2)$$

where  $s_{44}^E$  is a shear elastic compliance of the material, and  $A_s = \pi(R_{out}^2 - R_{in}^2)$  is the cross-section area of the tube ( $R_{in}$  is the inner radius of the tube).

However, in the piezoelectric motor, the torsional actuator, Fig. 1(a), must operate at resonance in order to take the advantage of additional amplification of displacement, which occurs at electromechanical resonance in piezoelectric materials [9]. Therefore, in this paper we will first investigate in detail the resonance behavior of the tube. We follow a common approach to describe electromechanical vibrations of piezoelectric bodies [9]. Taking into account cylindrical geometry of the actuator, we choose a cylindrical coordinate system  $(z, r, \theta)$  with  $z$  axis directed along the length of the tube, and used the following choice of crystallographic axes: "3" is along  $z$ , "2" is along the radius, and "1" is along  $\theta$ . Assuming that the tube is long and has thin walls, the corresponding set of piezoelectric equations can be written as:

$$S_5 = s_{44}^E \sigma_5 + d_{15} E_1, \quad (3)$$

$$D_1 = d_{15} \sigma_5 + \epsilon_{11}^T E_1, \quad (4)$$

where  $\sigma_5$  is shear stress,  $D_1$  is electrical displacement, and  $\epsilon_{11}^T$  is dielectric constant of the material in the stress-free conditions. We also assumed that the electric field is uniform in each segment because the thickness of the wall is

much smaller than the average radius of the tube, which is a good approximation for the tubes studied in [5], [7], [8]. Using the same assumptions, the appropriate equation of motion can be derived as [9]:

$$s_{44}^E \rho \frac{\partial^2 \xi_1}{\partial t^2} = \frac{\partial^2 \xi_1}{\partial z^2}, \quad (5)$$

where  $\xi_1$  is the particle displacement defined as:  $\partial \xi_1 / \partial z = S_5$ . This equation describes the plane shear wave propagating along the length of the tube.

Using (3)–(5), one can derive an equivalent circuit for the tube, which will be used for the analysis of vibrations in the stator. The circuit is shown in Fig. 1(b). In this circuit,  $Z_1$  and  $Z_2$  are the impedances of the acoustic network, and  $\psi$  is the electromechanical transformation factor. Their expressions are as follows:

$$Z_1 = j\rho v I \tan(\alpha L/2), \quad (6)$$

$$Z_2 = -j\rho v I / \sin(\alpha L), \quad (7)$$

$$\psi = A_s N_s d_{15} / 2\pi s_{44}^E, \quad (8)$$

where  $N_s$  is the number of segments,  $I = \pi(R_{out}^4 - R_{in}^4)/2$  is the moment of the inertia of the tube,  $\rho$  is the density of PZT ceramics,  $v = 1/(\rho s_{44}^E)^{1/2}$  is sound speed of shear wave, and  $\alpha = 2\pi f(\rho s_{44}^E)^{1/2}$  is the wave number. Clamped electrical capacitance of the PZT tube,  $C_0$ , is defined as  $C_0 = C_0^T(1 - k_{15}^2)$ , where  $k_{15}$  is a piezoelectric coupling coefficient, and  $C_0^T$  is a free electrical capacitance of the tube given by:

$$C_0^T = \frac{N_s^2 L \epsilon_{11}^T}{2\pi} \cdot \ln \left[ \frac{R_{out}}{R_{in}} \right]. \quad (9)$$

Using (5) or an equivalent circuit, one can show that, if one end of the tube is clamped and another is mechanically free, the angular displacement at the free end of the tube,  $\beta = \xi_1 / R_{out}$ , is given by:

$$\beta = d_{15} E_1 \cdot \tan(\alpha L) / \alpha R_{out}, \quad (10)$$

where we also took into account that the wall of the tube is thin,  $R_{out} \gg R_{out} - R_{in}$ . According to (10), the resonance occurs when,  $L = n\lambda/4$ , where  $\lambda$  is the wavelength of shear wave and  $n$  is the odd number. The corresponding resonant frequency is given by:

$$f_n = nL/4(\rho s_{44}^E)^{1/2}. \quad (11)$$

It is worth noting that, in the case of quasi-static response,  $\alpha L \ll 1$ , (10) reduces to (1), which was derived by considering only the geometry of the tube. This indicates that both considerations were consistent. Similarly, from the equivalent circuit, one can show that the blocking torque generated at resonance by the tube is given by:

$$T = \psi U = \frac{A_s R_{out}}{s_{44}^E} \cdot d_{15} E_1, \quad (12)$$

which coincides with the torque developed in the quasi-static regime, (2).

In order to verify the model of the resonance in torsional actuator, the frequency dependence of angular displacement,  $\beta$ , was measured using the PZT tube described in [5], [8]. The tube was made of eight segments of soft PZT ceramics, EC-65 (EDO, Inc.), with  $\rho = 7.5 \text{ kg/m}^3$ ,  $s_{44}^E = 48 \cdot 10^{-12} \text{ m}^2/\text{N}$ , and had a length  $L = 6.4 \text{ cm}$ .  $\beta$  was measured using an MTI-2000 fonic sensor (Mechanical Technology, Inc.) by attaching a mirror on the top of the tube, and measuring the distance change between the mirror and the probe of the MTI-2000. The bottom of the tube was tightly clamped to the optical table. Fig. 2(a) shows the measured values of  $\beta$  and the phase difference between  $\beta$  and driving voltage as a function of frequency. In the plot, one can see two peaks in  $\beta(f)$  that correspond to the first and third resonance harmonics [ $n = 1$  and  $3$  in (11)]. Their positions are in very good agreement with the values calculated from the material properties and the length of the tube using (11), which are shown by arrows in Fig. 2(a). However, when  $n = 2, 4$ , etc., the angular displacement drops to zero, Fig. 2(a), in agreement with prediction of (10). Finally, one can see, Fig. 2(a), that the model reproduces the frequency dependence of the phase difference, which changes on  $180^\circ$  when  $\alpha L = \pi/2, \pi$ , etc., (10).

Another parameter describing the electromechanical resonance is the complex electrical admittance,  $Y^*$ , of piezoelectric element [9]. Using the equivalent circuit of the tube, Fig. 1(b), one can show that, when one end of the tube is free and another is clamped, the admittance is described by:

$$Y^* = j2\pi f C_0^T (1 - k_{15}^2 + k_{15}^2 \tan(\alpha L)/\alpha L) = Y \cdot \exp(j\theta_Y). \quad (13)$$

For the same tube as in Fig. 2(a), the measured frequency dependence of the amplitude of electrical admittance,  $Y$ , of the tube, and its phase angle,  $\theta_Y$ , is shown in Fig. 2(b). In this plot, the positions of maxima and minima in  $Y(f)$  correspond to resonance,  $f_r$ , and antiresonance,  $f_a$ , frequencies [9] of the shear mode, respectively.  $f_r$  is given by (11), and  $f_a$  is defined by the condition  $Y(f_a) = 0$  in (13). The arrows in the plot indicate their positions, which were calculated using material parameters of EC-65 (EDO, Inc.),  $\rho = 7.5 \text{ kg/m}^3$ ,  $s_{44}^E = 48 \cdot 10^{-12} \text{ m}^2/\text{N}$ , and  $k_{15} = 0.69$ , and the length of the tube,  $L = 6.4 \text{ cm}$ . Similarly to  $\beta(f)$ , the estimated values agreed well with the measured ones, Fig. 2(b).

To summarize, the experimental and theoretical study of piezoelectric resonance in torsional actuator, Fig. 1(a), demonstrated that, in the tube the resonance is related to the shear wave propagating along the length of the tube, and that this wave is a fundamental mode. The resonance frequency,  $f_r$ , is determined by the length of the tube and sound speed of the shear wave, (11).

In [8], we also proposed to use another geometry of torsional actuator in order to significantly simplify the fabrication process. Piezoelectric tube with a polygonal cross

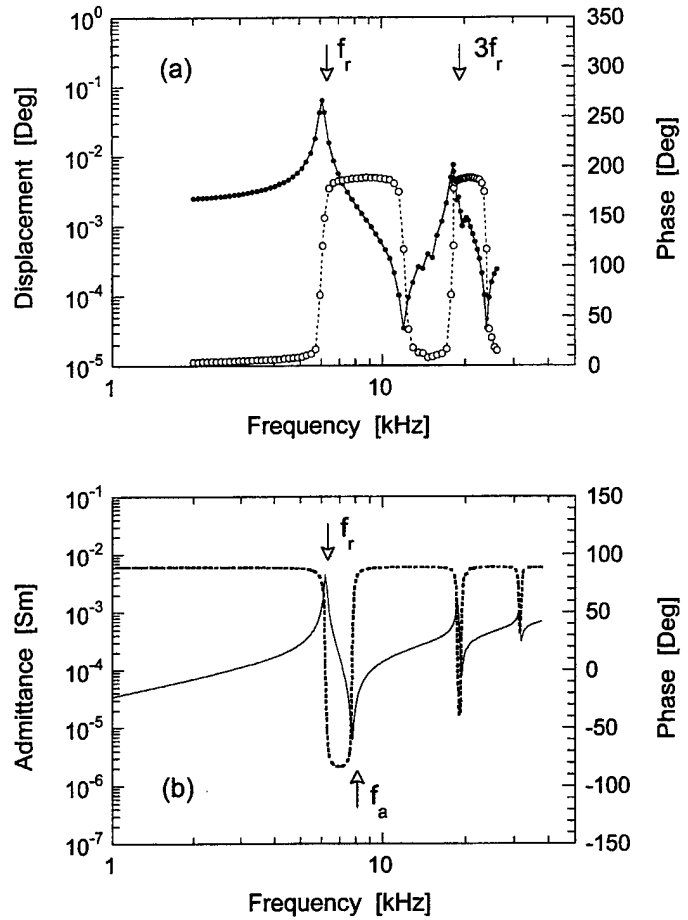


Fig. 2. (a) Frequency dependence of the amplitude of angular displacement,  $\beta$ , generated by cylindrical PZT tube, and of the phase shift between  $\beta$  and driving voltage. Arrows indicate positions of first and third resonance harmonics, calculated from (11). (b) Frequency dependence of electrical admittance of the PZT tube.  $f_r$  and  $f_a$  are the frequencies of resonance and antiresonance, calculated using material parameters for PZT and the length of the tube.

section was proposed and studied both experimentally and theoretically, using the finite element modeling. It was shown that, in the quasi-static regime, the magnitudes of angular displacement and the blocking torque generated by polygonal tube were close to those by the cylindrical tube, given by (1) and (2) [7]. In this work, the resonance behavior of the polygonal tube was studied, and the data are summarized in Fig. 3, in comparison with those for the cylindrical tube from Fig. 2. As one can see, the polygonal tube has a similar resonance pattern, and the difference in the positions of maxima and minima in  $Y(f)$ , Fig. 3(a), and peaks in  $\beta(f)$ , Fig. 3(b), can be attributed only to the difference in the length of the tube (the polygonal tube was approximately two times longer than the cylindrical one). For the polygonal tube, the resonance frequency determined from  $\beta(f)$  and  $Y(f)$ , Fig. 3, were compared with (11), and the values agreed well. Taken together, these experimental data indicate that, even in the tube with the polygonal cross section, the electromechanical resonance is related with the shear wave propagating along the length of the tube. The standing shear wave excited at resonance

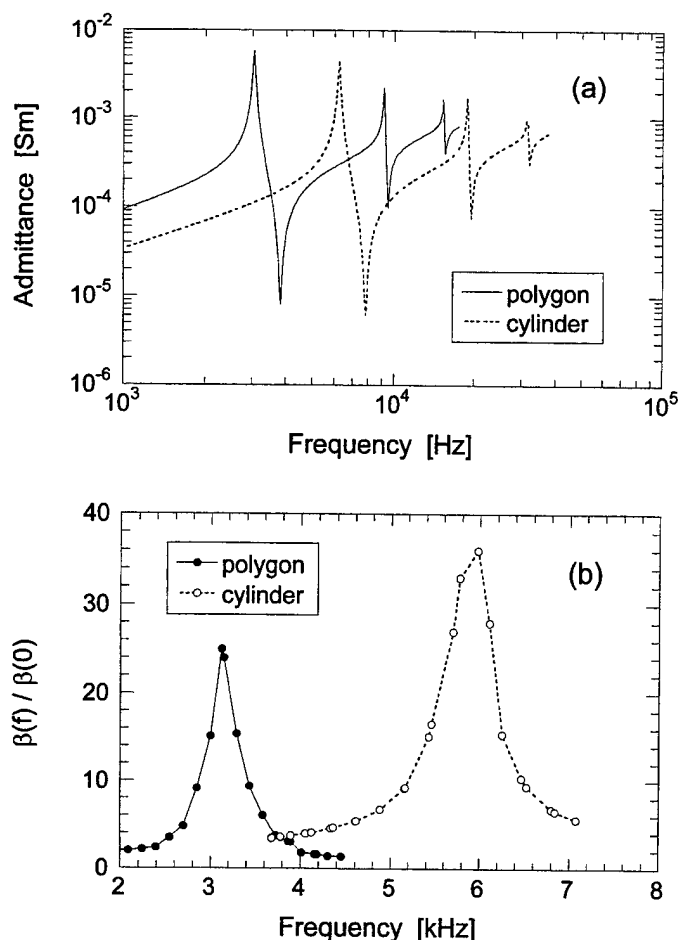


Fig. 3. (a) Frequency dependence of the electrical admittance of two piezoelectric tubes, with polygonal (solid line) and cylindrical (dotted line) shapes. (b) Frequency dependence of the torsional angle normalized over its quasi-static value for the same tubes as in (a). The frequency range is now limited to the interval around the first resonant harmonic.

produces a pure twisting deformation of the tube, and the magnitude of deformation is strongly enhanced compared to the that produced in the quasi-static response [8]. Finite element modeling (B. Koc, personal communication) of the deformation in the polygonal tube at resonance supported this conclusion.

### III. DESIGN OF THE MOTOR

The design of the proposed motor is shown in Fig. 4(b). In order to transmit the high frequency torsional vibrations excited by the piezoelectric tube, Fig. 1(a), into unidirectional motion of the rotor, "6", the motor employs an one-way roller clutch, Fig. 4(a). The clutch sits in the housing, "4", which is connected to the tube, "1". When the tube with the clutch twists counterclockwise, Fig. 4, the clutch locks the rotor, "6", with rollers [because the rollers are wedged between the tilted slope of the cam and the surface of the rotor, Fig. 4(a)], and transmits the displacement. On the contrary, if the tube twists clockwise, the clutch releases the rollers, and they do not transmit

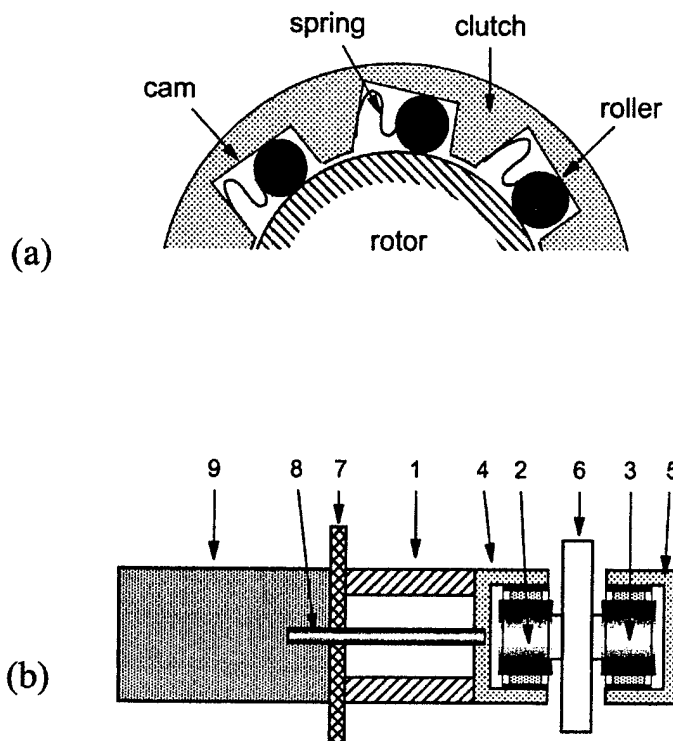


Fig. 4. (a) Roller clutch transmits the displacement to the rotor only if it moves in the counterclockwise direction, when the rollers are wedged between the tilted slope of the cam and the surface of the rotor. In the clockwise direction, the rollers disengage and do not transmit the displacement. (b) The proposed piezoelectric motor consists of piezoelectric tube shown in Fig. 1, "1", two clutches, shown in (a), "2" and "3", housing for clutches "4" and "5", metal shim, "7", and the rotor, "6". Bolt "8" tightens together piezoelectric tube and a metal cylinder "9", which is required in order to have zero angular displacement in the shim at resonance.

the displacement to the rotor in this direction. Thus, the clutch accumulates the angular displacement in one direction. To our knowledge, this direct coupling between stator and rotor, via locking the rotor, is an unique feature of the proposed motor as compared to other existing designs [1], [6], which all use a frictional contact to transmit the motion to the rotor.

The motor also includes the following components. An identical second clutch, "3", is mounted to the external support and used to prevent motion in the opposite direction [clockwise in Fig. 4(a)], when the external torque load is applied to the rotor. A thin metal shim, "7", is used for mounting the motor in the external support. A bolt, "8", tightly clamps together the housing "4" with clutch, the torsional tube, "1", and a metal cylinder, "9". The latter is required to have a displacement node at the shim, to avoid the transmission of displacement into external housing.

The condition to have a displacement node in the shim sets the requirement for dimensions of all the components of the motor. They must be such that, at the resonance frequency, the lengths of the part above the shim and below it are each equal to  $\lambda/4$ , in which  $\lambda$  is the wavelength of the shear waves in the two parts. To evaluate these dimensions, an equivalent circuit analy-

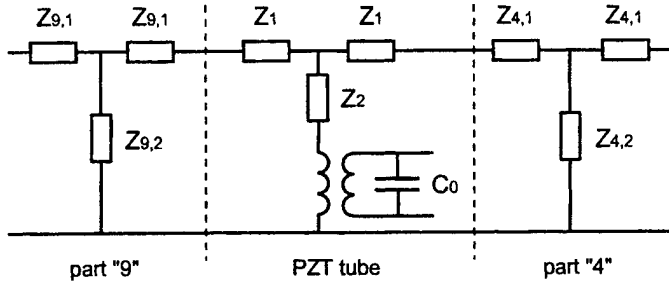


Fig. 5. Equivalent circuit for stator shown in Fig. 4.

sis of piezoelectric vibrations was employed. The equivalent circuit of the motor is shown in Fig. 5. It was constructed based on the equivalent circuit for torsional vibrations in the piezoelectric tube, Fig. 1(b). In the circuit, impedances of the acoustic network of metal parts "4" and "9" are denoted as  $Z_{4,1}$ ,  $Z_{4,2}$ , and  $Z_{9,1}$ ,  $Z_{9,2}$ , respectively. They are given by expressions similar to (6) and (7), such as:  $Z_{4,1} = j\rho_m \nu_m I_4 \tan(\alpha_m L_4/2)$ ,  $Z_{4,2} = -j\rho_m \nu_m I_4 / \sin(\alpha_m L_4)$ ,  $Z_{9,1} = j\rho_m \nu_m I_9 \tan(\alpha_m L_9/2)$ , and  $Z_{9,2} = -j\rho_m \nu_m I_9 / \sin(\alpha_m L_9)$ . In these expressions,  $I_4$  and  $I_9$  are the moments of the inertia of corresponding parts, and  $\rho_m$  is the density of the metal. The sound speed of shear wave in the metal and the corresponding wave number are given by  $\nu_m = (G_m/\rho_m)^{1/2}$  and  $\alpha_m = 2\pi f(\rho_m/G_m)^{1/2}$ , respectively, where  $G_m$  is the shear elastic modulus of the metal.

From an equivalent circuit in Fig. 5, one can show that in order to have  $\lambda/4$  parts both above and below the shim, the following relationships must be satisfied simultaneously:

$$\rho_m \nu_m I_4 \cdot \tan(\alpha_m L_4) \cdot \tan(\alpha L) = \rho \nu I, \quad (14a)$$

$$\alpha_m L_9 = \pi/2. \quad (14b)$$

We used both equations to evaluate the parameters necessary to build the motor. We first selected the dimensions of the piezoelectric tube, "1", and metal housing, "4", then determined the resonant frequency,  $f_r$ , by graphically solving (14a). Afterward, from (14b) we determined the length  $L_9$  of the metal part below the shim.

#### IV. PROTOTYPE MOTOR

A prototype motor was built according to the design shown in Fig. 4(b). Hard PZT ceramics (APC-841 from American Piezoceramics) for the tube, and hard aluminum for the metal parts were used in order to have low mechanical losses in the stator. The tube was made in the shape of 8-sided polygon by using the silver-filled epoxy compound MB-10HT/S (Master Bond, Inc.) as joints between the segments. The dimensions of the tube were:  $L \approx 24$  mm,  $R_{out} \approx 8$  mm, and  $R_{in} \approx 5$  mm. Both clutches, "2" and "3", were commercially available products from Torrington. In order to provide a good mechanical contact between

different components in the stator, the contact surfaces of each component were carefully polished using an abrasive mixture of  $Al_2O_3$  powder suspended in water. Final polishing was done with 50-nm size powder. The stator was assembled using the bolt to tighten together metal and ceramic components. The resonance frequency of the stator measured at low driving voltage, 1 Vrms, was approximately equal to 10 kHz and agreed well with the value of  $f_r$  determined from (14a).

To characterize the performance of the motor, the following experiments were performed. The angular displacement at the free end of the stator was measured as a function of the amplitude and frequency of the driving voltage. The voltage was applied from a SR-360 function generator (Stanford Research Systems) through an AVC-790A01 power amplifier (PCB Piezotronics, Inc.).  $\beta$  was measured by attaching a small mirror on the top of the housing "4", Fig. 4(b), and measuring the distance change between the mirror and the optical probe of the MTI-2000 fonic sensor. From these measurements, the resonance frequency,  $f_r$ , and the mechanical quality factor of the stator,  $Q_L$ , were determined. The latter relates the displacement produced at the resonance with the quasi-static one, (1), according to [9]:

$$\beta(f_r) = Q_L \cdot d_{15} E_1 \cdot L / R_{out}. \quad (15)$$

(15) directly follows from (10) if one takes into account mechanical losses in the material [9]. If the motor was driven continuously, revolution speed,  $\Omega$ , of the rotor was measured as a function of the amplitude of driving voltage and compared with the angular displacement,  $\beta(f_r)$ . For this motor, one expects the following relationship between the two parameters:

$$\Omega = 2\beta(f_r)f_r/360^\circ, \quad (16)$$

where factor 2 appears because the clutch drives the rotor during half of a period of the AC voltage when the displacement changes from  $-\beta$  to  $+\beta$ . In another experiment, the motor was driven in the stepwise mode, when the driving voltage was applied in the form of the tone-burst, using a given number,  $N$ , of the AC cycles at frequency  $f_r$ . Here, the angular displacement,  $\varphi$ , of the rotor accumulated over  $N$  cycles, was measured as a function of  $N$ .

#### V. RESULTS

Fig. 6 demonstrates proof of the concept of the proposed motor. When an AC voltage was applied to the piezoelectric tube, the rotor was moving with the revolution speed  $\Omega$ , which increased toward saturation with increasing voltage (open circles). This behavior of  $\Omega$  correlates with the voltage dependence of the amplitude of the torsional vibration  $\beta$  (closed circles). Both  $\Omega$  and  $\beta$  were measured at a fixed frequency,  $f = 9.8$  kHz, around the resonance.

Two other features should be noticed in Fig. 6. The first feature is that from (15), one would expect that  $\beta$ , and



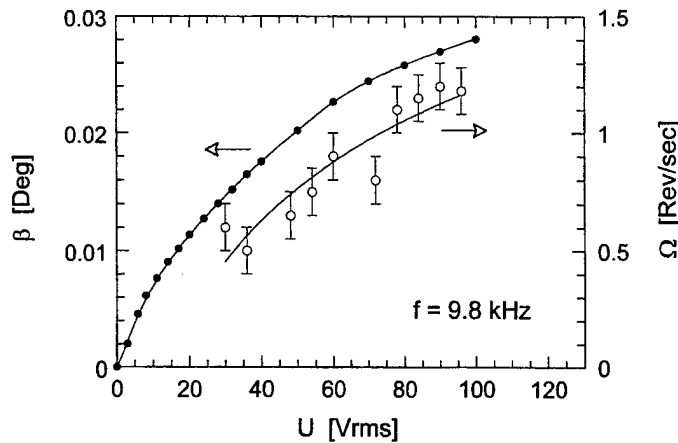


Fig. 6. Amplitude of torsional vibrations of the stator,  $\beta$ , and the revolution speed of the rotor  $\Omega$ , as a function of the AC driving voltage (the frequency is constant, 9.8 kHz).

therefore  $\Omega$ , should increase linearly with the voltage (or electric field). The deviation from the linear function, seen in Fig. 6, is due to the strong frequency and field dependence of the piezoelectric response around the resonance [10], which is illustrated in Fig. 7. When the amplitude of the driving voltage (electric field) is increased, the position of the resonance peak in  $\beta(f)$  shifts toward lower frequencies, Fig. 7(a), due to the softening of the piezoelectric material under the high stress developed in it at the resonance [9], [10]. As a result, this shift in the resonance peak will lead to the saturation in the field dependence of the displacement measured at a fixed frequency (for example,  $f = 9.9$  kHz). This is clear from a comparison of the plots in Figs. 7(a) and (b). At the same time, the displacement at the peak,  $f = f_r$ , still follows a linear dependence predicted by (15), as shown with open circles in Fig. 7(b). From the comparison of  $\beta(f_r)$  with  $\beta(f)$  measured at  $f = 20$  Hz, which corresponded to the quasi-static response, the mechanical quality factor of the stator was evaluated:  $Q_L \approx 100$ .

The second feature is that the rotation had some threshold and in the studied prototype the rotor did not move when the driving voltage was below 30 Vrms, Fig. 6. This threshold is due to the backlash, or lost displacement,  $\Delta\beta$ , which is a common feature of clutches available on the market. One can evaluate  $\Delta\beta$  from the data shown in Fig. 6. Without backlash, the amplitude of the torsional vibrations and the revolution speed should be related by (16). However, with the lost displacement, this relationship changes to:  $\Omega \cdot 360^\circ \cdot f_r^{-1} = 2\beta - \Delta\beta$ . Using this formula from Fig. 6, we can evaluate the backlash as:  $\Delta\beta \approx 0.01^\circ$ .

Even though the backlash is fairly small, it sets some limits on the performance of the prototype motor. Still, it is surprising that the motor could operate even using commercially available roller clutches, which in principle are not designed for operation with such small angular oscillations, of the order of  $0.01^\circ$  (Fig. 6). With improved clutch, the lost displacement can be completely eliminated, as it is done for example in watch mechanisms. This would

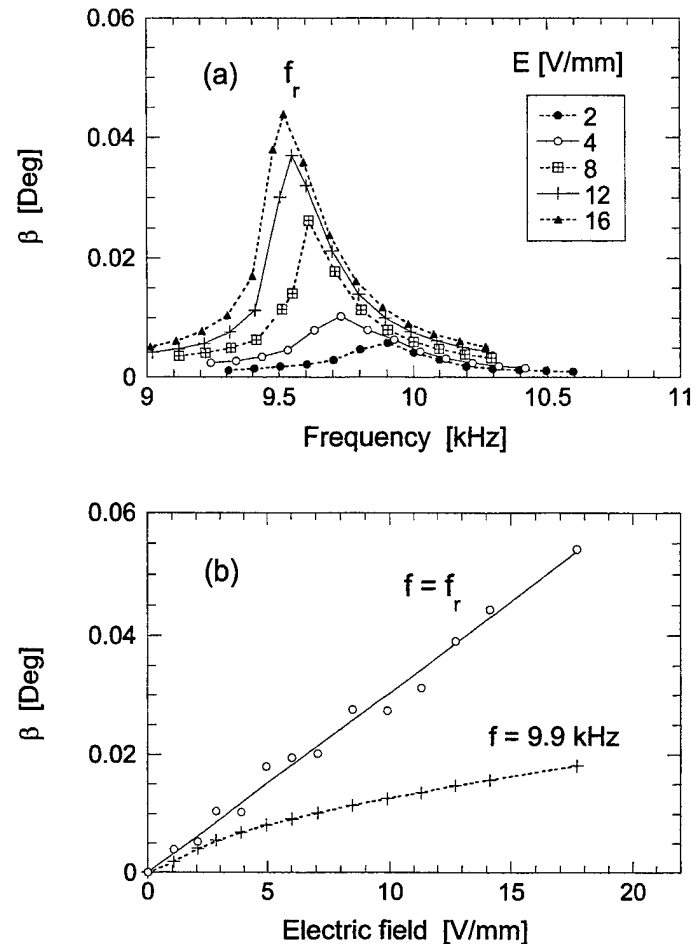


Fig. 7. Amplitude of torsional vibrations of the stator,  $\beta$ , around the resonance. (a) Frequency dependence of  $\beta$ , measured at different levels of the AC driving field,  $E$ , showing the peaks at the resonant frequency,  $f_r$ . (b) Field dependence of  $\beta$  measured at a fixed frequency, 9.9 kHz (plus signs), and at the resonance,  $f_r$  (open circles).

allow better control over the motion and would improve the torque transmitted to the rotor, which is also affected by the backlash, as will be discussed later in the paper.

Hence, the experimental data summarized in Fig. 6 prove the proposed concept. Namely, to use the clutch as a coupling mechanism to accumulate the angular displacement generated by the piezoelectric tube and produce unidirectional motion of the rotor. Moreover, because the clutch drives the rotor by locking it, this allows achieving not only a continuous rotation, but also a controlled stepwise motion of the rotor over a finite angle.

In order to produce the stepwise motion, the driving voltage can be applied in the form of the tone burst, using a given number,  $N$ , of AC cycles at a frequency  $f$ . The angular displacement,  $\varphi$ , of the rotor accumulated over  $N$  cycles can be written as:  $\varphi = [2\beta - \Delta\beta] \cdot N$ , where  $\beta$  is the amplitude of the vibrations of the stator corresponding to the same frequency of the driving voltage, and we took into account the backlash,  $\Delta\beta$ . Fig. 8(a) shows the example of the angular displacement as a function of  $N$ , measured using the AC voltage with frequency 9.6 kHz and amplitude 62 Vrms. The fit of the linear relationship,  $\varphi \propto N$ , to the

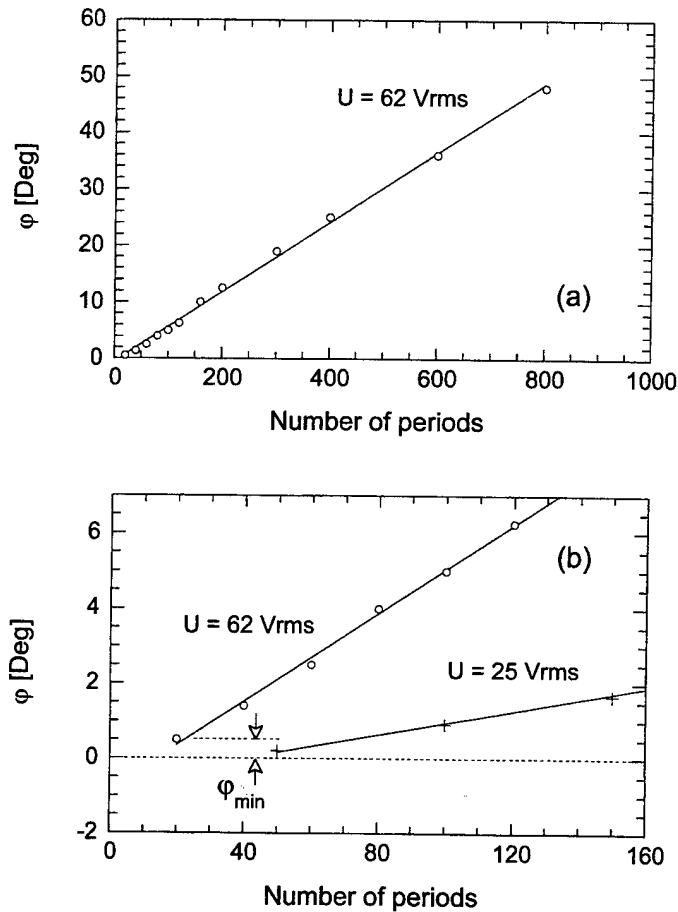


Fig. 8. The angular displacement of the rotor,  $\varphi$ , measured in the stepwise motion as a function of the number of the cycles,  $N$ , in the burst, and its fit to the linear law. Plot in (a) shows that  $\varphi$  can be controlled within  $360^\circ$  interval by controlling  $N$ . Here, the frequency of the driving voltage is 9.6 kHz and the amplitude is 62 Vrms. (b) The magnified part of the plot from (a) demonstrates that there exists a minimum value of  $N$  required to move the rotor, and the minimum achievable displacement  $\varphi_{\min}$ , which sets the resolution limit for the motion. By changing the voltage from 62 Vrms to 25 Vrms, one can achieve better control of angular positioning with resolution  $\varphi_{\min} = 0.2^\circ$ .

data yields the slope equal to  $0.058 \pm 0.002$  [Deg], which has a meaning of the displacement of the rotor per cycle of driving voltage. Using the obtained value of the slope,  $\varphi/N$ , and  $\beta = 0.04^\circ$  measured at 9.6 kHz, we can calculate  $\Delta\beta \approx 0.02^\circ$ , which is in a reasonable agreement with the value  $\Delta\beta \approx 0.01^\circ$  estimated from the data shown in Fig. 6.

The resolution limit for the stepwise motion can be determined by reducing the number of cycles,  $N$ , and measuring the smallest achievable displacement of the rotor,  $\varphi_{\min}$ . At 62 Vrms and 9.6 kHz, we found that this prototype motor could be easily controlled down to  $\varphi_{\min} = 0.5^\circ$ , as shown in Fig. 8(b). By changing the driving voltage to 25 Vrms, we could achieve even better control,  $\varphi_{\min} = 0.2^\circ$ , Fig. 8(b), because of the increase in the number of cycles required to move the rotor:  $N = 50$ , compared to  $N = 20$ . Hence, this experiment demonstrated that, even with the available clutch, the motor can pro-

duce a stepwise motion with a precise control over angular positioning.

## VI. TORQUE GENERATED BY THE MOTOR

Another characteristic of ultrasonic motors is a torque developed at the output at a given mechanical load and its maximum value, which is referred to as a stall torque [6]. In this work, we cannot present experimental data that would show the revolution speed vs. torque diagram. This is a subject of ongoing experiments. However, we will discuss the parameters that can determine the torque output in the proposed design of the motor.

In any piezoelectric motor, the stall torque is determined by the torque generated in the stator itself and by coupling mechanism, which transmits the torque from the stator to the rotor. To our knowledge, almost all of the existing designs of piezoelectric motors utilize frictional contact between stator and rotor as a coupling mechanism. It is clear that, in this case, the friction force determines the stall torque [6]. On the contrary, the present design of the motor uses the direct coupling mechanism, via locking the rotor by a one-way clutch. Now the friction force does not limit the torque any longer; and, in the ideal case, the stall torque will be equal to the blocking torque developed by the PZT tube. The only factor that can limit the torque transmission will be the backlash,  $\Delta\beta$ , in the clutch (obviously, the lost displacement reduces the torque transmitted). However, the backlash can be eliminated by redesigning the clutch mechanism. After this improvement, the torque will be transmitted from the stator to the rotor completely, and hence the performance of the motor will be fully determined only by the properties of the stator.

We now consider the blocking torque generated by the stator. It can be evaluated using equivalent circuit shown in Fig. 5. One obtains the following expression:

$$T = \frac{A_s R_{out}}{s_{44}^E} \cdot d_{15} E_1 \cdot \cos(\alpha_m L_4). \quad (17)$$

It differs from the blocking torque of PZT tube itself, (12), only by factor  $\cos(\alpha_m L_4)$ , which is related to the metal housing of clutch, "4" in Fig. 4. This factor appears because the housing is not an infinitely rigid body; therefore, some part of the torque generated by the PZT tube will be consumed on the twisting of the part, "4", when the external load is applied. However, one can neglect this term either if the metal is rigid enough,  $G_m \rightarrow \infty$ , and thus  $\alpha_m \rightarrow 0$ , or if the length of the metal housing is smaller than the length of PZT tube,  $L_4 < L$ .

Another factor can affect the torque, compared to the prediction of (17). It is related with the way the stator is assembled, and so far it has not been taken explicitly into account in the equivalent circuit in Fig. 5. Fig. 9 shows the voltage dependence of angular displacement  $\beta$  at the free end of the stator measured in the quasi-static regime, at 20 Hz. In the plot, circles show the data for two stators assembled with a bolt, as in Fig. 4. In one case

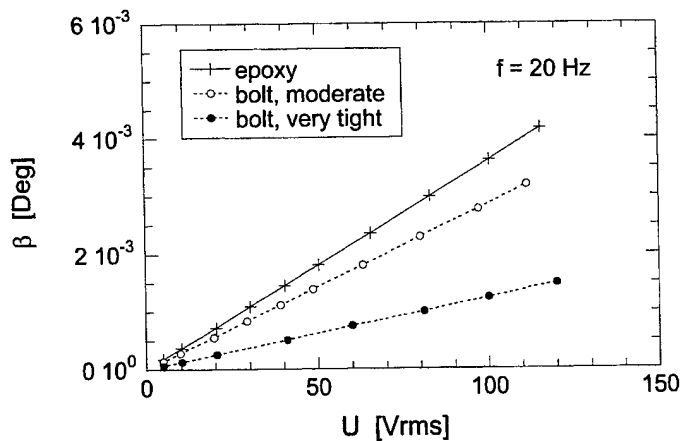


Fig. 9. Amplitude of torsional vibrations of the stator,  $\beta$ , as a function of the AC driving voltage measured at 20 Hz. The stator is assembled using either epoxy resin (plus signs) or bolt (open and closed circles). When the bolt is used, it introduces an additional rigidity into stator, and thus reduces angular displacement. The stronger the tightening of the bolt, the larger is the reduction of  $\beta$ .

the tightening of the bolt was stronger than in the other. The plus signs correspond to the data from the stator assembled without the bolt, using epoxy resin. Because all studied stators had the same dimensions, the difference in the slope of straight lines can be interpreted as a difference in the effective  $d_{15}$  coefficient, according to (1). In the case of epoxy adhesive, the effective  $d_{15}$  determined from Fig. 9, was equal to 450 pm/V, which agrees well with the data provided by the manufacturer (American Piezoceramics),  $d_{15} = 480$  pm/V. The stators assembled using the bolt had smaller values of effective piezoelectric coefficient:  $d_{15} = 350$  pm/V, and  $d_{15} = 200$  pm/V. The lowest value of  $d_{15}$  was observed in the stator with the strongest tightening of all the components (closed circles in Fig. 9).

The reduction in effective piezoelectric coefficient  $d_{15}$  can be attributed to the fact that the bolt could apply a compressive stress to the PZT, and thus change the material properties [11], and that it introduced an additional rigidity into the stator. The latter also manifests itself in the reduction of the effective shear elastic compliance,  $s_{44}^E$ , of the stator. However, we found that this effect was much weaker. We could make this conclusion based on the comparison of resonant frequencies,  $f_r$ , of stators assembled with bolt and with epoxy resin. The difference in  $f_r$  was very small. Using (11), we estimated that it corresponded to the change in effective  $s_{44}^E$  of about 10–20%. This effect is smaller than the reduction in  $d_{15}$  shown in Fig. 9, and therefore, is of less concern.

However, the use of bolt in the present design of piezoelectric motor is desirable, because it can eliminate problems related with epoxy adhesive, such as shear strength of adhesive and its mechanical fatigue due to high-shear stress developed at resonance, which are both well-known from the field of high-power ultrasound transducers [12]. However, as is clear from this work, the bolt reduces the value of effective  $d_{15}$ , which will reduce the blocking torque developed by the stator. It is worth noting that this reduc-

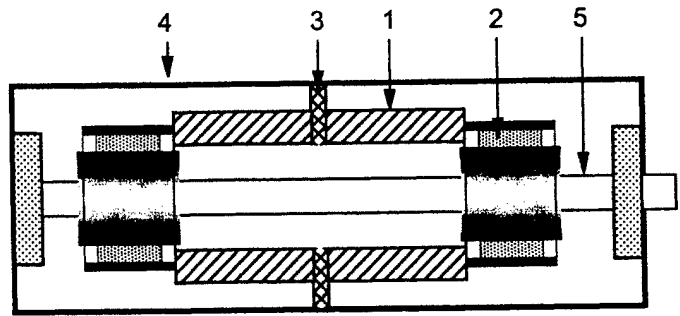


Fig. 10. Schematic drawing of the piezoelectric motor that operates in the full-cycle mode. The stator consists of two identical PZT tubes, "1", two clutches, "2". It is mounted to the housing, "4", through metal shim, "3". The rotor is now shaft, "5".

tion of  $d_{15}$  is not so dangerous for the angular displacement at resonance,  $\beta(f_r)$ , and revolution speed of the rotor,  $\Omega$ . Even though both depend upon  $d_{15}$  according to (15) and (16), they are also determined by the mechanical quality factor of the stator,  $Q_L$ . No special study of the effect of tightening of the bolt on  $Q_L$  was undertaken in this work. It only was noticed that the use of the bolt resulted in higher values of  $Q_L$ , which, therefore, compensated at the resonance the reduction of  $d_{15}$ .

## VII. OPERATION OF THE MOTOR IN THE FULL-CYCLE MODE

The motor shown in Fig. 4(b) drives the rotor during half of a period of the applied AC voltage, when the angular displacement generated at resonance changes from  $-\beta$  to  $+\beta$ . However, one can modify the design so that the stator will drive the rotor during the full cycle of the AC voltage. A possible solution [13] is shown in Fig. 10. The design of the stator is similar to that shown in Fig. 4(b), except now the metal part "9" is replaced by the identical PZT tube, which also has a clutch connected to it. The tubes, "1", and the clutches, "2", with their housings are assembled together using epoxy adhesive, and the stator is mounted to the housing, "4", through shim, "3". The rotor is the shaft, "5", inserted in both clutches. Because the two sides vibrate in opposite directions, one of them will drive the rotor during one-half of a period of the AC voltage, and the second side will drive during another half. Thus, both the speed and torque output will be improved compared to the design with a single tube.

## VIII. CONCLUSIONS

A novel design of a piezoelectric motor was proposed and demonstrated. It takes advantage of the torsional motion generated at the resonance in the stator, and of the direct coupling between the rotor and the stator in which the clutch drives the rotor via locking it. It was shown that the direct coupling makes it possible to produce a smooth motion either in the continuous or in the stepwise fashion

within a  $360^\circ$  interval. In the stepwise motion, a precise control over angular positioning with an accuracy of  $0.02^\circ$ , has been demonstrated. It has been shown that, due to direct coupling which eliminates the problem of energy loss in the friction contact, the whole power generated in PZT at the resonance can be transmitted to the rotor, and the direct coupling also does not limit the torque. Further improvement of the performance of the proposed motor can be achieved by improving the clutch mechanism to eliminate the backlash.

#### ACKNOWLEDGMENTS

The authors would like to thank Mr. B. Koc for finite element modeling of resonance behavior in polygonal tube, and Mr. C. Jabco for his help in making the motor.

#### REFERENCES

- [1] K. Uchino, *Piezoelectric Devices and Ultrasonic Motors*. Boston: Kluwer, 1997.
- [2] P. Niedermann, R. Emch, and P. Descouts, "Simple piezoelectric translation device," *Rev. Sci. Instrum.*, vol. 59, pp. 368-369, 1988.
- [3] C. J. Chen, "Electromechanical deflections of piezoelectric tubes with quartered electrodes," *Appl. Phys. Lett.*, vol. 60, pp. 132-134, 1992.
- [4] Y. Sugawara, S. Yoshikawa, Q. Xu, R. E. Newnham, and K. Uchino, "Metal-ceramic composite actuators," *J. Amer. Ceram. Soc.*, vol. 75, pp. 996-998, 1992.
- [5] A. E. Glazounov, Q. M. Zhang, and C. Kim, "Piezoelectric actuator generating torsional displacement from piezoelectric  $d_{15}$  shear response," *Appl. Phys. Lett.*, vol. 72, pp. 2526-2528, 1998.
- [6] S. Ueha and Y. Tomikawa, *Ultrasonic Motors: Theory and Applications*. Oxford: Oxford Univ. Press, 1993.
- [7] A. E. Glazounov, Q. M. Zhang, and C. Kim, "Torsional actuator based on mechanically amplified shear piezoelectric response," *Sens. and Actuators A*, vol. A79, pp. 22-30, 2000.
- [8] C. Kim, A. E. Glazounov, F. D. Flippen, A. Pattnaik, Q. M. Zhang, and D. Lewis, III, "Piezoelectric ceramic assembly tubes for torsional actuators," in *Proc. SPIE Smart Struct. and Mater.*, vol. 3675, pp. 53-62, 1999.
- [9] D. Berlincourt, D. Curran, and H. Jaffe, *Physical Acoustics*. vol. 1, pt. A, W. Mason, Ed. New York: Academic, 1969, pp. 169-269.
- [10] H. Beige and G. Schmidt, "Electromechanical resonances for investigating linear and nonlinear properties of dielectrics," *Ferroelectrics*, vol. 41, pp. 39-49, 1982.
- [11] Q. M. Zhang, J. Zhao, K. Uchino, and J. Zheng, "Change in the weak-field properties of  $\text{PbZrTiO}_3$  piezoceramics with compressive uniaxial stresses and its links to the effect of dopants on the stability of the polarizations in the materials," *J. Mater. Sci.*, vol. 12, pp. 225-234, 1997.
- [12] J. R. Frederick, *Ultrasonic Engineering*. New York: Wiley, 1965.
- [13] C. Kim, A. E. Glazounov, and Q. M. Zhang, "Development of piezoelectric ceramic torsional actuators based on shear piezoelectric response and their potential applications," in *Proc., 9th US-Japan Seminar on Dielectric and Piezoelectric Ceramics*, Okinawa, Japan: November 1999, unpublished.

**Alexandre E. Glazounov** was a post doctoral fellow at the Materials Research Laboratory of the Pennsylvania State University and is now with the University of Karlsruhe, Germany. He received his M.S. degree in 1989 from the State Technical University, St. Petersburg, Russia, and his Ph.D. degree in 1997 from the Swiss Federal Institute of Technology, Lausanne, Switzerland.

His current research interests include development of piezoelectric materials and devices, and understanding microstructure property relationships in electronic ceramics.

**Q. M. Zhang** (SM'97) is an associate professor of electrical engineering at the Materials Research Laboratory and Department of Electrical Engineering of Penn State University. He obtained his B.S. degree in 1981 from Nanjing University, China, and his Ph.D. degree in 1986 from Penn State University.

He worked at the Brookhaven National Laboratory as a research scientist in the area of solid state thin films. He returned to Penn State University at 1991 as faculty to conduct research in ferroelectric-based materials and devices and electroactive polymer-based materials and devices. The research activities in his research group include material development, modeling, and device development for transducers and actuators, dielectrics and capacitors, ferroelectric polymer thin film for memory devices, MEMS, photonic bandgap crystals, and electro-optic and acousto-optic materials and devices.

Dr. Zhang has delivered many invited presentations in those areas. There are 150 publications in those areas from his research group. He is a senior member of the IEEE, and a member of the Materials Research Society, and the America Physical Society.



**Chulho Kim** joined the Naval Research Laboratory's Materials Science and Technology Division following graduation from the Rensselaer Polytechnic Institute with a Ph.D. degree in materials engineering in 1976. He earned B.S. and M.S. degrees in physics from the Korea University in 1963 and 1965, joining Han Nam University in the Physics Department, where he taught for 7 years.

Dr. Kim has worked more than 20 years in the Materials Science and Technology Division of the NRL as a materials research engineer in various R&D programs, including functional ceramic devices and transducers, metallic superlattices, and metal matrix composites. He holds 7 U.S. patents and has published more than 100 research papers.

# **APPENDIX 70**

# Design, Modeling, and Performance of a High Force Piezoelectric Inchworm Motor

TIMOTHY GALANTE

*United Technologies Research Center, East Hartford, CT 06108*

JEREMY FRANK, JULIEN BERNARD, WEICHING CHEN, GEORGE A. LESIEUTRE\* AND GARY H. KOOPMANN

*Center for Acoustics and Vibration, Penn State University, University Park, PA 16802*

**ABSTRACT:** A linear inchworm motor was developed for structural shape control applications. One motivation for this development was the desire for higher speed alternatives to shape memory alloy based devices. Features of the subject device include compactness ( $60 \times 40 \times 20$  mm), large displacement range (6 mm), and large holding force capability (200 N). There are three active piezoelectric elements within the inchworm: two "clamps" and one "pusher." Large displacements are achieved by repetitively advancing and clamping the pushing element. Although each pusher step is small, on the order of 10 microns, if the step rate is high enough, substantial speeds may be obtained (8 mm/s). In the past, inchworm devices have been used primarily for precision positioning. The development of a robust clamping mechanism is essential to the attainment of high force capability, and considerable design effort focused on improving this mechanism. To guide the design, a lumped parameter model of the inchworm was developed. This model included the dynamics of the moving shaft and the frictional clamping devices, and used a variable friction coefficient. It enabled the simulation of the time response of the actuator under typical loading conditions. The effects of the step drive frequency, the pre-load applied on the clamps, and the phase shifts of the clamp signals to the main pusher signal were investigated. Using this tool, the frequency bandwidth, the optimal pre-load and phase shifts which result in maximum speed were explored. Measured rates of motion agreed well with predictions, but the measured dynamic force was lower than expected.

## INTRODUCTION

SOLID-STATE piezoceramic actuators are typically limited to low displacement applications, but may be used at high frequencies. Typical applications include vibration excitation and control actuators and positioning devices. While a desire for a smart materials actuator that produces high force and high displacement at relatively high frequencies persists, a functional, low-profile, manufacturable actuator has not yet been realized. Developed in pursuit of this goal, the Penn State H3C (High force, High displacement, High energy density) inchworm is a high authority device that capitalizes on the high forces produced by piezoceramic stacks, while overcoming low displacements using an inchworm actuation scheme. This paper discusses the history of inchworm actuators, design of the subject device, and modeling and experimental results which supported the design.

The successful actuator, which is to be used in shape control applications (see Figure 1), will ideally have several features, including: high force, high displacement, high energy density, compact design, ability to be easily integrated and replaced, cost effectiveness, and ease of control. An actuator that uses inchworm type actuation in conjunction with

multi-layer piezoceramic stacks was selected for development. Subsequently, a survey of existing inchworm methodology was performed to gain perspective on improvements needed to enable high authority operation.

## LITERATURE SURVEY: INCHWORM STATE-OF-THE-ART

The inchworm devices reviewed generally fell into one of three basic groups. The first group involves a "walker" configuration, in which the induced-strain activation elements (ISA) move with a shaft. The shaft appears to be walking or looping, as it were, along the desired path of actuation. The second basic configuration is the "pusher." In this arrangement the ISA elements are removed from the actuation shaft. The actuator pushes the shaft along using an inchworm technique. The third group is the hybrid walker-pusher. This type mixes the two kinds of actuation, with the ISA elements not completely removed from the actuation shaft.

The first group of actuators represents preliminary designs which paved the way for the inchworm actuators to come. Stibitz and Steele in 1964 were among the first to design an effective inchworm actuation technique. They used magnetostrictive materials to actuate a shaft using a typical "pusher" method. As shown in Figure 2, the Stibitz and

\*Author to whom correspondence should be addressed. E-mail: g-lesieutre@psu.edu

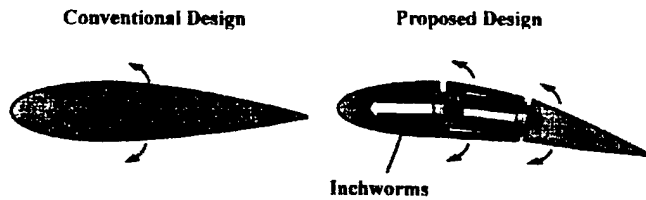


Figure 1. Concept for a deformable flow control surface.

Steele actuator was built in three segments which were each used for extending and clamping as a magnetic field was applied. The focus of their design was to create a positioning actuator for use in precision machining and tooling. The second major contribution to inchworm actuators was not itself an inchworm. McNancy, in late 1964, developed a method of piezoceramic actuation which used a multi-layer stacked piezoceramic actuator coupled with a motion amplifying structure. As shown in Figure 2, the stacked ISA element drove a combination of ball bearings to produce larger motions in the transverse direction. The use of multi-layer stacked actuators was important in the development of piezoceramic inchworms.

The first patented piezoceramic inchworm was introduced by Hsu in 1966. The design was a complicated walking actuator that used a single hollow cylindrical element to clamp and extend. As shown in Figure 2, the clamping end of the piezoceramic had an annular wedge surface which clamped with an alternating signal. The two-layer piezoceramic disks on each end of the actuator were used to bias the direction in which the wedge would restrict motion. To reverse the direction of travel the polarity of the signal was switched and the disks reversed their direction of bowing. The action switched the direction of motion that would cause the wedges to engage.

The next actuator improved on the previous actuators in several ways. Locher (1967) made several positive improvements in the field of precision linear induced strain actuators. The inchworm was configured in a hybrid structure with the clamping elements engaging a "clam-claw" mechanism as shown in Figure 2. The "clam-claw" allowed motion in one direction, but engaged instantly in the other. This method was the first hybrid inchworm actuator and the first which applied maximum holding force in the un-activated state. This device was designed exclusively for precision actuation and was capable of individual steps of 0.0005 inches.

In 1968, Brisbane designed the simplest actuator to date, as shown in Figure 2. He used a combination of three cylindrical piezoceramic elements, two for clamping and one for extension. This actuator was the first piezoceramic inchworm to use the simple "walking" method. The intent of the design was to have micron range positioning for tooling and claimed actuation speeds of 50 mm/sec.

The inchworm presented by Galutva in 1972 represented a vanguard design of inchworms for its time and the coming decade. This Russian group designed an actuator, as seen in Figure 2, that had micron-range positioning, used stacked

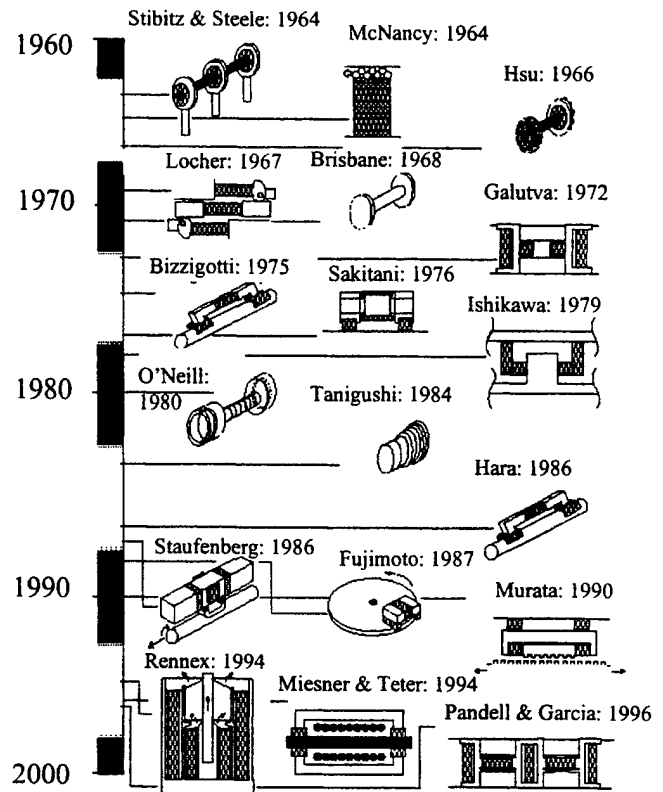


Figure 2. Illustrated timeline of inchworm history.

piezoceramic elements in a walker configuration, and fit into a slim and compact profile.

The design introduced by Bizzigotti and May in 1975, shown in Figure 2, was the first example of a "pusher" configuration piezoelectric inchworm. The goal of their design was to provide a very precise linear actuator capable of incremental steps of 0.004 micrometers. The piezoelectric elements formed a U shaped actuator which clamped and extended in the now-traditional inchworm manner. An important contribution was the introduction of the term "inchworm" to describe such devices. The next inchworm, patented by Sakitani in 1976, did not advance inchworm technology significantly, but was a fine design in its own right. It was a "walker," as shown in Figure 2, used for precision placement of a electron scanning microscope. The design presented by Ishikawa in 1979 was very similar to the Bizzigotti and May design, except it used two piezoelectric elements for extension, as opposed to one.

The inchworm presented by O'Neill in 1980 was the first to use the stacked piezoelectric actuator to increase the actuation length of the inchworm. The design, shown in Figure 2, used two clamping disks coupled with "cups" that pushed against the outer cylinder when zero charge was applied. When the disks were actuated, the cups retracted from the wall, and the "stacked" piezo-disks extended.

The actuator presented by Taniguchi in 1984 represented a new approach. The actuator, shown in Figure 2, used a multitude of piezoceramic elements stacked upon one another.

These elements acted as both clamps and extension actuators. Actuation resembled an earthworm more than an inchworm, in which the elements are driven so that they extend and contract in a wave-like or peristaltic motion. The device presented by Hara in 1986 used a great number of layers in a stacked piezoceramic actuator, by reducing the overall thickness of each layer and bonding them together. This design was a copy of the Bizzigotti and May device and differed mainly in that it made a conscious effort to be compact. This design represented the state of inchworm actuators in the middle of the 1980's, during which time few major improvements were made.

The design by Staufenberg in 1986 was an exception. As shown in Figure 2, the actuator was a pusher-type, capable of translational or rotational motion. Rotational actuation was provided by a method in which a clamping/tangential extension was applied by various actuators to produce torque. The translational method was slightly suspect because it used a rocking method to propel the shaft forward. Fujimoto in 1987 presented an inchworm "pusher" which replaced a stepper motor. The idea was to use a frictional clamp which could be applied to the edge of a disk in order to actuate it in much smaller increments than possible with a stepper motor. In 1990, Murata presented a patent which used a novel "pusher" piezoceramic inchworm configuration to push a shaft using a linear gear rack of extremely small pitch. The idea was to control the x-y position of the gear so that it engaged and disengaged in a method similar to annular gears. This method proved to be highly ineffective and Murata switched to a hybrid inchworm in which magnetic heads applied the clamp.

Rennex presented a novel arrangement of piezoceramics in 1994 in which the actuators were arranged in a parallel, hybrid pusher-walker configuration. This method resembled Locher's design, but removed the use of a "clam-claw" for a flexural clamp. The use of a parallel arrangement slimmed its profile considerably. In 1994, Miesner and Teter presented a paper which gave a detailed description of an inchworm using a hybrid TERFENOL-D and piezoceramic "pusher" system. As shown in Figure 2, the TERFENOL was used for ex-

tension and the piezoceramic was used for clamping. This was the first inchworm that was designed for high rate force application. The actuator produced 26 pounds at stall and a rate of 1 inch/sec at no load. The drawback of the design was that it was rather large, spanning almost half a foot. The resonant drive electronics were also of note.

The inchworm proposed by Lee in 1995 (not illustrated) represented a departure from previous designs. This particular design sought to create an inchworm using VLSI manufacturing techniques. The inchworm measured approximately 15 mm in length and produced forces in the mN range and speeds of 13 cm/min. These values are unimpressive compared to previous designs, but are very good considering the size of the inchworm.

The final design considered in this review was the piezoceramic caterpillar motor presented by Pandell and Garcia in 1996. Their design was very similar to that of Galutva, twenty years earlier, except (as with Lee) the focus had shifted to larger forces and displacements. A more detailed review of inchworm technology is contained in the thesis by Galante (1997).

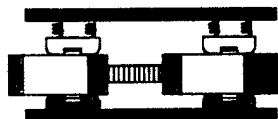
This new focus, emphasizing increased force capability, is also that of the research described herein. The goal is a device that operates at speeds rivaling those of previous devices, but that also provides forces like those of the range of the Miesner and Teter inchworm in a much smaller package.

## DESIGN AND STRESS MODELING

Piezoceramic inchworms, as described in the previous section, have historically been designed as micron-scale positioners for precision machining or scanning electron microscopes. The H3C inchworm actuator departs from its predecessors in that it is to be a high authority device, capable of large forces and large displacements. Initial shape control applications are anticipated to be relatively low frequency, nearly quasi-static.

Figure 3 illustrates the stepping mechanism employed by the device. The inchworm consists of three parts, two of

Starting position:  
both ends clamped



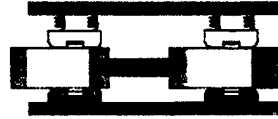
Step 1: release  
clamp 2



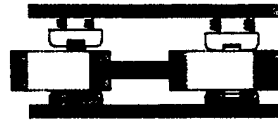
Step 2: Extend  
the pusher  
(leader indicates  
one step)



Step 3: reapply  
clamp 2



Step 4: release  
clamp 1



Step 5: Contract  
the pusher



Figure 3. Translational operation of the H3C inchworm motor.



which are clamping mechanisms, and one called a "pusher." The clamping mechanism consists of a mass-spring system (which applies the frictional clamp to the pusher) and a piezoceramic stack which lifts the clamp from the pusher to allow movement. The pusher consists of a piezoceramic stack embedded in a translating shaft, on which an exterior load may act.

Operation begins with both ends clamped. Step 1 shows release of the right clamp, permitting pusher motion to proceed to the right. In step 2, the pusher stack is activated so the front of the pusher extends to a new position. This extension distance is approximately 1–10  $\mu\text{m}$ , depending on the load acting on the shaft. In step 3, the right clamp is reapplied by de-energizing its piezoceramic stack. This position is identical to the original position except for two key points: (1) the right end of the pusher has been slightly displaced; and (2) the center piezoceramic is energized. In step 4, the left clamp is released by energizing its in-line stack. In step 5, the center stack is de-energized, thus contracting components of the pusher, and returning it to its original shape. Once the left clamp is re-applied (not shown) by de-energizing the left piezoceramic stack the inchworm has returned to its clamped state, having completed an incremental displacement of the pusher to the right.

As shown in Figure 3, the H3C inchworm actuator includes two clamping piezoceramic stacks and one transverse piezoceramic stack which extends the pusher. For best performance, the clamping stacks should have several times the blocked force of the pusher stack. For reasons of economy, all the stacks used in the H3C device are identical, and performance is limited by the capability of the clamping stacks. The stacks used are Sumitomo parts PSA-15C45N. They are  $5.2 \times 4.5 \times 20$  mm, with individual layer thicknesses of 0.11 mm. The material is a soft PZT-5D.

The clamping stacks are used to disengage an integral flexure which provides the clamping action on the pusher element. The design of this flexure, integral to the upper frame, was crucial to the successful operation of the actuator. The main design goals for this part were to provide maximum clamping force on the pusher when the stack is uncharged,

and to completely disengage the clamp when the stack is energized. Several conditions had to be satisfied for the inchworm to operate effectively in this manner: The impedance of the deformed structure needed to closely match the impedance of the piezoceramic stack, to facilitate energy transfer. The Von-Mises stress magnitudes were also required to remain within the yield stress envelope. A standard factor of safety was used to account for anticipated higher transient loads in operation. Further, the stiffness of the structure in the transverse direction was maximized, in order to minimize displacements due to friction applied by the pusher. Another desire was maximization of the resonance frequency of the clamp system, to ensure that it was higher than that of the stack. This would allow the maximum clamping frequency to be limited mainly by the stack. The last condition involved the surface region that defines the interaction of the pusher and the stack: the stress distribution across the stack should be fairly uniform and the structure should clamp onto the pusher in a uniform fashion.

The clamping mass/spring sub-structure was modeled, taking advantage of symmetry, using plane stress finite elements and the mesh shown in Figure 4(b). The model used spring elements to model the force-displacement characteristics of the piezoceramic stack at low frequency. These spring elements provided a distributed load across the interaction surface with the piezoceramic stack. The value of the combined stiffness was 35 MN/m, which represented the operating point at which the stack would produce a force of 350 N at a displacement of 10 microns. These spring elements were then displaced by 10 microns. Roller boundary conditions were applied to the symmetry line of clamping sub-structure, and clamps were applied at the edge and at the screw interaction point to simulate the relatively high stiffness of the rest of the upper frame. This technique made it unnecessary to model the rest of the upper frame and greatly reduced computation time.

The pusher, lower frame, panels and other small parts (see Figure 6) were designed with an emphasis on manufacturability and assembly. These parts were made from titanium at PCB Piezotronics, Inc., using wire EDM.

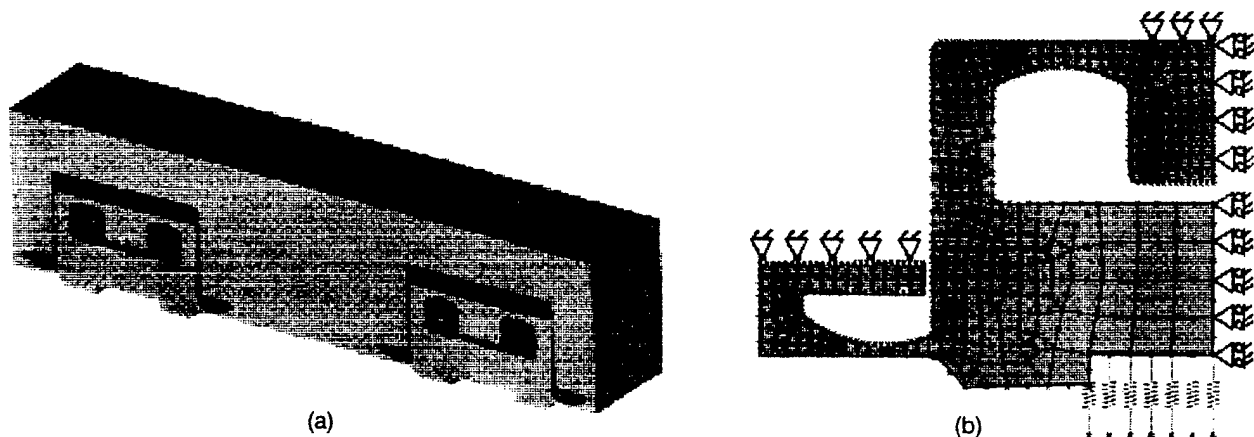
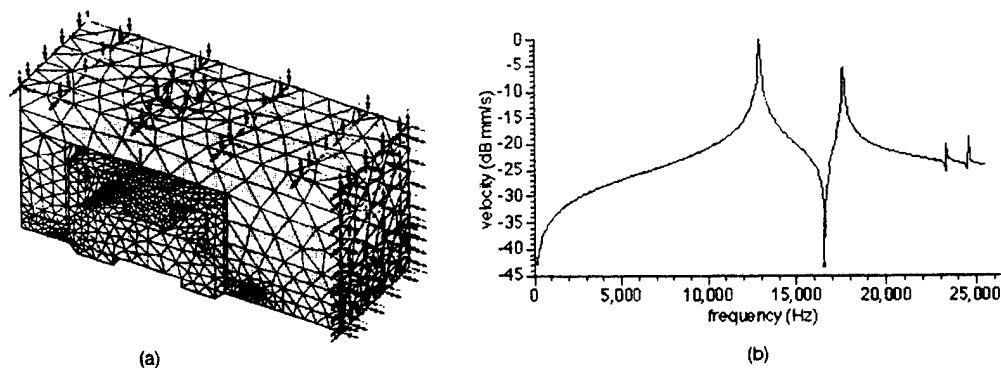


Figure 4. (a) Design of the H3C actuator frame and (b) static finite element model of the clamping substructure.



**Figure 5.** (a) Solid finite element model of the upper clamp with boundary conditions and (b) frequency spectrum of the finite element dynamic model.

The main function of the pusher is to transmit the actuation force and displacement to an exterior load. The design of the pusher was critical to the operation of the inchworm. The pusher has slots for the clamping stacks to pass through, a layout that restricts the total "throw" of the actuator, but acceptably so. The pusher slots allow the stacks to be centrally located in the overall device, without being part of the moving structure. Integral to the design of the pusher is a pre-load feature which allows the extensional stack to be placed under compressive load during assembly.

The area over which the clamping flexural sub-structure of the upper frame interacts with the pusher provides enough surface area for proper frictional force transmission. The material at the interaction surface was lapped to nearly a mirror finish, with rms surface variation on the order of 1–2 microns. This surface precision results in the maximum friction coefficient for the material, while allowing freedom of movement with only a few microns normal displacement of the clamp.

The upper frame dynamic characteristics are very important to the performance of the inchworm. Its modes of vibra-

tion should be at frequencies higher than the operating stack frequency range of 0–1000 Hz. It is also important that modes other than the plunging mode be excited only minimally upon impact so as not to disrupt high-rate repetitive operation.

As illustrated in Figure 5, the first mode at 12,660 Hz represents a plunging mode. This mode could be excited by high frequency actuation of the piezoceramic stack and should be avoided. Its excitation would disrupt clamping and likely cause excessive noise due to impact of the clamp on the pusher. The second mode at 17,634 Hz represents rotation of the mass/spring structure about the x axis. Excitation of this tipping motion would cause a stress gradient across the surface of the stack. The third mode at 23,407 Hz involves rotation of the mass/spring structure about the z axis. This rocking mode should have much lower amplitude than the first two modes because it should not be excited by forces applied at the center of the stack interface surface. Were this mode to be excited during operation it would also result in a detrimental stress gradient across the stack. The fourth mode at 24,633 Hz is a rotational mode about the y axis. The response of this

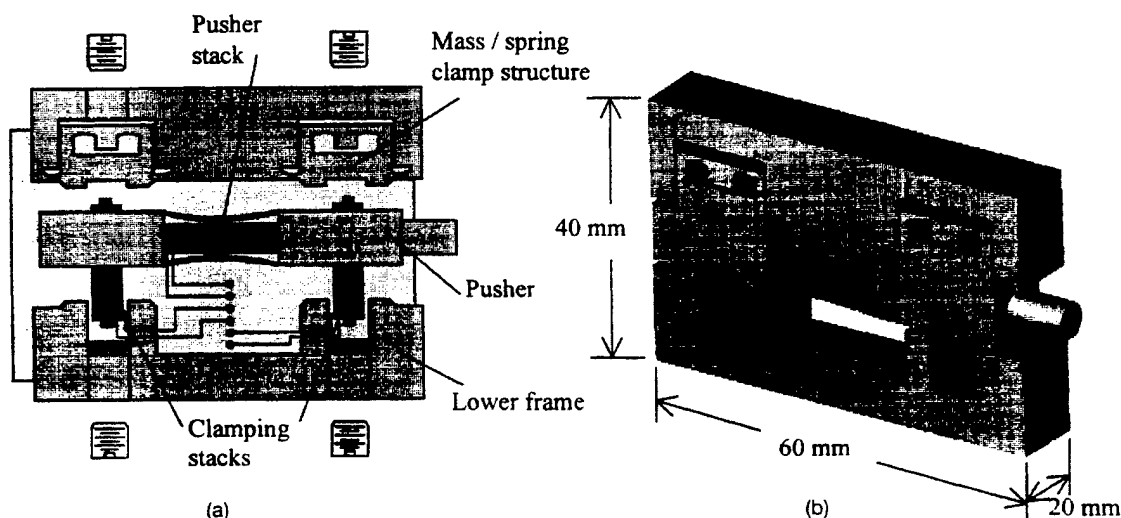


**Figure 6.** (a) Assembly layout of the inchworm actuator and (b) rendered solid model of the final design of the H3C inchworm actuator.

mode should also be small compared to that of the first two and should not be excited by any force on the stack interface surface. If excited it would torque the stack and could cause it to shear unnecessarily.

The pusher was modeled in a similar fashion, with results that affect the range of operation significantly. The first mode of the pusher is at about 1,065 Hz and involves bending along the  $x$ - $y$  plane. This mode is much lower in frequency than those of the upper clamp and represents an upper bound on the clamping frequency. Also important, the fundamental extensional mode is at about 11,806 Hz and, if excited, would interfere with the extensional motion sequence. This resonance is far beyond the intended operating frequency range, but with additional mass (i.e., loading condition) added to the end of the pusher the resonance frequency could quickly fall into the range of interest.

Easy assembly of the actuator was crucial. As a developmental device, it had to be designed for manufacturability, reparability and integration. The assembly [shown in Figure 6(a)] allowed ready access to the internal structure.

### TESTING THE PROTOTYPE H3C ACTUATOR

With the actuator designed, manufactured and assembled, it was tested to characterize its performance. Many features of the drive signals must be specified, including waveform shape, level, duty cycle and relative phasing. These variables must be simultaneously optimized in order to attain the best possible performance. With this need for flexibility in mind, LABVIEW software was used to generate inchworm drive signals through a PC digital to analog output board. This software was used to create waveforms of virtually any shape, and allowed the frequency, amplitude, duty cycle and phase of the signals to be easily adjusted. Figure 7 shows sample drive signals generated using this software.

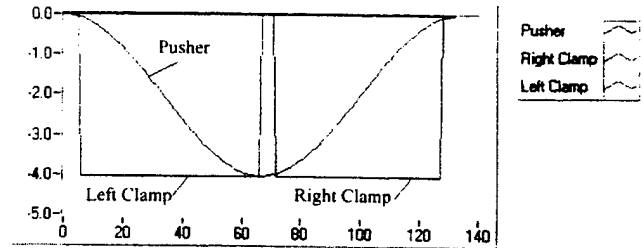


Figure 7. Example of waveform signals generated using LABVIEW software.

A special-purpose calibration fixture was developed for characterization of the inchworm, as shown in Figure 8. Its main feature is a stiff beam pivoted on one end in a precision bearing. An important aspect of this fixture is the ability to selectively drive loads that are primarily inertial in nature, primarily stiffness in nature, or a combination of both. The beam can be driven against a compression spring for a stiffness load, or a mass can be attached to the beam to increase the inertial load. A high-sensitivity strain gage load cell and an LVDT position transducer were used to measure performance. Further, an analog to digital input board was used to record the output force and velocity in LABVIEW, a feature of the experimental setup that will eventually enable closed-loop operation of the inchworm.

There were three objectives of the initial inchworm experiments. The first was to characterize the performance of the inchworm in terms of dynamic force and velocity, the second was to optimize the clamp and pusher drive signals, and the third was to generate experimental data to test the validity of the dynamic model. Two initial experiments were devised to characterize performance. First, the actuator was driven against the compression spring until the maximum dynamic force was reached, and no further displacement was possible. The piezoceramic clamp stacks were driven with square

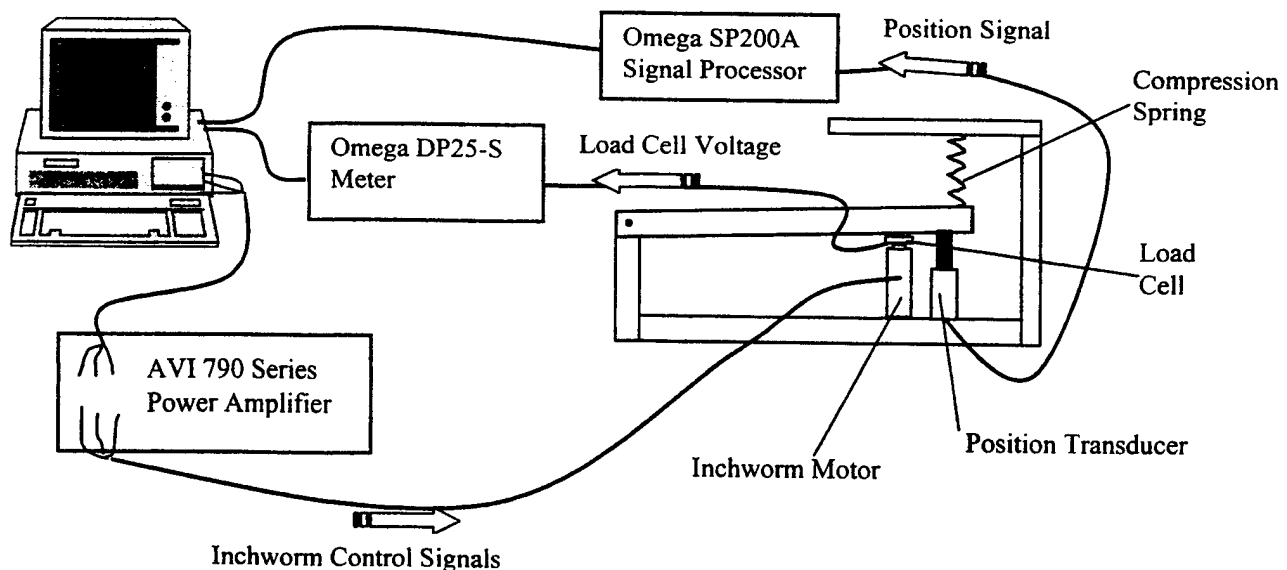


Figure 8. Schematic of the H3C inchworm actuator performance characterization experiment.

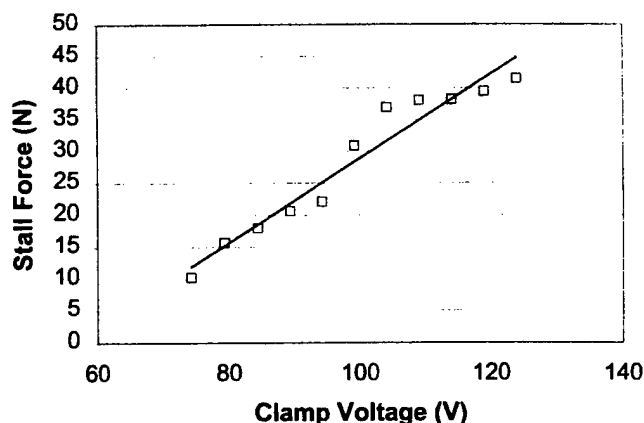


Figure 9. Maximum dynamic driving force against a compression spring.

waves, at voltages up to a maximum of 124 V. The signal to the pusher was an offset 0 to 87 V sine wave. As seen in Figure 9, the stall force increased with voltage due to correspondingly higher clamping forces. The maximum dynamic force was 41.5 N.

A second characterization experiment was to measure the no-load maximum velocity. This time, two different types of signals were used to drive the clamping stacks: a square wave and a sine wave. The amplitude of both kinds of waves was fixed at 97 V. As shown in Figure 10, the maximum velocity attained for a square signal was 3.3 mm/s at a drive frequency of 500 Hz; presumably because of clamping force degradation due to dynamic effects, the inchworm would not run at higher frequencies. For a sinusoidal signal, however, a maximum velocity of 5.4 mm/s was attained at a drive frequency of 900 Hz. Higher driving rates were possible with the sinusoidal signal because the clamp motion was smooth, with less noise and vibration. This is a potentially important ob-

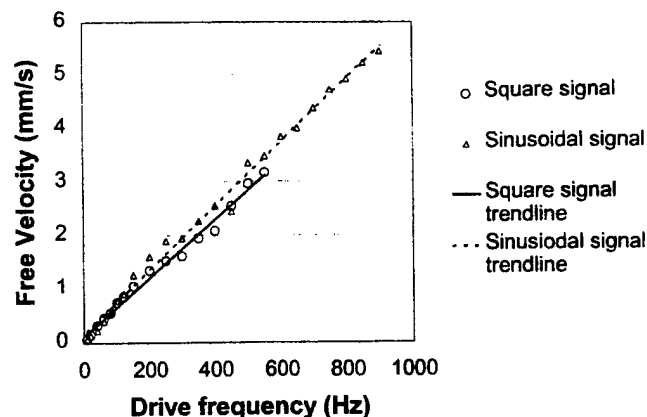
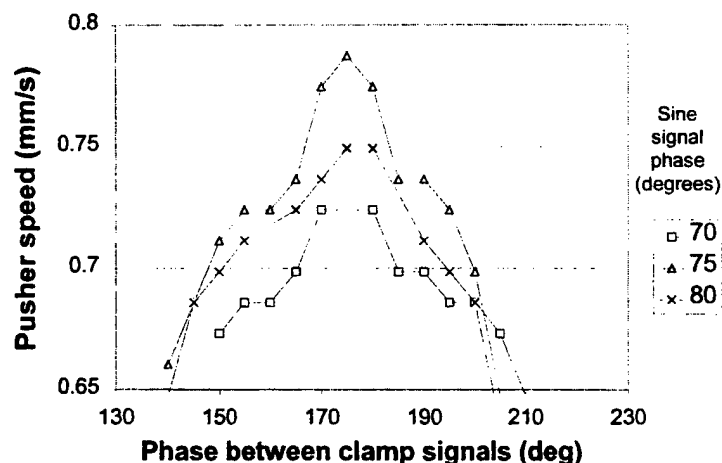


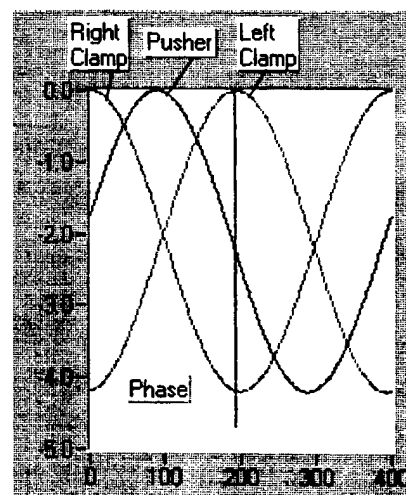
Figure 10. Inchworm velocity vs. cycle frequency, driven with square and sinusoidal clamp signals.

servation, since a sinusoidal signal could be easily created using standard AC voltage, perhaps reducing the need for separate, complex signal generators and amplifiers.

The ongoing goal of experimentation is to increase inchworm performance by optimizing clamp signal parameters: waveform shape, voltage, phase, cycle frequency and duty cycle. Because of the large number of signal parameters, each must be independently optimized. With sinusoidal clamp signals, for example, the drive voltage and frequency were held at 90 V and 100 Hz, respectively, while the relative phases of the sine waves were changed. As shown in Figure 11, there was an increase and then a decrease in performance as the phase between the clamp signals was changed. This experiment was carried out for several pusher phases (the relative phase between the pusher and the first clamp signal), and demonstrated that the best performance was obtained when the clamp signals were 175 degrees apart, and the pusher signal was 75 degrees after the first clamp signal.



(a)



(b)

Figure 11. (a) Determination of the optimal relative phases between waveform signals and (b) sample of waveform signals from LABVIEW showing phase.

## DYNAMIC MODEL FORMULATION AND VALIDATION

Dynamic operation of the H3C inchworm was modeled using a 4 DOF lumped parameter system, as shown in Figure 12. The rear and front end of the pusher were modeled as rigid masses, the flexures as massless springs, and the clamping devices as mass-spring systems. The stacks were represented by spring elements in series with induced displacement elements. The four degrees of freedom corresponded to the displacements of the two ends of the pusher and the two free ends of the clamping elements. The external load consists of a single degree of freedom system and a static force. The connection between the external system and the pusher is assumed to be perfectly rigid, so that any external mass is included in the mass of the front end of the pusher.

The dynamic response of the system to time-varying drive voltages in the stacks was calculated by the Runge-Kutta-Nystrom method. At step (i), the displacements ( $i + 1$ ) are integrated using the forces of step (i), which include friction forces, induced forces and external forces. The rest of the algorithm evaluates the friction forces for step ( $i + 1$ ). The resultant normal force applied to the pusher by each of the clamping devices is first checked. If it is positive (upward), the friction force is zero and the corresponding end of the pusher is free. If it is negative (downward), the friction force is non-zero and can be either a static or a dynamic friction force. The sum of all the forces of step ( $i + 1$ ) applied to the end of the pusher, including elastic, viscous, and inertial forces, is then computed. If this exceeds the value of the static friction force, the friction force is set to its dynamic value. If it is lower, the displacement ( $i + 1$ ) is set to zero and the friction force is set to the sum of all other forces of step ( $i + 1$ ) acting on the end of the pusher, given the zero displacement.

The governing equation of motion of the model was as follows:

$$\begin{bmatrix} M_{r1} + 2M_{af} & 0 & 0 & 0 \\ 0 & M_{r1} + 2M_{af} + M & 0 & 0 \\ 0 & 0 & M_{ac} + M_u & 0 \\ 0 & 0 & 0 & M_{ac} + M_u \end{bmatrix} \begin{bmatrix} \ddot{X}_1 \\ \ddot{X}_2 \\ \ddot{Y}_1 \\ \ddot{Y}_2 \end{bmatrix} + \begin{bmatrix} 0 & 0 & 0 & 0 \\ 0 & C & 0 & 0 \\ 0 & 0 & C_u & 0 \\ 0 & 0 & 0 & C_u \end{bmatrix} \begin{bmatrix} \dot{X}_1 \\ \dot{X}_2 \\ \dot{Y}_1 \\ \dot{Y}_2 \end{bmatrix} + \begin{bmatrix} K_{af} + 2K_f & -(K_{af} + 2K_f) & 0 & 0 \\ -(K_{af} + 2K_f) & K_{af} + 2K_f + K & 0 & 0 \\ 0 & 0 & K_{ac} + K_u & 0 \\ 0 & 0 & 0 & K_{ac} + K_u \end{bmatrix} \begin{bmatrix} X_1 \\ X_2 \\ Y_1 \\ Y_2 \end{bmatrix} = \begin{bmatrix} -T_1 - K_{af}X_{free} \\ -T_2 + K_{af}X_{free} \\ -N_1 + K_{ac}Y_{1,free} \\ -N_2 + K_{ac}Y_{2,free} \end{bmatrix}$$

where,

$K_f$  = equivalent stiffness coefficient of one membrane of the flexure

$K_{af}$  = equivalent stiffness coefficient of the free-free longitudinal stack

$M_{af}$  = equivalent mass coefficient of the free-free longitudinal stack

$M_{r1}$  = mass of the rear block of the pusher

$M_{r2}$  = mass of the front block of the pusher

$X_1$  = displacement of the rear rod

$X_2$  = displacement of the front rod

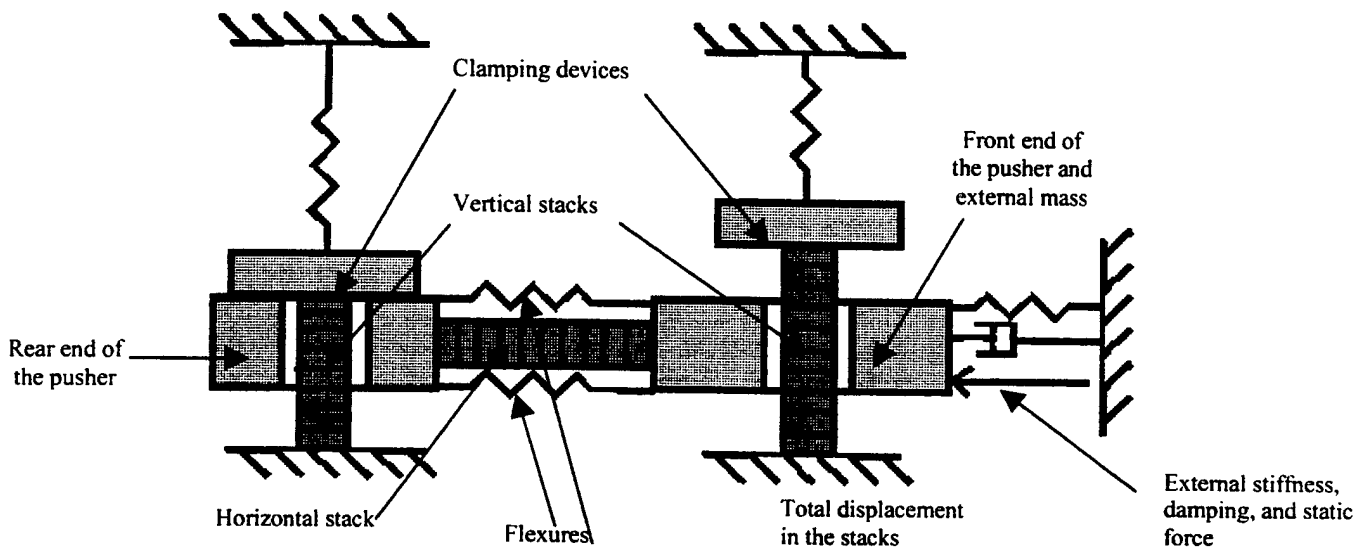


Figure 12. Lumped parameter model of the H3C inchworm.

- $X_{free}$  = free displacement of the longitudinal stack  
 $K_{ac}$  = equivalent stiffness coefficient of the clamped-free longitudinal stack  
 $M_{ac}$  = equivalent mass coefficient of the clamped-free longitudinal stack  
 $Y_1$  = displacement of the rear transverse stack  
 $Y_2$  = displacement of the front transverse stack  
 $Y_{1free}$  = free displacement of the rear transverse stack  
 $Y_{2free}$  = free displacement of the front transverse stack  
 $K_u$  = equivalent stiffness coefficient of the clamps  
 $C_u$  = equivalent damping coefficient of the clamps  
 $M_u$  = equivalent mass coefficient of the clamps  
 $K$  = external stiffness  
 $C$  = external damping  
 $M$  = external mass  
 $T_1$  = frictional force acting on the rear of the pusher  
 $T_2$  = frictional force acting on the front of the pusher  
 $F$  = external force acting on the pusher

Figures 13(a) and 13(b) show the displacements of the rear and front of the pusher, and the friction forces, for the following loading and driving conditions: a mass of 0.5 kg, a spring stiffness of 0.1% of the stiffness of the stack, and a static force equal to the weight of the mass; the clamping stacks were driven with square waves with zero phase shift, 100 Volts peak, and 300 Hz; the pusher stack was driven with a sine wave, 100 Volts peak, and 300 Hz. In this nearly free condition, the numerical model yielded good results, as shown in Figure 14. However, as the external mass increased, the results degraded. The numerical model tended to overestimate the displacements for large external loads, giving results similar to the free case. One shortcoming of this model is that no friction force is applied to the pusher if the clamping devices bounce on the surface due to oscillations. When attempting to move large external loads, the precompression forces applied to the clamping devices need to be high. The clamping devices are thus more likely to bounce on the sur-

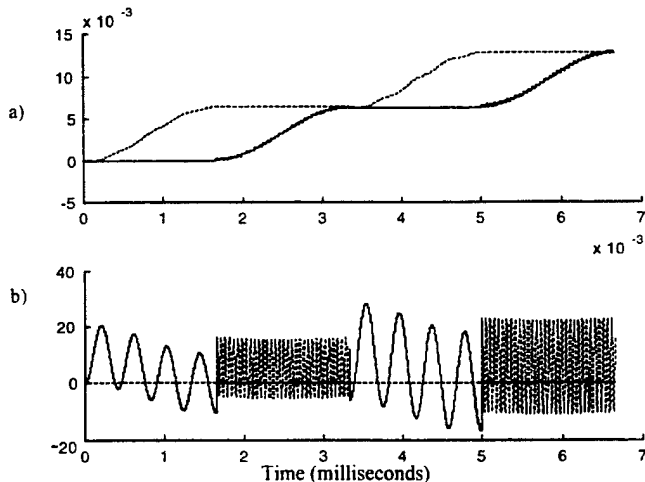


Figure 13. (a) Displacements of the pusher (mm ends) and (b) friction forces on the pusher ends (N) (dashed: front, solid: rear).

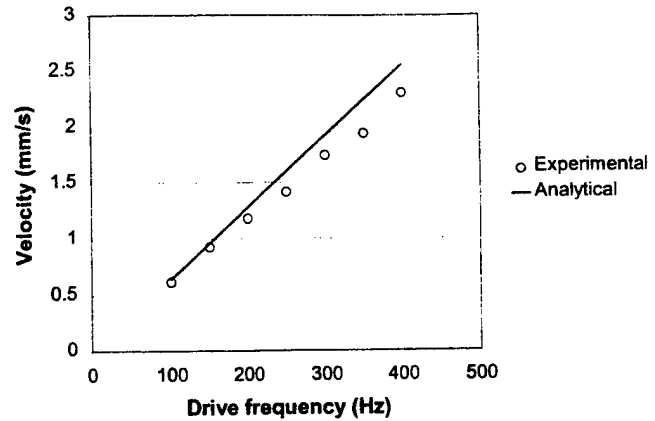


Figure 14. Experimental and computed inchworm speeds under 0.5 kg mass loading.

face of the pusher, and to slow it down during the extension phase.

Figures 15(a) and 15(b) show the force applied by the inchworm on the external structure in the following loading and driving conditions: a mass of 0.5 kg, a spring stiffness of 1% of the stiffness of the stack and a static force equal to the weight of the mass. For Figure 15(a), the same voltages as in Figures 13(a) and 13(b) were used, and for Figure 15(b) an 18 degree phase lag was applied to the front clamp. The purpose of the delay was to ensure that the pusher developed some initial force by the time its front end was released. On the other hand, the delay reduced the time over which the pusher was free to extend. The results show that the front end of the pusher experienced less backlash with delayed voltages. This suggests the existence of an optimal phase shift for the clamp signals.

The model was validated further by comparing the simulation to experimental measurements of the step size and characteristics at various loading conditions. In Figure 16, the

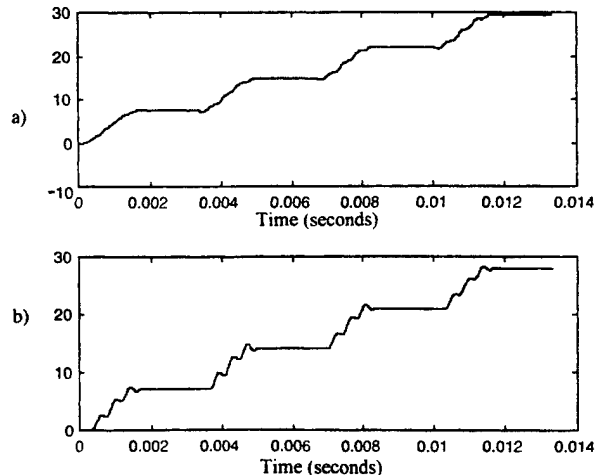
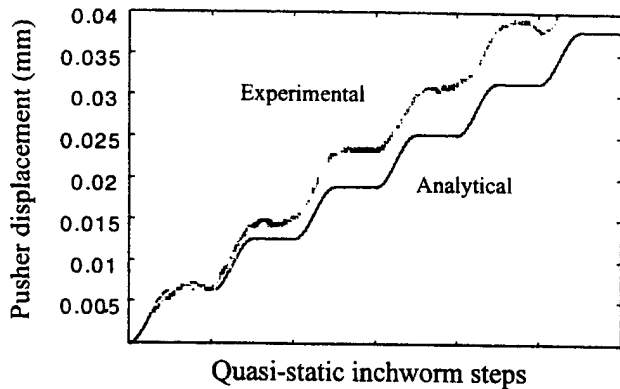


Figure 15. (a) Force output with zero phase lag (N), and (b) force output with an 18 degree phase lag (N).



**Figure 16.** Inchworm steps against a 4 N spring load, analytical and experimental.

inchworm was driven against a load of 4 N, and the position output measured is plotted for six steps. Under the same loading and signal waveforms, the simulated behavior of the model is plotted in Figure 16. Note most importantly that the shapes of the two curves are similar. The position output in each case is the shape of a sine wave (corresponding to the sine wave input to the pusher stacks) followed by a flat portion of the curve (corresponding to the case when the front of the pusher is clamped and the rear of the pusher is allowed to step forward). The lack of exact agreement between the two curves is the result of two effects. First, there are time dependent vertical forces due to wave motion in the spring component of the spring/mass load. These forces tend to add unsteady clamping forces to the analytical simulation, slowing the steps. Also, the step size experimentally measured is slightly higher than predicted, because the PZT stacks produced more displacement than expected.

In Figure 17 the experiment is repeated, but now against a 10 N load. The experimental and computed results agree fairly well again, with the same discrepancy as explained above. A new behavior is seen in the experimental plot, in that the pusher slips backwards slightly at the beginning of each new step. This takes place because the combined effect of the spring load and the inertial reaction on the inchworm is

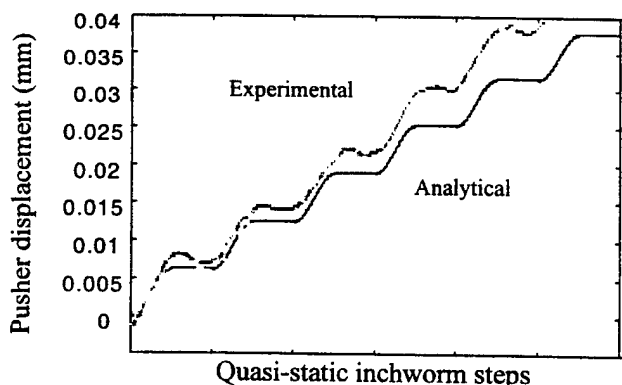


**Figure 17.** Inchworm steps against a 10 N spring load, analytical and experimental.

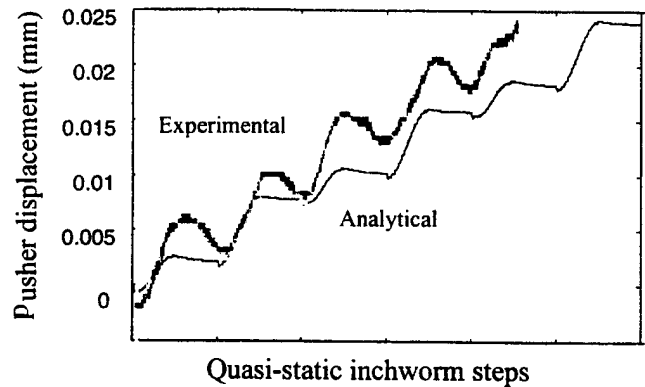


**Figure 18.** Inchworm steps against a 40 N spring load, analytical and experimental.

greater than the friction force applied by the rear clamp. Also, the rear clamping force may be lower than expected because of chatter effects caused by using a square wave to activate the clamp. The backslip is not as large in the simulated plot, because the dynamic loss of clamping force is difficult to predict.

The next experiment is performed against a spring load of 40 N, which has been shown to be near the maximum force capacity of the motor. The backlash discussed above is significantly more noticeable in this case, as seen in Figure 18. At the beginning of each step, the pusher slips backwards a distance equal to half of a step before extending forward. Once the forward step has begun, however, the pusher stacks still extend forward a distance of about 10 microns, similar to the step size against smaller loads. From this, it is determined that the maximum pushing force is limited by the clamping force on the rear of the pusher, rather than the force limit of the pushing stacks. The simulated response against the 40 N load also shows the backslip of the pusher. The alternating difference in the predicted step size is probably due to the inchworm pushing out of phase against the external load.

An additional verification of the model is that it accurately predicts the maximum dynamic force against which the inchworm can advance. Against an external load of 50 N, the sim-

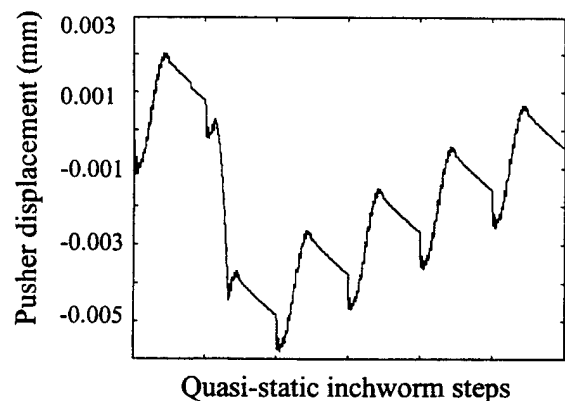


**Figure 19.** Simulated output of the inchworm against a 50 N load.

ulated response takes half a step forward, then slips back, far past its original position. This is shown in Figure 19. Accordingly, the maximum dynamic force of the actuator has been measured to be just under 50 N.

## CONCLUSIONS

A linear inchworm motor was developed for structural shape control applications. Features of the subject device include small size ( $60 \times 40 \times 20$  mm), stroke of 0.6 cm, free speed of 0.6 cm/s, stall load of more than 40 N, and static holding force capability greater than 200 N. There are three active piezoelectric elements within the inchworm: two "clamps" and one "pusher." Large displacements are achieved by repetitively advancing and clamping the pushing element. The development of a robust clamping mechanism is essential to attain high force capability, and considerable design effort focused on improving this mechanism. To guide the design, a lumped parameter model of the inchworm was developed. This model included the dynamics of the moving shaft and the frictional clamping devices and used a variable friction coefficient. It enabled the simulation of the time response of the actuator under typical loading conditions. The effects of the step drive frequency, the pre-load applied on the clamps, and the phase shifts of the clamp signals relative to that of the main pusher signal were investigated. Using this tool to guide the experiments, the driving frequencies and phase shifts that result in maximum speed were explored. Measured rates of motion agreed well with predictions, but the measured dynamic force was lower than expected.

## ACKNOWLEDGEMENTS

This work was supported by DARPA under the SAMPSON project, performed in collaboration with engineers at Boeing St. Louis, General Dynamics, Penn State's

Applied Research Laboratory, and PCB Piezotronics.

## REFERENCES

- Bizzigotti, R. A., "Electromechanical translational apparatus," *U.S. Patent: 3,902,085*, 1975.
- Brisbane, A. D., "Position control device," *U.S. Patent: 3,377,489*, 1968.
- Burleigh INCHWORM Nanopositioning Systems Brochure, Burleigh Instruments Inc., Fishers, NY, USA, 1995.
- Fujimoto, T., "Piezo-electric actuator and stepping device using same," *U.S. Patent: 4,714,855*, 1987.
- Galante, T., "Design and fabrication of a high-force linear piezoceramic actuator," M.S. thesis, Penn State University, August 1997.
- Galutva, G. V., "Device for precision displacement of a solid body," *U.S. Patent: 3,684,904*, 1972.
- Hara, A., Takao, H., Kunio, Y., Sadayuki, T. and Keiji, N., "Electromechanical translation device comprising an electrostrictive drive of a stacked ceramic capacitor type," *U.S. Patent: 4,570,096*, 1986.
- Hsu, K. and Biatler, A., "Transducer," *U.S. Patent: 3,292,019*, 1966.
- Ishikawa, I. and Sakitani, Y., "Two-directional piezoelectric driven fine adjustment device," *U.S. Patent: 4,163,168*, 1979.
- Lee, S. K. and Esachi, M., "Design of the electrostatic linear microactuator based on the inchworm motion," *Mechatronics*, Vol. 5, No. 8, pp. 965-972, 1995.
- Locher, G. L., "Micrometric linear actuator," *U.S. Patent: 3,296,467*, 1967.
- McNancy, J. T., "Piezoelectric transducer force to motion converter," *U.S. Patent: 2,154,700*, 1964.
- Meisner, J. E. and Teter, J. P., "Piezoelectric/magnetostrictive resonant inchworm motor," SPIE, Vol. 2190, pp. 520-527, 1994.
- Murata, T., "Drive apparatus and motor unit using the same," *U.S. Patent: 4,974,077*, 1990.
- O'Neill, G., "Electromotive actuator," *U.S. Patent: 4,219,755*, 1980.
- Pandell, T. and Garcia, E., "Design of a piezoelectric caterpillar motor," *Proceedings of the ASME aerospace division*, AD-Vol. 52, pp. 627-648, 1996.
- Rennex, G., "Inchworm actuator," *U.S. Patent: 5,332,942*, 1994.
- Sakitani, Y., "Stepwise fine adjustment," *U.S. Patent: 3,952,215*, 1976.
- Staufenberg, C. W., Jr. and Hubbell, R. J., "Piezoelectric electromechanical translation apparatus," *U.S. Patent: 4,622,483*, 1986.
- Stibitz, R., "Incremental Feed Mechanisms," *U.S. Patent: 3,138,749*, 1964.
- Taniguchi, T., "Piezoelectric driving apparatus," *U.S. Patent: 4,454,441*, 1984.



# **ACTUATOR STUDIES**

*Piezoelectric Motors*

# **APPENDIX 71**

# 6.34

## Piezoelectric Ultrasonic Motors

B. KOC and K. UCHINO

*Pennsylvania State University, University Park, PA, USA*

---

6.34.1 INTRODUCTION	651
6.34.2 CLASSIFICATION OF PIEZOELECTRIC ULTRASONIC MOTORS	652
6.34.2.1 <i>Traveling Wave Type Motors</i>	653
6.34.2.2 <i>Standing Wave Type Motors</i>	654
6.34.2.3 <i>Multi- (or Mixed-) Mode Excitation Type Motors</i>	654
6.34.2.3.1 <i>Single-element vibrator exciting multimode vibrations</i>	655
6.34.2.3.2 <i>Multielement vibrators exciting single-mode vibrations</i>	656
6.34.2.4 <i>Mode Rotation (Stepper) Type Motors</i>	656
6.34.3 PIEZOELECTRIC ELEMENTS USED IN STATOR VIBRATOR	657
6.34.4 RELIABILITY OF PIEZOELECTRIC ULTRASONIC MOTORS	658
6.34.4.1 <i>Heat Generation</i>	658
6.34.4.2 <i>Contact Mechanics</i>	659
6.34.4.3 <i>Frictional Materials</i>	659
6.34.4.4 <i>Drive Control Techniques</i>	659
6.34.5 APPLICATIONS OF PIEZOELECTRIC ULTRASONIC MOTORS	659
6.34.5.1 <i>Actuators for Consumer Goods</i>	659
6.34.5.2 <i>Actuators for Precise Positioning Devices</i>	659
6.34.5.3 <i>Actuators for Miniaturized Machines</i>	659
6.34.5.4 <i>Actuators for Machines Used in Space</i>	660
6.34.5.5 <i>Actuators for Medical Uses</i>	660
6.34.6 REFERENCES	660

---

### 6.34.1 INTRODUCTION

In general, piezoelectric ultrasonic motors contain two basic components that are the stator and the rotor. Piezoelectric and elastic materials in a stator are combined in various ways forming a composite structure. Exciting at least two orthogonal mechanical vibration modes of the composite stator using single or orthogonal multiple high-frequency a.c. signals generates mechanical elliptical motion on the stator surface. The rotor is pressed against the stator's surface and a rotation is produced by frictional interaction between the touching stator and rotor surfaces.

In 1942, Williams and Brown proposed the first piezoelectric ultrasonic motor using the

principle described above. Figure 1 shows the structure of the motor's stator in which four piezoelectric rectangular elements were bonded to all faces of a quadratic bar forming a composite structure. A wobble motion was generated at one end of the bar upon exciting the piezoelectric elements with two-phase potential. This motor's operating principle is identical to a traveling wave motor if the phase difference is set to 90°.

Although the working mechanisms of ultrasonic motors had been known for almost 50 years, only a few different types of ultrasonic motors have been developed since the 1980s (Kleesattel and Kuris, 1959; Archangelskij, 1963; Lavrinenko, 1964; Barth, 1973; Wiscniewski, 1975).

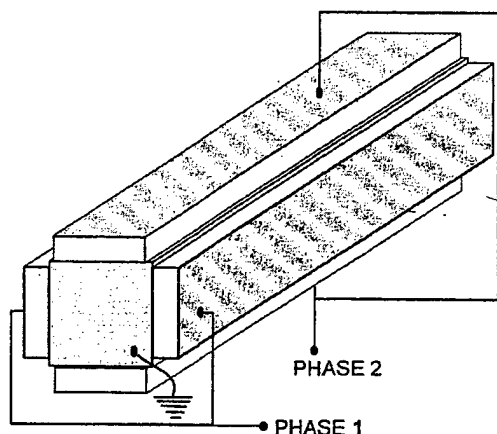


Figure 1 Piezoelectric motor using bending vibration of a bar (after Williams and Brown, 1942).

An instrument for driving a small-diameter drill by using the principle of high-frequency, low-amplitude elliptic motion was invented in 1959 (Kleesattel and Kuris, 1959). Although the body of the rod is vibrating longitudinally, an elliptical vibratory motion is generated at the working end of the rod due to the indirect bending mode of the tip of the rod. This vibratory motor was applied to dental and surgical instrumentation.

In 1963, Archangelskij described the conversion of a vibratory motion along the surface of a rod into rotational or linear motion of a body in contact with it. He explained this phenomenon on the basis of superposition of longitudinal and flexural vibrations in the rod and subsequent interrupted contact conditions between the bodies.

Barth, in 1973, proposed a motor driven by ultrasonic vibration. The rotor is pressed against two horns placed at different locations. By exciting one of the horns, the rotor is rotated in one direction, and by stopping this rotation and exciting the other horn, direction reversal is possible. Lavrinenko (1964) proposed various mechanisms based on the same principles.

The motor proposed by Vasiliev *et al.* in 1980 used an ultrasonic transducer consisting of a piezoelectric element between two metal blocks. The blocks served to lower the resonance frequency and magnify the vibration amplitude. The longitudinal vibration of the vibrator is transmitted to a vibrating piece in contact with the rotor. The rotor is driven by friction contact as it flexurally vibrates. A feedback control was used to control vibration amplitude. Because of the difficulty in maintaining a constant vibration amplitude at a high temperature and with wear, the motor was not of practical use.

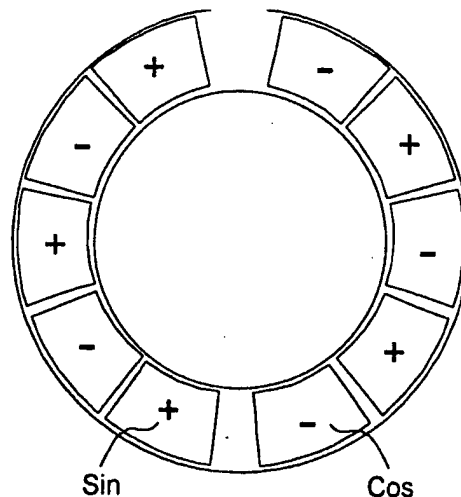


Figure 2 Stator structure of Sashida's motor.

Sashida proposed and experimentally fabricated a vibratory motor in 1980. The ultrasonic vibration and rotor are in the same plane and share a common axis with the transducer. The rotor is driven through friction by vibrating pieces at a slight angle to normal of the rotor. This motor uses a bolted type Langevin transducer at a frequency of 27.8 kHz. Other technical specifications include a torque of 0.25 N·m, power of 90 W, and mechanical power output of 50 W. This was the first practical motor demonstrated. In order to counteract the problem of wear, Sashida proposed a traveling wave ultrasonic motor in 1982 (Figure 2). After Sashida's traveling wave ultrasonic motor, many new ultrasonic motor designs were proposed. These motors display some exceptional properties: high resolution of displacement control, absence of a parasitic magnetic field, frictional locking at the power-off stage, and high thrust-to-weight ratio. These properties make them good candidates for use in precision microrobots.

As has been noticed, the ceramic-metal composite structure is a key to designing a motor stator, where the ceramic generates the actuation, and the metal amplifies the displacement and transfers the force. How to compose these two parts is one of the important issues in realizing reliable ultrasonic motors.

#### 6.34.2 CLASSIFICATION OF PIEZOELECTRIC ULTRASONIC MOTORS

A common feature of all piezoelectric ultrasonic motors is their two-stage energy conversion mechanism. In the first stage, piezoelectric

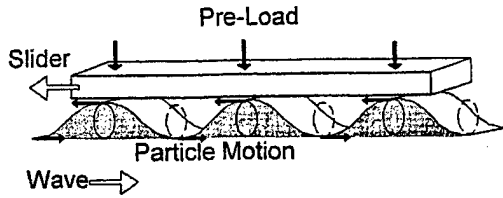


Figure 3 Operating example of traveling wave piezoelectric ultrasonic motors.

elements convert electrical energy into high-frequency mechanical oscillations. In the second stage, the high-frequency oscillatory vibration is rectified into microscopic unidirectional rotary or linear motion of a driven component. Depending on the geometry of the stator and the nature of the piezoelectric excitation, two orthogonal vibration modes can be superimposed on the surface point undergoing elliptical motion. There are many ways of generating an elliptical trajectory on the surface of the vibratory pieces and many researchers have classified piezoelectric ultrasonic motors into two groups according to the vibration modes used to generate the elliptical motion (Ueha and Tomikawa, 1993; Sashida and Kenjo, 1993; Wallaschek, 1998; Uchino, 1998). However, there are some structures that generate neither traveling wave nor standing waves types. We classify piezoelectric ultrasonic motors into four categories based on the generation of an elliptical trajectory on the stator surface:

- (i) traveling wave type,
- (ii) standing wave type,
- (iii) mode rotation (stepper) type,
- (iv) multi- (or mixed-) mode excitation type,
- (a) single-excitation,
- (b) multivibrator excitation.

#### 6.34.2.1 Traveling Wave Type Motors

Intensive research on piezoelectric ultrasonic motors started after the invention of Sashida's first practical ultrasonic motor in 1982. The elliptical motion on the stator surface is generated by a proper superposition of two orthogonal flexural waves. The piezoelectric ring has a segmented electrodes and the piezoelectric ceramic under each segment is polarized in such a way that one group of segments excites the sine mode and the other group excites the cosine mode. Figure 3 shows the operation principle of a traveling wave motor. In the literature, the operating principle of a traveling wave motors is described in detail (Inaba *et al.*, 1987; Hagerdorn and Wallaschek, 1992a, 1992b; Sashida and Kenjo, 1993; Ueha and Tomikawa, 1993; Uchino, 1997).

The generation of an elliptical motion on the vibrating piezoelectric ring takes place according to the following procedure. Due to symmetry, the two sinusoids with a phase difference

$$u_x = u_{xo} \sin \omega t \quad \text{and} \quad u_y = u_{yo} \sin(\omega t + \gamma) \quad (1)$$

Rearranging Equation (1) gives the following relations

$$\sin \omega t = \frac{u_x}{u_{xo}} \quad \text{and} \quad \cos \omega t = \sqrt{1 - \frac{u_x^2}{u_{xo}^2}} \quad (2)$$

The  $u_y$  term can be expanded to give

$$u_y = u_{yo} [\sin \omega t \cos \gamma + \cos \omega t \sin \gamma] \quad (3)$$

Substituting Equation (2) into (3), we have

$$u_y = u_{yo} \left[ \frac{u_x}{u_{xo}} \cos \gamma + \left( \sqrt{1 - \frac{u_x^2}{u_{xo}^2}} \right) \sin \gamma \right] \quad (4)$$

Rearranging Equation gives

$$\left[ \frac{u_y}{u_{yo}} - \frac{u_x}{u_{xo}} \cos \gamma \right]^2 = \left( 1 - \frac{u_x^2}{u_{xo}^2} \right) \sin^2 \gamma \quad (5)$$

Expanding Equation (5)

$$\frac{u_y^2}{u_{yo}^2} - \frac{2u_x u_y}{u_{xo} u_{yo}} \cos \gamma + \frac{u_x^2}{u_{xo}^2} \cos^2 \gamma = \sin^2 \gamma - \frac{u_x^2}{u_{xo}^2} \sin^2 \gamma \quad (6)$$

Finally, the following expression can be obtained

$$\frac{u_x^2}{u_{xo}^2} + \frac{u_y^2}{u_{yo}^2} = \sin^2 \gamma + 2 \sin \omega t \sin(\omega t + \gamma) \cos \gamma \quad (7)$$

For the case of  $\gamma = \frac{\pi}{2}$

$$\frac{u_x^2}{u_{xo}^2} + \frac{u_y^2}{u_{yo}^2} = 1 \quad (8)$$

Equation (8) is the trajectory of the elliptical motion. The particles have elliptical trajectories on the surface of the material when excited by two sinusoids with a phase difference of  $90^\circ$ . Although the most common structure for rotary motors is a disk, ring, or cylinder, a traveling wave type piezoelectric motor using a rectangular plate was also proposed by Manceau *et al.* in 1998. Motors using high-frequency surface acoustic waves (SAW) may also be classified in this group (Kurosawa, 1996). Flynn *et al.* (1992) attempted to miniaturize traveling wave type piezoelectric motors using ferroelectric thin films.

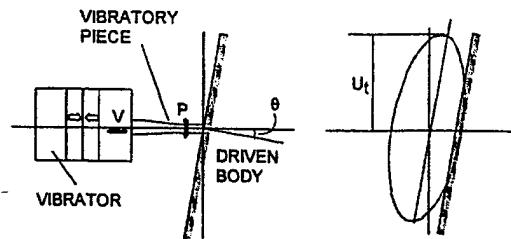


Figure 4 Vibratory piece and elliptical trajectory on the slider surface (after Sashida, 1982).

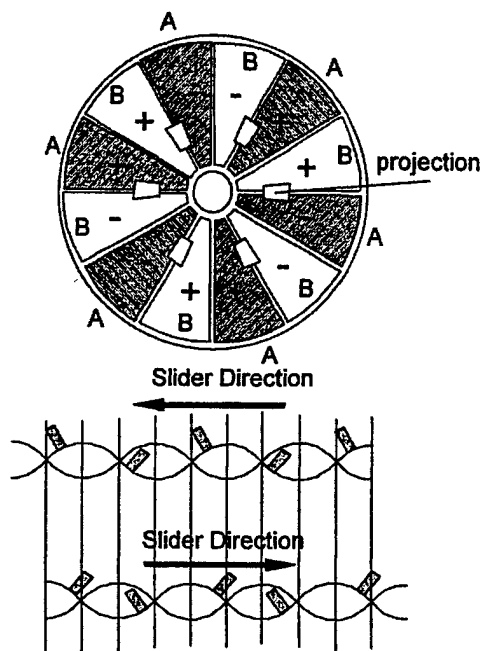


Figure 5 Standing wave type ultrasonic motor operating in the (3,1) mode (after Takano, 1992b).

#### 6.34.2.2 Standing Wave Type Motors

There are two different designs of piezoelectric ultrasonic motors of the standing wave type. In the first class, only the longitudinal vibration of the piezoelectric actuator is excited (Figure 4). The oblique impact between the

stator and slider/rotor elements cause an indirect bending mode excitation, converting longitudinal vibration into tangential vibration in the case of rotary motors (Barth, 1973; Wisniewski *et al.*, 1975; Lavrinenko, 1964; Sashida, 1982). In the second class, two groups of electrodes on the vibratory pieces, such as on a ring, are excited in order to have clockwise and counterclockwise rotation. Such a motor design was proposed by Takano *et al.* (1990, 1992) and the principle is illustrated in Figure 5.

The circular shape of the piezoelectric element shown in Figure 5 is divided into 12 parts of  $1/4$  wavelengths. The parts of each pattern are alternately polarized in positive (+) and negative (−) pairs. The six projections on the vibrator are placed on the border between parts of the same polarity and are adhered to the piezoelectric element. When the shaded (Group A) electrodes are excited at the operating frequency of the motor, the projections leading to the left rise and those leading to the right fall (the position of the hills and valleys alternate in half-periods). The rotor is then driven to the left by the three rising projections. When the drive signal is applied to the non-shaded area (Group B), the entire process is reversed. By driving the rotor in this manner, it is possible to easily change the direction of the rotor. The principle described above is also valid for linear piezoelectric ultrasonic motors.

#### 6.34.2.3 Multi- (or Mixed-) Mode Excitation Type Motors

The type of vibrations and vibration transformations on the composite stator elements of multimode type motors are summarized in Table 1. An elliptical motion on the vibratory pieces is generated when at least two orthogonal vibration modes are superimposed. If multivibrators are used, either the vibration or orientations of the vibrators need to be oriented orthogonally.

Table 1 Vibrations on stator transducers used in multimode excitation type motors.

Single mode	Coupled mode	Vibration transformation through vibration coupler
Longitudinal	Longitudinal–Transversal	Longitudinal to torsional
Transversal	Longitudinal–Torsional	Longitudinal to flexural
Radial	Longitudinal–Flexural	Torsional to longitudinal
Bending	Flexural–Flexural	Flexural to torsional
Flexural	Radial–Torsional	Radial to torsional

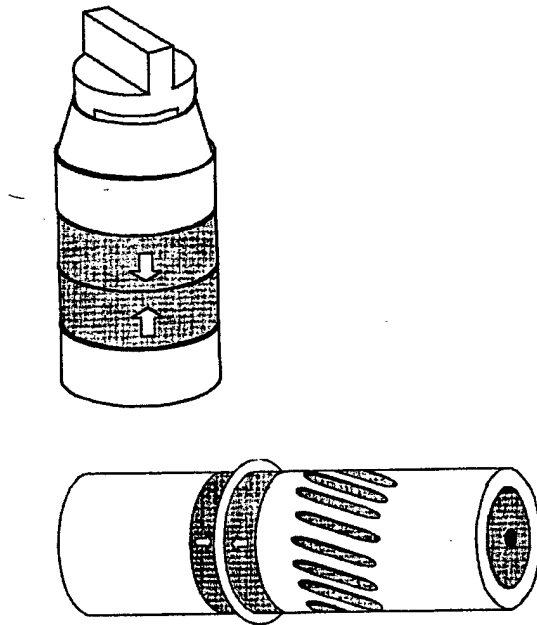


Figure 6 Configuration of longitudinal torsional vibrator: (a) (after Kumada, 1985); (b) (after Tsujino *et al.*, 1992).

#### 6.34.2.3.1 Single-element vibrator exciting multimode vibrations

Exciting at least two resonance modes of the stator vibrator generates elliptical motion on the stator surface. According to the shape of the stator transducer, these orthogonal resonance modes may generate longitudinal-torsional (Kumada, 1985; Tsujino *et al.*, 1992; Aoyagi *et al.*, 1997a, 1997b), radial-torsional, longitudinal-flexural (Fleischer *et al.*, 1989a, 1989b; Tomikawa 1992), or flexural-flexural motions.

The most popular shapes for active piezoelectric elements used in the stator structure are a ring, cylinder, or rectangular plate. Figures 6(a), 6(b), 7, and 8 show some of the

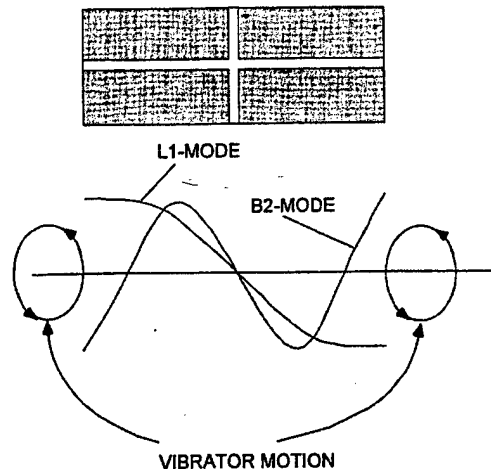


Figure 8 Rectangular stator transducer of a multimode resonator (after Tomikawa *et al.*, 1992).

motor structures operating according to the multimode excitation principle. The stators of these types of motors may have some elastic additions, which are called vibration couplers or concentrators. Single-mode vibration on the piezoelectric element is converted into multimode vibration at the tip of the concentrator.

Either exciting two different electrode groups one at a time or tuning the driving frequency of the stator vibrator to a different orthogonal frequency pair controls the rotation or direction of the linear motion.

A motor proposed by Lee and Li (1998) uses piezoelectric laminated three-layer composite materials, comprising a layer of piezoelectric ceramic material sandwiched between two anti-symmetric composite laminates, which can also be assumed a single vibrator multimode type motor. The required anisotropy of the laminate was obtained by arranging the laminate so that the fibers in the two outer layers of the piezoelectric beam run in  $\theta$  and  $-\theta$  directions.

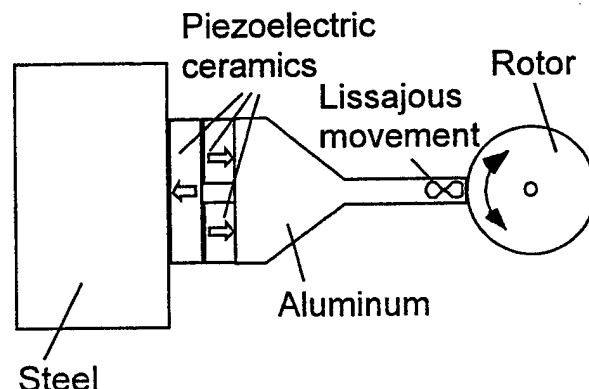


Figure 7 Bimodal type piezoelectric motor (after Fleischer *et al.*, 1989a, 1989b).

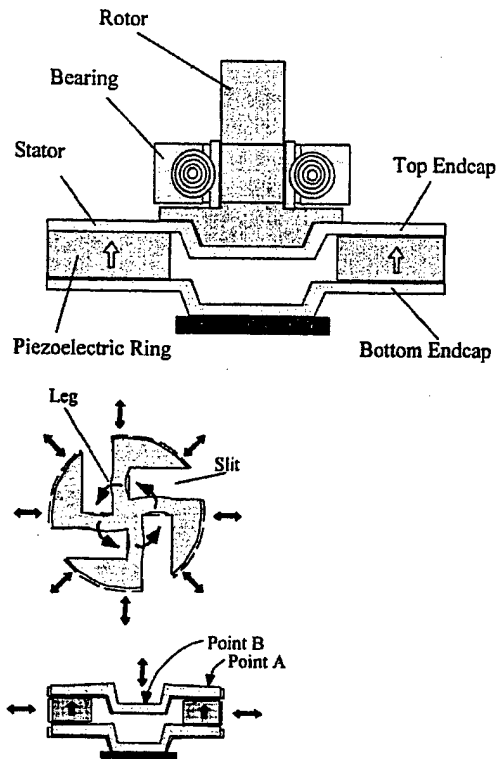


Figure 9 (a) Structure of the ultrasonic motor. Metal end caps were bonded to the piezoelectric ring using adhesive epoxy. (b) Top and cross-sectional view of the stator displacement. Windmill-like slits were cut by EDM.

Another multimode motor was developed using a metal ceramic composite structure (Koc *et al.*, 1998a, 1998b). The basic configuration of the designed piezoelectric ultrasonic motor is shown in Figure 9(a). The motor is composed of three components: a stator, a rotor, and a ball bearing. The stator is made of an active piezoelectric ring, poled in its thickness direction and bonded with two windmill-like slotted metal end caps. The stator is excited through its two electrodes, generating ultrasonic vibration in the radial direction at a radial mode resonance frequency. The two identical metal end caps on both sides of the ring, bonded after shifting 45° with each other, transfer the radial vibration into longitudinal and tangential vibrations. The combination of these vibrations (longitudinal and tangential) generates rotation due to the frictional interaction between the center part of the top end cap and the periphery of the rotor.

The principle of the motor is as follows. When the piezoelectric ring vibrates in the radial direction, the metal end caps, bonded to the outside circumference of the ring, will also move together with the piezoelectric ring. The legs connecting the outer to the center part of

the end caps make the latter deformed not only in the tangential but also in the longitudinal direction. Referring now to Figure 9(b), the displacement top and cross-sectional view of the stator, a poled and electroded piezoelectric single ring was bonded with two metal end caps. The metal end caps were cut by electrical discharge machining (EDM). Before the metal end caps were bonded using adhesive epoxy to the piezoelectric ring, the center parts of the end caps were indented from the rest of the body. The purposes of the indent were: (i) to hold the rotor at the center of the stator and (ii) to provide a contact surface between the periphery of rotor and the indented surface of the top end cap. The last step before mounting the motor was to join the stator to a metal base or to the bottom of the housing unit that had acoustic impedance different from the end cap material.

Later this motor structure was modified and it was fabricated to be as small as 3.0 mm in diameter (Koc *et al.*, 1998a, 1998b). A uniformly electroded piezoelectric ring bonded to a metal ring was used as the stator of the motor. Four inward arms at the inner circumference of the metal ring transfer radial displacements into tangential displacements. The rotor ends in a truncated cone shape and touches the tips of the arms. A rotation takes place by exciting coupled modes of the stator element, such as a radial mode and a second bending mode of the arms.

#### 6.34.2.3.2 Multielement vibrators exciting single-mode vibrations

In this type of motor, superimposing two orthogonal single-mode vibrations with a phase shift generates elliptical motion. Either actuators, shown in Figure 10 (Mori *et al.* 1988), or vibrations generated by actuators, as shown in Figure 11 (Nakamura *et al.* 1991), are oriented orthogonally. The motor designed by Claeysen *et al.* (1996) uses two longitudinal multilayer actuators that are placed oppositely but the vibration generated by the actuators were superimposed on a vibration coupler.

#### 6.34.2.4 Mode Rotation (Stepper) Type Motors

These types of motors are based on the phenomenon that an object on a vibrating body moves to the nodal point of the vibration and rests there. The use of circular structures (i.e., ring, disk, or cylinder) as a stator element simplifies the motor structure. The nodal point on



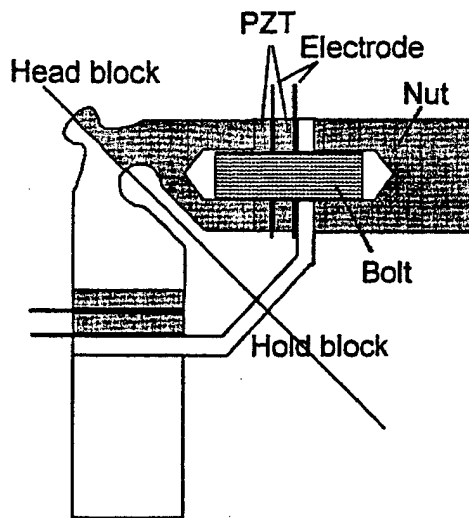


Figure 10 Piezoelectric motor with two longitudinal vibrators with a temporal phase shift (after Mori *et al.* 1988).

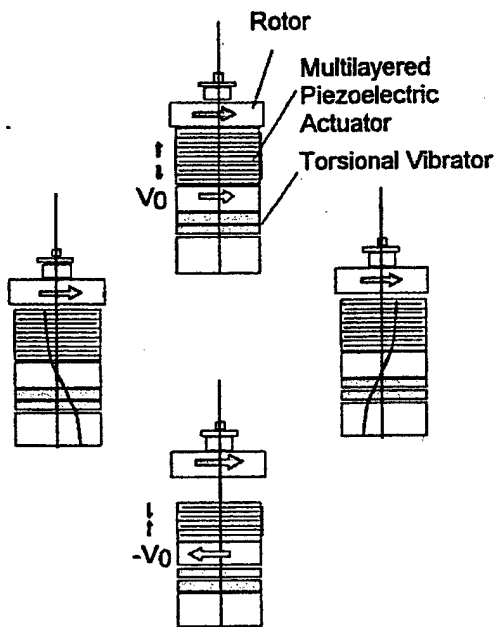


Figure 11 Hybrid transducer type ultrasonic motor. Torsional and longitudinal vibration with a temporal phase shift generate an elliptical motion at the interface of stator and rotor (after Nakamura *et al.* 1991).

a circular stator element can be generated by exciting a group of electrodes which are shifted one after another on the circular structure. Typical examples of these types of motors are discussed in papers by Nakamura *et al.* (1997) who used flexural modes of a ring (Figure 12), Lamberti *et al.* (1996) who used flexural modes of a disk (Figure 13), and Morita *et al.* (1996), who used the bending vibration of a cylinder

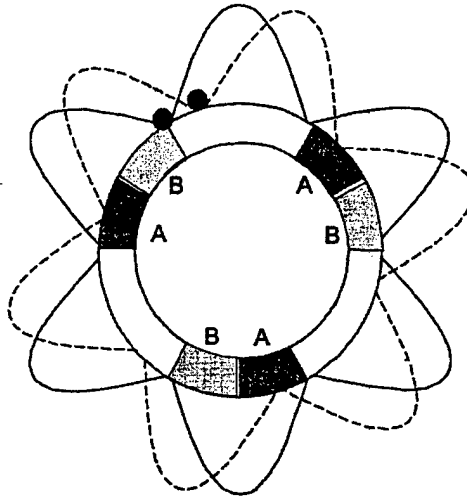


Figure 12 Operating principle of mode rotation type ultrasonic motor (after Nakamura *et al.*, 1997).

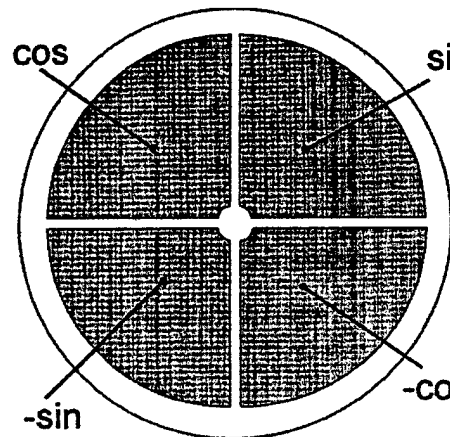


Figure 13 Mode rotation type ultrasonic motor using thin disk structure (after Lamberti *et al.*, 1998).

(Figure 14). When the number of segmented electrode on the piezoelectric piece are set to four, driving conditions of a mode rotation type motor becomes identical to a traveling wave type.

#### 6.34.3 PIEZOELECTRIC ELEMENTS USED IN STATOR VIBRATOR

Circular and rectangular shapes are the most common forms of vibratory pieces used as stators for piezoelectric ultrasonic motors (Figure 15). Depending on the electrode configuration and poling direction of piezoelectric element, different vibrations such as longitudinal, transverse, or torsional can be generated. The shape of elements and type of vibrations on a piezoelectric vibrator used for stators are tabulated in Table 2.

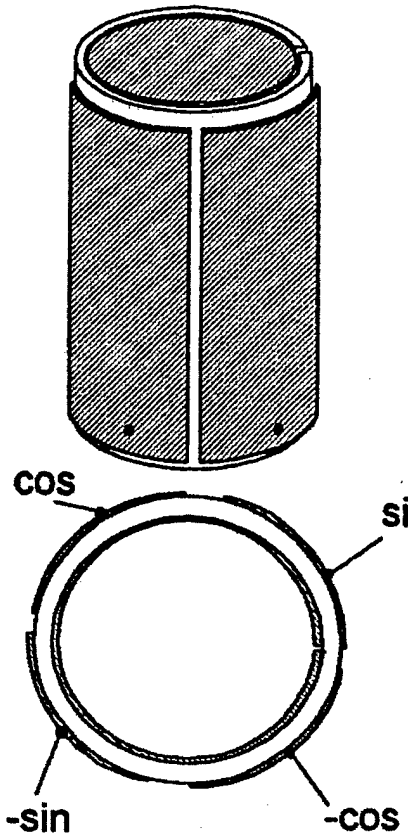


Figure 14 Mode rotation type ultrasonic motor using circular cylinder structure (after Morita *et al.* 1996).

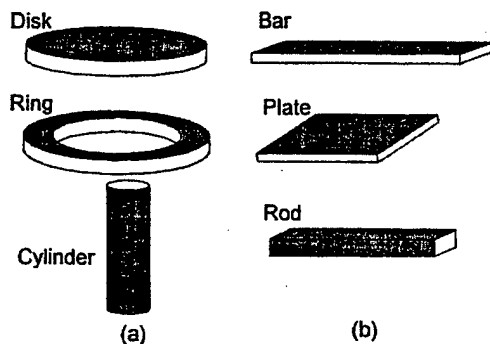


Figure 15 Shape of piezoelectric element used in stator: (a) circular, (b) rectangular.

#### 6.34.4 RELIABILITY OF PIEZOELECTRIC ULTRASONIC MOTORS

Although piezoelectric ultrasonic motors have been investigated for quite some time, these motors still have some fundamental problems which need to be solved before using these motors as high-performance actuators. The fundamental problems are:

Table 2 Shape and type of vibrations on piezoelectric elements used in a stator vibrator.

Shape of piezoelectric element	Type of vibration
<i>Circular</i>	
Disk	Radial Flexural
Ring	Radial Shear/torsional Flexural
Cylinder	Bending Shear/torsional Longitudinal
<i>Rectangular</i>	
Plate	Bending Shear/torsional Longitudinal Transverse
Bar	Bending Shear/torsional Longitudinal
Rod	Bending Shear/torsional Longitudinal

(i) Resonance drive causes a temperature rise in the piezoelectric ceramic material, and motor.

(ii) Rotor and stator contact determine the performance and lifetime of a motor.

(iii) Friction and wear limit force transformation from the composite stator element to the rotor or slider. Selection of frictional materials with high wear resistance and stable mechanical properties is very important.

(iv) High frequency, high voltage drive requires expensive and bulky power supplies.

##### 6.34.4.1 Heat Generation

Piezoelectric ultrasonic motors are resonant devices. The piezoelectric ceramic material used in a stator element is subjected to intense vibration at a resonance frequency in order to obtain the necessary displacement to push the rotor or slider. Lead zirconate titanate (PZT) based piezoelectric ceramics are most commonly used in a motor's stator. However, under continuous driving, the mechanical quality factor  $Q_m$  decreases (which means vibration velocity saturation) when the stator transducer is operated under a high vibration level. Under such a high vibration level operation, when the applied electric power is further increased, the vibration amplitude/velocity does not increase, but the temperature rises. The piezoelectric material used in a motor's stator or transformer needs to have the following features: high

piezoelectric coupling constant ( $k_{ij}$ ), high mechanical quality factor ( $Q_m$ ), and low loss factor ( $\tan \delta$ ).

#### 6.34.4.2 Contact Mechanics

The contact mechanics of piezoelectric ultrasonic motors not only determines motor performance such as rotational speed, output torque, power, and efficiency, it also determines the lifetime of these motors. Therefore, the mathematical modeling of contact mechanics is an important topic and much research has been done especially in the 1980s and 1990s (Fleischer *et al.*, 1989a, 1989b; Ragulskis *et al.*, 1988; Flynn, 1995; Maeno *et al.*, 1992a, 1992b). A more comprehensive overview of the contact mechanics of piezoelectric ultrasonic motors can be found in Wallaschek (1998).

#### 6.34.4.3 Frictional Materials

Since force transformation from the composite stator element to the rotor or slider of a piezoelectric ultrasonic motor is determined by friction at the interface of the rotor and the stator, frictional materials are very important in the design of piezoelectric motors. Good frictional materials for piezoelectric ultrasonic motors need to have a high wear resistance and stable mechanical properties with respect to temperature and other environmental changes. Experimentally, different polymer blends have been tested and the most detailed discussion on this subject is given by Ueha and Tomikawa (1993). High-ranking materials include PTFE (polytetrafluoroethylene), PPS (Ryton), PBT (polybutylterephthalate), and PEEK (polyethylethylketone) (Ishii *et al.*, 1995). In practical motors, Econol (Sumitomo Chemical), carbon fiber reinforced plastic (Japan Carbon), PPS (Sumitomo Bakelite), and polyimide have popularly been used. Ishii *et al.* (1995) investigated the wear properties of a carbon fiber reinforced plastic frictional material.

#### 6.34.4.4 Drive Control Techniques

Basic control parameters are the amplitude, frequency, and phase of the a.c. drive signal. The dynamic and steady-state mathematical modeling of piezoelectric ultrasonic motors is extremely difficult from a theoretical point of view because it contains many complicated and nonlinear characteristics dependent on operating temperature, load torque, applied voltage,

and static pressure force between the stator and the rotor of the motor. Therefore, some modern control techniques such as the predictive-base self-tuning control system (Snitka *et al.*, 1996) or adaptive fuzzy/neural network control techniques (Izuno *et al.*, 1992; Lin *et al.*, 1999) have been applied to control piezoelectric ultrasonic motors and excellent performance has been obtained.

### 6.34.5 APPLICATIONS OF PIEZOELECTRIC ULTRASONIC MOTORS

Piezoelectric ultrasonic motors are of increasing interest in high-tech industry. High torque, light weight, no electromagnetic induction interference, high efficiency, and low-speed operation without a gear mechanism are some of the attractive characteristics which motivate the study of these motors. With these characteristics, ultrasonic motors have been used in various industrial applications such as drives for autofocusing camera lenses. They also have potential for other applications.

#### 6.34.5.1 Actuators for Consumer Goods

Ultrasonic motors have been commercialized for drive mechanisms in camera autofocus lenses and computer-related equipment such as disk drives. They are also used in applications where a large number of motors are incorporated but only few are used regularly and the rest occasionally.

#### 6.34.5.2 Actuators for Precise Positioning Devices

Piezoelectric motors are used in rapid-positioning devices with accuracy of the order of nanometers. An important application includes semiconductor production. Inevitable backlash due to the use of a gear transmission system makes it difficult to achieve high accuracy with electromagnetic motors.

#### 6.34.5.3 Actuators for Miniaturized Machines

Electromagnetic motors cannot be miniaturized because of saturation of the magnetic circuit and the number of windings required. The smallest electromagnetic motor is several millimeters in diameter (Stefanini *et al.*, 1996).

#### 6.34.5.4 Actuators for Machines Used in Space

Efficient miniature actuators that are compact and consume low power are needed to drive telerobotic devices and outer space mechanisms for future NASA missions (Bar-Cohen *et al.*, 1998). Actuators for space mechanisms need to be small, light, and energy efficient. Actuators meeting the aforementioned requirements can be used for telerobotic devices that include robotic arms, rovers, release mechanisms, antenna and instrument deployment mechanisms, positioning devices and aperture opening and closing devices. Piezoelectric ultrasonic motors have the potential to meet these NASA requirements.

#### 6.34.5.5 Actuators for Medical Uses

Piezoelectric motors can also be used for intravascular ecographic systems. In addition to being small (2–3 mm in diameter), the motor must be disposable and the price should be low.

#### 6.34.6 REFERENCES

- M. Aoyagi, Y. Murasawa, T. Ogasawara and Y. Tomikawa, *Jpn. J. Appl. Phys.*, 1997, **36**(5B), 3126–3129.
- M. Aoyagi, S. Tsuchiya and Y. Tomikawa, *Jpn. J. Appl. Phys.*, 1997, **36**(9B), 6106–6109.
- M. E. Archangelskij, *Acoust. J.*, 1963, **9**, 275.
- Y. Bar-Cohen, X. Bao and W. Grandia, in 'Proceedings of the Smart Structures and Materials', San Diego, CA, 1–5 March, 1998.
- H. V. Barth, *IBM Technical Disclosure Bulletin*, 1973, **16**(7).
- F. Claeysen, R. Le Letty, L. Chouteau, N. Lhermet, L. Petit, R. Briot and P. Gonnard, in 'Actuator 96, 5th International Conference on New Actuators', Bremen, Germany, AXON, Bremen, Germany, 1996, pp. 152–156.
- M. A. Dubois and P. Muralt, *IEEE Trans. Ultrason. Ferroelect. Freq. Cont.*, 1998, **45**, 1169–1177.
- A. M. Flynn, Ph.D. Thesis, Massachusetts Institute of Technology, 1995.
- A. M. Flynn, L. Tavrow, S. Bart, R. Brooks, D. Ehrlich, K. R. Udayakumar and L. E. Cross, *IEEE J. Microelectromech. Syst.*, 1992, **1**, 44–51.
- M. Fleischer, D. Stain and H. Meixner, *IEEE Trans. Ultrason. Ferroelect. Freq. Cont.*, 1989a, **36**, 607–613.
- M. Fleischer, D. Stain and H. Meixner, *IEEE Trans. Ultrason. Ferroelect. Freq. Cont.*, 1989b, **36**, 614–619.
- M. M. Guillemot-Amadei, L. Petit, L. Lebrun, R. Briot and P. Gonnard, *Meas. Sci. Technol.*, 1995, **6**, 458–466.
- P. Hagerdorn and J. Wallaschek, *J. Sound Vibration*, 1992a, **155**(1), 31–46.
- P. Hagerdorn and J. Wallaschek, in 'Actuator 96, 4th International Conference on New Actuators', AXON, Bremen, Germany, 1992b, pp. 32–37.
- H. Hirata and S. Ueha, *IEEE Trans. Ultrason. Ferroelect. Freq. Cont.*, 1995, **42**, 225–231.
- J. H. Hu, T. Yamazaki, K. Nakamura and S. Ueha, *Jpn. J. Appl. Phys.*, 1995, **34**(5B), 2702–2706.
- T. Iijima, K. Sano, Y. Nakagawa and H. Ito, *Jpn. J. Appl. Phys.*, 1993, **32**(5B), 2402–2404.
- R. Inaba, A. Tokushima, O. Kawasaki, Y. Ise and H. Yoneno, in 'IEEE, Ultrasonics Symposium', ed. B. R. McAvoy, IEEE, Piscataway, NJ, 1987, pp. 747–756.
- T. Ishii, S. Ueha, K. Nakamura and K. Ohnishi, *Jpn. J. Appl. Phys.*, 1995, **34**(5B), 2765–2770.
- Y. Izuno, R. Takeda, and M. Nakaoka, *IEEE Trans. Industrial Applications*, 1992, **2**(3), 613–618.
- M. Kasuga, A. Iino, K. Suzuki, M. Suzuki and S. Kotanagi, *Int. J. Jpn. Soc. Pres. Eng.*, 1998, **21**(1), 5–8.
- M. Kasuga, T. Satoh, J. Hirotsu and M. Kawata, in '4th Congress Eur. De Chronometrie', Lausanne, 1992, pp. 53–56.
- T. Kawai, K. Asai, S. Naito, T. Fukui, Y. Adachi, N. Handa, K. Ikeda and K. Tusuda, *Jpn. J. Appl. Phys.*, 1995, **34**, 2711–2714.
- C. Kleesattel and A. Kuris, *US Pat.* 3 058 218 (1959).
- B. Koc, A. Dogan, Y. Xu, R. E. Newnham and K. Uchino, *Jpn. J. Appl. Phys.*, 1998a, **37**(10), 5659–5662.
- B. Koc, Y. Xu and K. Uchino, in 'IEEE Ultrasonic Symposium', Sendai, Japan, eds. S. C. Schneider, M. Levy and B. R. McAvoy, IEEE, New York, 1998b, pp. 687–690.
- J. W. Krome and J. Wallaschek, in 'IEEE Ultrasonics Symposium', eds. S. C. Schneider, M. Levy and B. R. McAvoy, IEEE, New York, 1995, pp. 413–416.
- A. Kumada, *Jpn. J. Appl. Phys.*, 1985, **24**(2), 739–741.
- M. Kurosawa, K. Nakamura, T. Okamoto and S. Ueha, *IEEE Trans. Ultrason. Ferroelect. Freq. Cont.*, 1989, **36**, 517–521.
- M. K. Kurosawa, M. Takahashi and T. Higuchi, *Ultrasonics*, 1996, **34**, 243–246.
- M. K. Kurosawa, M. Takahashi and T. Higuchi, *IEEE Trans. Ultrason. Ferroelect. Freq. Cont.*, 1998, **45**, 1229–1237.
- N. Lamberti, A. Iula and M. Pappalardo, *IEEE Trans. Ultrason. Ferroelect. Freq.*, 1998, **45**, 23–29.
- V. V. Lavrinenko, *Sov. Pat.* 217 509 (1964).
- S.-W. R. Lee and H. L. Li, *Smart Mater. Struct.*, 1998, **7**, 327–336.
- R. Le Letty, F. Claeysen, P. Gonnard and B. Hamonic, in 'IEEE Ultrasonics Symposium', IEEE Service Center, Piscataway, NJ, 1994, pp. 531–534.
- F. J. Lin, R. J. Wai and R. Y. Duan, *IEEE Trans. Industrial Electronics*, 1999, **46**, 999–1011.
- T. Maeno and D. B. Bogy, *IEEE Trans. Ultrason. Ferroelect. Freq.*, 1992, **39**, 675–682.
- T. Maeno, T. Tsukimoto and A. Miyake, *IEEE Trans. Ultrason. Ferroelect. Freq.*, 1992, **39**, 668–674.
- J. F. Manceau, S. Biwersi and F. Bastien, *Smart Mater. Struct.*, 1998, **7**, 337–344.
- K. Mori, H. Hirai and I. Kobayashi, *Eur. Pat. Appl.* EP 0297 574 A2 (1988).
- T. Morita, M. Kurosawa and T. Higuchi, *Jpn. J. Appl. Phys.*, 1996, **35**, 3251–3254.
- K. Nakamura, M. Kurosawa and S. Ueha, *IEEE Trans. Ultrason. Ferroelect. Freq.*, 1991, **38**, 188–193.
- K. Nakamura, J. Margairaz, T. Ishii and S. Ueha, *IEEE Trans. Ultrason. Ferroelect. Freq.*, 1997, **44**, 823–828.
- K. Ragulskis, R. Bansevicius, R. Barauskas and G. Kulvietis, 'Vibromotors for Precision Microrobots', Hemisphere Publishing Corporation, New York, 1988.
- T. Sashida, *Oyo Butsiuri*, 1982, **51**(6), 713–718.
- T. Sashida and T. Kenjo, 'An Introduction to Ultrasonic Motors', Clarendon Press, Oxford, UK, 1993.
- M. Shimanuki, M. Aoyagi and Y. Tomikawa, *Jpn. J. Appl. Phys.*, 1994, **33**, 3075–3080.
- V. Snitka, V. Mizariene and D. Zukauskas, *Ultrasonics*, 1996, **34**, 247–250.
- C. Stefanini, M. C. Carrozza and P. Dario, in 'Proceedings of the Seventh International Symposium on Micro Machine and Human Science, MHS'96', Nagoya, Japan, October 2–4, IEEE Service Center, Piscataway, NJ, 1996, pp. 195–201.

- T. Takano, Y. Tomikawa and C. Kusakabe, *IEEE Trans. Ultrason. Ferroelect. Freq.*, 1992, **39**(2), 180-186.
- T. Takano, Y. Tomikawa, T. Ogasawara, S. Sugawara and M. Konno, *IEEE Trans. Ultrason. Ferroelect. Freq.*, 1990, **37**(3), 224-229.
- S. Tashiro, M. Ikehiro and H. Igarashi, *Jpn. J. Appl. Phys.*, 1997, **36**, 3004-3009.
- Y. Tomikawa, T. Ogasawara and T. Takano, *Ferroelectrics*, 1989, **91**, 163-178.
- Y. Tomikawa, T. Takano and H. Umeda, *Jpn. J. Appl. Phys.*, 1992, **31**, 3073-3076.
- J. Tsujino, M. Takeuchi and H. Koshisako, in 'IEEE Ultrasonics Symposium', ed. B. R. McAvoy, IEEE Service Center, Piscataway, NJ, 1992, pp. 887-892.
- K. Uchino, 'Piezoelectric Actuators and Ultrasonic Motors', Kluwer Academic Publishers, Boston, 1997.
- K. Uchino, *Smart Mater. Struct.*, 1998, **7**, 273-285.
- S. Ueha, *Jpn. J. Appl. Phys.*, 1989, **28**(suppl. 28-1), 3-6.
- S. Ueha and Y. Tomikawa, 'Ultrasonic Motors, Theory and Applications', Clarendon Press, Oxford, UK, 1993.
- P. E. Vasiliev, K. M. Ragulskis, I. A. Savitskas, V. M. Misikov and O. D. Topolaitsky, *US Pat.* 4 210 837 (1980).
- J. Wallaschek, *Smart Mater. Struct.*, 1998, **7**, 369-381.
- A. L. W. Williams and W. J. Brown, *US Pat.* 2 439 499 (1942).
- V. C. Wiscniewski, *Deutsches Pat.* DE 2 530 045 C 2 (1975).
- Q. C. Xu, S. Yoshikawa, J. R. Belsick and R. E. Newnham, *IEEE Trans. Ultrason. Ferroelect. Freq. Cont.*, 1991b, **38**(6), 634-639.
- O. Y. Zharii, in 'Actuator 96, 4th International Conference on New Actuators', AXON, Bremen, Germany, 1994a, pp. 156-159.
- O. Y. Zharii, in 'IEEE Ultrasonic Symposium', eds. M. Levy, S. C. Schneider and B. R. McAvoy, IEEE Service Center, Piscataway, NJ, 1994b, pp. 545-548.
- J. Zumeris, *US Pat.* 5 453 653 (1995).

# **APPENDIX 72**

# COMPACT PIEZOELECTRIC ULTRASONIC MOTORS

KENJI UCHINO AND BURHANETTIN KOC

*International Center for Actuators and Transducers, Materials Research Laboratory,  
The Pennsylvania State University  
University Park, PA 16802, USA*

## Abstract

This paper reviews recent developments of compact ultrasonic motors using piezoelectric resonant vibrations. Following the historical background, ultrasonic motors using the standing and travelling waves are introduced. Driving principles and motor characteristics are explained in comparison with the conventional electromagnetic motors.

## 1. Introduction

In office equipment such as printers and floppy disk drives, market research indicates that tiny motors smaller than  $1\text{ cm}^3$  would be in large demand over the next ten years. However, using the conventional electromagnetic motor structure, it is rather difficult to produce a motor with sufficient energy efficiency. Piezoelectric ultrasonic motors, whose efficiency is insensitive to size, are superior in the mm-size motor area.

In general, piezoelectric and electrostrictive actuators are classified into two categories, based on the type of driving voltage applied to the device and the nature of the strain induced by the voltage: (1) rigid displacement devices for which the strain is induced unidirectionally along an applied dc field (servo displacement transducers and pulse drive motors), and (2) resonating displacement devices for which the alternating strain is excited by an ac field at the mechanical resonance frequency (ultrasonic motors). The AC resonant displacement is not directly proportional to the applied voltage, but is, instead, dependent on adjustment of the drive frequency. Although the positioning accuracy is not as high as that of the rigid displacement devices, very high speed motion due to the high frequency is an attractive feature of the ultrasonic motors.

The materials requirements for these classes of devices are somewhat different, and certain compounds will be better suited for particular applications. The servo-displacement transducer suffers most from strain hysteresis and, therefore, a PMN electrostrictor is preferred for this application. The pulse-drive motor requires a low permittivity material aiming at quick response with a limited power supply rather than a

small hysteresis, so that soft PZT piezoelectrics are preferred to the high-permittivity PMN for this application. On the contrary, the ultrasonic motor requires a very hard piezoelectric with a high mechanical quality factor  $Q_m$ , in order to minimize heat generation and maximize displacement. Note that the resonance displacement is equal to  $\alpha \cdot dEL$ , where  $d$  is a piezoelectric constant,  $E$ , applied electric field,  $L$ , sample length and  $\alpha$  is an amplification factor proportional to the mechanical  $Q$ .

This paper deals with ultrasonic motors using resonant vibrations, putting a particular focus on miniaturized motors. Following the historical background, various ultrasonic motors are introduced. Driving principles and motor characteristics are explained in comparison with the conventional electromagnetic motors.

## 2. Classification of ultrasonic motors

### 2.1 *HISTORICAL BACKGROUND*

Electromagnetic motors were invented more than a hundred years ago. While these motors still dominate the industry, a drastic improvement cannot be expected except through new discoveries in magnetic or superconducting materials. Regarding conventional electromagnetic motors, tiny motors smaller than 1cm long are rather difficult to produce with sufficient energy efficiency. Therefore, a new class of motors using high power ultrasonic energy, ultrasonic motor, is gaining wide spread attention. Ultrasonic motors made with piezoceramics whose efficiency is insensitive to size are superior in the mini-motor area. Figure 1 shows the basic construction of an ultrasonic motor, which consists of a high-frequency power supply, a vibrator and a slider. Further, the vibrator is composed of a piezoelectric driving component and an elastic vibratory part, and the slider is composed of an elastic moving part and a friction coat.

Though there had been some earlier attempts, the practical ultrasonic motor was proposed firstly by H. V. Barth of IBM in 1973 [1]. A rotor was pressed against two horns placed at different locations. By exciting one of the horns, the rotor was driven in one direction, and by exciting the other horn, the rotation direction was reversed. Various mechanisms based on virtually the same principle were proposed by V. V. Lavrinenko [2] and P. E. Vasiliev [3] in the former USSR. Because of difficulty in maintaining a constant vibration amplitude with temperature rise, wear and tear, the motors were not of much practical use at that time. In 1980's, with increasing chip pattern density, the semiconductor industry began to request much more precise and sophisticated positioners which do not generate magnetic field noise. This urgent request has accelerated the developments in ultrasonic motors. Another advantage of ultrasonic motors over the conventional electromagnetic motors with expensive copper coils, is the improved availability of piezoelectric ceramics at reasonable cost. Japanese manufacturers are producing piezoelectric buzzers around 30 - 40 cent price range at the moment.



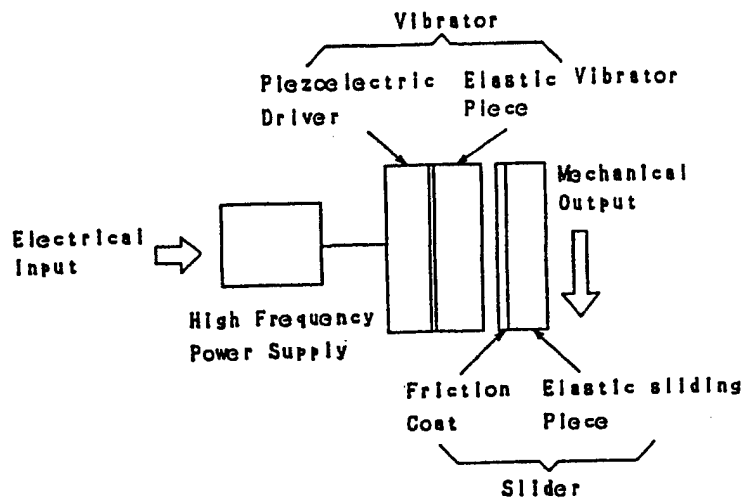


Figure 1. Fundamental construction of ultrasonic motors.

Let us summarize the merits and demerits of the ultrasonic motors:

#### Merits

1. Low speed and high torque -- Direct drive
2. Quick response, wide velocity range, hard brake and no backlash
  - Excellent controllability
  - Fine position resolution
3. High power / weight ratio and high efficiency
4. Quiet drive
5. Compact size and light weight
6. Simple structure and easy production process
7. Negligible effect from external magnetic or radioactive fields, and also no generation of these fields

#### Demerits

8. Necessity for a high frequency power supply
9. Less durability due to frictional drive
10. Drooping torque vs. speed characteristics

## 2.2 CLASSIFICATION AND PRINCIPLES OF ULTRASONIC MOTORS

From a customer's point of view, there are rotary and linear type motors. If we categorize them from the vibrator shape, there are rod type, shaped, ring (square) and cylinder types. Two categories are being investigated for ultrasonic motors from a vibration characteristic viewpoint: a standing-wave type and a travelling-wave type. The standing wave is expressed by

$$u_s(x,t) = A \cos kx \cdot \cos \omega t, \quad (1)$$

while the propagating wave is expressed as

$$u_p(x,t) = A \cos(kx - \omega t). \quad (2)$$

Using a trigonometric relation, Eq. (2) can be transformed as

$$u_p(x,t) = A \cos kx \cdot \cos \omega t + A \cos(kx - \pi/2) \cdot \cos(\omega t - \pi/2). \quad (3)$$

This leads to an important result, i. e. a propagating wave can be generated by superimposing two standing waves whose phases differ by 90 degree to each other both in time and in space. This principle is necessary to generate a propagating wave on a limited volume/size substance, because only standing waves can be excited stably in a finite size.

The standing-wave type is sometimes referred to as a vibratory-coupler type or a "woodpecker" type, where a vibratory piece is connected to a piezoelectric driver and the tip portion generates flat-elliptical movement. Figure 2 shows a simple model proposed by T. Sashida [4]. A vibratory piece is connected to a piezoelectric driver and the tip portion generates flat-elliptical movement. Attached to a rotor or a slider, the vibratory piece provides intermittent rotational torque or thrust. The standing-wave type has, in general, high efficiency, but lack of control in both clockwise and counterclockwise directions is a problem.

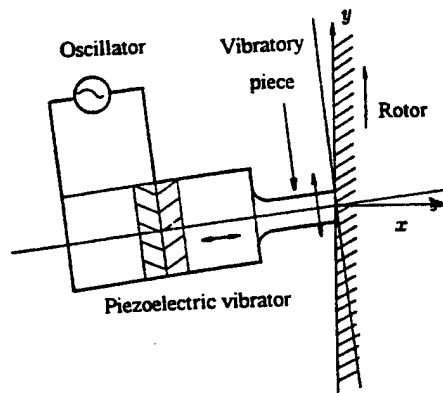


Figure 2. Vibratory coupler type motor.

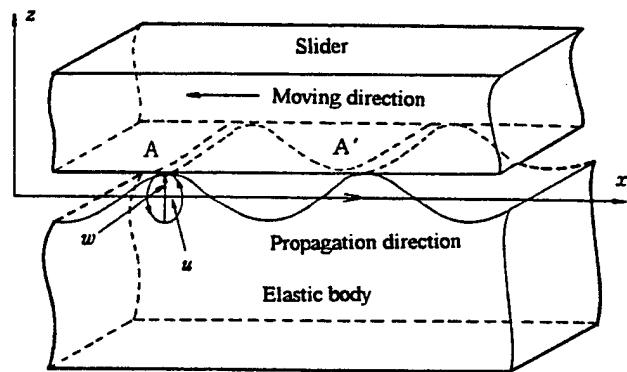


Figure 3. Principle of the propagating wave type motor.

By comparison, the propagating-wave type (a surface-wave or "surfing" type) combines two standing waves with a 90 degree phase difference both in time and in space. The principle is shown in Fig. 3. A surface particle of the elastic body draws an elliptical locus due to the coupling of longitudinal and transverse waves. This type requires, in general, two vibration sources to generate one propagating wave, leading to low efficiency (not more than 50 %), but it is controllable in both the rotational directions.

### 3. Conventional motor designs

#### 3.1 SASHIDA MOTOR

Figure 4 shows the famous Sashida motor [5]. By means of the travelling elastic wave induced by a thin piezoelectric ring, a ring-type slider in contact with the "rippled" surface of the elastic body bonded onto the piezoelectric is driven in both directions by exchanging the sine and cosine voltage inputs. Another advantage is its thin design, which makes it suitable for installation in cameras as an automatic focusing device. Eighty percent of the exchange lenses in Canon's "EOS" camera series have already been replaced by the ultrasonic motor mechanism. Most of the studies on ultrasonic motors done in the US and Japan have been modifications of Sashida's type.

The PZT piezoelectric ring is divided into 16 positively and negatively poled regions and two asymmetric electrode gap regions so as to generate a 9th mode propagating wave at 44 kHz. A proto-type was composed of a brass ring of 60 mm in outer diameter, 45 mm in inner diameter and 2.5 mm in thickness, bonded onto a PZT ceramic ring of 0.5 mm in thickness with divided electrodes on the back-side. The rotor was made of polymer coated with hard rubber or polyurethane. Figure 5 shows Sashida's motor characteristics.

Canon utilized the "surfing" motor for a camera automatic focusing mechanism, installing the ring motor compactly in the lens frame. It is noteworthy that the stator elastic ring has many teeth, which can magnify the transverse elliptical displacement and improve the speed. The lens position can be shifted back and forth through a screw mechanism. The advantages of this motor over the conventional electromagnetic motor are:

Silent drive due to the ultrasonic frequency drive and no gear mechanism (i. e. more suitable to video cameras with microphones).

Thin motor design and no speed reduction mechanism such as gears, leading to space saving.

Energy saving.

A general problem encountered in these travelling wave type motors is the support of the stator. In the case of a standing wave motor, the nodal points or lines are generally supported; this causes minimum effects on the resonance vibration. To the contrary, a travelling wave does not have such steady nodal points or lines. Thus, special considerations are necessary. In Fig. 4, the stator is basically fixed very gently along the axial direction through felt so as not to suppress the bending vibration. It is important to note that the stop pins which latch onto the stator teeth only provide high rigidity against the rotation.

#### 3.2 INCHWORM DEVICES

Although the motion principle is different, inchworm devices move fast in apparent similarity to ultrasonic motors. The inchworm is driven by a rectangular wave below the resonance frequency, and moves intermittently and discretely. Sophisticated linear

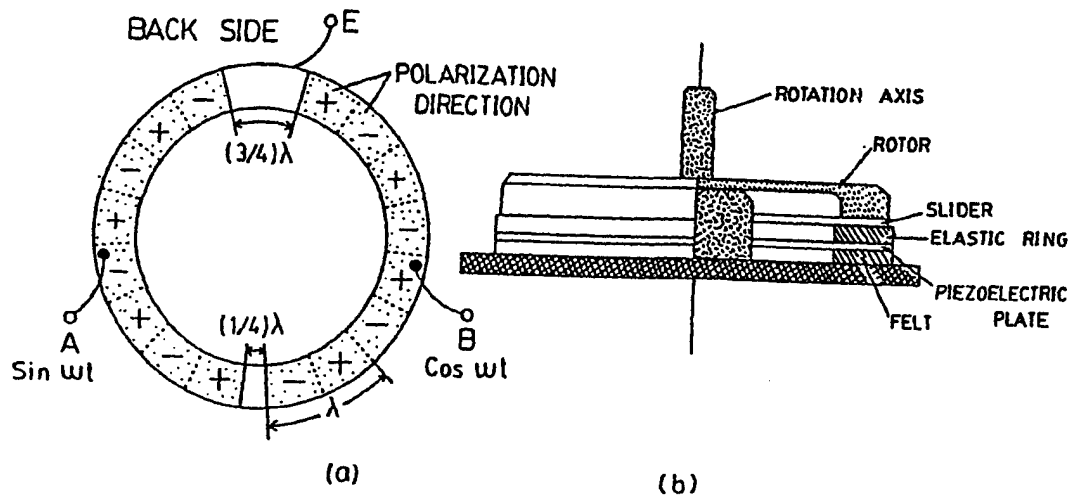


Figure 4. Stator structure of Sashida's motor.

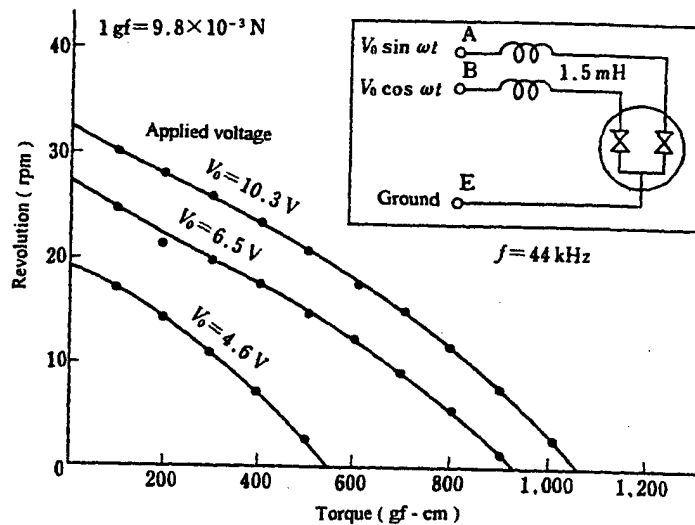


Figure 5. Motor characteristics of Sashida's motor.

walking machines have been developed by two German companies. Philips fabricated a linear drive inchworm using two  $d_{33}$  (longitudinal mode) and two  $d_{31}$  (transverse mode) multilayer actuators (Fig. 6) [6]. Very precise positioning of less than 1 nm was reported. The problems with this type of device are: (1) audible noise, and (2) heat generation, when driven at high frequency. Physik Instrumente manufactured a two-leg inchworm [7].

A pair of inchworm units consisting of two multilayer actuators, are coupled with  $90^\circ$  phase difference in time so as to produce a smooth motion instead of a discrete step motion.

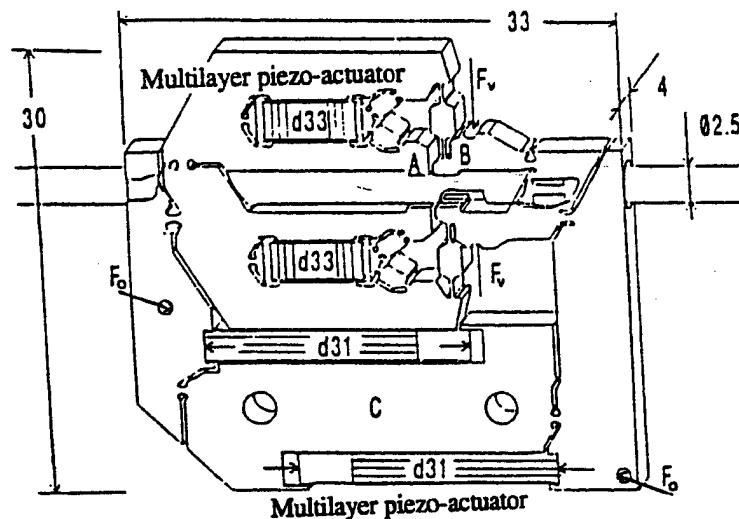


Figure 6. Philips' inchworm.

#### 4. Compact motor designs

##### 4.1 TRAVELING WAVE TYPES

Using basically the same principle as Sashida's, Seiko Instruments miniaturized the ultrasonic motor to as tiny as 10 mm in diameter [8]. Figure 7 shows the construction of this small motor with 10 mm diameter and 4.5 mm thickness. A driving voltage of 3 V and a current 60 mA provides 6000 rev/min (no-load) with torque of 0.1 mN·m. Seiko installed this tiny motor into a wrist watch as a silent alarm. Rotating an imbalanced mass provides enough hand shake to a human without generating audible noise. AlliedSignal developed ultrasonic motors similar to Shinsei's, which would be utilized as mechanical switches for launching missiles [9].

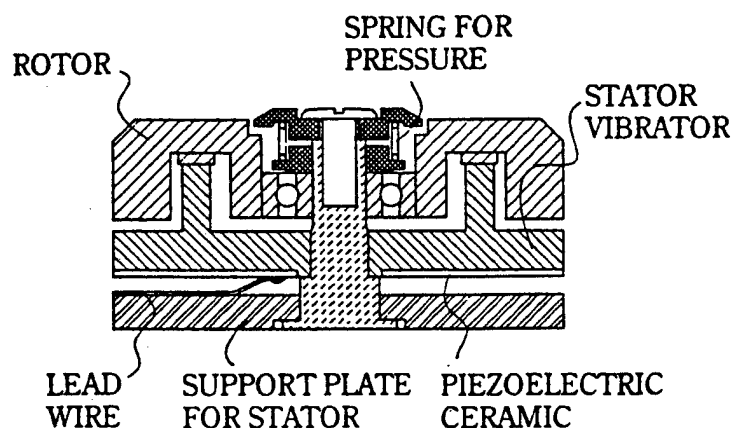


Figure 7. Construction of Seiko's motor.

A significant problem in miniaturizing this sort of travelling wave motor can be found in the ceramic manufacturing process; without providing a sufficient buffer gap between the adjacent electrodes, the electrical poling process (upward and downward) easily initiates the crack on the electrode gap due to the residual stress concentration. This may restrict the further miniaturization of the traveling wave type motors. To the contrary, standing wave type motors, the structure of which is less complicated, are more suitable for miniaturization as we discuss in the following. They require only one uniformly poled piezo-element, less electric lead wires and one power supply.

## 4.2 STANDING WAVE TYPES

### 4.2.1 Linear motors

Uchino et al. invented a  $\pi$ -shaped linear motor [10]. This linear motor is equipped with a multilayer piezoelectric actuator and fork-shaped metallic legs as shown in Fig. 8. Since there is a slight difference in the mechanical resonance frequency between the two legs, the phase difference between the bending vibrations of both legs can be controlled by changing the drive frequency. The walking slider moves in a way similar to a horse using its fore and hind legs when trotting. A test motor  $20 \times 20 \times 5 \text{ mm}^3$  in dimension exhibited a maximum speed of 30 cm/s and a maximum thrust of 0.9 kgf with a maximum efficiency of 20%, when driven at 98 kHz at 6V (actual power = 0.7 W). This motor has been employed in a precision X-Y stage.

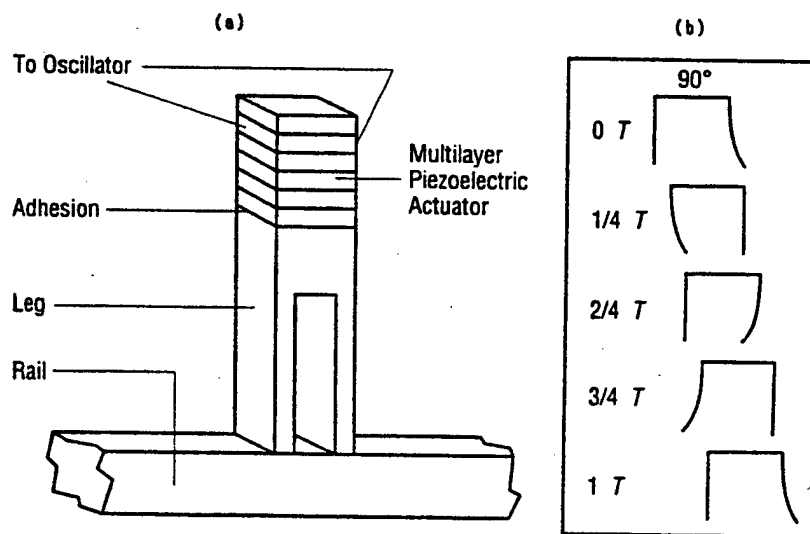


Figure 8.  $\pi$ -shaped linear ultrasonic motor. (a) construction and (b) walking principle. Note the 90 degree phase difference like human walk.

We further miniaturized this "Shepherd" shape by 1/10 into a "Dachshund" shape by reducing the leg length (Fig. 9) [11]. According to this miniaturization, we utilized a unimorph type drive mechanism in conjunction with a coupling mode between 1st longitudinal and 4th bending modes. Under 100 V<sub>p-p</sub> applied (0.6 W), this linear motor exhibited the maximum speed of 160 mm/sec and the thrust of 0.25 - 1.00 N.

One ceramic multilayer component actuator was proposed by Mitsui Chemical [12]. Figure 10 shows the electrode pattern. Only by the external connection, a combined vibration of the longitudinal  $L_1$  and bending  $B_2$  modes could be excited.

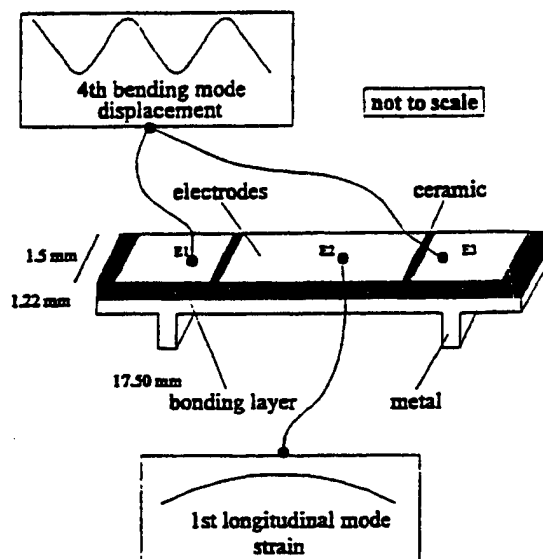


Figure 9. Miniature ultrasonic linear motor.

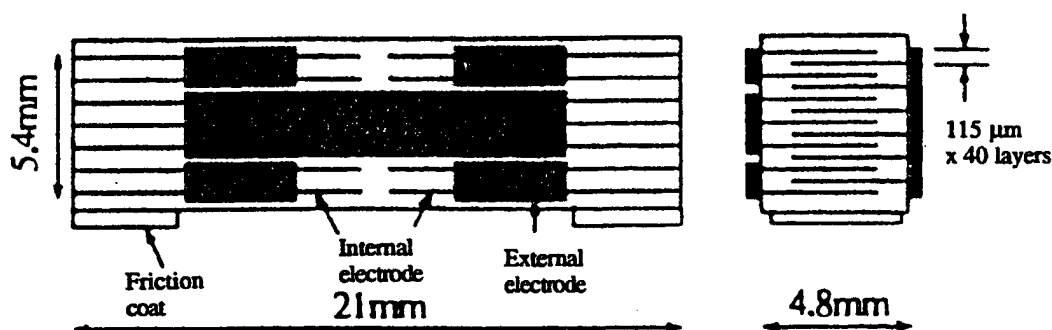


Figure 10. Multilayer ceramic simple linear motor (Mitsui Chemical).

#### 4.2.2 Rotary motors

Hitachi Maxel significantly improved the torque and efficiency by using a torsional coupler, and by the increasing pressing force with a bolt [13]. The torsional coupler looks like an old fashioned TV channel knob, consisting of two legs which transform longitudinal vibration generated by the Langevin vibrator to a bending mode of the knob disk, and a vibratory extruder. Notice that this extruder is aligned with a certain cant angle to the legs, which transforms the bending to a torsion vibration. This transverse moment coupled with the bending up-down motion leads to an elliptical

rotation on the tip portion. A motor with 30mm x 60mm in size and  $20 - 30^\circ$  in cant angle between a leg and a vibratory piece provided the torque as high as 1.3 N·m and the efficiency of 80%. However, this type provides only unidirectional rotation.

The Penn State University has developed a compact ultrasonic rotory motor as tiny as 3 mm in diameter. As shown in Fig. 11, the stator consists basically of a piezoelectric ring and two concave/convex metal endcaps with "windmill" shaped slots bonded together, so as to generate a coupled vibration of up-down and torsional type [14]. Since the component number and the fabrication process were minimized, the fabrication price would be decreased remarkably, and it would be adaptive to the disposable usage. When driven at 160 kHz, the maximum revolution 2000rpm and the maximum torque 0.8mN·m were obtained for a 5 mm $\varnothing$  motor. Notice that even the drive of the motor is intermittent, the output rotation becomes very smooth because of the inertia of the rotor. Figure 12 shows motor characteristics plotted as a function of motor size for modified "windmill" motors [15].

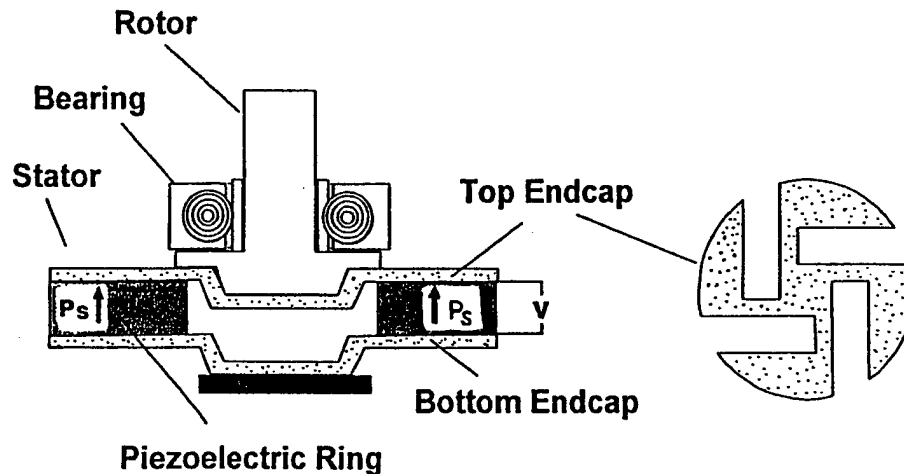


Figure 11. "Windmill" motor with a disk-shaped torsional coupler.

## 5. Integrated motor designs

We will introduce an ultrasonic motor fabricated on a Si substrate, jointly developed by MIT and Penn State [16]. After coating a PZT thin film on a Si membrane (2.2mm x 2.2mm), an 8-pole stator (1.2mm and 2.0mm inner and outer. diameters) was patterned on the surface electrode. The 8 segmented electrode pads were driven in a four phase sequence repeated twice. A small contact glass lens was used as a rotor. This simple structure provided already  $10^3$  time higher torque than the conventional electrostatic MEMS motors. Another intriguing surface acoustic wave motor has been proposed by Kurosawa and Higuchi [17]. Rayleigh waves were excited in two crossed directions on a  $127.8^\circ$ -rotation Y-LiNbO<sub>3</sub> plate with two pairs of interdigital electrode patterns. A



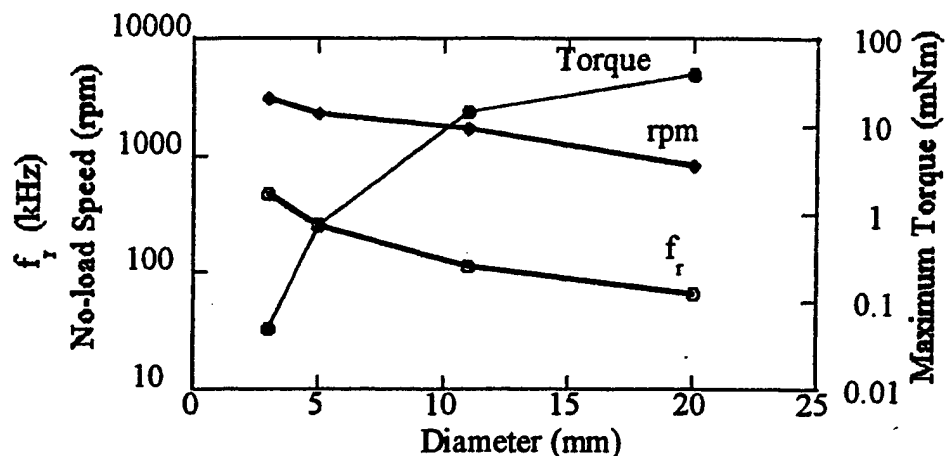


Figure 12. Radial mode resonance frequency, no-load speed and starting torque vs. diameter of the stator. Speed and torque were measured at 15.7 V.

A slider was composed of three balls as legs. The driving vibration amplitude and the wave velocity of the Rayleigh waves were adjusted to 6.1 nm and 22 cm/sec for both x and y directions.

It is important to note that even though the up-down vibrational amplitude is much smaller ( $< 1/10$ ) than the surface roughness of the  $\text{LiNbO}_3$ , the slider was transferred smoothly. The mechanism has not been clarified yet, it might be due to the locally enhanced friction force through a ball-point contact.

## 6. Summary

Ultrasonic motors are characterized by "low speed and high torque," which are contrasted with "high speed and low torque" of the conventional electromagnetic motors. Thus, the ultrasonic motors do not require gear mechanisms, leading to very quiet operation and space saving. Negligible effects from external magnetic or radioactive fields, and no generation of these fields are suitable for the application to electron beam lithography etc. relevant to the semiconductor technology. Moreover, high power / weight ratio, high efficiency, compact size and light weight are very promising for the future micro actuators adopted to catheter or tele-surgery.

For the further applications of the ultrasonic motors, systematic investigations on the following issues will be required:

- (1) development of low loss & high vibration velocity piezo-ceramics,
- (2) piezo-actuator component designs with high resistance to fracture and good heat dissipation,
- (3) ultrasonic motor designs;
  - a. motor types (standing-wave type, traveling-wave type, hybrid type, integrated type),
  - b. simple displacement magnification mechanisms of vibratory piece

- (4) (horn, hinge-lever),  
c. frictional contact part,  
inexpensive and efficient high frequency/high power supplies.

## 7. Acknowledgement

This work was partially supported by the Office of Naval Research through Contract No. N00014-96-1-1173.

## 8. References

1. Barth H. V., (1973) Ultrasonic Motors, *IBM Technical Disclosure Bull.* **16**, 2263.
2. Lavrinenko, V.V., Vishnevski S. S. and Kartashev I. K. (1976). Piezoelectric Motors, *Izvestiya Vysshikh Uchebnykh Zavedenii, Radioelektronika* **13**, 57.
3. Vasiliev, P. E. et al. (1979) UK Patent Application GB 2020857 A.
4. Sashida, T. (1982) Ultrasonic Motors *Oyo Butsuri* **51**, 713.
5. Sashida, T. (1983) Ultrasonic Motors, *Mech. Automation of Jpn.*, **15** (2), 31.
6. Coster, M.P.A (1994) Walking Piezo Motor *Proc. 4th Int'l Conf. on New Actuators*, Germany **2.6**, p.144,
7. Gloess, R. (1994) A High Resolution Piezo Walk Drive *Proc. 4th Int'l Conf. on New Actuators*, Germany **P26**, p.190,
8. Kasuga, M. T. Satoh, N. Tsukada, T. Yamazaki, F. Ogawa, M. Suzuki, I. Horikoshi and T. Itoh, (1991) Compact Ultrasonic Motor *J. Soc. Precision Eng.*, **57**, 63
9. Cummings J. and Stutts, D. (1994) Design for Manufacturability of Ceramic Components *Am. Ceram. Soc. Trans.*, **147**.
10. Uchino, K. Kato K. and Tohda, M. (1988) Ultrasonic Linear Motor Using a Multilayered Piezoelectric Actuator, *Ferroelectrics* **87**, 331.
11. Bein, T., Breitbach E. J. and Uchino, K. (1997) Linear Ultrasonic Motor Using the First Longitudinal and the Fourth Bending Mode, *Smart Mater. Struct.* **6**, 619.
12. Saigo, H. (1994) 15th Symp. Ultrasonic Electronics (USE 94), No. PB-46, p.253
13. Kumada, A. (1985) Kumada Motors *Jpn. J. Appl. Phys.*, **24**, Suppl. 24-2, 739.
14. Koc, B. Dogan, A. Xu, Y. Newnham R. E. and Uchino, K. (1998) An Ultrasonic Motor Using a Metal-Ceramic Composite Actuator Generating Torsional Displacement, *Jpn. J. Appl. Phys.* **37**, 5659.
15. Koc, B, Xu Y. and Uchino K., (1998) Composite Ultrasonic Motors *Proc. IEEE Int'l Ultrasonic Symp.*, Sendai, Japan [in press].
16. Flynn, A. M., Tavrow, L. S., Bart, S. F., Brooks, R.A., Ehrlich, D.J., Udayakumar, K.R. and Cross, L. E. (1992) *J. Microelectro-mechanical Systems*, **1**, 44
17. Takahashi, M., Kurosawa, M., and Higuchi, T. (1994). *Proc. 6th Symp. Electro-Magnetic Dynamics '94*, No. 940-26 II, D718, 349.

### For further reading:

18. Uchino, K. (1998) Piezoelectric ultrasonic motors: overview" *Smart Mater. Struct.* **7**, 273.
19. Uchino, K. (1996) *Piezoelectric Actuators and Ultrasonic Motors*, Kluwer Academic Publishers, MA.

# FLEXTENSIONAL COMPOSITE TRANSDUCERS: DESIGNING, FABRICATION AND APPLICATION

Aydin Dogan, Kenji Uchino\*, Robert E. Newnham \*

Anadolu University, Ceramic Engineering Department

26470 Eskisehir TURKEY; \* The Pennsylvania State University,

Materials Research Laboratory, University Park- PA 16802

## Abstract

The design, fabrication and application of flextensional composite transducers are summarized in this study. The moonie and cymbal type flextensional transducer consist of a ceramic driving element sandwiched between two truncated conical metal or plastic endcaps. These transducers can be used as both sensors and actuators. Piezoelectric, electrostrictive and antiferroelectric-ferroelectric switching types of ceramic can be used as the driving element in either single layer or multilayer form. In the cymbal and moonie transducer designs, the flexibility and durability of metals and the driving power of the ceramic element are combined.

Poled ferroelectric ceramics (Curie groups  $oom$ ) possess three independent piezoelectric coefficients:  $d_{31}$ ,  $d_{33}$ , and  $d_{15}$ . Each of the piezoelectric coefficients can be used as the driving element of a composite cymbal or moonie transducer. Cymbal transducers can also be fabricated from ring shaped ceramics sandwiched between truncated metal endcaps. Polarization and electric field directions of the samples can be altered systematically to make use of the three different piezoelectric coefficients as driving elements. The cymbal is a versatile performer. Desired actuation and sensing performance can be tailored by engineering the flexibility of the endcaps or changing the cavity dimensions beneath the endcaps. Possible design changes can be also investigated with FEM by using computational tools. Cymbal and moonie transducers can be used as headphones, acceleration sensors, positioners, and in many other applications.

## 1. Introduction

Accentric materials show piezoelectricity, which is defined as the ability of developing an electrical charge proportional to a mechanical stress. The piezoelectric response may be either direct or converse. For the direct piezoelectric response, the electrical displacement is proportional to the stress applied to the material. In the converse effect, material strain is proportional to the field applied across the material. This quality of piezoelectric materials has led to their use in transducers, which convert electrical energy to mechanical energy, and vice versa. These electromechanical transducers have

found applications where they are used in either active, e.g. ultrasonic probes, or passive modes, e.g. hydrophones.

A number of monolithic materials exhibit piezoelectric behavior. Ceramics, polymers and as well as their composites belong to this materials group. Conflicting goals in optimizing physical and electromechanical properties of transducers have led the researchers to look at the composite materials.

Superior properties have been obtained with piezocomposites consisting of an active piezoelectric ceramic in an inactive polymer. The microstructural arrangement of component phases in the composite, sometimes referred to as connectivity, is a critical parameter for the electromechanical performance of the composite. For a composite containing two phases, there are sixteen different connectivity patterns. Over the past two decades, researchers have investigated several methods to process piezocomposites and improve their properties. The 0-3, 3-1, and 2-2 connectivities have been worked on extensively. There are several excellent review papers on connectivity patterns and the processing techniques used to form piezocomposites [1], [2]. Various composite have different applications. Competition is still going on to determine the composite with the best electromechanical performance.

Second generation piezocomposites include the moonie and cymbal with 2-(0)-(2) connectivity. Ceramic-metal composites generally have a simple design with metal faceplates, shells or caps that couple the ceramic to the surrounding medium. The metal component transfers the incident stress to the ceramic or the displacement to the medium. Flextensional transducers are good examples of ceramic-metal composites. In flextensional transducers, the flexural vibration of the metal shell causes an extensional vibration of the piezoelectric ceramic. The moonie and cymbal transducers possessing 2-(0)-2 connectivity are miniaturized versions of flextensionals. This paper describes the moonie and cymbal type composite transducers.

## 2. Principle

The moonie and cymbal transducers consist of an electro-active ceramic driving element sandwiched between two metal endcaps with shallow cavities on their inner surface. Designs of the moonie and cymbal transducers are illustrated graphically in Figure 1 and Figure 2. In the case of the moonie, the cavities are in the shape of a half moon, whereas the cymbal has a truncated cone-shaped cavity. The presence of these cavities allows the metal caps to serve as mechanical transformers for converting and amplifying a portion of the incident axial-direction stress into tangential and radial stresses of opposite sign. Thus, the  $d_{33}$  and  $d_{31}$  contributions of the PZT now add together (rather than subtracting) in the effective  $d$  value of a device, such as a hydrophone or accelerometer. Regarding the converse effect, the radial motion of the ceramic driving element is transferred and amplified by the metal endcaps in axial direction. Hence, moonie and cymbal can be used as both sensors and actuators.

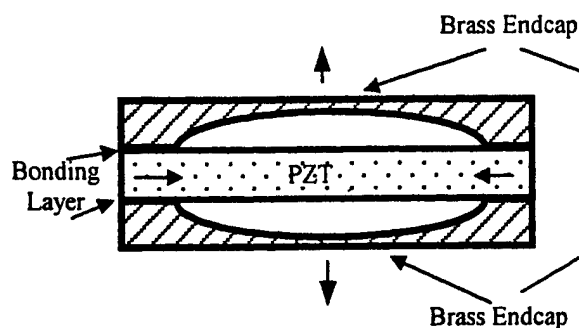


Figure 1. Schematic of Moonie Transducer.

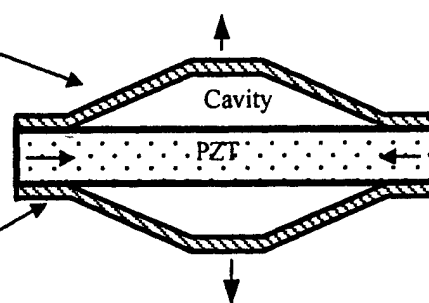


Figure 2. Schematic Cymbal Transducer.

## 2.1 FIRST APPROXIMATION FOR THE CHARGE CALCULATION ON THE CYMBAL AND MOONIE TRANSDUCER

Let us assume that we have a flextensional transducer which has cone shaped endcaps. The charge created under an applied stress on the cymbal transducer at uniaxial direction perpendicular to the metal endcaps can be estimated as follows.

The force is applied to the cone on the summit and transferred to the piezoelectric ceramic. The essential parameters for the calculation are marked on Figure 3.

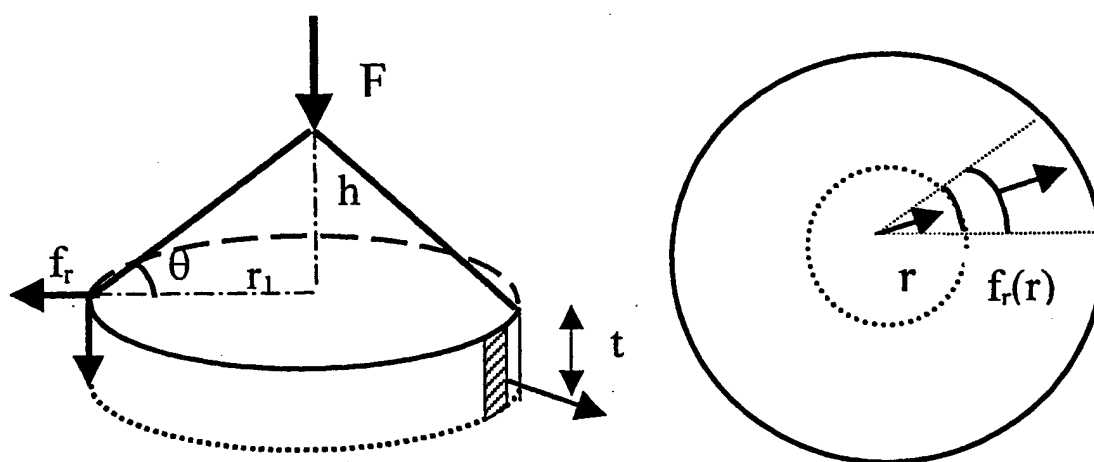


Figure 3. Front and top view of flextensional transducer cone shaped endcap  
Where:  $h$ , cavity depth;  $r_1$ , cavity radius;  $t$ , thickness of ceramic,  
 $\theta$  angle between cone and piezoelectric ceramic.

$$\frac{h}{r_1} = \tan \theta \quad (1)$$

The total force on the entire circumference is

$$2\pi r_1 f_r = \frac{F}{2 \tan \theta} \quad (2)$$

and the force per unit area at  $r = r_1$  is

$$\frac{f_r}{t} = \frac{F}{4\pi r_1 t \tan \theta} \quad (3)$$

where  $t$  is the thickness of the ceramic disk.

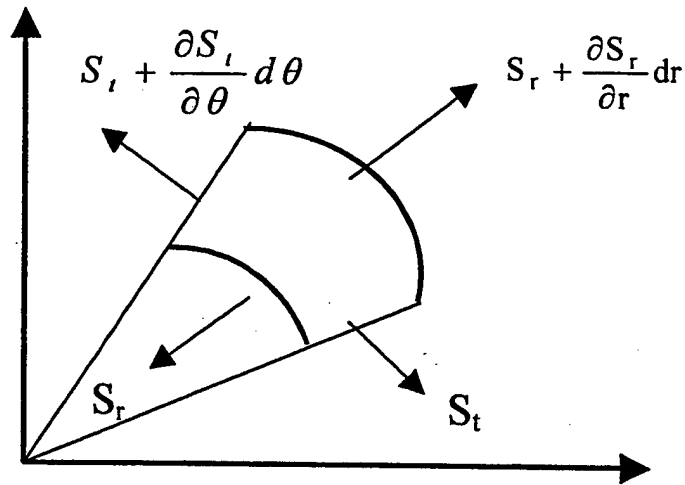


Figure 4. Stress distribution on a finite segment of ceramic element.

When a force balance is written and solved for plane stress case, the following equation is obtained.

$$S_r = S_t = \frac{F}{4\pi r_1 t \tan \theta} \quad (4)$$

The charge generation is calculated from,

$$(1) \quad \int_0^{r_1} \underbrace{d_{31} (S_r + S_t)}_{P(r)} \cdot 2\pi r dr = d_{31} \frac{r_1}{2t} \frac{F}{\tan \theta} \quad (5)$$

when two endcaps are used:

$$(2) \quad Q = d_{31} \frac{r_1}{t} \frac{F}{\tan \theta} \quad (6)$$

$$(3) \quad C = \epsilon \frac{\pi r_1^2}{t} \quad (7)$$

$$V = \frac{Q}{C} = d_{31} \frac{1}{\epsilon \pi r_1} \frac{F}{\tan \theta} \quad (8)$$

where  $Q$  is the charge;  $C$ , Capacitance;  $V$ , voltage, and  $\epsilon$  the dielectric permittivity.

For example: For a flextensional transducer with conical endcap, which has 9.0 mm cavity diameter and 0.2 mm cavity depth and consisting of 1.0-mm thick PZT-5A ceramic disc with 153 pC/N  $d_{31}$  coefficient, the calculated effective charge is around 17,500 pC/N

The effective piezoelectric coefficients of moonie and cymbal transducers, with a 12.7-mm outer diameter and 9.0-mm cavity diameter and 0.2-mm cavity depth consisting of PZT-5A ceramic, are shown in Figure 5. In moonie and cymbal structure  $d_{31}$  and  $d_{33}$  coefficients work together (in general in piezoceramics they work always against each other due to poisson effect). This is part of the reason of high effective charge coefficient. The moonie shows highly position dependent behavior for the effective piezoelectric coefficient. The cavity beneath the endcap of the moonie actuator plays a crucial role on the characteristics of the moonie [3]. The effective piezoelectric coefficient increases with increasing cavity diameter and cavity depth. The effective piezoelectric coefficient of the moonie transducer decreases rapidly with increasing the endcap thickness. The piezoelectric charge coefficient of moonie transducers also show position dependent behavior similar to that of the displacement.

equation

(4)

Placing a groove 9.0-mm in diameter, 0.2-mm in depth, and 1.0-mm in width in the

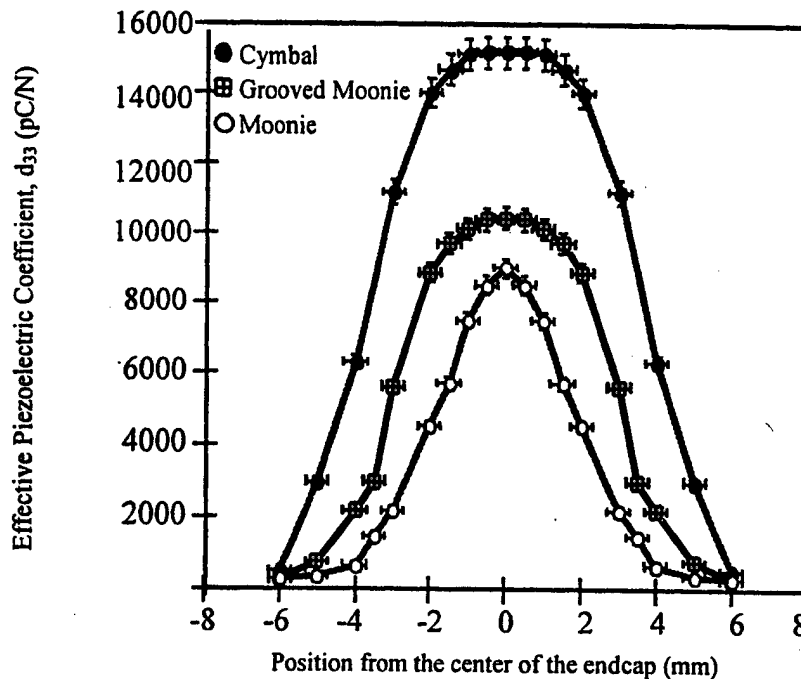


Figure 5. Effective piezoelectric charge coefficient of same size various design of flextensional transducers.

brass endcaps increased the effective piezoelectric coefficient almost 20%. The piezoelectric charge coefficient is simply the ratio of the applied stress and the induced charge. Thus, we can say that the groove on the endcaps increases the stress transformation ratio and therefore the generated charge. The moonies with grooved endcaps also showed less position-dependent behavior. For the 2-mm diameter section at the center of the samples, the effective piezoelectric coefficient is about 11,000 pC/N.

With the cymbal endcaps, the piezoelectric coefficients increased almost 60%. For a cymbal 12.7-mm in diameter and 1.7-mm in total thickness, an effective piezoelectric coefficient of more than 15,000 pC/N was measured over the 4-mm diameter center section of the cymbal transducer. We have concluded that the thick metal region near the edge of the moonie metal endcaps is a passive region, which does not assist stress transfer, and acts to decrease the total efficiency. Cymbal endcaps transfer the stress more efficiently and improve the energy transfer markedly. The calculated result for conical endcap and the measured result for cymbal with truncated conical endcaps are in very good agreement.

### 3. Fabrication Method

When fabricating the composite moonie and cymbal transducers, piezoelectric, electrostrictive, or antiferro- to- ferroelectric ceramics can be used as the driving element in either single layer or multilayer form. Shallow cavities beneath the endcaps of the moonie transducers are machined into the inner surface of each of the end caps. Brass, phosphor bronze, other flexible metals and their alloys, and even acrylic can be



used as endcap materials.

For cymbals the truncated conical endcaps are punched using a specially designed punch to fabricate the transducers rapidly at minimal cost. Shaping and cutting operations are carried out simultaneously during processing. The final product requires only surface treatment for good bonding. Moreover, endcaps can be easily fabricated from metal sheets by punching. With this fabrication routes it is possible to fabricate identical endcaps with minimal labor.

The metal moonie and cymbal endcaps are bonded to the electro-active ceramic disks around the circumference using soldering alloy or epoxies such as Eccobond epoxy resin from Emerson & Cuming, taking special care not to fill the cavity. The thickness of the epoxy bonding layer must be very thin, approximately 20  $\mu\text{m}$ . Using silver epoxy as a gluing agent, composite actuators may also be stacked together at the center of the endcaps to achieve still higher displacements. Moonie and cymbal transducers can be easily fabricated 3-50 mm in diameter and 1-3 mm in total thickness. Currently most of the studies are done on the 12.7-mm diameter 1.5-mm thick samples.

#### **4. Design Optimization With the Support of Finite Element Analysis**

Finite element programs ATILA, MARK, and ANSYS were used for the design and development stages of the moonie and cymbal transducers. The cymbal actuator is a second-generation moonie-type composite developed using FEA analysis in collaboration with experiment. Finite Element Analysis has identified high stress concentration in the metal endcaps just above the edge of the ceramic metal bonding layer near the edge of cavity [4].

The stress concentration on the brass endcap just above the bonding layer reduces the effective force transfer from the PZT to the cap. It is possible to eliminate part of the stress concentration by removing a portion of the endcap just above the bonding region where the maximum stress concentration is observed. An enhancement in properties has been observed by introducing a ring shaped groove on the exterior surface of the endcaps [5]. By moving the groove toward the edge of the actuator, the displacement increases. The highest displacement was achieved when the groove was above the edge of bonding layer. It is found that the deeper and wider the groove, the higher the displacement [6].

In reality, placing a ring shaped groove on the endcap does not eliminate the stress but further concentrates it into a very narrow region. Stress concentrations at the groove edges are a potential source of fatigue and may eventually produce failure under long-term usage. Moreover, additional labor is required to machine the groove into the endcaps.

The cymbal transducer with truncated endcaps has been designed to remove much of the stress concentration and to produce higher and more reproducible displacements.

Although this new design looks similar to the earlier moonie design, it has a different displacement mechanism. Displacement is primarily a flexural motion of the endcap for the original moonie design, but for the new design, the displacement is created by the combination of flexural and rotational motions. Figure 6 shows the displacement values of the different endcap designs with a fixed cavity depth (0.20-mm) and diameter (9.0 mm). A linear Voltage Differential Transformer (LVDT) was used for displacement analysis of the transducers. A variable electric field up to 1kV/mm with triangular waveform at 0.1 Hz is applied to the sample. A moonie actuator with 0.30-mm thick brass endcaps provides a 22- $\mu\text{m}$  displacement. Using the ring-shaped groove design, the displacement was increased to 32  $\mu\text{m}$  with a groove 9.0 mm in diameter, 0.2 mm in depth, and 1.0 mm in width machined into the brass endcaps of the same actuator. A cymbal actuator with uniformly thick punched endcaps exhibits around 40- $\mu\text{m}$  displacements, about twice the moonie displacement, and about 50 times larger than uncapped PZT.

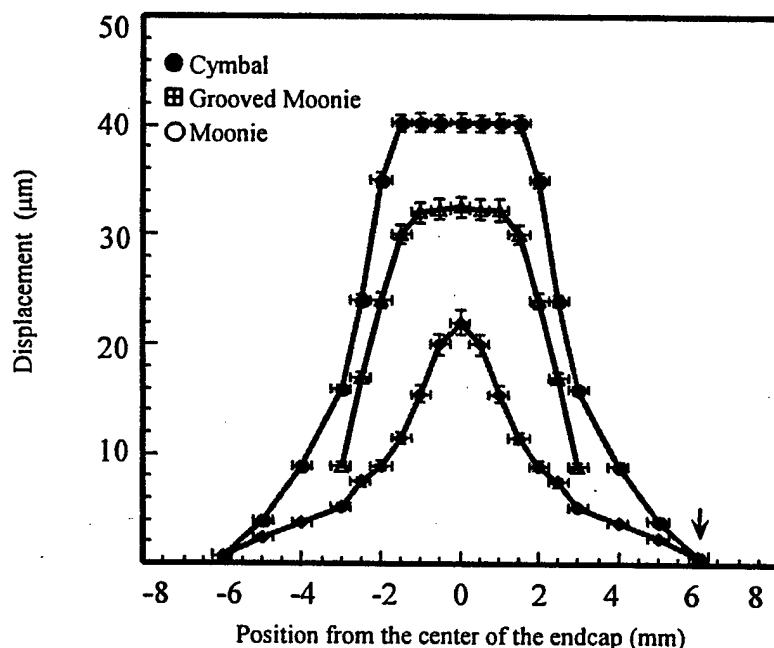


Figure 6. Displacement characteristics of moonie and cymbal flextensional transducers.

#### 4.1 EFFECT OF SIZE AND SHAPE

The dimensions of the cavity beneath the endcaps play a crucial role in the cymbal performance. Engineering the flexibility of the endcaps or changing cavity dimensions can tailor the desired actuation. The displacement, which is the result of converse piezoelectric effect, has a quadratic relationship with the cavity diameter. Figure 7 shows the calculated and experimental results of displacement cavity relation of cymbal transducer with constant endcap thickness (0.25mm) and PZT thickness (1.0 mm). Figure 8 shows the optimal cavity depth, which is around 0.25 mm for a cymbal transducer with constant cavity diameter (9.0 mm) and PZT thickness (1.0 mm).

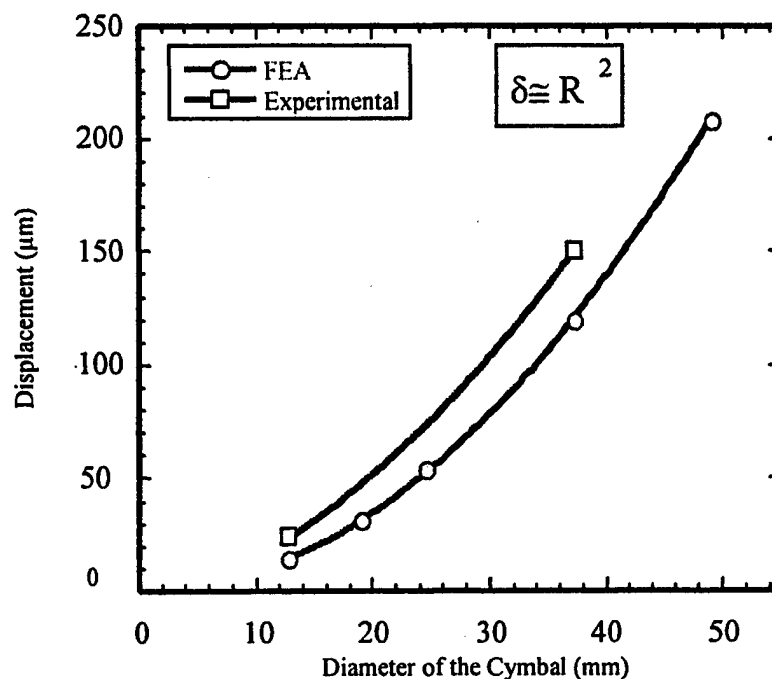


Figure 7. Displacement cavity relation of cymbal transducer with constant endcap thickness (0.25mm) and PZT thickness (1.0 mm).

#### 4.2 EFFECT OF ENDCAP MATERIAL

The flexibility and modulus of elasticity of the endcap material are important parameters defining the important actuator properties: displacement, response speed and generative force, of moonie and cymbal actuators and transducers. Figure 9 shows the effects of the Young's modulus of the metal endcaps and the hardness of the PZT ceramics on the displacement of composite cymbal actuators. Increasing the Young's modulus of the metal endcaps reduces the displacement of the cymbal actuator. This reduction is almost linear and the displacement of the highest Young's modulus metal endcaps is approximately 55% lower than that achieved using the most compliant metal endcaps. Similar behavior is observed for all PZT ceramic types. The linear decrease of the displacement with the increase if the Young's modulus of the metal confirms the spring-like nature of the endcaps.

Figure 10 shows the net displacement of the cymbal actuators made with different metal endcaps. The net displacement is the displacement produced by the actuator when it is electrically driven. If the actuator is loaded, a free deflection is produced and at each load, the application of an electric field produced a net displacement. The free deflection of the composite is related to the spring characteristics of the composite. Metals with low modulus of elasticity show higher displacement and higher free deflection. On the contrary, the maximum load, defined as the load for which 90% of the initial net displacement is maintained, increased with the modulus of the elasticity of the metal endcaps.

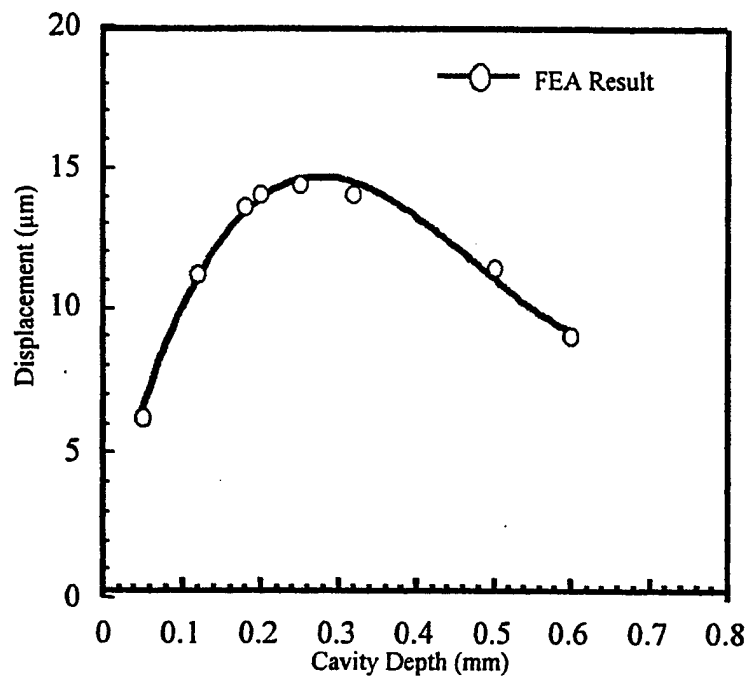


Figure 8. The optimal cavity depth for a cymbal transducer with constant cavity diameter (9.0 mm) and PZT thickness (1.0 mm).

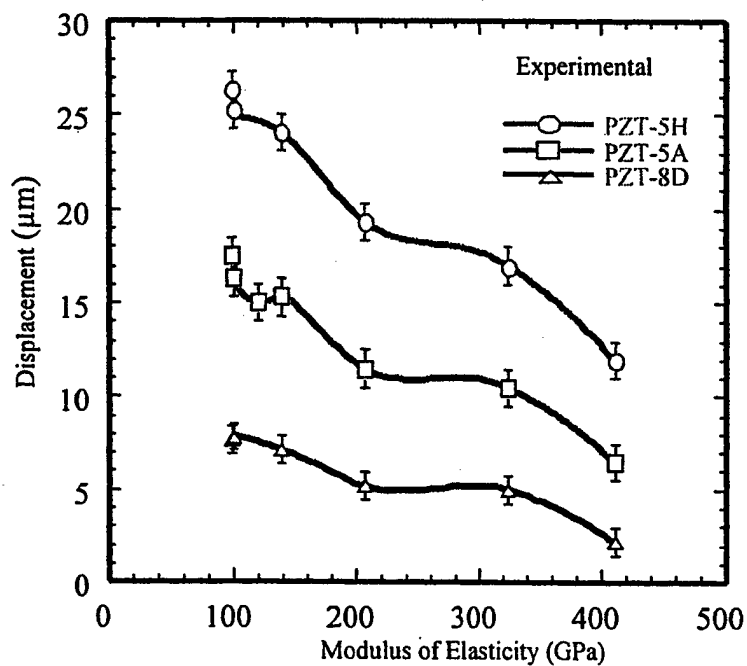


Figure 9. Effect of endcap modulus of elasticity on the displacement performance.

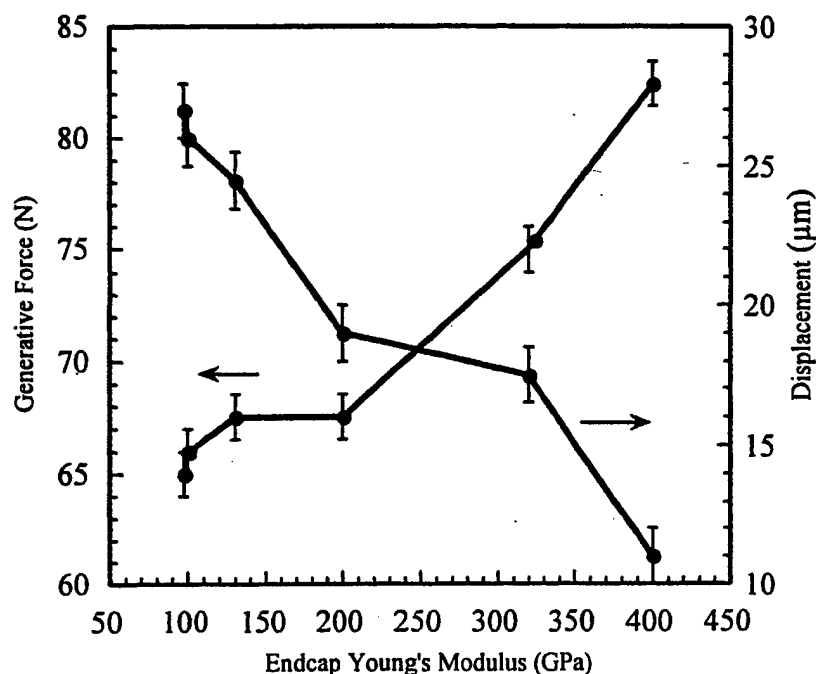


Figure 10. Trade-off between generative force and displacement for the cymbal.

1d PZT

#### 4.3 EFFECT OF ELECTRO-ACTIVE CERAMIC DRIVING ELEMENT

PZT ceramics, PMNPT relaxor ferroelectrics and PNZST type antiferro-ferroelectric ceramic elements can be used in single layer or in multilayer form. Typical displacement hysteresis graphs of 12.7-mm diameter 1-mm thick samples made of all three kinds of electro-active ceramics materials are shown in the Figure 11. Displacement hysteresis for the cymbal transducers, 12.7 mm diameter 1.0 mm PZT thickness, and 9.0 mm cavity diameter 0.2 mm cavity depth, fabricated with all three kind of electro-active ceramic element are shown in Figure 12. Cymbal actuators with soft PZT ceramics exhibit linear displacement with a rather large hysteresis, which is the indication of losses. The cymbal actuator with the PMN-PT type of ceramic driving element shows larger displacement with lower losses. However, it exhibits a nonlinear displacement consistent with the relaxor characteristics of the PMN-PT ceramics. Linear displacement characteristics can be achieved by using charge driving electrical circuitry. PNZST is an antiferroelectric-ferroelectric type phase transition material. Unique property of this material is the volumetric expansion under applied electric field. With cymbal endcap design, this volumetric expansion is converted to a negative axial displacement.

#### 4.4 VARIOUS DRIVING MODES TO ACTIVATE THE CYMBAL TRANSDUCER

Poled ferroelectric ceramics (Curie groups  $\infty$ m) possess three independent piezoelectric coefficients:  $d_{31}$ ,  $d_{33}$ , and  $d_{15}$ . By careful designing, each of the piezoelectric coefficients can be activated as the driving mode of a composite cymbal or moonie transducer.

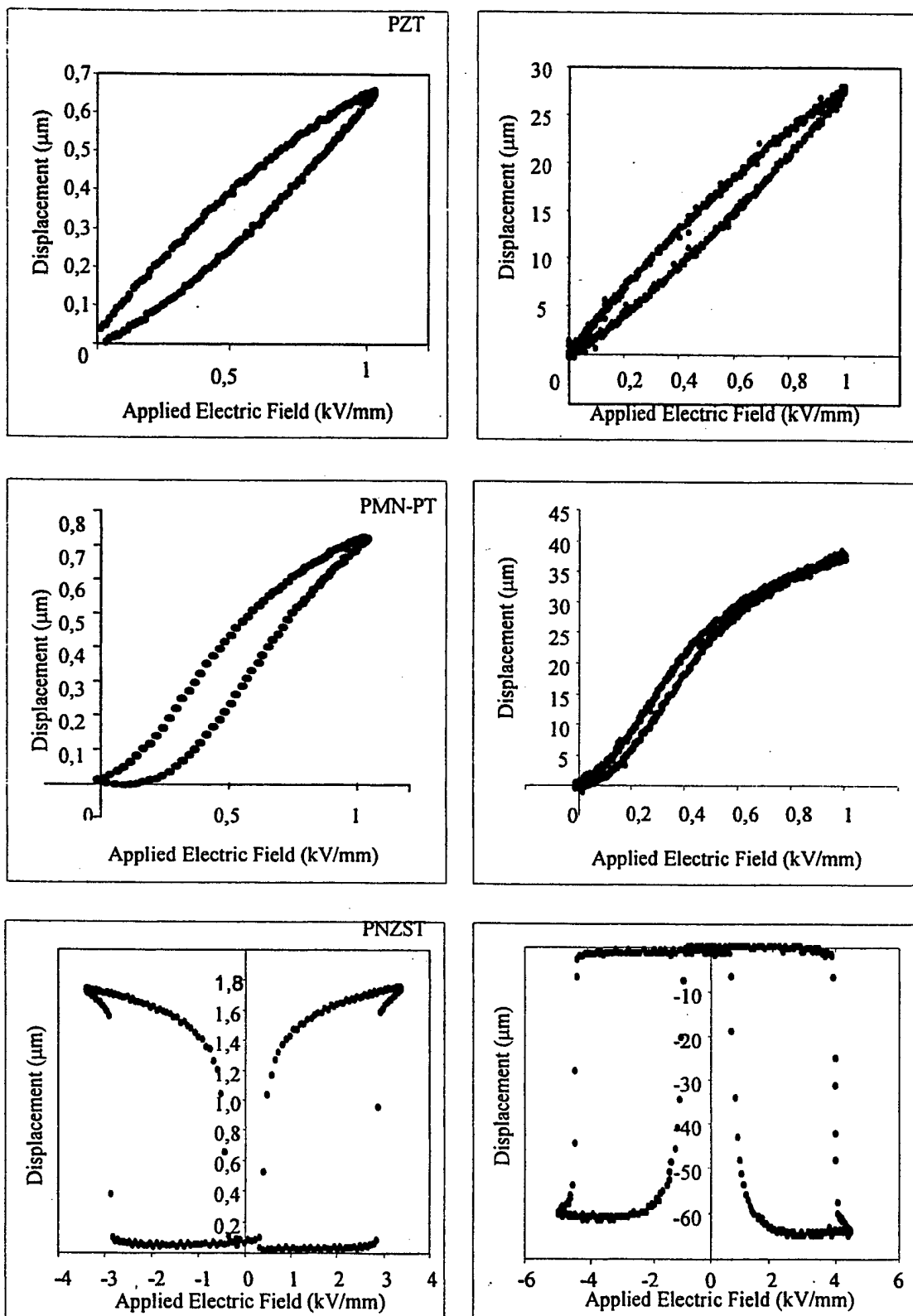


Figure 11. Hysteresis of various electro-active ceramics.

Figure 12. Hysteresis of cymbals with various electro-active ceramics.

Cymbal transducers can be fabricated from ring shaped ceramics sandwiched between truncated metal endcaps. Polarization and electric field directions of the samples can be altered systematically to make use of the three different piezoelectric coefficients as driving power. Figure 13 shows four combinations between electric field and internal polarization of the ceramic driving element. In case one, the radial mode  $d_{31}$  of the piezoelectric ceramic element is used to activate the endcaps. In case two, the longitudinal coefficient  $d_{33}$  is used to activate the metal endcaps. The shear mode  $d_{15}$  of the piezoceramic possesses the highest value piezoelectric coefficient value. Cases 3 and 4 are designed to activate the ceramic in a shear mode. Figure 14 shows the displacement versus inner ring diameter of the piezoelectric driving element relation of the cymbal transducer. From the graph, it may be seen that the  $d_{31}$  mode, which exhibits the highest displacement, is still the best mode to drive the cymbal transducer. Although  $d_{15}$  is the highest piezoelectric coefficient, it is not effective for driving cymbal transducer in the present design. It has to be kept in mind that the shear mode is a rather soft mode. A rigid solid disc has to be placed between the rings. In general increasing the size of the inner diameter decreases the displacement value, because of decreasing volume of the ceramic body and volumetric efficiency of transducer. From the manufacturing point of view, case 1 is the best, because it is easy to fabricate and easy to apply electric field without developing a short circuit. The other three cases are more difficult to fabricate and requires rather careful electric wiring.

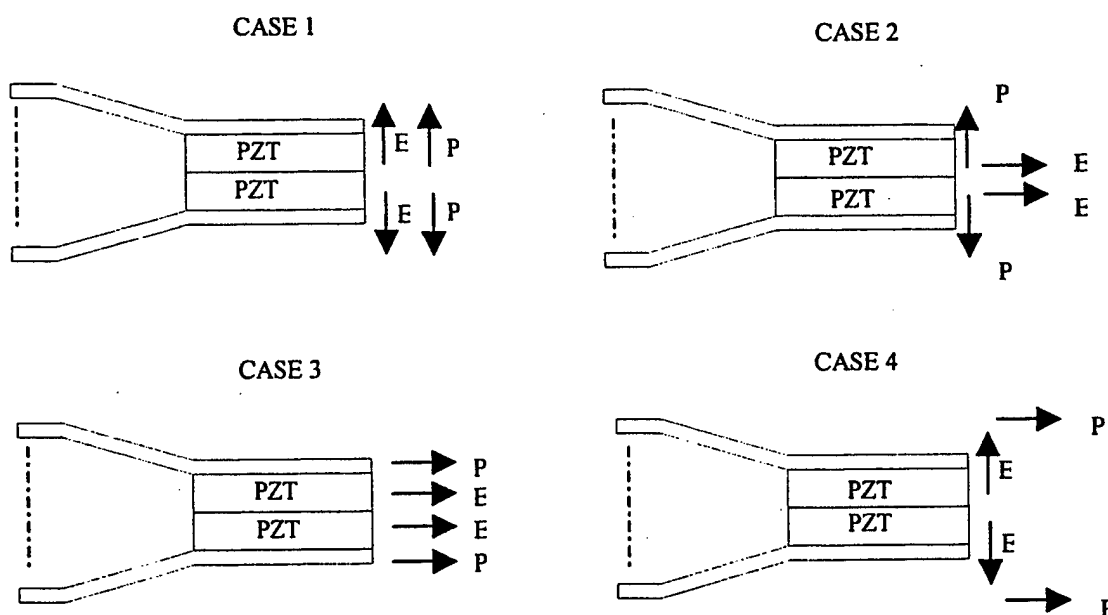


Figure 13 Various driving modes of the cymbal transducer with a ceramic ring.

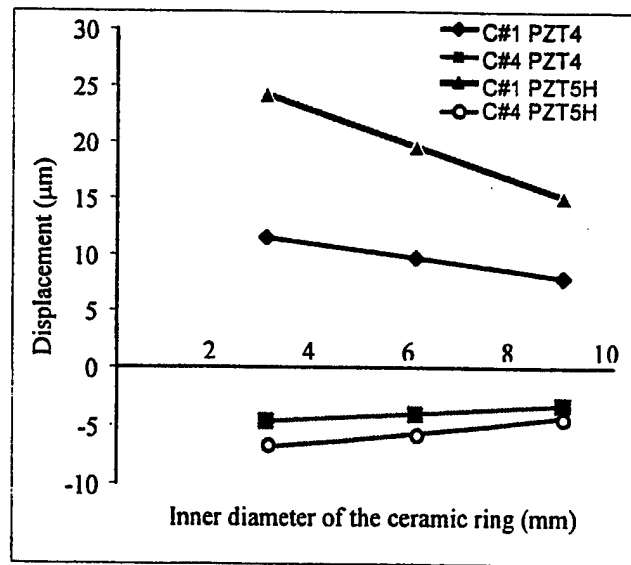


Figure 14. FEA results for displacement ceramic inner diameter relation.

## 5. Application of the moonie and cymbal transducers

Moonie and cymbal transducers have great potential for both sensor and actuator applications [7], [8]. They can also be utilized as the switching element in valve designs. There is a volume change inside the moonie and cymbal transducers during cycling. This volume change can be utilized in minipump applications.

### 5.1 ACTUATORS

Flexensional moonie and cymbal actuators with their moderate generative force and displacement values fill the gap between multilayer and bimorph actuators. Each solid-state actuator design has attractive features that can be exploited for certain applications. The advantages of the moonie and cymbal actuators are the easy tailoring of the desired actuator properties by altering the cavity size and endcap dimensions. Easy fabrication is another advantage. Several features of the various solid-state actuator designs are listed in Table I. It is rather difficult to compare the different actuators because of differences in geometry and various operating conditions for specific applications. To make a fair comparison, similar dimensions for each actuator were selected, and the measurement conditions are those specified in Table I. The rainbow actuator also partially covers the gap between multilayer and bimorph actuators [9]. For that type of actuator, a reduction step during processing of the ceramic element at high temperature results in a semiconducting layer and stress-bias. Although it shows flexural motion, the rainbow can be categorized as a monomorph or a unimorph type of actuator. The effective coupling factor of rainbow is theoretically smaller than the moonie and cymbal. High applied electric field, position-dependent displacement and cost are the main disadvantages of the rainbow actuator in comparison with the cymbal. In the moonie and cymbal design, multilayer piezoelectric ceramics can be used as the driving element



to reduce the applied voltage. The moonie and cymbal actuator can be used as a micropositioner for applications requiring small size with relatively quick response. OMRON Corporation has already succeeded in using the multilayer moonie actuator for an optical scanner [10]. Other applications for the cymbal and moonie include sensing and vibration suppression elements in the automotive and aerospace industry, switching element in valve design, micropositioners requiring small size with relatively quick response for precise positioning device in CD-ROM and magneto-optic memory storage driver, mini-pumps, relays, and switches, printer hammers, and linear and rotary ultrasonic motors

Table I. Comparison of the Solid State Ceramic Actuator Designs.

Features	Multilayer	Bimorph	Rainbow	Cymbal	Moonie
Dimensions	5x5x12. (LxWxT) mm <sup>3</sup>	12.7x10x0. 6 (LxWxT) mm <sup>3</sup>	F 12.7 mm T= 0.5 mm	F 12.7 mm T= 1.7 mm	F 12.7 mm T= 1.7 mm
Drive Voltage (V)	100	100	450	100	100
Displacement ( $\mu$ m)	10	35	20	40	20
Contact surface (mm <sup>2</sup> )	25	1	1	3	1
Generative Force (N)	900	0.5-1	1-3	15-60	3
Position dependent of displacement	None	Maximum at the tip	Maximum at the center	Maximum at the center but more diffuse	Maximum at the center
Stability under loading	Very high	very low	low	high	low
Fastest Response Time ( $\mu$ sec)	1- 5	100	100	5-50	5-50
Fabrication method	Tape casting and cofiring at 1200 °C	Bonding ceramic element with metal shim	Reducing ceramic element at 950 °C	Bonding ceramic element with metal endcaps	Bonding ceramic element with metal endcaps
Fabrication Cost	high	low	medium	low	medium

## 5.2 HYDROPHONE APPLICATION

Because of their very high piezoelectric charge coefficients, moonie and cymbal transducers can be used as hydrophones, accelerometers and air acoustic transducers. The advantages of the cymbal-type hydrophone are very large  $d_h$  (hydrostatic charge) and  $g_h$  (hydrostatic voltage) coefficients along with lightweight and inexpensive fabrication. Cymbal also has excellent potential for use as a shallow water projector.

Cymbal has a  $Q$  less than 10 when water loaded. The moderate TVR exhibited by a single element device can be greatly enhanced by incorporating them into a close packed array [11], [12]. Hydrophone figures of merit ( $d_h g_h$ ) of some of the widely used composites and single element transducers are compared in the plot in Figure 15. Due to the size dependence of some transducers, the figure of merit is calculated for a  $1\text{-cm}^2$  transducer for a valid comparison. Cymbal exhibits the highest figure of merit among all composites. Figure 16 shows the pressure dependence of the effective  $d_h$  and  $g_h$  coefficient of identical transducers with different cap materials and 0.25 mm cavity depth. These data clearly show that caps made of stiffer metals are capable of withstanding higher pressures without degradation in performance. Stiffer caps are not as efficient in transferring stress to the piezoceramic, which is why the effective  $d_h$  coefficient drops for cymbals with stiffer.

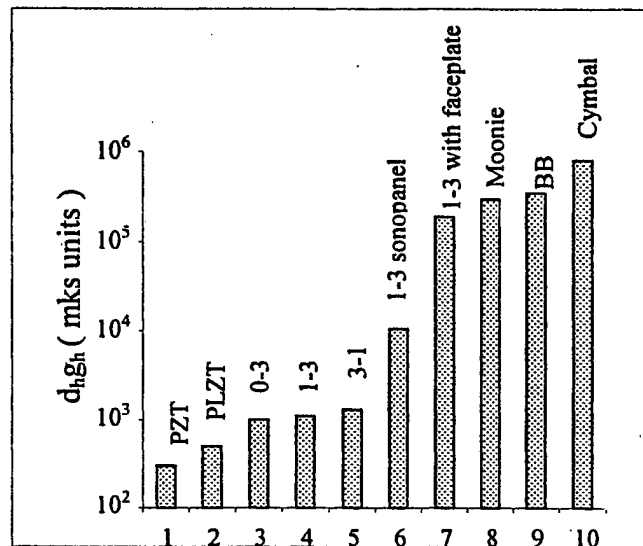


Figure 15. Hydrophone figures of merit ( $d_h g_h$ ) of some of the widely used composites and single element transducers.

## 5.3. ULTRASONIC MOTOR APPLICATION

An ultrasonic motor was derived from moonie and cymbal design [13]. The motor is named the windmill because of the appearance of the slitted endcaps. Detailed information concerning this motor can be obtained from the article of K. Uchino and B. Koc "Compact piezoelectric ultrasonic motors" in this proceeding.

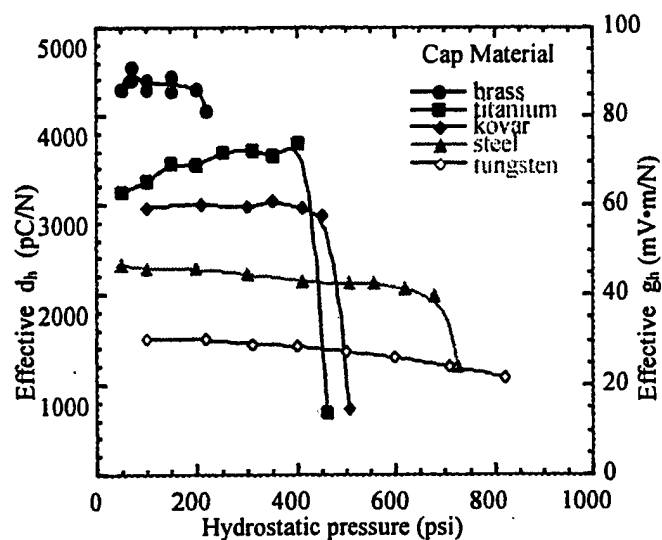


Figure 16. The pressure dependence of the effective  $d_h$  and  $g_h$  coefficients for same size cymbal transducers with different cap materials.

#### 5.4 ACCELEROMETER APPLICATION

Cymbal transducer has been investigated for accelerometer applications [14]. A high effective piezoelectric charge coefficient ( $d_{33}$ ) of the cymbal transducer was observed around 15000 pC/N, which is much higher than that of piezoelectric ceramic, around 550 pC/N. With this feature, the cymbal transducer is a good candidate for highly sensitive accelerometer applications. Figure 17 shows the Log sensitivity frequency relation of cymbal accelerometers with various endcaps in comparison with PZT itself. Cymbal accelerometers have more than two orders of magnitude higher sensitivity than PZT ceramics at low frequencies.

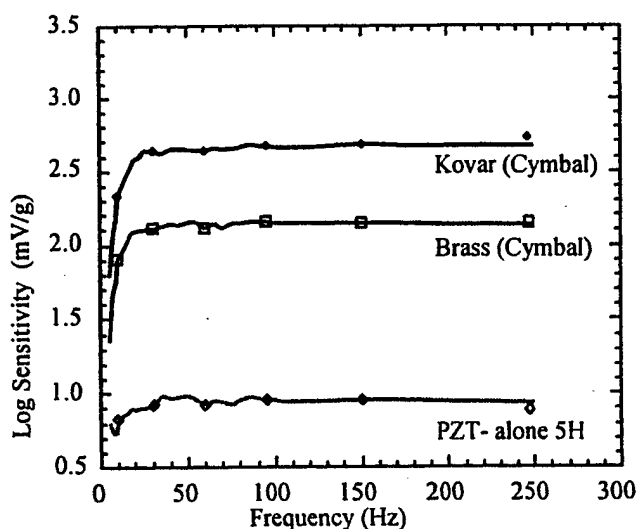


Figure 17. Acceleration sensitivity of cymbal in comparison with PZT itself.

## REFERENCES

1. Newnham R.E., Skinner D.P. Cross L.E., "Connectivity and Piezoelectric-Pyroelectric Composites," *Mater Res Bull* 1978, 13, 525
2. Gururaja, T.R., A. Safari, R.E. Newnham and L.E. Cross, "Piezoelectric Ceramic-Polymer Composites for Transducer Applications," *Electronic Ceramics*, Edited by L.M. Levinson. Marcell Dekker. Inc., New York, 92 (1987)
3. A. Dogan, S. Yoshikawa, K. Uchino, R.E. Newnham, "The Effect of Geometry on the Characteristics of the Moonie Transducer and Reliability Issue", *IEEE Ultrasonic Symposium Proceedings*, Vol. II. pp. 935-939, 1994
4. Q. C. Xu, S. Yoshikawa, J. R. Belsick and R. E. Newnham, "Piezoelectric composites with high sensitivity and capacitance for use at high pressure," *IEEE Trans. on UFFC* Vol. 38, pp. 634-639, 1991.
5. Y. Sugawara, "Development of metal-ceramic composite piezoelectric actuators and their applications," M.S. Thesis, Sophia University, Tokyo Japan, 1991.
6. K. Onitsuka, A. Dogan, Q.C. Xu, S. Yoshikawa, R.E. Newnham, "Design Optimization for Metal-Ceramic Composite Ceramic Composite Actuator," *Ferroelectrics* Vol. 156, pp. 37-42, 1994.
7. J. F. Tressler, "Smart ceramic-metal composites for active vibration control," *M.S. Thesis*, Ceramic Science, The Pennsylvania State University, 1993.
8. K. Onitsuka, A. Dogan, J.F. Tressler, Q.C. Xu, S. Yoshikawa, R.E. Newnham, "Metal-Ceramic Composite Transducer, The Moonie", *J. Int. Mat. Sys. & Struct.*, Vol. 6, pp. 447-455, 1995.
9. H. Goto, K. Imanaka, "Super compact dual axis optical scanning unit applying a torsional spring resonator driven by a piezoelectric actuator," *Proc. of SPIE*, Vol. 1544, pp. 272-281, 1991
10. G. Haertling, "Rainbow ceramics, a new type of ultra high displacement actuator," *Bull. of Am. Ceramic Soc.*, Vol. 73, No 1, pp. 93-96, January 1994
11. J.F. Tressler, A. Dogan, J.F. Fernandez, J.T. Fielding, K. Uchino, R. E. Newnham "Capped Ceramic Hydrophone" *IEEE-UFFC Ultrasonic Symposium Proceeding*, Seattle 1995.
12. J.F. Tressler, R. E. Newnham, W.J. Hughes "Capped Ceramic underwater sound projector: The 'cymbal' transducer" *J. Acoust. Soc. Am.* 105 (2), pp 591-600 February 1999
13. B. Koc, A. Dogan, Y. Xu, R.E. Newnham, and K. Uchino "An Ultrasonic Motor Using a Metal-Ceramic Composite Actuator Generating Torsional Displacement," *Jpn. J. Appl. Phys.* Vol. 37 (1998), pp 5659-5662
14. B. Koc, A. Dogan J.F. Fernandez, R.E. Newnham, and K. Uchino "Accelerometer application of the moonie and cymbal transducers" *Jpn. J. Appl. Phys.* Vol. 35 (1996) pp 4547-4549.

# **APPENDIX 73**

# A MINIATURE PIEZOELECTRIC ROTARY MOTOR USING TWO ORTHOGONAL BENDING MODES OF A HOLLOW CYLINDER

**B. Koc, J. F. Tressler\* and K. Uchino**

Materials Research Laboratory  
The Pennsylvania State University  
University Park, PA 16802, USA

\*Naval Research Laboratory  
Physical Acoustics Branch  
Washington, DC 20375, USA

## Abstract:

This paper presents a new miniature piezoelectric ultrasonic rotary motor that utilizes two orthogonal bending modes of a hollow cylinder. The design consists of a hollow metal cylinder whose outside surface is flattened on two sides (at 90-degrees to each other). Rectangular piezoelectric plates are bonded to these two flattened surfaces. Wobble motion is generated on the cylinder when only one piezoelectric plate is excited at a frequency between the two orthogonal bending modes. The behavior of the stator vibrator was simulated using ATILA finite element software. Since this motor uses simple piezoelectric plates as the active drive elements, it is highly scalable and can be driven by a single AC source. The prototype motor has a size 2.8 mm in diameter and 12.0 mm in length, operated at 62 kHz.

## Introduction

In a piezoelectric ultrasonic motor, an active piezoelectric element is excited in such a way that a high frequency small amplitude elliptic motion is generated on the stator's surface. The rotor is pressed against the stator's surface and a rotation is produced by frictional interaction between the touching surfaces of the stator and rotor. Williams and Brown proposed the first investigation of ultrasonic motors using the principle described above in 1942. Four piezoelectric rectangular plates were bonded to all faces of a quadratic elastic beam forming a composite structure. A wobble motion was generated at one end of the bar upon exciting piezoelectric elements with two-phase potential at a bending mode resonance frequency of the bar [1].

Depending on the geometry of the stator and the nature of the piezoelectric excitation, two orthogonal vibration modes can be superimposed on the surface point undergoing elliptical motion. There are many ways to generate an elliptical trajectory on the surface of the vibratory pieces. Many researchers have classified piezoelectric ultrasonic motors into two groups according to the vibration modes used to generate the elliptical motion: travelling wave and standing waves types [2,3,4,5]. However, there are structures that are neither travelling wave nor standing waves types. A typical example is multi- (or mixed-) mode excitation type piezoelectric ultrasonic motors. Exciting at least two orthogonal resonance modes of the stator vibrator generates elliptical motion on the stator surface. According to the shape of the stator transducer, these orthogonal resonance modes may generate longitudinal-torsional [6,7] radial-torsional [8], longitudinal-flexural [9], or flexural-flexural motions. The stators

of these types of motors may have some additional elastic part, which is called vibration coupler or concentrator. Single mode vibration on the piezoelectric element is converted into multi mode vibration at the tip of the concentrator.

Either exciting two different electrode groups one at a time or tuning the driving frequency of the stator vibrator to a different orthogonal frequency pair controls the rotation or direction of the linear motion. If multi-vibrators are used, either the vibration or orientations of the vibrators need to be orthogonal. In this type of motor, superimposing two orthogonal single mode vibrations with a phase shift generates elliptical motion.

The motor presented in this paper is a multi-mode-single-vibrator excitation type, which uses two orthogonal bending modes of a hollow cylinder. Since the structure and poling configuration of the active piezoelectric elements used in the stator are simple, this motor structure is very suitable for miniaturization. The multi-mode excitation mechanism of the stator can generate wobbling motion with a single driving source. This motor may find applications in the medical industry (endoscopes and prosthetic devices), micromechatronic (miniature telerobotic), information devices (silent alarm) and horology.

## Operating Principle of the Motor

The orthogonal bending mode frequencies in the x and y-axes for a quadratic beam are the same. The bending mode frequencies in any direction for circular cylinders are also equal. The motor's stator presented in this study combines the circular and

quadratic cross-sections. The outside surface of a hollow metal cylinder was flattened on two sides (at 90-degrees to each other) and two rectangular piezoelectric plates were bonded to these two flattened surfaces (Fig. 1). This causes the cylinder to have two degenerate orthogonal bending modes, where the bending mode resonance frequencies are close to each other. The split of the bending mode frequencies is due to the partially square/partially circular outside surface of the hollow cylinder. Driving one piezoelectric plate (while short circuiting the other to ground) at a frequency between the two orthogonal bending modes excites both modes, which makes the cylinder generate a wobbling motion. When the other piezoelectric plate is driven at this same frequency, the direction of wobble motion is reversed.

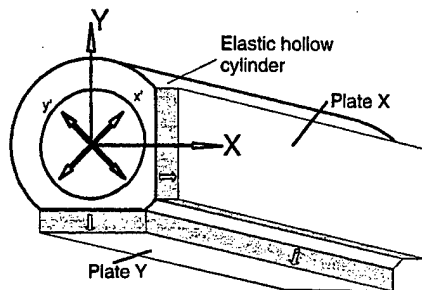


Fig. 1: Structure of the motor's stator. Poling direction in the plates is indicated by the arrows.

### Finite Element Analysis

The behavior of the free stator vibrator was simulated using ATILA finite element software. Tailoring dimensions of the metal and piezoelectric ceramics equated the two orthogonal bending mode frequencies of the stator vibrator. The piezoelectric plates on the surface of the cylinder were placed in such a way that one piezoelectric plate can excite the two orthogonal bending modes of the stator vibrator. Figs. 2a and 2b show the orthogonal bending mode shapes when only the plate on the x-axis (Plate X) was excited the electrode of the plate Y was open circuited. Wobble motion is generated on the cylinder when only one piezoelectric plate is excited at a frequency between the two orthogonal bending modes. When the other piezoelectric plate is excited at the same frequency, the direction of wobble motion can be reversed. These mode shapes are shown in Figs. 2c and 2d.

### Experiment

#### A. Stator Fabrication

The prototype motor's stator was constructed using a hollow metal tube (brass) with dimensions of 1.2 mm outer radius, 0.8 mm inner radius and 12 mm in length and two rectangular piezoelectric plates with dimensions 10 mm in length, 1.5 mm in width and 0.5 mm in thickness. The outside surface of the

metal cylinder was polished on two sides at 90-degrees to each other to obtain two orthogonal flat surfaces. The distance from the flat surface to the center of the tube was 1.0 mm. The PZT plates (APC841, APC International Ltd.), which were electroded uniformly and poled in the thickness direction, were bonded to the flat orthogonal surfaces on the cylinder using epoxy and cured around 60°C.

The rotor of this motor is a cylindrical rod with a pair of stainless steel ferrule pressed with a spring. The basic configuration of the motor is shown in Fig. 3.

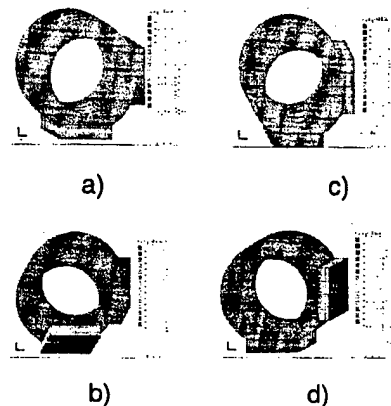


Fig. 2: a, b) Top view of orthogonal bending mode shapes when only the plate on x-axis (Plate X) was excited. c, d) Bending mode shapes when only the plate on the y-axis was excited.

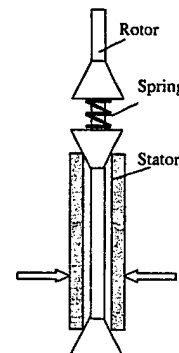


Fig. 3: Assembly of the motor.

#### B. Free Stator Characterization

As a first step to clarify the stator behavior, the admittance spectra of the free stator was measured under three conditions (Fig. 4). When the plate X was excited with short-circuiting the electrodes of the plate Y to ground, the stator had two degenerate bending modes resonance frequencies around 61.2 and 65.0 kHz. When the plate Y was excited, the stator showed the same behavior. However, when both plates were excited, only one bending mode

frequency in the direction of the  $y'$ -axis (Fig.1) was obtained.

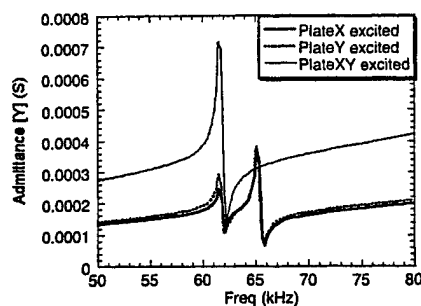


Fig. 4: Admittance spectrum of the free stator.

The peak-to-peak displacement in the  $x$  and  $y$ -axes directions was also measured by exciting the plate  $X$  and plate  $Y$  using a Laser Fiberoptic Interferometer (Politec OFV-3001/OFV-311). The displacement spectrum in the  $x$  and  $y$  directions when only the plate  $X$  was excited is shown in Fig. 5a. When only plate  $Y$  was excited, similar behavior was obtained (Fig. 5b).

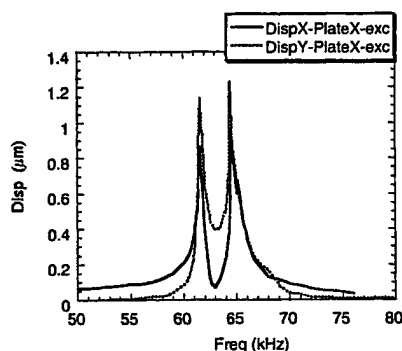


Fig. 5a: Measured displacement in  $x$  and  $y$ -axes by exciting only plate  $X$ .

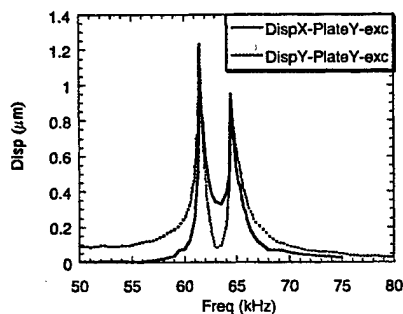


Fig. 5b: Measured displacement in  $x$  and  $y$ -axes by exciting only plate  $Y$ .

At frequencies of 60.5, 61.5, 62.0, 63.5 and 64.5 kHz, we measured the magnitude of the wobble motions in the  $xy$ -plane when only plate  $X$  was

excited (Fig. 6a). In order to do this measurement with a single Laser Fiberoptic Interferometer, we compared the phase of the displacements in  $x$  and  $y$  directions with the input applied AC voltage of 80.0 V (p-to-p). Then, we plotted the displacement  $y$  as a function of the displacement  $x$ . The same type of measurements were performed by exciting only plate  $Y$  and the results are shown in Fig. 6b. The interesting points here are: i) the direction of wobble motions when only plate  $X$  was excited was clockwise, and counterclockwise when only plate  $Y$  was excited, ii) the wobble motions, when only plate  $X$  was excited, were almost identical to the wobble motions when only plate  $Y$  was excited at the same frequency. In conclusion, the designed motor can be driven with a single AC source and exciting the plate  $X$  or  $Y$  simultaneously controls the direction of the rotation.

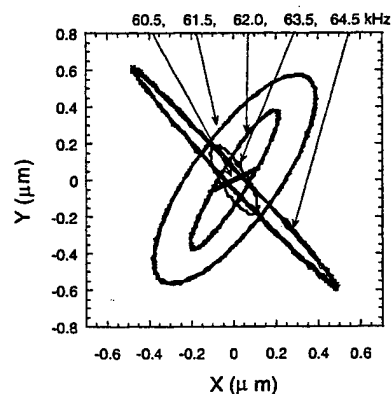


Fig. 6a: Measured elliptical displacements at 60.5, 61.5, 62, 63.5 and 64.5kHz when only plate  $X$  was excited. The most suitable frequency to drive the motor is 61.5kHz.

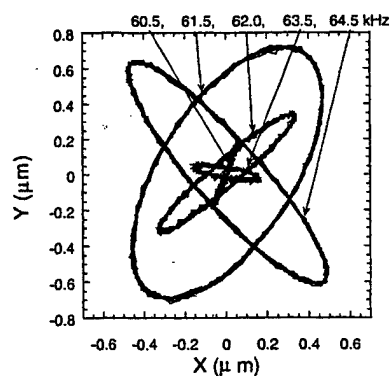


Fig. 6b: Measured elliptical displacements at 60.5, 61.5, 62, 63.5 and 64.5kHz when only plate  $Y$  was excited. Note that the most suitable frequency to drive the motor is again 61.5kHz.



## Motor Performance

The no-load speed in the clockwise and counterclockwise directions as a function of input rms voltage is shown in Fig. 7. The speed (N) in the clockwise and counterclockwise directions increased by the same amount with input voltage from 20 to 120V. The motor was driven at 62.1 kHz for both directions. According to the first preliminary measurements, the output torque at 80V is more than 1.0 mNm.

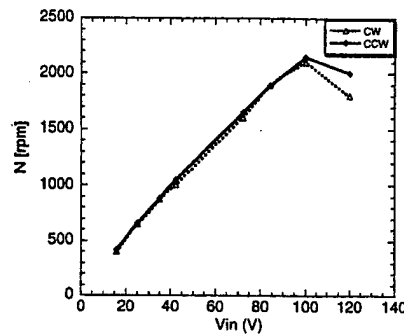


Fig. 7: Speed [N] vs. input voltage.

## Conclusions

A new Multi-Mode-Single-Vibrator type Piezoelectric Ultrasonic motor design has been designed.

The motor is driven with single AC power source. The structure of the motor is simple and highly scalable. The rotation in this motor takes place by exciting two orthogonal bending modes of a hollow cylinder. The structure of the stator was analyzed using the ATILA finite element code, and its dynamic behavior was predicted. The proposed motor may find application in medical industries such as catheter and other micromechatronic device applications

## References

- [1] W. Williams and W.J. Brown, US Patent, 2439499, (1942).
- [2] S. Ueha and Y. Tomikawa, Ultrasonic motors, Theory and Applications, Oxford science publication, Clarendon press, (1993).
- [3] T. Sashida and T. Kenjo, An introduction to ultrasonic motors, Oxford science publication, Clarendon press, (1993).
- [4] J. Wallaschek, Smart Mater. Struct., 7, (1998), 369-381.
- [5] K. Uchino, Smart Mater. Struct. 7, (1998), 273-285.
- [6] J. Tsujino, M. Takeuchi and H. Koshisako, IEEE Ultrasonics Symposium, (1992), 887-892.
- [7] M. Aoyagi, Y. Murasawa, T. Ogasawara and Y. Tomikawa, Jpn. J. Appl. Phys, 36, Part1, No. 5B, (1997), 3126-3129.
- [8] B. Koc, A. Dogan, Y. Xu, R.E. Newnham and K. Uchino, Jpn. J. Appl. Phys. Vol. 37 Part 1, No. 10, , (1998), 5659-5662.
- [9] M. Fleischer, D. Stain and H. Meixner, *IEEE Trans. Ultrason. Ferroelect. Freq. Cont.* 36, (1989), 607-613.

# **APPENDIX 74**

## COMPACT ULTRASONIC ROTARY MOTORS

K. UCHINO, B. KOC, and S. DONG

*International Center for Actuators and Transducers  
Materials Research Laboratory, The Pennsylvania State University  
University Park, PA 16802, USA*

This paper reviews recent developments of compact ultrasonic rotary motors using piezoelectric resonant vibrations. Following the historical background, three ultrasonic motors recently developed are introduced; *windmill*, *PZT tube* and *metal tube* types. Driving principles and motor characteristics are described in comparison with the conventional ultrasonic motors. Motors with 1.5 mm in diameter and 0.1 mNm in torque have been actually developed.

**Keywords:** Ultrasonic motor, Piezoelectric actuator, Standing wave motor

### INTRODUCTION

This paper deals with ultrasonic motors using resonant vibrations, putting a particular focus on miniaturized motors. Following the historical background, three compact ultrasonic motors recently developed are introduced; *windmill*, *PZT tube* and *metal tube* types. Driving principles and motor characteristics are described in comparison with the conventional ultrasonic motors. Motor sizes less than 3 mm  $\phi$  is of our particular interest.

### CLASSIFICATION OF ULTRASONIC MOTORS

#### Historical Background

Electromagnetic motors were invented more than a hundred years ago. While these motors still dominate the industry, a drastic improvement cannot be expected except through new discoveries in magnetic or superconducting materials. Regarding conventional electromagnetic motors, tiny motors smaller than 1cm long are theoretically difficult to produce with sufficient energy efficiency. Therefore, a new class of motors using high power ultrasonic energy, i.e., *ultrasonic motor*, is gaining wide spread attention. Ultrasonic motors made with piezoceramics whose efficiency is insensitive to size

are superior in the mini-motor area. For example, a commercialized electromagnetic motor by Motorola with 7 mm in diameter and 16 mm in length can generate 0.075 mNm in torque and 5000 rpm in no-load speed under an input power of 0.2 W, which is more than one order of magnitude higher than the power required for our ultrasonic motors with similar specifications.

Figure 1 shows the basic construction of an ultrasonic motor, which consists of a high-frequency power supply, a vibrator and a slider. Further, the vibrator is composed of a piezoelectric driving component and an elastic vibratory part, and the slider is composed of an elastic moving part and a friction coat.

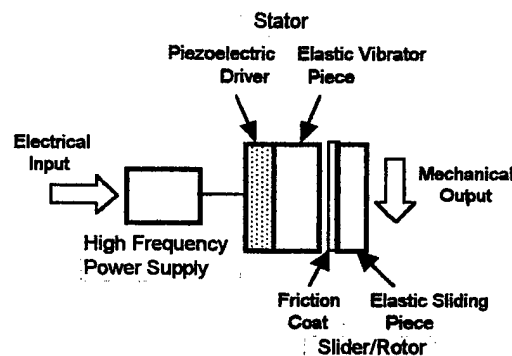


Fig. 1 Fundamental construction of an ultrasonic motor.

Though there had been some earlier attempts, the practical ultrasonic motor was proposed firstly by H. V. Barth of IBM in 1973 [1]. A rotor was pressed against two horns placed at different locations. By exciting one of the horns, the rotor was driven in one direction, and by exciting the other horn, the rotation direction was reversed. Various mechanisms based on virtually the same principle were proposed by V. V. Lavrinenko [2] and P. E. Vasiliev [3] in the former USSR. Because of difficulty in maintaining a constant vibration amplitude with temperature rise, wear and tear, the motors were not of much practical use at that time.

In 1980's, with an increase of chip pattern density, the semiconductor industry began to request much more precise and sophisticated positioners which do not generate magnetic field noise. This urgent request has accelerated the developments in ultrasonic motors. Another advantage of ultrasonic motors over the conventional electromagnetic motors with expensive copper coils, is the improved availability of piezoelectric ceramics at reasonable cost.

The merits and demerits of the ultrasonic motors are [4]:

---

Merits

1. Low speed and high torque                      -- Direct drive
2. Quick response, wide velocity range, hard brake and no backlash  
   -- Excellent controllability  
   -- Fine position resolution
3. High power / weight ratio and high efficiency
4. Quiet drive
5. Compact size and light weight
6. Simple structure and easy production process
7. Negligible effect from external magnetic or radioactive fields,  
    and also no generation of these fields

Demerits

8. Necessity for a high frequency power supply
  9. Less durability due to frictional drive
  10. Drooping torque vs. speed characteristics
- 

**Classification and Principles of Ultrasonic Motors**

Two categories are being investigated for ultrasonic motors from a vibration characteristic viewpoint: a standing-wave type and traveling-wave type [4]. The standing wave is expressed by

$$u_s(x,t) = A \cos kx \cdot \cos \omega t, \quad (1)$$

while the traveling wave is expressed as

$$u_p(x,t) = A \cos (kx - \omega t). \quad (2)$$

Using a trigonometric relation, Eq. (2) can be transformed as

$$u_p(x,t) = A \cos kx \cdot \cos \omega t + A \cos (kx - \pi/2) \cdot \cos (\omega t - \pi/2). \quad (3)$$

This leads to an important result, i.e., a traveling wave can be generated by superimposing two standing waves whose phases differ by 90 degree to each other both in time and in space. This principle is necessary to generate a traveling wave on a limited volume/size substance, because only standing waves can be excited stably in a finite size.

The standing-wave type is sometimes referred to as a vibratory-coupler type or a "woodpecker" type, where a vibratory piece is connected to a piezoelectric driver and the tip portion generates flat-elliptical movement. The standing-wave type has, in general, high efficiency, but lack of control in both clockwise and counterclockwise directions is a problem.

By comparison, the traveling-wave type (a surface-wave or "surfing" type) combines two standing waves with a 90° phase

difference both in time and in space. A surface particle of the elastic body draws an elliptical locus due to the coupling of longitudinal and transverse waves. This type requires, in general, two vibration sources to generate one traveling wave, leading to low efficiency (not more than 50 %), but it is controllable in both the rotational directions just by exchanging sine and cosine supplied voltages. Due to the necessity of the dual drive system, the traveling wave type is more complicated in structure and expensive in manufacturing cost than the standing wave type.

### **Conventional Motor Designs**

Figure 2 shows the famous Sashida motor [5]. By means of the traveling elastic wave induced by a thin piezoelectric ring, a ring-type slider in contact with the "rippled" surface of the elastic body bonded onto the piezoelectric is driven in both directions by exchanging the sine and cosine voltage inputs. The PZT piezoelectric ring is divided into 16 positively and negatively poled regions and two asymmetric electrode gap regions so as to generate a 9th mode propagating wave at 44 kHz. A prototype was composed of a brass ring of 60 mm in outer diameter, 45 mm in inner diameter and 2.5 mm in thickness, bonded onto a PZT ceramic ring of 0.5 mm in thickness with divided electrodes on the back-side. The rotor was made of polymer coated with hard rubber or polyurethane.

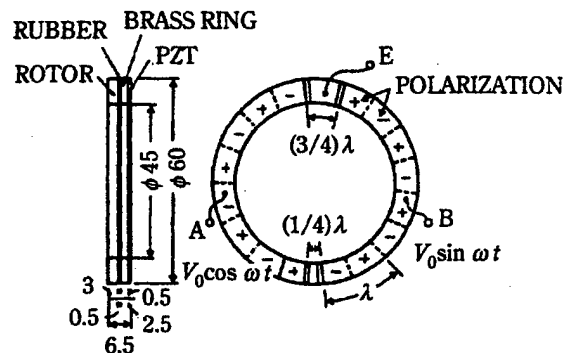


Fig. 2 Stator structure of Sashida's motor.

Canon utilized the "surfing" motor for a camera automatic focusing mechanism, installing this ring-type motor compactly in the lens frame. Using basically the same principle, Seiko Instruments miniaturized the ultrasonic motor to a diameter as small as 10 mm [6]. A driving voltage of 3 V provides torque of 0.1 mN·m. Seiko installed this tiny motor into a wrist watch as a silent alarm. AlliedSignal

developed ultrasonic motors similar to Shinsei's, which would be utilized as mechanical switches for launching missiles [7].

A significant problem in miniaturizing this sort of traveling wave motor can be found in the ceramic manufacturing process; without providing a sufficient buffer gap between the adjacent electrodes, the electrical poling process (upward and downward) easily initiates the crack on the electrode gap due to the residual stress concentration. This may restrict the further miniaturization of the traveling wave type motors. To the contrary, standing wave type motors, the structure of which is less complicated, are more suitable for miniaturization as we will discuss in the following. They require only one uniformly poled piezo-element, less electric lead wires and one power supply.

Another problem encountered in these traveling wave type motors is the support of the stator. In the case of a standing wave motor, the nodal points or lines are generally supported; this causes minimum effects on the resonance vibration. To the contrary, a traveling wave does not have such steady nodal points or lines. Thus, special considerations are necessary. In Fig. 2, the stator is basically fixed very gently along the axial direction through felt so as not to suppress the bending vibration.

We point out here also that one of the key factors for the actual commercialization of ultrasonic motors is to develop low loss and high mechanical quality factor piezoelectric materials, in order to suppress the heat generation during driving, which limits the continuous operation. We developed new ceramic series based on PZT-Pb(Mn,Sb)O<sub>3</sub> system, which can be used for 10 times higher input/output power range than the commercially available *Hard* PZT's without generating significant heat. Refer to some recent papers [8,9] on this issue.

## COMPACT MOTOR DESIGNS

We adopted the following concepts for developing new compact ultrasonic motors: (a) simplify the structure and reduce the number of component, (b) use simple (i.e., uniform) poling configuration, and (c) use the standing-wave type to reduce the drive circuit components.

### Windmill Motor

We have developed a *Windmill* motor design with basically a flat and wide configuration, using a metal-ceramic composite structure [10,11]. The motor is composed of four components: stator, rotor,

ball-bearing and housing unit [Fig. 3(a)]. The piezoelectric part has a simple structure of a ring electroded on its top and bottom surfaces ( $\phi$  3.0mm) poled uniformly in the thickness direction. The metal ring machined by Electric Discharge Machining has four inward arms placed  $90^\circ$  apart on its inner circumference. The metal and piezoelectric rings are bonded together, but the arms remain free; they thus behave like cantilever beams [Fig. 3(b)]. The length and cross-sectional area of each arm were selected such that the resonance frequency of the second bending mode of the arms is close to the resonance frequency of the radial mode of the stator. The rotor is placed at the center of the stator and rotates when an electric field is applied at a frequency between the radial and bending resonance modes. The truncated cone shape at the rotor end guarantees a permanent contact with the tips of the arms.

The operating principle of this motor is as follows: in the contraction cycle of the stator, the four arms at the center of the metal ring clamp the rotor and push it in the tangential direction. Since the radial mode frequency of the stator is close to the second bending mode frequency of the arms, the respective deformations are added and the tips of the arms bend down. In the expansion cycle, the arms release the rotor from a different path such that their tips describe an elliptical trajectory on the surface of the rotor. This motion seems to be a human finger's grasping-and-rotating action.

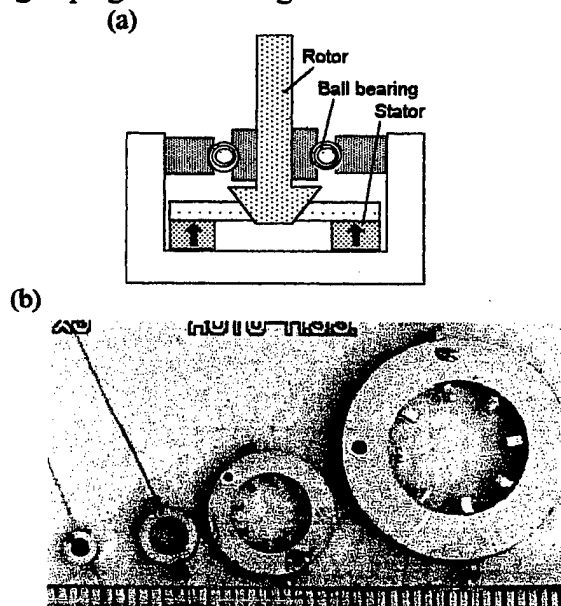


Fig. 3 "Windmill" motor using a metal coupler with multiple inward arms. (a) Cross sectional view, and (b) photos of various size stators (3-20 mm $\phi$ ).



Figure 4 shows the size dependence of the motor characteristics. When driven at 160 kHz, the maximum revolution 2000 rpm and the maximum torque 0.8 mNm were obtained for a 5 mm  $\phi$  motor. Figure 5 shows motor characteristics in a 3 mm  $\phi$  motor plotted as a function of load torque. A starting torque of 17  $\mu$ Nm is one order of magnitude higher than that of a thin film motor with a similar size [12].

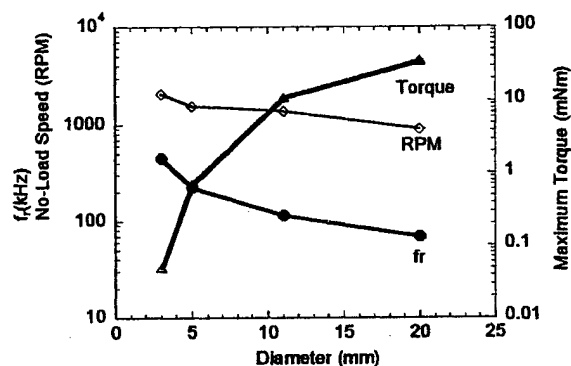


Fig. 4 Radial mode resonance frequency, no-load speed and starting torque vs. diameter of the stator, measured at 15.7 V.

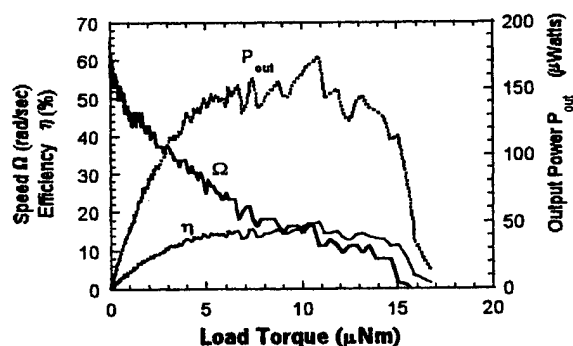


Fig. 5 Speed, efficiency, and output power versus load torque for a 3 mm  $\phi$  motor.

### **PZT Tube Motor**

In collaboration with Institute of Materials Research and Engineering, Singapore, we developed a PZT tube motor with a slim and long configuration [13]. The principle is similar to the one proposed by Tokin [14], which is schematically illustrated in Fig. 6. Four segmented electrodes were made on a PZT tube (1.5 mm or 2.2 mm in outer diameter) uniformly poled along the radial direction. A rotary bending vibration mode was excited on the PZT cylinder by

combining sine and cosine voltages to the segmented electrodes, then two rotors were made to contact the wobbling tube ends for achieving rotation. The motion is analogous to a "dish-spinning" performance.

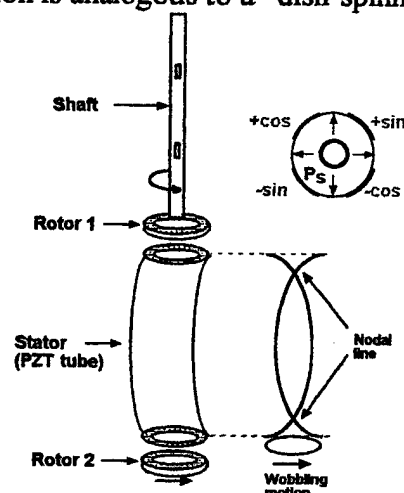


Fig. 6 Structure of a PZT tube type motor.

Our motor with 1.5/2.2 mm in diameter, 7 mm in length and 0.3 g in weight could generate 0.1 mNm in torque and 1000-2000 rpm in no-load speed. Table I summarized the specification comparison with other commercialized motors. Our motors sustain the efficiency more than 20% in this size, which is one order of magnitude higher than the electromagnetic motors. Compared with Seiko motors, the PZT tube type exceeds more than 10 times in the power density (output mechanical energy/unit volume).

Table I Comparison of the motor specifications from Motorola, Seiko Instruments, and ICAT/Penn State.

	Motorola Electromagnetic Micromotor	Seiko Ultrasonic Micromotor		ICAT/PSU Ultrasonic Micromotor
Outer diameter (mm)	7	8		2.2
Length (mm)	16	4.5		8
Power source (V)	1.5	1.5*	3.5*	3 - 6*
(mA)	126	60	12	2 - 5
No-load speed (rpm)	5000	1200	1200	1000-2000
Starting torque (mN m)	0.075	0.05	0.1	0.1

\* A booster circuit is required.

Although the motor characteristic is satisfactory for various applications such as intra-vascular medical micro surgery, there is one big problem, that is, difficulty in manufacturing fine and accurate PZT tubes, which leads to the expensive manufacturing cost.

### **Metal Tube Motor**

In order to lower the manufacturing cost with keeping the motor performance, we have developed a metal tube type, as shown in Fig. 7(a) [15]. Instead of the PZT tube, we utilized a metal hollow cylinder, bonded with two PZT rectangular plates uniformly poled. Both can be easily found/prepared and cheap in price. When we drive one of the PZT plates, Plate X, a bending vibration is excited basically along x axis. However, because of an asymmetrical mass (Plate Y), another hybridized bending mode is excited with some phase lag along y axis, leading to an elliptical locus in a clockwise direction. On the other hand, when Plate Y is driven, counterclockwise wobble motion is excited. Also note that only a single-phase power supply is required.

The rotor of this motor is a cylindrical rod with a pair of stainless ferrule pressed with a spring. The assembly is shown in Fig. 7(b).

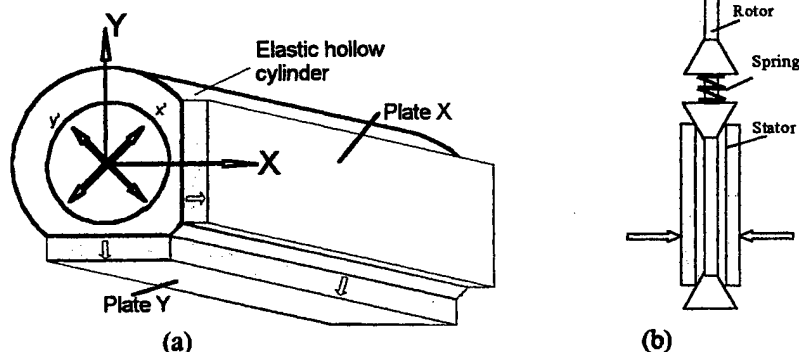


Fig. 7 (a) Structure of a metal tube stator, and (b) assembly of the motor.

The no-load speed in the clockwise and counterclockwise directions as a function of input rms voltage was measured for a motor with 2.4 mm  $\phi$  in diameter and 12 mm in length. The motor was driven at 62.1 kHz for both directions, just by exchanging the drive PZT plate. The no-load speed of 1800 rpm and the output torque of more than 1.0 mNm were obtained at 80 V for both directions. This significantly high torque was obtained due the dual stator configuration and the high pressing force between the stator and rotors made of metal.

## SUMMARY

Ultrasonic motors are characterized by "low speed and high torque." Thus, the ultrasonic motors do not require gear mechanisms, leading to very quiet operation and space saving. Moreover, high power/weight ratio, high efficiency, compact size and light weight are very promising for the future micro actuators adopted to catheter or tele-surgery.

We introduced here three compact motors recently developed; flat type *Windmill*, thin & long PZT tube, and its cheaper version, metal tube. For the further applications of the ultrasonic motors, systematic investigations on the following issues will be required: (1) low loss & high vibration velocity piezo-ceramics, (2) piezo-actuator component designs with high fracture resistance, (3) ultrasonic motor designs (standing-wave type, frictional contact), and (4) inexpensive and efficient high frequency/high power supplies.

## Acknowledgement

This work was partially supported by the Office of Naval Research through Contract No. N00014-96-1-1173.

## References

- 1) H. V. Barth: IBM Technical Disclosure Bull. 16, 2263 (1973).
- 2) V. V. Lavrinenko, S. S. Vishnevski and I. K. Kartashev: *Izvestiya Vysshikh Uchebnykh Zavedenii, Radioelektronika* 13, 57 (1976).
- 3) P. E. Vasiliev et al.: UK Patent Application GB 2020857 A (1979).
- 4) K. Uchino: "*Piezoelectric Actuators and Ultrasonic Motors*," Kluwer Academic Publishers, MA (1996).
- 5) T. Sashida: *Mech. Automation of Jpn.*, 15 (2), 31 (1983).
- 6) M. Kasuga, T. Satoh, N. Tsukada, T. Yamazaki, F. Ogawa, M. Suzuki, I. Horikoshi and T. Itoh: *J. Soc. Precision Eng.*, 57, 63 (1991).
- 7) J. Cummings and D. Stutts: *Amer. Ceram. Soc. Trans. "Design for Manufacturability of Ceramic Components"*, p.147 (1994).
- 8) S. Takahashi, Y. Sasaki, S. Hirose and K. Uchino: *Proc. MRS '94 Fall Mtg. Vol.360*, p.2-5 (1995).
- 9) K. Uchino, J. Zheng, A. Joshi, Y. H. Chen, S. Yoshikawa, S. Hirose, S. Takahashi, and J. W. D. de Vries: *J. Electroceramics*, 2, 33 (1998).
- 10) B. Koc, A. Dogan, Y. Xu, R. E. Newnham and K. Uchino: *Jpn. J. Appl. Phys.* 37, 5659 (1998).
- 11) B. Koc, P. Bouchilloux, and K. Uchino: *IEEE Trans.-UFFC*, 47, 836 (2000).
- 12) G. A. Racine, P. Muralt and M.A. Dudois: *Smart Mater. Struct.*, 7, 404 (1998).
- 13) S. Dong, L. C. Lim and K. Uchino: *IEEE Trans.-UFFC* [submitted].
- 14) T. Yoshida: *Proc. 2<sup>nd</sup> Memorial Symp. Solid Actuators of Japan: Ultra-Precise Positioning Techniques*, p.1 (1989).
- 15) B. Koc, J. F. Tressler and K. Uchino: *Proc. 7<sup>th</sup> Actuator 2000*, p.242-245, Axon, Bremen (2000).

# **APPENDIX 75**

# NEW CONCEPT FOR RESONANT LONGITUDINAL-SHEAR ULTRASONIC MOTOR

P. BOUCHILLOUX\*, B. KOC\*\*, K. UCHINO\*\*

\*Active Materials and Smart Structures Laboratory, Department of Mechanical Engineering, Aeronautical Engineering and Mechanics, Rensselaer Polytechnic Institute, Troy, NY 12180, bouchp@rpi.edu

\*\*International Center for Actuators and Transducers, Materials Research Laboratory, The Pennsylvania State University, University Park, PA 16802

## ABSTRACT

This paper presents an original linear piezoelectric motor for applications in space and robotics. The originality of this motor consists in the combination of longitudinal and shear modes of vibration of the stator. These two modes are mixed to produce an elliptical vibration of the surface of the stator in contact with a slider. The motion of the linear slider is obtained through friction forces that develop at the interface between the stator and the slider.

This motor is being developed for applications in active truss members of variable geometry structures, such as those used in space. Currently, these structures employ stepper motors. It is expected that replacing these electromagnetic devices with ultrasonic motors will offer the following advantages: position-locking without power supply, compactness, nonmagnetic operation, and lower power consumption.

This paper details the design of this motor and emphasizes the novel concept that was developed to combine the longitudinal and shear modes of vibration.

## INTRODUCTION

The purpose of our research is to develop ultrasonic motors that will be used in 1L-2L actuators for variable geometry structures. These actuators are found in deployable truss structures sent into space, for use in modular habitation units, satellite antennas, cranes, and other structural units. At the present time, the active truss members that are used to deploy and retract these structures usually employ stepper motors. Our motivation was to replace those with ultrasonic motors, thereby obtaining the following advantages over the electromagnetic motors: more compact and rugged solid-state design, position-locking without power supply, lower power consumption, and nonmagnetic operation.

The most fundamental requirement for active truss members is that they be able to double their length from their fully retracted state to their fully deployed state. This is why we refer to them as 1L-2L actuators. This requirement is probably higher than necessary, since in most classical variable geometry structures, a length variation of square root of two is often sufficient, as shown in Fig. 1.

To actuate such truss members by means of an ultrasonic motor, we considered the following criteria:

- the motor should be embedded into the truss member; this would result in a more compact truss member than what is currently used, since in most cases, the stepper motor is fixed to the outside of the truss
- the motor can be linear or rotary (although linear would result in a simpler system), and must provide reversible motion
- the motor should deliver a large force (and large locking force), which is defined according to the structure size and function

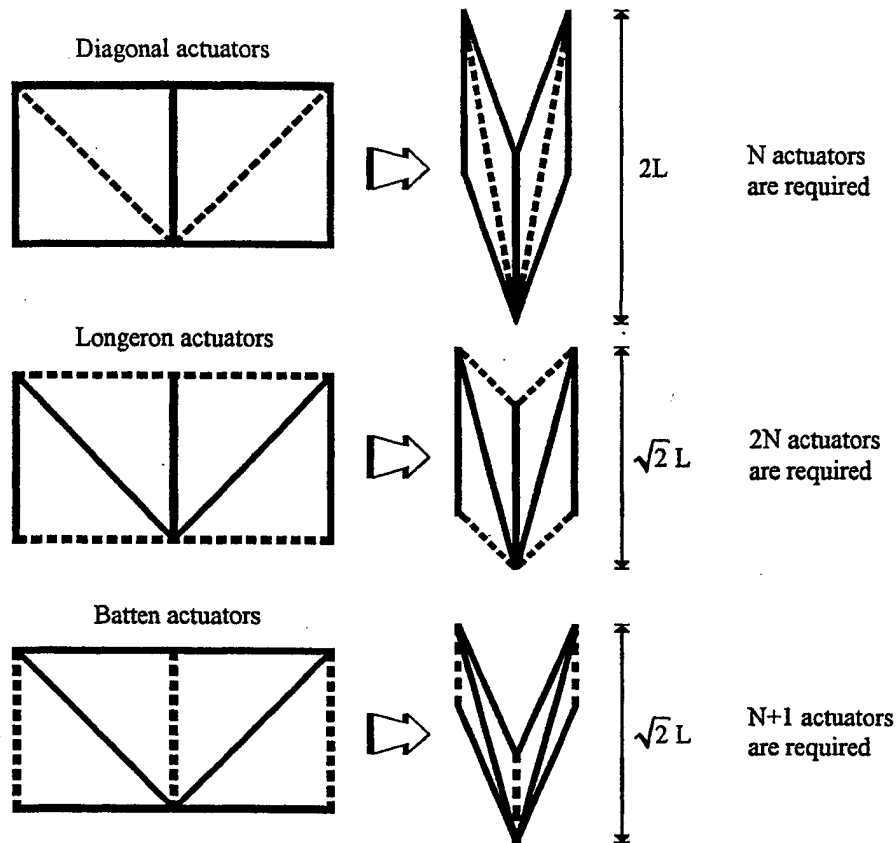


Figure 1: Classical types of variable geometry structures

In the first section of this paper, we briefly review existing motor designs that we have considered for implementation into a 1L-2L actuator. Since none of these designs seemed to correspond exactly to what we wanted, we decided to develop a new ultrasonic motor that would be better suited to our application. The design of this motor is thoroughly discussed in the next section of this paper.

Finally, we present finite element results and preliminary experimental results obtained for this motor and discuss its weak and strong points.

## DESIGN ASPECTS AND OPERATING PRINCIPLE

### Background

A 1L-2L actuator can be operated either with a rotary motor or a linear motor. In the case of a rotary motor, the rotation must be transformed into linear motion by means of a gear or a screw assembly, which is the current solution employed in variable geometry structures.

To simplify the actuation mechanism, and to take full advantage of the large force output offered by the piezoelectric motor technology, we preferred to investigate direct-drive linear motors.

Several designs of linear motors have been explored. We can cite, for instance, the multi-mode ultrasonic motors (MMUM) that combine longitudinal and flexure vibrations, such

as the L1B2 and L1B4 [2,3,4]. These motors have a low profile, and could be implemented in a 1L-2L actuator. Variations of the L1B4 design could offer interesting actuation possibilities [5]. Unfortunately, because they use a low-coupled bending mode, such motors usually have a small force output. They would therefore not be suitable for implementation in active truss members.

Other linear motors, such as the  $\pi$ -shaped ultrasonic motor [6] or Cedrat Recherche's ring-shaped motor [7], offer stronger force outputs and would be valid candidates for application in truss members, but we were more interested in another class of motors: the hybrid-type ultrasonic motors (HTUM). These motors, usually rotary, display large torques [8,9,10]. The large torque is obtained by mixing a longitudinal vibration with a torsional vibration of a Langevin-type transducer. The reason for using these two vibrations is that they are well coupled with the piezoelectric element. Indeed, the  $k_{33}$  and  $k_{15}$  intrinsic coupling coefficients of a hard-type PZT ceramic are larger than the  $k_{13}$ , which is used in popular traveling-wave type motors (TWUM).

It is important to note that, in general, HTUMs use only one resonance mode. Indeed, the first torsion mode of the stator is mixed with an off-resonance longitudinal vibration. Therefore, even though these motors exhibit interesting characteristics, it is certainly possible to improve them if shear (or torsion) and longitudinal vibrations can be combined at the resonance of both modes.

### Modal Frequencies

The ultrasonic motor we propose is a compact multi-mode ultrasonic motor (MMUM) that is operated by mixing the first longitudinal mode of a clamped-free bar with its first shear mode. For this motor to be successful, it is necessary that these two modes be matched, i.e. that their respective resonance frequencies be identical, or at least within a few hundred hertz.

The longitudinal modes of a clamped-free bar are given by the following expression [11]:

$$f_{L_i} = \frac{\lambda_i}{2\pi L} \sqrt{\frac{E}{\rho}} \text{ with } \lambda_i = \frac{2(i-1)\pi}{2}, i = 1, 2, 3... \quad (1)$$

where  $L$  is the length of the bar,  $E$  the Young's modulus of the isotropic material that makes the bar and  $\rho$  its density.

The shear modes of the same bar in the same conditions, granted that the bar is sufficiently short for pure shear to be assumed, are given by:

$$f_{S_i} = \frac{\lambda_i}{2\pi L} \sqrt{\frac{KG}{\rho}} \text{ with } \lambda_i = \frac{2(i-1)\pi}{2}, i = 1, 2, 3... \quad (2)$$

where  $G$  is the shear modulus of the bar's material and  $K$  a factor of shape of the bar's cross-section.

Using these simple relations, we immediately notice that the shear and longitudinal modes of the bar both depend on the same geometry and material parameters and in the same proportion. Also, if we consider a bar with a rectangular cross-section, then:

$$K = \frac{10(1+\nu)}{12+11\nu} \quad (3)$$

and taking:

$$G = \frac{E}{2(1+\nu)} \quad (4)$$

we obtain:

$$f_{L_i} \approx \frac{1}{\sqrt{3}} f_{S_i} \quad (5)$$



This shows that the first shear mode has a frequency of almost half that of the first longitudinal mode. In other words, it is not possible to match the shear and longitudinal modes in the bar, unless material properties or boundary conditions are modified.

To match the two modes, we can consider the following options:

- use an anisotropic material, with a shear modulus approximately two times larger than its longitudinal elastic modulus; fiber-reinforced polymers could be used to achieve such properties
- modify the boundary conditions of the system to decouple the two modes; in this case, the above equations no longer apply, and the two modes can be tuned more easily

We decided to select the second method, and decoupled of the two modes by adding arms on the side of the structure, as it is shown in Fig. 2. These arms significantly increase the stiffness of the stator in the shear direction without appreciably modifying the stiffness of the stator in the longitudinal direction. By selecting the size and position of these arms, it becomes possible to match the longitudinal and shear modes of the stator.

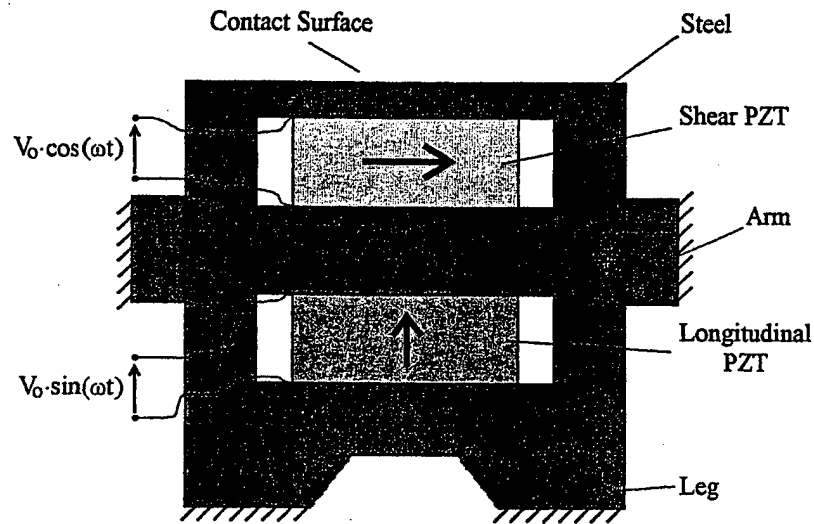


Figure 2: Stator of the proposed ultrasonic motor with the boundary conditions and the electrical connections

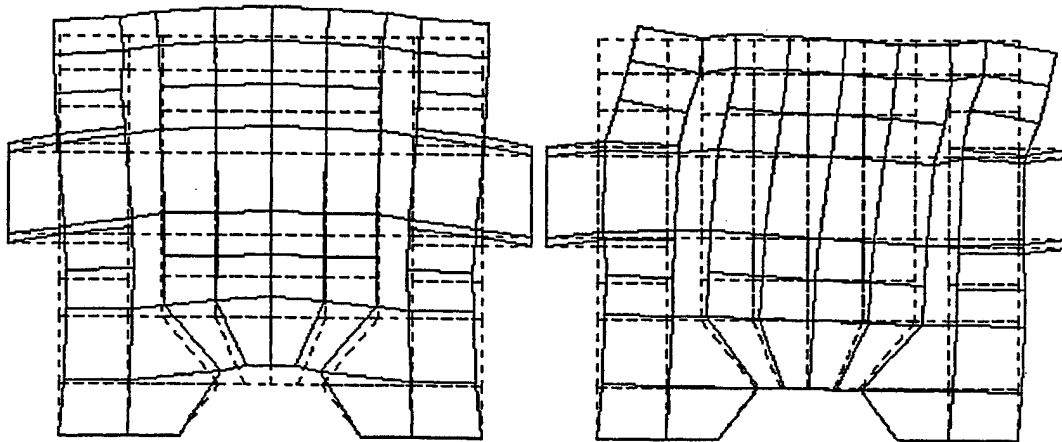


Figure 3: (left) Mode shape for the longitudinal mode; (right) Mode shape for the shear mode

The matching of the two resonance modes is obtained by performing finite element computations on the stator. The results are shown in Fig. 3, where we show the mode shape obtained for each mode. These computations were performed with the Atila finite element program [12], which takes into account the piezoelectric coupling of the ceramic elements. The frequencies and effective coupling factors obtained are given in Table 1.

	Resonance Frequency (kHz)	Antiresonance Frequency (kHz)	Effective Coupling Coefficient (%)
Longitudinal Mode	54.43	56.28	25.4
Shear Mode	54.46	55.57	19.9

Table 1: Finite element results for the modal response of the structure

### Active Elements

Another important aspect of the design concerns the dimensioning of the piezoelectric elements. The expansion of a rod in its longitudinal mode can be approximated as:

$$a = Qd_{33}E_3L \quad (5)$$

where  $Q$  represents the amplification obtained at resonance. According to this expression, and using material values found in commercial hard-type piezoelectric ceramics ( $d_{33} \approx 300$  pC/N), we find that a length  $L = 5$  mm and  $Q = 100$  are sufficient to obtain at least  $2 \mu\text{m}$  of expansion, which is the minimum level required to operate the motor.

The same approach can be used to determine the transverse displacement obtained with the shear mode. Using finite element modeling to confirm these estimates, we find that using a length  $L = 5$  mm is satisfactory, as shown in Tables 2 and 3. Table 2 gives the longitudinal and transverse displacements computed when each mode is excited independently at its own resonance frequency. This table clearly indicates that the longitudinal and transverse displacements are completely decoupled. Table 3 gives the displacements when the two modes are excited at the same time, with a phase shift of  $90^\circ$  between the two input signals. The frequency selected for this computation was 54.44 kHz.

	Longitudinal Mode nm/V	Shear Mode nm/V
Longitudinal Displacement	127	0
Transverse Displacement	0	176

Table 2: Finite element results for the displacements when each mode is excited independently

	Displacement nm/V
Longitudinal direction	111
Transverse direction	115

Table 3: Finite element results for the displacement when the two modes are excited at 54.44 kHz with a  $90^\circ$  phase shift

## Boundary Conditions

In the proposed design, the stator is clamped at the bottom and at the two side arms. The role of the side arms is to decouple the shear mode from the longitudinal mode in the bar. The decoupling effect is clearly visible in the results of the finite element analysis shown in Fig. 3.

These clamping boundary conditions clearly constitute weakness of the design, because they may become difficult to achieve in the final device. Special attention is therefore needed when installing the stator onto its support.

## Operating Principle

The operating principle of the motor is shown in Fig. 4. It follows classical MMUM operating rules: two electric signals with a  $90^\circ$  phase shift excite two piezoelectric elements. The longitudinally poled piezoelectric element produces the longitudinal vibration of the stator, and the transversely poled piezoelectric element produces the shear vibration of the stator. As a result of the mixing of these two vibrations, an elliptical motion is obtained at the top of the stator. Motion is then transferred to a linear slider via friction forces that develop at the interface between the two bodies.

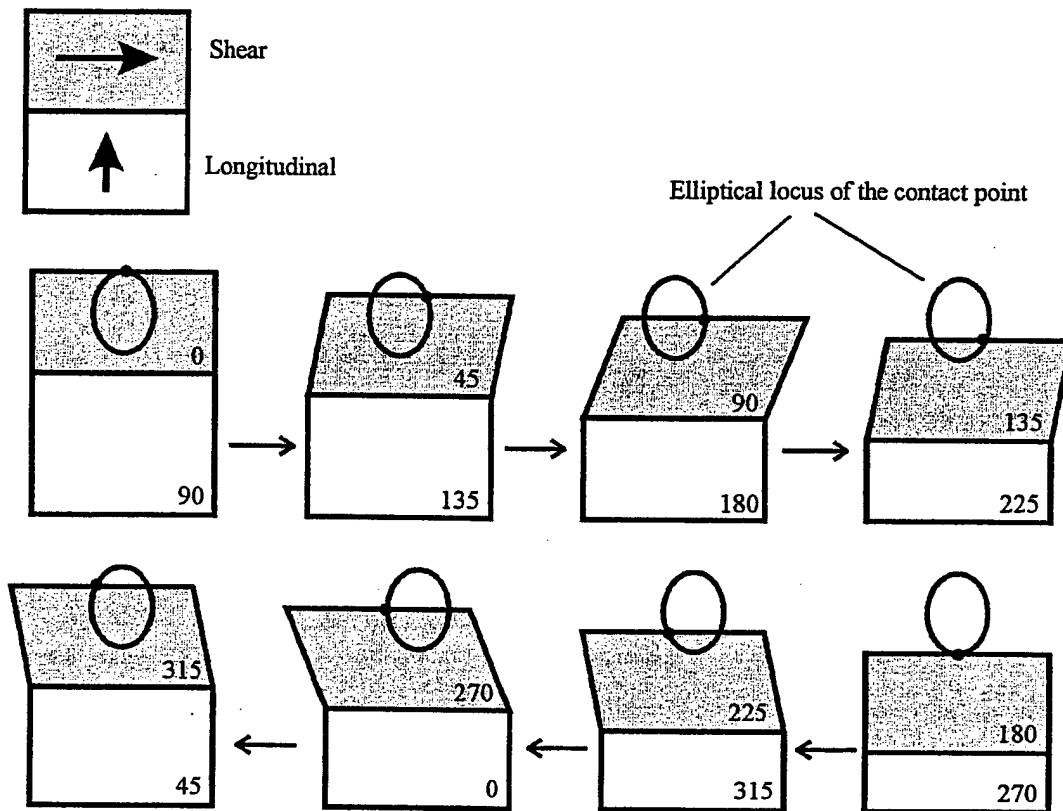
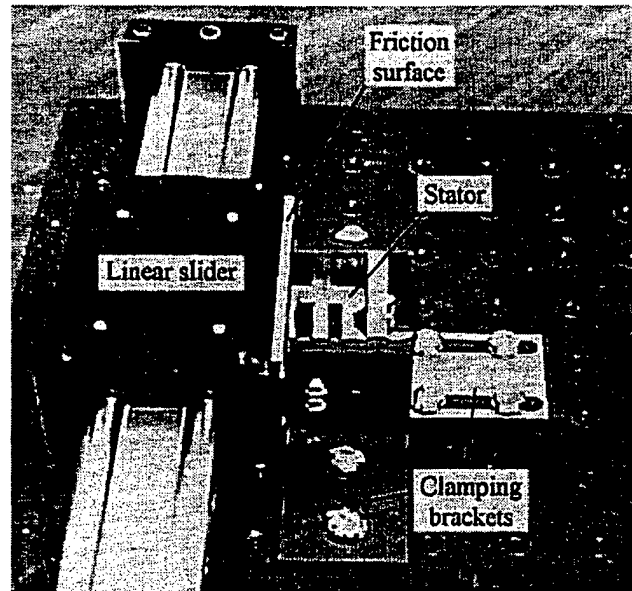


Figure 4: Operating principle of the Longitudinal-Shear motor

## Preliminary Experimental Results

The experimental setup is shown in Fig. 5. This setup will be used to test the motor force output under various conditions of mechanical prestress. This setup will also allow us to test various friction materials.



**Figure 5: Linear ultrasonic motor test setup**

Preliminary results were obtained with this setup in unloaded conditions, which are achieved by removing the slider. Results using a laser interferometer indicated that an elliptical vibration could be formed at the top of the stator, as shown in Fig. 6. Due to problems during the fabrication of the stator, it appeared that the modes were not sufficiently matched. This prevented obtaining further results with the current prototype.

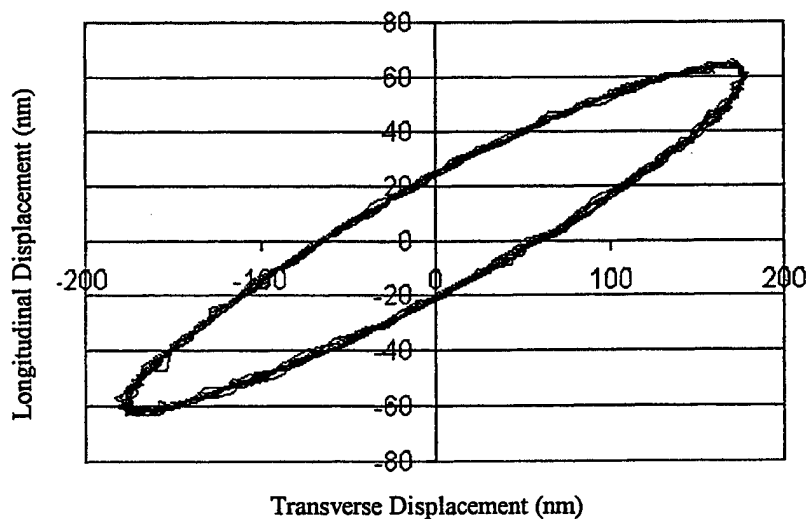


**Figure 6: Measured ellipse at the top of the stator under low-field excitation**

## CONCLUSIONS

We have presented an original design concept for a linear ultrasonic motor. Characteristics of this motor are: compact and direct-drive design, reversible motion by control of the phase between the two electric input ports, and nonmagnetic operation.

One of the major difficulties of the proposed design concerns the boundary conditions, which may be difficult to implement in the real device. The quality of the tuning of the longitudinal and shear resonances depends in large part on achieving these boundary conditions.

On the other hand, the proposed design is extremely simple and relatively easy to manufacture. It is expected that this design will also be easy to scale up and down to address various implementation issues.

## REFERENCES

- [1] M. M. Mikulas Jr., B. K. Wada, C. Farhat, G. Thorwald, P. Withnell, *Initially Deformed Truss Geometry For Improving The Adaptive Performance Of Truss Structures*, Conference Proceedings, 1992
- [2] T. Bein, E. J. Breitbach, K. Uchino, *A Linear Ultrasonic Motor Using The First Longitudinal And The Fourth Bending Mode*, *Smart Materials and Structures*, vol. 6, no. 5, pp. 619-627, 1997
- [3] H. Saigoh, M. Kawasaki, N. Maruko, K. Kanayama, *Multilayer Piezoelectric Motor Using The First Longitudinal And The Second Bending Vibrations*, *Japanese Journal of Applied Physics*, vol. 34, no. 5B, pp. 2760-2764, May 1995
- [4] Y. Tomikawa, T. Takano, H. Umeda, *Thin Rotary And Linear Ultrasonic Motors Using A Double-Mode Piezoelectric Vibrator Of The First Longitudinal And Second Bending Modes*, *Japanese Journal of Applied Physics, Part 1*, vol. 31, no. 9B, pp. 3073-3076, September 1992
- [5] P. Bouchilloux, B. Koc, K. Uchino, *Piezoelectric Motion Couplers*, Proc. of the 4th ARO Workshop on Smart Materials, August 1999.
- [6] K. Uchino, *Piezoelectric Ultrasonic Motors: Overview*, *Smart Materials and Structures*, vol. 7, no. 3, pp. 273-285, June 1998
- [7] R. Le Letty, F. Claeysen, F. Barillot, M.F. Six, P. Bouchilloux, *New Linear Piezomotors for High Force/Precise Positioning Applications*, Proc. of SPIE, 1998
- [8] K. Nakamura, M. Kurosawa, S. Ueha, *Characteristics Of A Hybrid Transducer-Type Ultrasonic Motor*, *IEEE Transactions on Ultrasonics, Ferroelectrics, and Frequency Control*, vol. 38, no. 3, May 1991
- [9] K. Nakamura, M. Kurosawa, S. Ueha, *Design Of A Hybrid Transducer Type Ultrasonic Motor*, *IEEE Transactions on Ultrasonics, Ferroelectrics, and Frequency Control*, vol. 40, no. 4, July 1993
- [10] J. Satonobu, N. Torii, K. Nakamura, S. Ueha, *Construction Of Megatorque Hybrid Transducer Type Ultrasonic Motor*, *Japanese Journal of Applied Physics, Part 1*, vol. 35, no. 9B, pp. 5038- 5041, September 1996
- [11] R. D. Blevins, *Formulas For Natural Frequency And Mode Shape*, Van Nostrand Reinhold, 1979, ISBN 0-89464-894-2, pp.171-185
- [12] Atila, *Finite Element Program For Smart Structures*, dist. by Magsoft Corp., Troy, NY

# **APPENDIX 76**

# Piezoelectric Micromotor Using a Metal-Ceramic Composite Structure

Burhanettin Koc, *Student Member, IEEE*, Philippe Bouchilloux, and Kenji Uchino, *Member, IEEE*

**Abstract**—This paper presents a new piezoelectric micro-motor design, in which uniformly electroded piezoelectric ring bonded to a metal ring is used as the stator. Four inward arms at the inner circumference of the metal ring transfer radial displacements into tangential displacements. The rotor ends in a truncated cone shape and touches the tips of the arms. A rotation takes place by exciting coupled modes of the stator element, such as a radial mode and a second bending mode of the arms. The behavior of the free stator was analyzed using the ATELA finite element software. Torque vs. speed relationship was measured from the transient speed change with a motor load. A starting torque of 17  $\mu\text{Nm}$  was obtained at 20 Vrms. The main features of this motor are low cost and easy assembly because of a simple structure and small number of components.

## I. INTRODUCTION

ULTRASONIC motors are generally categorized as travelling-wave or standing-wave types according to the type of vibration wave used on the stator. Currently, most miniaturized motors utilize a travelling elastic wave [1], [2] and present two major drawbacks. First, the piezoelectric element of a travelling-wave motor, typically an annular ring, must be divided in sectors poled in alternately opposite directions. This makes the poling process complicated and damages many samples. Second, to produce a travelling wave on a vibrating piezoelectric element, at least two AC power sources with a 90-degree phase difference, both in time and space, are required. This results in a more complex drive and wiring.

Another important factor in the miniaturization of piezoelectric ultrasonic motors comes from the maximum level of vibrations that can be obtained from a piezoelectric element. The maximum vibration velocity of the piezoceramic limits the vibration amplitude [3]. As the size of a piezoelectric ultrasonic motor decreases, the resonance frequency of its stator increases. The vibration level, however, cannot be increased beyond a certain vibration velocity due to the limitation of the piezoelectric material. Therefore, a vibration magnification and transformation mechanism (vibration concentrator) is necessary on a stator element to amplify vibration amplitude on the piezoceramic material similar to projection teeth on the stator elements of traveling wave motors.

An alternative design to miniature piezoelectric motors consists of PZT thin films [4], [5], even though their properties are inferior to those of bulk piezoelectric ceramics. However, the performance of thin-film motors is on the way of improvement in parallel with quality of thin films [6], [7].

In order to miniaturize piezoelectric motors, we used a bulk piezoelectric material and took the following approaches: the structure of the active piezoelectric element, including its poling configuration, should be simple to be manufactured in small size; the number of components used in the motor should be as few as possible to decrease the production cost. We proposed such an ultrasonic motor design using a metal-ceramic composite structure [8]. The stator in that motor consisted of a piezoelectric ring, poled uniformly in its thickness direction, bonded to two metal endcaps. Due to the multi-mode excitation (radial mode of the piezoelectric ring and bending mode of the metal endcaps), an elliptical motion was generated at the center of the top endcap where the rotor was placed.

The operating principle and structure of the motor presented in this work is similar to our previous design. However, in this new design, only one metal endcap was used. It was bonded to the piezoelectric ring and its center part was removed. Finally, the size of the stator vibrator was decreased to a diameter of 3.0 mm.

The structure and operating principle of the motor are provided first, then the finite element analysis of the stator vibrator is presented. The motor characteristics obtained with the transient response method are described last.

## II. STRUCTURE AND OPERATING PRINCIPLE OF THE MOTOR

The motor is composed of four components: stator, rotor, ball-bearing, and housing unit (Fig. 1). The key element to this motor is a multifunctional stator, which has a metal-piezoelectric composite structure. The piezoelectric part has a simple structure of a ring electroded on its top and bottom surfaces ( $\phi$  3.0 mm) poled uniformly in the thickness direction (Table I). The metal ring, the dimensions are shown in Fig. 2, is machined using electric discharge machining (EDM). It has four inward arms placed 90° apart on its inner circumference. The metal and piezoelectric rings are bonded together, but the arms remain free; they thus behave like cantilever beams. The length and cross-sectional area of each arm were selected such that the resonance frequency of the second bending mode of the arms is close to the resonance frequency of the

Manuscript received March 4, 1999; accepted May 19, 1999. The authors would like to thank the Office of Naval Research for supporting this work through contract: N00014-96-1-1173.

B. Koc and K. Uchino are with the Materials Research Laboratory, Pennsylvania State University, University Park, PA (e-mail: bxx142@psu.edu).

P. Bouchilloux is with the Magsoft Corporation, Troy, NY.

TABLE I  
DIMENSIONS OF THE STATOR.

Outer diameter of piezoelectric ring	$R_{OP}$	3.0 mm
Inner diameter of piezoelectric ring	$R_{IP}$	1.5 mm
Thickness of piezoelectric ring	$t_p$	0.5 mm
Outer diameter of metal (brass) ring	$R_{OM}$	3.0 mm
Inner diameter of metal ring	$R_{IM}$	2.4 mm
Thickness of metal ring	$t_m$	0.15 mm
Length of the arm	$L$	1.02 mm
Radius of the circular part at the tip of the arms	$r$	0.5 mm
Width of the arm	$w_m$	0.4 mm
Angle between arm and radial force direction	$\varphi$	25°
Angle between tips of the arm and radial force direction	$\theta$	28.7°
Tapering angle at the tips of the arms	$\alpha$	17°

radial mode of the stator. The rotor is placed at the center of the stator and rotates when an electric field is applied at a frequency between the radial and bending resonance modes. The truncated cone shape at the end of the rotor guarantees a permanent contact with the tips of the arms.

The operating principle of this motor is as follows: in the contraction cycle of the stator, the four arms at the center of the metal endcap clamp the rotor and push it in the tangential direction. Because the radial mode frequency of the stator is close to the second bending mode frequency of the arms, the respective deformations are added and the tips of the arms bend down. In the expansion cycle, the arms release the rotor from a different path such that their tips describe an elliptical trajectory on the surface of the rotor.

#### A. Design of the Arms at the Inner Circumference of the Metal Ring

The length of the inward arms was chosen such that the resonance frequency of the second bending mode of each individual arm neighbors the resonance frequency of the first radial mode of the stator. Using this strategy, it becomes possible to produce multi-mode excitations with only a single electrical source [9], [10]. If we assume that each arm behaves like a simply cantilevered elastic beam, their bending frequencies can be estimated according to the following expression [11]:

$$\omega_{b1} = \frac{X_n^2}{L^2} \sqrt{\frac{Et_m^2}{12\rho}} \quad (1)$$

where,  $L$ ,  $t_m$ ,  $\rho$  and  $E$  represent the length, thickness, density, and Young Modulus of the beam, respectively. The frequency constants  $X_n'$  are determined from the following equation:

$$\cos X_n \cosh X_n = -1. \quad (2)$$

The first three values of the  $X_n'$ 's are 3.516, 22.03, and 61.7. Using these values and the dimensions and mechanical properties of the arms, the first three bending mode

frequencies of the arms are estimated at 90.2, 494.1, and 1380 kHz. The second bending mode frequency of the arms is close to the stator's radial mode resonance frequency, which is 461 kHz.

#### B. Force Transformation Mechanism

The force in the radial direction generated by the stator is transferred to the tangential direction at the periphery of the rotor via a mechanism, which is analogous to a slider-crank mechanism, assuming that the inward arms and the rotor are rigid (Fig. 2). When the stator is electrically excited to generate ultrasonic vibrations at its radial mode resonance frequency, the piezoelectric and metal rings expand and contract in the radial direction. The stator force due to the piezoelectric effect in the radial direction is transferred to the rotor via the inward arms. Because of the angular orientation of the arms (angle  $\varphi$  with respect to the radial direction), there are normal and tangential force components at the periphery of the rotor. The normal ( $N_2$ ) and tangential ( $T_2$ ) force components at the rotor surface are calculated as a function of the angles  $\phi$  (the angle between the origin of an arm and the contact point with the rotor),  $\varphi$  and the radial force  $F_A$ .

$$T_2 = F_A \cos(\varphi) \sin(\theta + \varphi), \quad (3a)$$

$$N_2 = F_A \cos(\varphi) \cos(\theta + \varphi). \quad (3b)$$

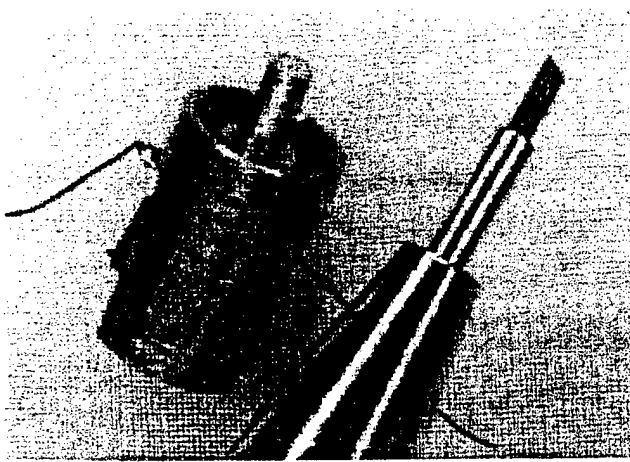
The normal force on the rotor surface is:

$$N_3 = F_A \cos(\varphi) \cos(\theta + \varphi) \cos(\alpha). \quad (4)$$

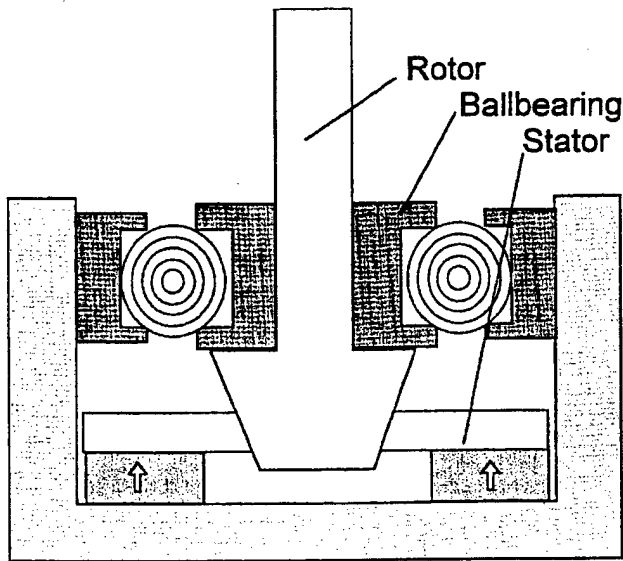
Because the length, width, and thickness of the arms as well as the radius of the rotor, which touches tangentially to the arms, are fixed to match the bending frequency of the arms to the radial mode resonance frequency of the stator, the angles  $\theta$  and  $\varphi$  were decided automatically. Small  $\varphi$  and large  $\theta$  values are desirable to increase tangential force  $T_2$ , because the normal force between stator and rotor can be controlled by static pressing force  $F_N$ .

The maximum torque that the motor can generate is limited by the static pressing force, which is provided by  $F_N / \sin \alpha$  where  $\alpha$  is the taper angle at the tips of the arms





(a)



(b)

Fig. 1. (a) Encapsulated motor next to a 0.5 mm metallic pencil (steel housing was coated with an epoxy insulator). (b) Structure of the motor showing the number of components.

ranging from 10 to 30 degrees (17 degrees for this experiment). The stator and the rotor contact surfaces are two mating cones kept in contact by the normal force. They thus constitute a conical clutch mechanism. The relation between the normal force  $F_N$  and torque capacity  $T$  is known by the following equation [12]:

$$T = \mu \frac{F_N}{\sin \alpha} \frac{r_o + r_i}{2} \quad (5)$$

where,  $\mu$ ,  $r_o$ , and  $r_i$  are friction coefficient, outer and inner radii of the rotor contact surface, respectively. The above torque, which is also called blocking torque, is the maximum torque this motor can generate.

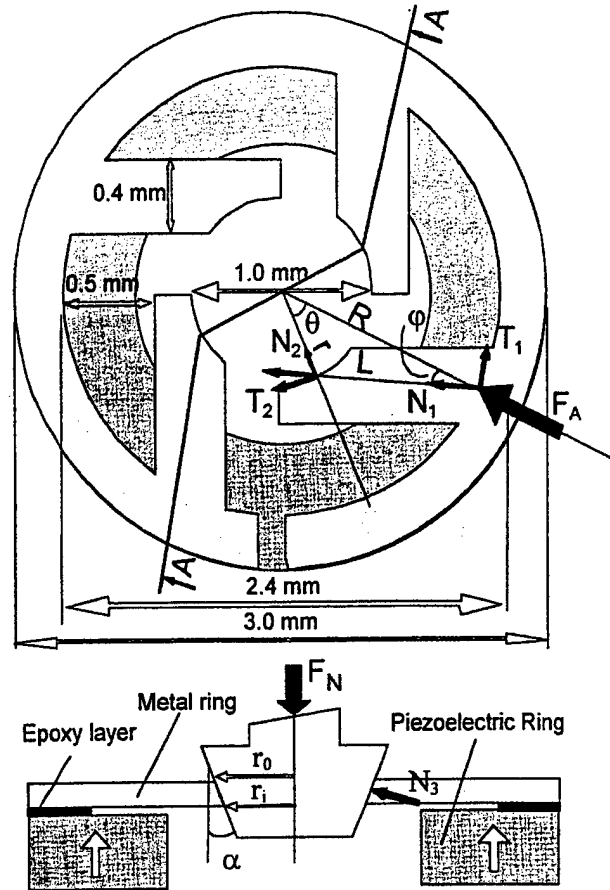


Fig. 2. Top and cross-sectional view of the stator vibrator. The metal ring is bonded to a piezoelectric ring from its outer circumference. Interface between inwardly directed arms and piezoelectric ring needs to be empty. Force is transferred from radial to tangential direction through the arms.

Because the normal force and the geometrical parameters used in the above expressions are all known, the friction constant can be estimated after measuring the stopping time of the motor, that is, after measuring the blocking torque of the motor.

### III. FINITE ELEMENT ANALYSIS

In order to verify the conceptual operation principle described in the previous section, the ATILA finite element code was used extensively to analyze the behavior of the stator and the vibration transformation mechanism at the tips of the arms. Because of the asymmetrical behavior of the structure and the angular orientation of the inward arms, we modeled the entire stator. Fig. 3 shows the 3D mesh of the free stator. The total number of nodes and second order brick elements used in the model were 2036 and 256, respectively, which caused computation times to be long (20 min per frequency, approximately). The dimensions and material properties used for modeling are given in Tables I and II. The epoxy layer between the metal and piezoelectric ring was not included in the model.

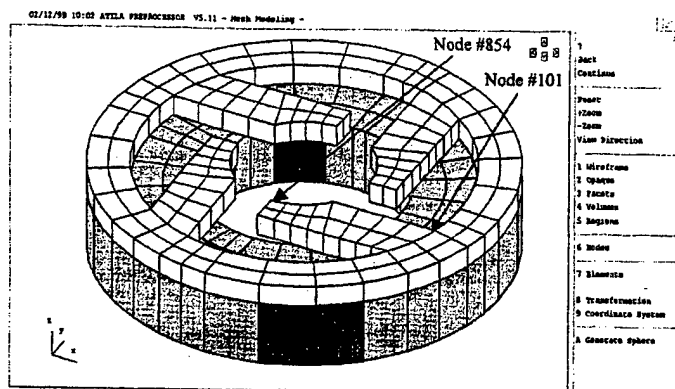


Fig. 3. ATILA 3D mesh of the stator vibrator (256 brick elements were used in the model with 2036 nodes).

TABLE II

PHYSICAL AND PIEZOELECTRIC PROPERTIES OF CERAMIC MATERIAL (APC INTERNATIONAL LTD.).

Parameter	Symbol	Units	APC 841
Relative permittivity	$\epsilon_{33}^T/\epsilon_0$	1	1380
	$\epsilon_{11}^T/\epsilon_0$	1	1490
Dielectric loss	$\tan \delta$	%	.35
Coupling factors	$k_p$	I	.56
	$k_{31}$	I	.32
	$k_{33}$	I	.65
	$k_{15}$	I	.65
	$k_L$	I	.48
Piezoelectric strain constants	$-d_{31}$	$10^{-12}\text{C/N}$	109
	$d_{33}$		323
Stiffness	$S_{11}^E$		11.7
Constants	$S_{33}^E$	$10^{-12}\text{m}^2/\text{N}$	17.3
Mechanical quality factor	$Q_m$	I	1400
Density	$\rho$	g/cc	7.9

#### A. Admittance Spectrum

The computed and experimental admittance spectra of the stator are compared in Figs. 4a and b, respectively. Fig. 4 shows that the 3D finite element model estimates all modes generated by the stator. It also makes it possible to identify some of these resonance modes [Fig. 4(a)]. For instance, the highest peak at 477 kHz is the radial mode of the stator; the mode shape is shown in Fig. 5(a). Because only one side of the piezoelectric ring is mechanically loaded (the metal ring was bonded to one side of the piezoelectric ring), the displacement is not purely in plane. The stator takes a convex/concave shape as it contracts and expands in the radial direction. Also, a flexure mode is generated on the ring because the arms are located in four discrete locations [Fig. 5(b)]. This mode, which is very close to the radial mode of the stator, is excited at 489 kHz and is the second peak in Fig. 4(a). The third peak on the admittance spectrum corresponds to the second bending mode of the arms, which is shown in Fig. 5(c). A (4,1)-like flexure mode also is excited in the ring at the

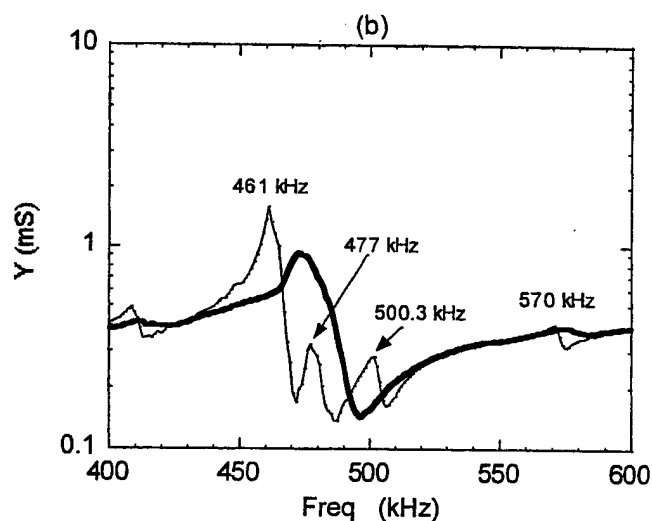
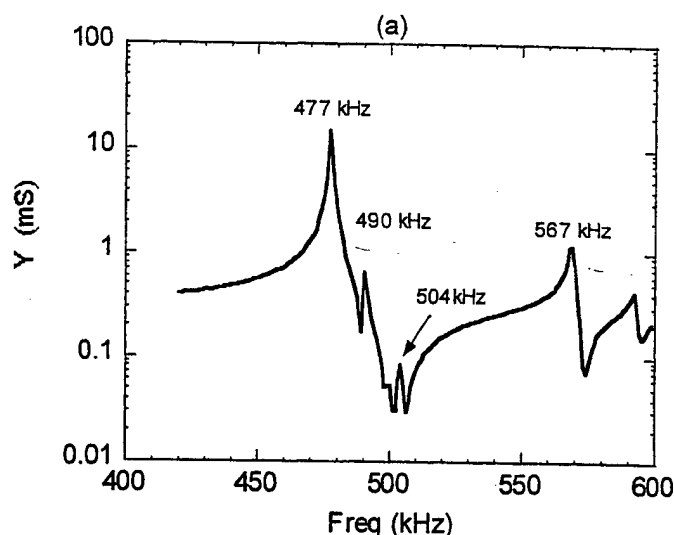


Fig. 4. (a) Calculated admittance spectrums of the free stator, b) measured admittance spectrums of the free stator and the motor (thick line).

bending mode frequency of the arms, which bend in the width direction.

Although the fundamental radial resonance mode was estimated within less than 5% error, magnitudes of the motional admittance values are not so good. Because the epoxy layer between the piezoelectric ring and the metal ring, as well as the damping caused by the cable connections, were not included in the finite element model, the losses in the FEA are less than in the experimental structure. As a result, the calculated motional admittance values are larger than the measured ones. Nevertheless, the magnitude of calculated off-resonance admittance matches very closely to the measured admittance.

#### B. Displacement Transformation Mechanism

In order to better understand the mechanism of transformation of the displacements that takes place at the

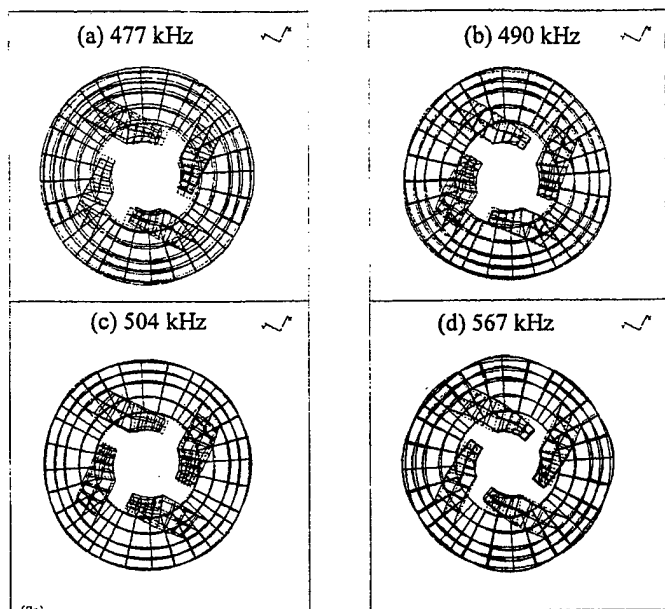


Fig. 5. Top view of calculated mode shapes of the free stator. (a) Mode shapes at fundamental radial resonance frequency at 477 kHz. Nonsymmetric structure of the metal ring distorts radial mode shape and causes the stator to take a convex/concave shape. (b) A flexure mode close to radial mode resonance at 490 kHz. (c) Mode shape corresponds to bending mode resonance frequency of the arms at 504 kHz. (d) Another flexural mode at 569 kHz of the stator in lateral direction corresponding to the bending mode of the arms in the width direction.

stator/rotor interface (from the radial to the tangential direction), displacements versus frequency were also calculated using harmonic analyses of the ATILA code. The calculated displacement spectrum at nodes 101 and 854 are shown in Figs. 6(a) and (b). The node numbers 101 and 854 are nodes on the inner circumference of the metal ring, at which the inward arms are connected, and on the tip of one arm, respectively (Fig. 3). Figs. 6(a) and (b) illustrate the displacement magnitudes of the arms as a function of frequency. For instance, the displacements in the z-axis are amplified for the second and third peaks of Fig. 6(a) and (b). This is due to the flexural mode of the stator and the bending modes of the metal arms. Elliptical trajectories at nodes 101 and 854 were calculated for three different frequencies (477, 490, and 500 kHz) and plotted in Fig. 7, which also demonstrates that the magnitudes of the elliptical trajectories are amplified at the tips of the arms.

#### IV. MOTOR CHARACTERISTICS

When a motor size is decreased, characterizing the motor becomes more difficult. A noncontact characterization method, which was initially proposed by Nakamura et al. [13], was used to characterize the motor. The principle of this method consists of mounting a load (usually a disk whose moment of inertia is known) onto the motor, running the motor, then, analyzing the transient speed

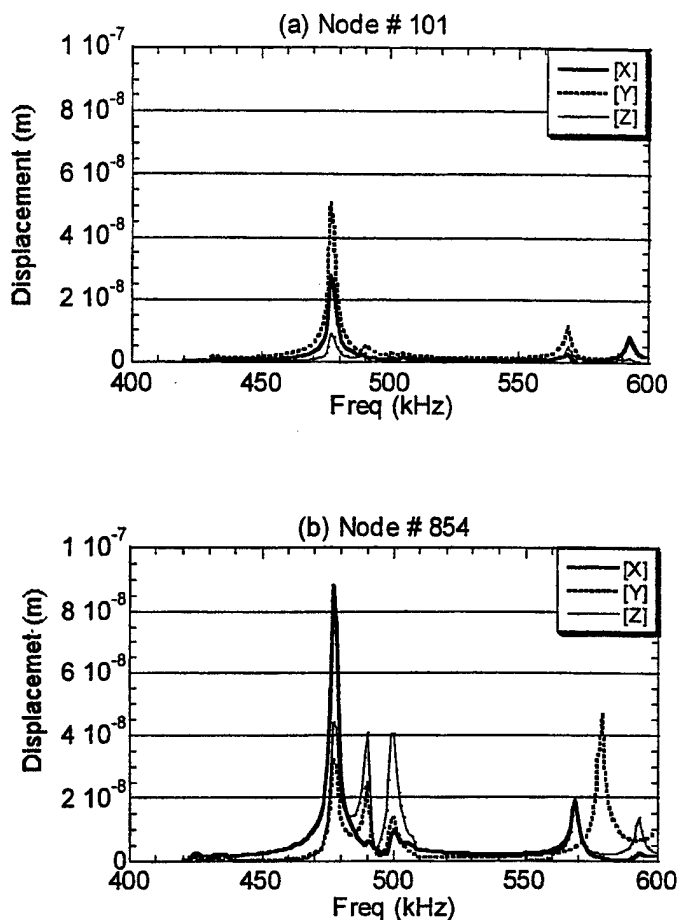


Fig. 6. Magnitude of calculated displacement spectrums (a) at node 101, and (b) at node 854 (for location of nodes 101 and 854, see Fig. 3).

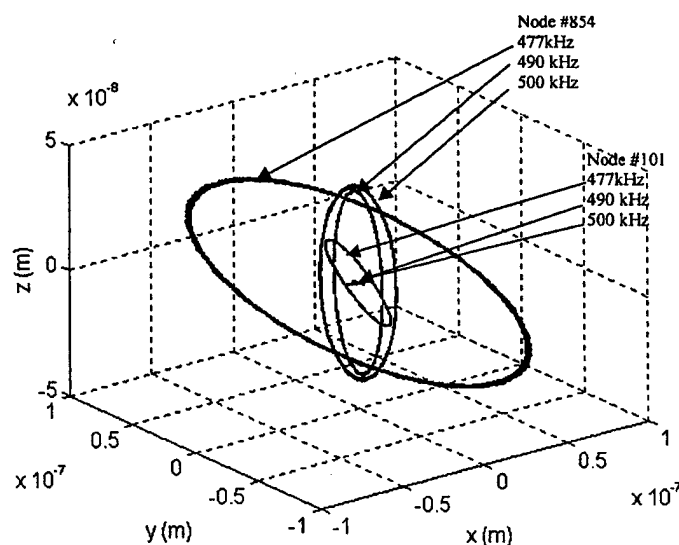


Fig. 7. Transformation and amplification of elliptical trajectories from circumference of the stator (node 101) to the tips of the arms (node 854) at frequencies: 477, 490, and 500 kHz (for location of node 101 and 854, see Fig. 3).

obtained as a function of time. More explicitly, the angular acceleration of the motor can be calculated by taking derivative of the measured speed. The transient torque is then calculated by multiplying the angular acceleration by the moment of inertia of the load, which is known. Using this method, the starting transient response of the motor gives the speed-torque relation. Similarly, the friction coefficient between the rotor and the stator is estimated from the transient response for stopping the motor.

Instantaneous output mechanical power ( $P_{out}$ ) also can be calculated by multiplying torque ( $\Gamma$ ) with angular speed ( $\Omega$ ). Input electrical power ( $P_{in}$ ) is calculated from measured input voltage, current, and phase angle between them. From input and output powers, the efficiency can be calculated by dividing output mechanical power to input electrical power.

#### A. Estimation of Load Characteristics

The load consists of a metal disk (10 g) with a high moment of inertia ( $0.2 \text{ kg} \cdot \text{mm}^2$ ) compared to that of the rotor. It is mounted onto the stator (0.25 g) and guided by two ball bearings. The motor, whose frequency spectrum is shown in Fig. 4(b) (thick line), was driven with an AC voltage of 20 V at 468 kHz.

The position of the loaded motor is detected in a form of square pulses through an optical sensor (OMRON EE-SPZ401Y) that utilizes a photocell pair. The frequency of the square wave, which is proportional to the position, was converted into voltage using a frequency-to-voltage converter. Because the output voltage of the converter is proportional to the input frequency, the transient speed of the motor was obtained with a simple gain factor. Second derivative of the recorded data gives the angular acceleration. The product of the angular acceleration and the moment of inertia of the rotating disk ( $I$ ) give the motor transient torque.

A typical transient response of the motor under loaded condition is shown in Fig. 8. An exponential curve fits the transient speed of the rotor:

$$\Omega = \Omega_0(1 - \exp(t/\tau_r)) \quad (6)$$

where,  $\Omega_0$  is the steady-state speed and  $\tau_r$  is the time constant, which can be found by trial and error. The initial value of  $\tau_r$  can be chosen as a quarter of the rise time. Then, it can be adjusted to obtain the best fit. For this particular measurement,  $\Omega_0$  and  $\tau_r$  were found as 62 rad/sec and 0.74 sec, respectively.

A blocking torque of  $25 \mu\text{Nm}$  was obtained from the stopping time of the motor. Substituting  $25 \mu\text{Nm}$  in the torque capacity (5), gives an estimate of the friction constant as 0.15. This number is almost half of the expected friction constant between brass (stator) and steel (rotor). The load characteristics obtained from the transient speed are shown in Fig. 9. A starting torque of  $17 \mu\text{Nm}$  is one order of magnitude higher than that of a thin film motor with a similar size [7].

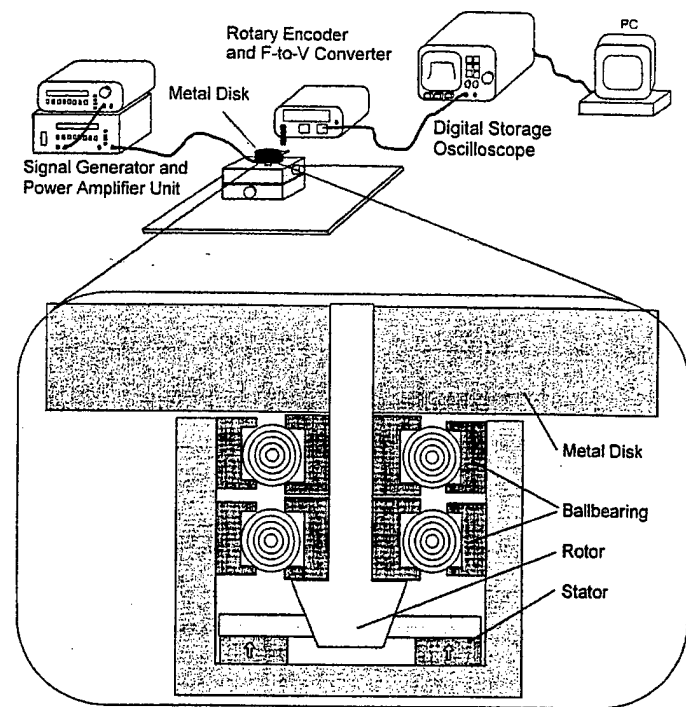


Fig. 8. Experiment setup to characterize small size motor using transient response method.

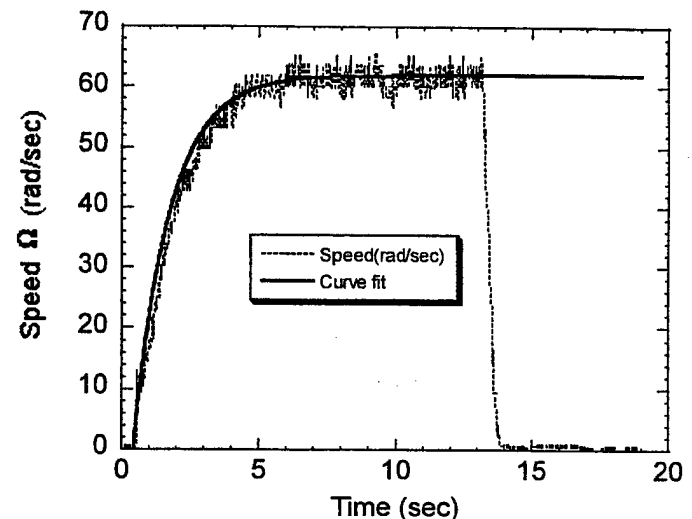


Fig. 9. Transient response of the motor at 20V. Transient speed was curve fitted to an exponential function.

The difference between blocking torque ( $25 \mu\text{Nm}$ ) and starting torque ( $17 \mu\text{Nm}$ ) states that the arms, which were chosen thin enough to match their bending mode frequency to the stator radial mode frequency, are not strong enough to push the rotor, but they deform. However, an efficiency of more than 10% is sufficient for real application with an output power of around  $150 \mu\text{ Watts}$ .

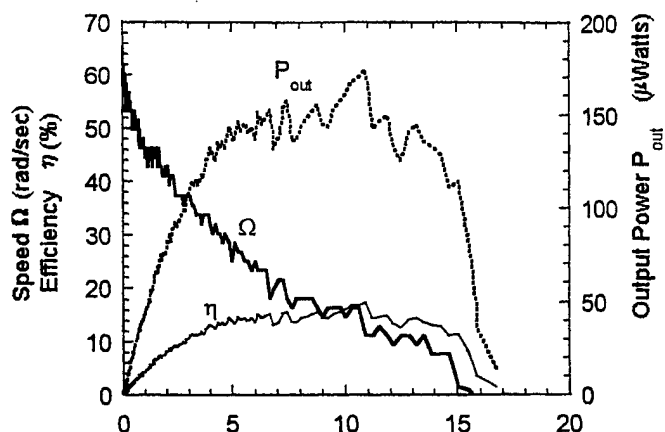


Fig. 10. Load characteristics of the motor.

## V. CONCLUSIONS

This paper presented a small piezoelectric ultrasonic motor with an active element that is a bulk piezoelectric ring 3.0 mm in diameter and 0.5 mm in thickness. The stator produces a displacement transformation such that multi-mode resonance frequencies can be excited with only one AC source. The stator was analyzed with a 3D model of the ATILA finite element analysis code, and its dynamic behavior was predicted. In particular, the FEA illustrated the bending and asymmetrical flexure modes that are generated close to the fundamental radial resonance frequency of the stator.

The rotation in this motor occurs by exciting the stator with a combination of two modes: the fundamental radial mode of the stator and the second bending mode of the arms.

The major applications of this motor will be micromechanical devices for the medical and microrobotic areas.

## REFERENCES

- [1] M. Kasuga, T. Satoh, J. Hirotsu, and M. Kawata, "Development of ultrasonic motor and application to silent alarm analog quartz watch," *4th Congress Eur. De Chronometrie*, Lausanne, 1992, pp. 53-56.
- [2] A. M. Flynn, "Performance of ultrasonic mini-motors using design of experiment," *Smart Mater. Struct.*, vol. 7, pp. 286-294, Jan. 1998.
- [3] S. Takahashi, Y. Sasaki, and S. Hirose, "Driving electric field effects on piezoelectric transducers," *Jpn. J. Appl. Phys.*, vol. 36, pp. 3010-3015, May 1997.
- [4] A. M. Flynn, L. Tavrow, S. Bart, R. Brooks, D. Ehrlich, K. R. Udayakumar, and L. E. Cross, "Piezoelectric micromotors for microrobots," *IEEE J. Microelectromech. Syst.*, vol. 1, pp. 44-51, Jan. 1992.
- [5] P. Muralt, M. Kohli, T. Maeder, A. Kholkin, K. Brooks, N. Setter, and R. Luthier, "Fabrication and characterization of PZT thin-film vibrators for micromotors," *Sens. Actuators*, vol. A48, pp. 157-165, 1995.
- [6] T. Morita, M. Kurosawa, and T. Higuchi, "Design of cylindrical ultrasonic micromotor to obtain mechanical output," *Jpn. J. Appl. Phys.*, vol. 35, pt. 1, no. 5B, pp. 3251-3254, 1996.
- [7] G. A. Racine, P. Muralt, and M. A. Dudois, "Flexural-standing-wave elastic force motor using ZnO and PZT thin film on micro-machined silicon membranes for wristwatch applications," *Smart Mater. Struct.*, vol. 7, pp. 404-416, Jan. 1998.

- [8] B. Koc, A. Dogan, Y. Xu, R. E. Newnham, and K. Uchino, "An ultrasonic motor using a metal-ceramic composite actuator generating torsional displacement," *Jpn. J. Appl. Phys.*, vol. 37, pt. 1, no. 10, pp. 5659-5662, Oct. 1998.
- [9] M. Fleischer, D. Stein, and H. Meixner, "New type of piezoelectric ultrasonic motor," *IEEE Trans. Ultrason., Ferroelect., Freq. Contr.*, vol. 36, pp. 614-619, Nov. 1989.
- [10] Le Letty, R. F. Claeys, F. Barillot, M. F. Six, and P. Bouchilloux, "New linear piezomotors for high force/precise positioning application," *SPIE Conference on Smart Structures and Integrated Systems*, San Diego, CA, Mar. 1998, pp. 784-755.
- [11] I. H. Shames, *Energy and Finite Element Methods in Structure Mechanics*, New York: Hemisphere, 1995, p. 333.
- [12] H. A. Rothbart, *Mechanical Design and System Handbook*. New York: McGraw-Hill, 1964, vol. 28.
- [13] K. Nakamura, M. Kurosawa, H. Kurebayashi, and S. Ueha, "An Estimation of load characteristics of an ultrasonic motor by measuring transient response," *IEEE Trans. Ultrason., Ferroelect., Freq. Contr.*, vol. 38, pp. 481-485, Sep. 1991.



**Burhanettin Koc (S'98)** was born in Kars, Turkey, in 1968. He earned his B.S. and M.S. degrees from Hacettepe University, Ankara, Turkey, in 1989 and 1992, respectively, both in electrical and electronics engineering. He was a teaching and research assistant in the Electrical and Electronic Engineering Department at Hacettepe University from 1989 to 1993. He enrolled as a Ph.D. candidate in 1994 in the Electrical Engineering Department at Pennsylvania State University.

His research interests include high power piezoelectric devices: ultrasonic motors, piezoelectric transformers, and microrobotics. He is a student member of IEEE.



**Philippe Bouchilloux** currently is working on his Ph.D. degree in the Active Materials and Smart Structures Laboratory, headed by Dr. Kevin Craig, in the Department of Mechanical Engineering, Aeronautical Engineering and Mechanics at Rensselaer Polytechnic Institute. He received his master's degree from the same department in May 1997.

Mr. Bouchilloux currently conducts his research on the design and applications of piezoelectric motors in the International Center for Actuators and Transducers at the Materials

Research Laboratory of the Pennsylvania State University under the direction of Dr. Kenji Uchino.



**Kenji Uchino, (M'89)** one of the pioneers in piezoelectric actuators, is the Director of the International Center for Actuators and Transducers, and Professor of Electrical Engineering at the Pennsylvania State University.

After being awarded his Ph.D. degree from the Tokyo Institute of Technology, Japan, Dr. Uchino became a research associate in the Physical Electronics Department at this university. He joined the Sophia University, Japan, as an associate professor in physics in 1985. He moved to Penn State in 1991: He also was involved with the Space Shuttle Utilizing Committee in NASDA, Japan, from 1986-88, and he was the Vice President of NF Electronic Instruments, USA, from 1992-94. He is the Chairman of the Smart Actuator/Sensor Study Committee, partly sponsored by the Japanese Government, MITI. He is also the executive associate editor for the *Journal of Advanced Performance Materials*, and the

associate editor of *J. Intelligent Materials Systems and Structures*.

His research interests are in solid state physics, especially dielectrics, ferroelectrics, and piezoelectrics, including basic research on materials, device designing, and fabrication processes, as well as the development of solid state actuators for precision positioners, ultrasonic motors, etc. He has authored 300 papers, 30 books and received 19 patents in the ceramic actuator area.

Dr. Uchino is a Fellow of the American Ceramic Society since 1997, and is a recipient of the Outstanding Research Award from Penn State Engineering Society (1996), Best Movie Memorial Award at Japan Scientific Movie Festival (1989), and the Best Paper Award from the Japanese Society of Oil/Air Pressure Control (1987).

# **APPENDIX 77**



## AN ACTIVELY TUNED SOLID-STATE VIBRATION ABSORBER USING CAPACITIVE SHUNTING OF PIEZOELECTRIC STIFFNESS

CHRISTOPHER L. DAVIS

*Smart Structures Technology, The Boeing Company, Seattle, WA 98032, U.S.A.*

AND

GEORGE A. LESIEUTRE

*Center for Acoustics and Vibration, Penn State University, University Park, PA 16802, U.S.A.*

*(Received 10 August 1998, and in final form 2 November 1999)*

A tunable solid-state piezoelectric vibration absorber and an active tuning method were developed and demonstrated. A passive vibration absorber generally acts to minimize structural vibration at a specific frequency associated with either a tonal disturbance or a lightly damped structural vibration mode. Because this frequency is rarely stationary in real applications, damping is usually added to ensure some level of effectiveness over a range of frequencies. Maximum response reductions, however, are achieved only if the absorber is lightly damped and accurately tuned to the frequency of concern. Thus, an actively tuned vibration absorber should perform better than a passive one and, furthermore, could be made lighter. In its simplest form, a vibration absorber consists of a spring-mass combination. A key feature of the tunable vibration absorber described herein is the use of piezoelectric ceramic elements as part of the device stiffness. The effective stiffnesses of these elements were adjusted electrically, using a passive capacitive shunt circuit, to tune the resonance frequency of the device. The tuning range of the absorber is thus bounded by its short- and open-circuit resonance frequencies. An alternative tuning approach might employ resistive shunting, but this would introduce undesirable damping. Another feature of the device is the ability to use the piezoelectric elements as sensors. A control scheme was developed to estimate the desired tuning frequency from the sensor signals, to determine the appropriate shunt capacitance, and then to provide it. The shunt circuit itself was implemented in 10 discrete steps over the tuning range, using a relay-driven parallel capacitor ladder circuit. Experimental results showed a 20 dB maximum, and a 10 dB average improvement in vibration reduction across the tuning range, as compared to a pure passive absorber tuned to the center frequency, with additional benefit extending beyond the tuning range.

© 2000 Academic Press

### 1. INTRODUCTION

Vibration is an important aspect of many engineering systems, from machine tools to structure-borne noise in aircraft [1]. In most cases, such vibration is undesirable and requires attenuation. Attenuation techniques range in complexity from relatively simple narrowband passive elastomeric vibration absorbers to fully active broadband vibration control systems.



Passive attenuation methods represent an important class of approaches to the control unwanted structural vibrations [2]. One particular method of passive vibration suppression involves the use of passive vibration absorbers (PVAs). Passive vibration absorbers are conceptually simple devices consisting of a mass attached to a structure via a spring or via a parallel spring-damper combination. PVAs are commonly constructed of an elastomeric material sandwiched between the structure and a reaction (or proof) mass. The primary function of these devices is to increase the effective dynamic stiffness of a structure over a relatively narrow frequency band. Increasing the dynamic stiffness of a structure reduces its dynamic displacement (assuming the forcing level remains constant). In practice, PVAs are typically used to minimize vibration at a specific frequency associated with either a lightly damped structural mode or a tonal disturbance. The advantages of using vibration absorbers are low cost, low weight, and ease of attachment. The fact that a PVA may only be used effectively at a single frequency, however, can sometimes be a significant drawback.

While a common use of PVAs is to reduce vibration in tall buildings or towers [3], they have also been successfully used in the aviation industry for some time. For example, the DC-9 for many years used a set of four PVAs attached to each engine pylon to reduce aft cabin noise associated with the operating spool frequency of the engines [4]. Similarly, both the Fokker F27 and the Saab 340 aircraft use PVAs attached directly to fuselage frames to reduce interior cabin noise levels [5].

In these applications, the absorbers provide considerable vibration attenuation at specific frequencies. Performance can be seriously degraded, however, if the disturbance source changes frequency. If this occurred, the PVA could, in principle, be physically re-tuned to maintain optimal performance, but this is generally impractical. Thus, there is a need for vibration absorbers with tunable variable properties.

Tunable vibration absorbers are passive vibration absorbers having stiffness, mass, or damping that can be (actively) adjusted to change one or more device resonance frequencies. Such tunable absorbers are sometimes used to track frequency-varying disturbances or to increase the bandwidth of a vibration attenuation method. Recently, Northwest Airlines initiated plans to upgrade 173 of its DC-9s with active tuned mass absorbers built by Bary Controls [6, 7]. Due to the increased weight and complexity of using such devices, however, they have not found widespread use.

Recently, PCB Piezotronics, Inc. and the Center for Acoustics and Vibration at Penn State were involved in the development of a piezoelectric ceramic inertial ("proof mass") actuator [8]. When used passively, this actuator behaves like a vibration absorber. This device provided a starting point for the development of an actively tuned vibration absorber, based on a previously unexploited tuning mechanism.

Two key features of a tunable vibration absorber are the method by which the stiffness or mass of the device is altered and the magnitude of the resulting change in resonance frequency. Because it is difficult to vary the effective mass of a solid-state device, the present work focused on a way to vary the effective stiffness. Because they exhibit relatively strong coupling between electrical and mechanical behavior, piezoelectric materials offer an attractive means of implementing variable stiffness: changing the electrical boundary conditions can change the effective stiffness of the material. If some of the stiffness of a vibration absorber is provided by piezoelectric elements, the resonance frequencies of the device could be modified by using an adjustable external electric circuit.

## 2. BACKGROUND

A mathematical model was developed to assist in the development of insight concerning tuning of a vibration absorber in which some of the effective stiffness is provided by

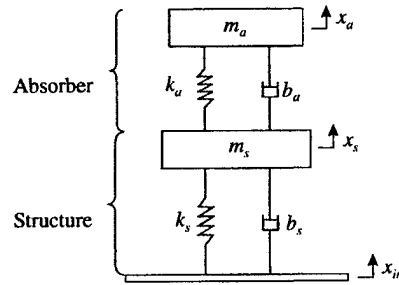


Figure 1. Lumped parameter model of passive vibration absorber attached to a s.d.o.f. structure.

piezoelectric elements. First, a single-degree-of-freedom (d.o.f.) structure and passive absorber model is created. Next, this model is modified to incorporate a piezoceramic stiffness element. Finally, an external adjustable electrical shunt circuit is added for frequency tuning.

## 2.1. VIBRATION ABSORBER/STRUCTURE INTERACTION

Consider a damped vibration absorber attached to a single d.o.f. structural system, as shown in Figure 1. Let  $m_s$ ,  $k_s$ , and  $b_s$  represent the effective mass, stiffness, and damping of the structure, and  $m_a$ ,  $k_a$ , and  $b_a$  represent the mass, stiffness, and damping of the absorber. This is a textbook model of the simplest system that can be used to study the behavior of a structure including a vibration absorber [9].

Recall that the natural frequency of the undamped s.d.o.f. structure without an attached vibration absorber,  $\omega_s$ , is

$$\omega_s = \sqrt{\frac{k_s}{m_s}}. \quad (1)$$

The transfer function from the input disturbance displacement,  $X_{in}$ , to the structural displacement (at the point of attachment of the vibration absorber),  $X_s$ , may be found as

$$\frac{X_s(s)}{X_{in}(s)} = \frac{k_s(m_a s^2 + k_a)}{m_s m_a s^4 + (m_a(k_s + k_a) + m_s k_a) s^2 + k_s k_a}. \quad (2)$$

The frequencies of the poles ( $\omega_1$  and  $\omega_2$ ) and zero ( $\omega_{abs}$ ) of this coupled structure/absorber system are

$$\omega_{1,2} = \frac{\sqrt{2}}{2} \sqrt{\frac{m_a(k_a + k_s) + m_s k_a \mp \sqrt{m_a k_a(m_a(k_a + 2k_s) + 2m_s k_a) + (m_a k_s + m_s k_a)^2}}{m_a m_s}}$$

$$\text{and } \omega_{abs} = \sqrt{\frac{k_a}{m_a}}. \quad (3a, b)$$

Note that  $\omega_{abs}$  defines the frequency of minimum response of the coupled structure/absorber system, and is equal to the natural frequency of the (undamped) vibration absorber itself.

Figure 2 shows the magnitude of the frequency response functions from an input base displacement to the structural displacement, both with and without an attached vibration

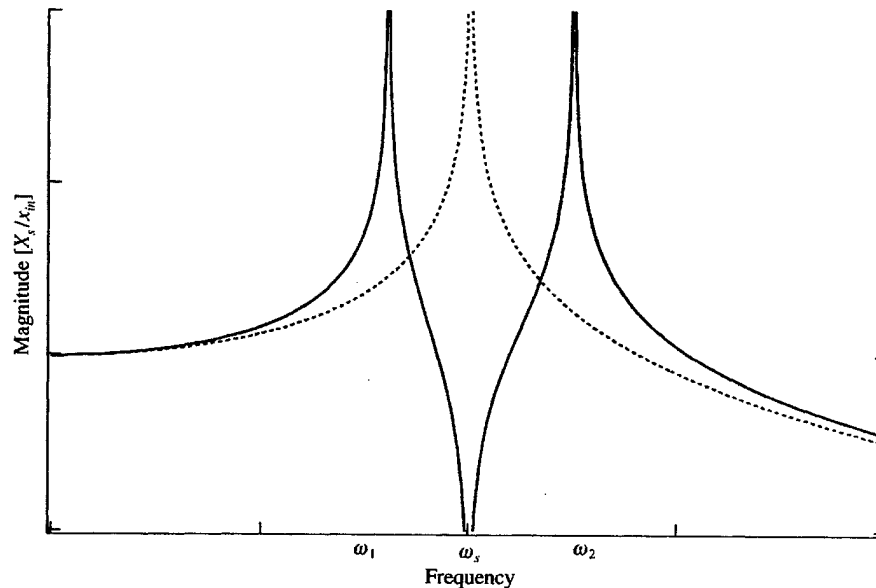


Figure 2. Sample frequency response functions for the s.d.o.f. structure and the s.d.o.f. structure with attached PVA: ----, without PVA; —, with PVA.

absorber. The structure without a vibration absorber exhibits high response at the frequency  $\omega_s$ . In the case where a vibration absorber is used, its natural frequency is tuned to that of the structure alone. The structural response is reduced dramatically at the frequency of the absorber, but increased at frequencies both above and below this frequency (i.e., at the frequencies of the poles of the coupled system,  $\omega_1$  and  $\omega_2$ ). Note that damping reduces the amplitude of the peaks as well as the depth of the minimum, and that the mass ratio affects the spacing of the two resonance frequencies [9].

Evidently (from equation (2)), the frequency at which structural response is a minimum depends only on the absorber mass and stiffness. Thus, structural response may be greatly reduced at any disturbance frequency, by tuning the natural frequency of the absorber to that of the disturbance, and by using an absorber with little damping. This observation may be exploited to develop a tuning control strategy that maintains optimum absorber performance when the structure is subjected to tonal forcing.

## 2.2. FREQUENCY TUNING VIA PASSIVE ELECTRICAL SHUNTING

With the knowledge that the natural frequency of the absorber defines the frequency of minimum structural response, the next step involved developing a method for changing the stiffness of the absorber in real time. Electrical shunting of a piezoelectric device has the effect of changing the effective stiffness (and thus the natural frequency) of the device. The theory behind such a shunting approach is presented in the conference paper by Davis *et al.* [10] as well as in the thesis by Davis [11], and is summarized here for completeness.

As already noted, a vibration absorber may be modelled using lumped parameters such as a spring,  $k_a$ , and mass,  $m_a$ , as shown in Figure 3(a). Similarly, an inertial actuator may be modelled as a spring-mass system with a forcing element,  $F_p$ , in parallel with the spring element,  $k_a$ , of the absorber, as shown in Figure 3(b). Placing the effective stiffness of the forcing element of an internal actuator in parallel with the inherent structural stiffness of the

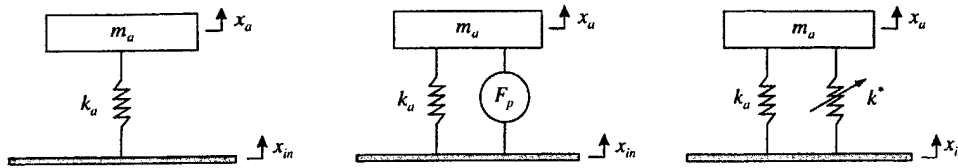


Figure 3. (a) Passive vibration absorber lumped parameter model; (b) inertial actuator lumped parameter model; (c) passively shunted inertial actuator lumped parameter model.

absorber, as shown in Figure 3(c), results in a passive device stiffness that is the sum of the two stiffnesses.

Electrically shunting the piezoceramic elements in a piezoceramic vibration absorber can change their effective stiffness. An expression for the effective stiffness,  $k^*$ , of an electrically shunted piezoceramic elements is [11]

$$k^* = k^E \left( 1 + \frac{k_p^2}{1 - k_p^2 + \alpha(s)} \right), \quad (4)$$

where  $k^E$  is the effective short-circuit stiffness of the piezoelectric ceramic element,  $k_p$  is its electromechanical coupling coefficient,  $\alpha(s)$  is the non-dimensional ratio of the electrical impedance of the piezoceramic (i.e.,  $1/sC_p^T$ , where  $C_p^T$  is the capacitance of the piezoceramic measured under constant stress) to the electrical impedance of the shunt circuit, and  $s$  is the Laplace parameter (i.e.,  $s = i\omega$  where  $\omega$  is radian frequency).

Regardless of the type of simple electrical shunt circuit used (e.g., resistor, capacitor, inductor), there are limits on the range of values  $k^*$  can take on. These limits are conveniently defined in terms of the short- and open-circuit stiffnesses of the piezoelectric element, as well as the shunt circuit electrical impedances. When short circuited, the shunt impedance is effectively zero and equation (7) reduces to  $k^* = k^E$ . At open circuit, the shunt impedance is effectively infinite and  $k^* = k^E(k_p^2/(1 - k_p^2))$ . Thus the tunable range of  $k^*$  is bounded by its short- and open-circuit stiffnesses, which are related by the electromechanical coupling coefficient,  $k_p$ .

In the application described here, the value of  $k_p$  (the planar coupling coefficient of the piezoelectric material) was approximately 0.6. For a device made solely of this type of piezoceramic material, the change in stiffness from short to open circuit could be as high as 56%, resulting in an almost 25% change in natural frequency. In practice, however, the stiffness of the piezoceramic is in parallel with the inherent mechanical stiffness of the actuator, and only some fraction of the net device stiffness may be changed due to electrical shunting.

Note that equation (4) may be complex depending upon the type of shunt circuit used (e.g., if a resistor is used as the shunt circuit). A complex stiffness would indicate that the device has mechanical properties similar to those of an anelastic material, including hysteretic damping. In terms of vibration absorber performance, adding damping has the effect of increasing the response magnitude at the natural frequency of the absorber. Because the goal of this research was to maintain minimum structural response at  $\omega_{abs}$ , shunt circuits that added damping to the system were not considered.

An ideal capacitor is a purely reactive element and does not dissipate energy or provide damping. Figure 4 shows the ratio of the effective stiffness of a capacitively shunted piezoceramic element to its short-circuit stiffness. Note that, for this case, the tuning ratio is the ratio of the shunt capacitance,  $C_{sh}$ , to the clamped capacitance of the piezoceramic. The tunable piezoceramic stiffness varies smoothly with increasing shunt capacitance. Also note

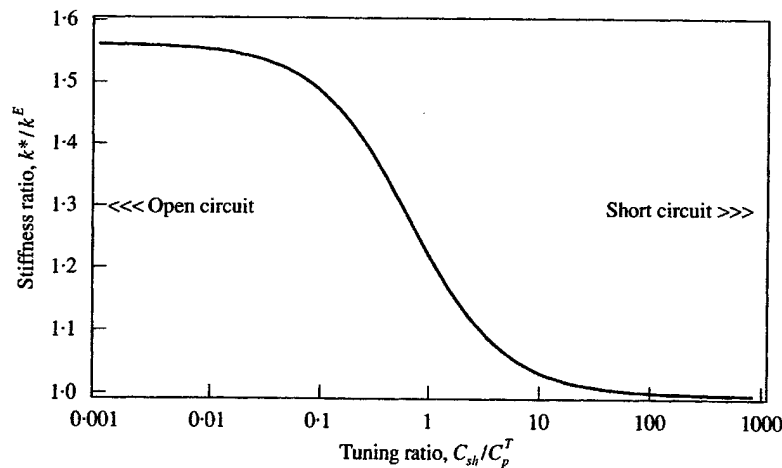


Figure 4. Effect of shunt capacitance on effective piezoceramic stiffness.

that roughly a four-order-of-magnitude change in shunt capacitance is necessary to effectively change from open to short circuit (or *vice versa*).

As mentioned previously, the total stiffness of a piezoceramic vibration absorber may be considered the sum of the effective tunable piezoceramic stiffness and the inherent stiffness of the device. The relative magnitudes of the two stiffnesses determine the net frequency change possible via electrical shunting.

An experiment was conducted using a commercially available piezoceramic inertial actuator as a passive, electrically shunted vibration absorber. Figure 5 shows a schematic of the device used for the experiments, PCB Model X712A02. The actuator (the lower flat cylinder in Figure 5) is approximately 2 in in diameter and approximately 3/8 in thick. The reaction mass is attached to its top by a standard 10-32 threaded stud, making it relatively easy to coarsely tune the device frequency by changing the mass. The base of the device also has a 10-32 threaded stud used for attaching it to a structure.

Note that the thickness and the radius of the piezoelectric element relative to that of the base metal disk was determined by design to maximize the device electromechanical coupling coefficient [8], and that this also maximizes the tuning range for this type of device configuration. Other device configurations might have higher device coupling coefficients and tuning ranges.

The purpose of the experiment was to measure the natural frequency and modal damping ratio of the device under a variety of capacitive shunt conditions ranging between short and open circuit. In the experiment, the device was attached to a shaker and accelerometers were used to measure both the input (i.e., the shaker) acceleration and the reaction mass acceleration. The ratio of the two acceleration measurements formed a frequency response function which was then curve-fit to approximate the natural frequency and modal damping ratio of the actuator for a given shunt condition. The electrodes of the inertial actuator were attached to a solderless breadboard where discrete values of capacitance could be used to shunt the device.

The results of the passive shunting experiment verified the ability to predictably tune the natural frequency of the piezoceramic vibration absorber between a short-circuit natural frequency of 313 Hz and an open-circuit natural frequency of 338 Hz. The resulting change in natural frequency was approximately 7.5% from short to open circuit. Next,

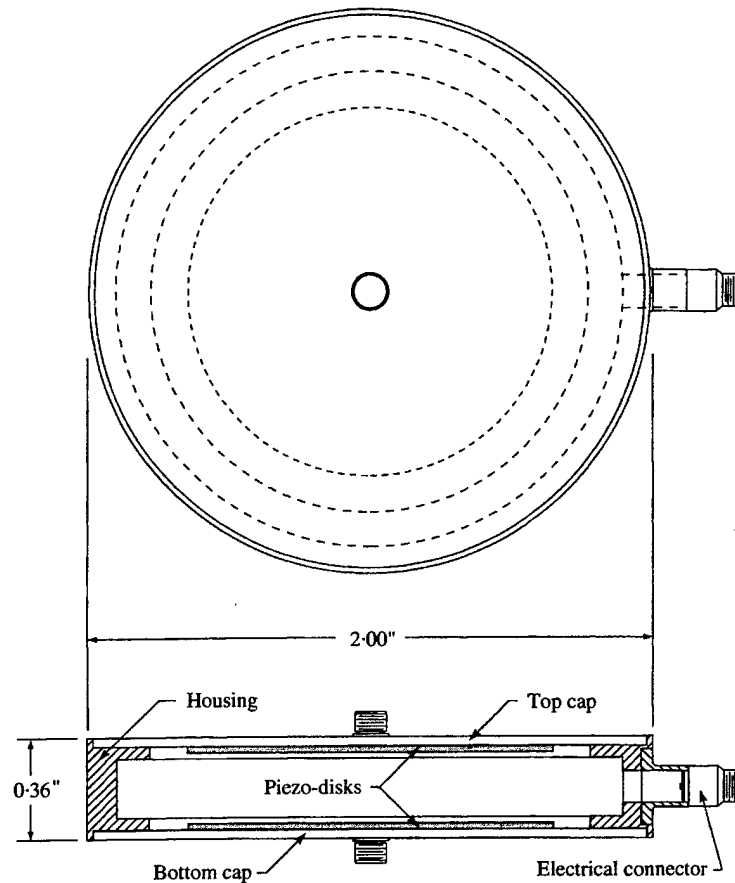


Figure 5. Schematic of the PCB Model X712A02 inertial actuator.

a frequency tuning control method for the shunted piezoceramic vibration absorber was developed.

### 3. ACTIVE TUNING CONTROLLER

The preceding section showed that the natural frequency of a vibration absorber that uses a piezoelectric stiffness element can be passively tuned with an external capacitive shunt circuit. This section describes the approach used to implement an active tuning method.

#### 3.1. CONCEPT

Consider a flexible structure with several well-spaced structural modes of vibration subjected to a tonal disturbance. Attaching a conventional passive vibration absorber to the structure, tuned to the tonal disturbance frequency, would reduce structural response at that frequency. Thus, as long as the disturbance frequency remained constant, a high level of attenuation would be achieved (i.e., structural vibration would be minimized). If, however,

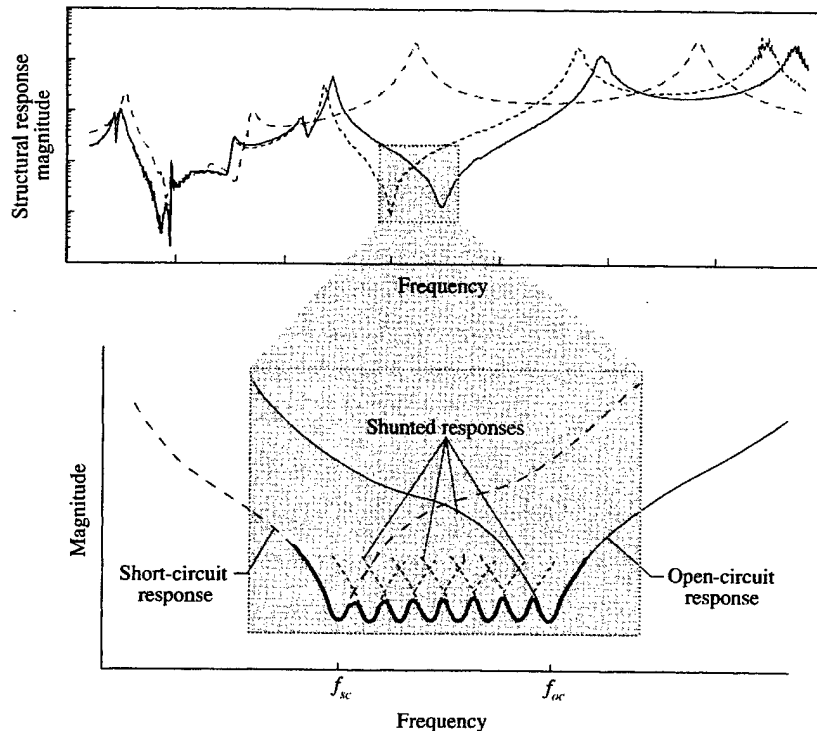


Figure 6. Conceptual tuned vibration absorber structural response: — — —, no absorber; ---, short circuit; —, open circuit.

the total disturbance frequency changed, performance would decrease (i.e., the vibration level would increase). Therefore, it would clearly be beneficial to have a tunable vibration absorber and a tuning method to track a changing disturbance frequency and appropriately re-tune the frequency of the absorber.

Developing a tuning method for the vibration absorber involved three steps: first, an appropriate system signal was identified, from which the desired tuning frequency could be estimated. Next, a method for actually estimating the frequency of structural vibration from the signal was developed. The final step involved formulating a control scheme to determine and provide the proper shunt capacitance.

The concept of monitoring the disturbance frequency and tuning the absorber to maintain minimum structural response is illustrated in Figure 6. The upper plot represents the broadband structural response for a structure both with and without an attached vibration absorber. The highlighted area of the upper plot is enlarged in the lower portion of Figure 6 to show the transfer function zeros (or minima) created by the addition of a short-circuit, shunted, and open-circuit vibration absorber to the structure.

First, consider the case when the piezoceramic element within the vibration absorber is short circuited (indicated by the dashed line in the highlighted section in the lower plot of Figure 6). If a tonal disturbance acted on the structure at a frequency equal to  $f_{sc}$ , the structural response would be minimal. If the disturbance frequency were to decrease while the PIA remained short circuited, the structural response would increase. Similarly, if the disturbance frequency were to increase to the frequency  $f_{oc}$ , while the piezoelement remained short circuited, the structural response would again increase. However, if the absorber were "re-tuned" by adjusting the electrical shunt impedance to an open-circuit

condition, the structural response would remain minimal. In addition, if the disturbance frequency were to fall anywhere between  $f_{sc}$  and  $f_{oc}$ , there exists a shunt impedance that will deliver minimum structural response.

Consider the following situation: a structural mode is excited by a pure tone harmonic disturbance which varies in frequency by a few percent of some nominal frequency. In principle, a piezoelectric vibration absorber could be added to the structure such that at a shunt tuning ratio of one, the natural frequency of the absorber would be equal to the nominal disturbance frequency (i.e., the natural frequency of the absorber for a tuning ratio of one is half-way between  $f_{sc}$  and  $f_{oc}$ ). If sensing (in the form of determining the frequency of the disturbance), control (in the form of a command signal based on the sensed frequency to alter the electric shunt impedance), and actuation (in the form of a means to alter the electrical shunt condition) were provided, then a minimum structural response could be maintained within the band defined between the open- and short-circuit frequencies.

The heavy solid line in Figure 6 illustrates the conceptual response of a discretely tuned vibration absorber. In this illustration, the shunt capacitance does not vary smoothly between  $f_{sc}$  and  $f_{oc}$ , but instead is discretized. Thus, determining a means to estimate the disturbance frequency, choosing the correct value of shunt impedance based on the estimated frequency, and physically changing the shunt impedance are the main subject of the next section. Two important questions to be addressed are: (1) what sensor(s) could be used and (2) once a sensed signal is acquired, how can frequency information be extracted from it?

### 3.2. IMPLEMENTATION

It is clearly desirable to try to use the fewest number of sensors in order to reduce control system complexity, weight, and power consumption. With this in mind, a method for sensing the tonal disturbance frequency based on the voltage produced by the piezoceramic within the PIA was developed.

Assuming a linear model for the coupled structure/absorber system, the voltage produced by the piezoceramic elements within the absorber is directly proportional to the piezoceramic strain and the shunt circuit electrical impedance. Thus, for an open-circuit vibration absorber being forced near resonance, the piezoelements would be under considerable strain due to the motion of the reaction mass (and corresponding small motion of the attached structure), producing considerable voltage. If, however, the vibration absorber were short circuited, there would be no measurable voltage across its terminals. Instead, short-circuiting would produce a large current (for the same forcing conditions). Thus, because shunting the absorber can vary the electrical impedance of the device from nearly short circuit to nearly open circuit, using the electrical state of the piezoceramic to estimate vibration frequency can only be effective if both voltage and current are used as sensor variables.

For the prototype system described here, a control system was used in which the A/D conversion process required voltages within a prescribed range. Thus, it was necessary to convert the current to a corresponding voltage. The current estimation process was realized using an op-amp as an ideal current-to-voltage converter [12].

The controller used for tuning the vibration absorbed is shown in Figure 7. The controller used two inputs and one output. The inputs were the voltage,  $V_v$ , and a voltage proportional to the current  $V_i$ . The output was a voltage proportional to the tuning impedance of the shunt circuit. The main elements of the controller were: (1) the band-pass filters (2) the frequency estimation logic and (3) the control voltage calculation.



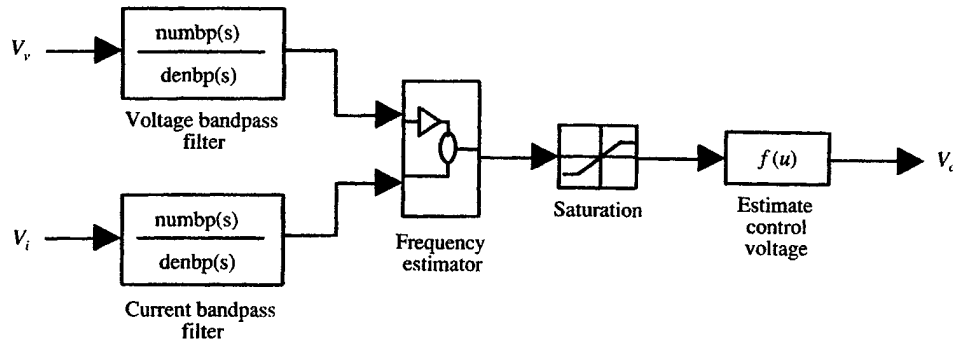


Figure 7. Control system block diagram.

The band-pass filters removed any DC-component of the input signals and attenuated high-frequency noise. The filters were second order with low and high cut-off frequencies of approximately 130 and 780 Hz respectively. Note that for the prototype system, the frequency range of interest (i.e., the range of frequencies defined by the short- and open-circuit resonance frequencies of the absorber) was approximately 290–350 Hz. Thus the pass-band encompassed the range of interest well.

The filtered signals were next used to estimate the frequency of the tonal disturbance. For the prototype version, frequency estimation was done by the control computer. For increased performance, analog circuitry could be implemented in the form of a phase-locked loop to convert the sensed voltages to a voltage proportional to frequency for use by the control system.

With a proper estimate for the frequency of vibration, the remaining task of the controller was to calculate an appropriate control voltage with which to vary the shunt impedance. Before the controller could be programmed, however, it was necessary to determine a method for physically altering the shunt capacitance. Recall that in Figure 4, the effective tuning ratio range for capacitive shunting is roughly 0.01–100 times the capacitance of the vibration absorber measured at constant stress. The measured capacitance of the prototype system at constant stress was approximately 0.072  $\mu\text{F}$ . Therefore, to tune the natural frequency of the PIA between  $f_{sc}$  and  $f_{oc}$ , a shunt capacitance range of roughly 0.7 nF to 7  $\mu\text{F}$  was required.

Variable capacitors do exist. However, the majority of variable capacitors have relatively small ranges (e.g., even a range of 12–100 pF is not common) and must be tuned by physical means. Programmable capacitors also exist, but due to their added complexity and resistance, they were not considered for the prototype system. Instead, a "ladder" circuit of discrete capacitors wired in parallel was used to tune the vibration absorber.

The effect of placing capacitors in parallel is a net capacitance equal to the sum of the individual capacitances. Figure 8 illustrates a conceptual shunt circuit with several parallel capacitors. If the frequency tuning band of the shunted absorber were discretized into a finite number of capacitive impedances, a control law could be developed to select a number of parallel capacitors whose sum would be the net electrical impedance needed to tune the actuator very close to the estimated disturbance frequency. Clearly, the number of discrete capacitance values used in a specific application will depend on the overall size of the frequency tuning range, the intrinsic damping of the absorber, and the acceptable deviation from minimum response. Finer discretization of the tuning band will yield a more uniformly low system response.

Consider a discretized shunt circuit with 10 discrete capacitance levels ranging from approximately 0.7 nF to 7  $\mu\text{F}$ . Ideally, each discrete shunt capacitance will tune the

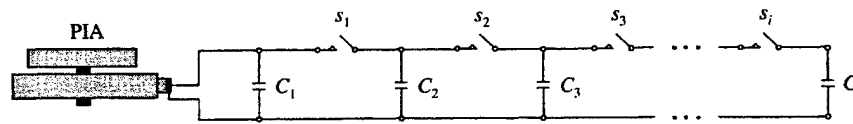


Figure 8. Conceptual "ladder" capacitive shunt circuit.

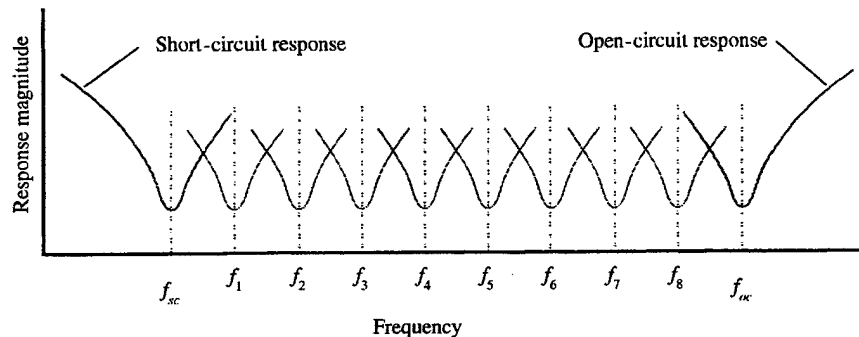


Figure 9. Frequency band shunt discretization.

absorber such that structural response will be a minimum for a prescribed frequency within the control bandwidth. Thus, the tunable frequency band was divided into nine frequency bands between the short- and open-circuit natural frequencies of the absorber, as shown in Figure 9.

The frequencies at the minima of each frequency band (labeled as  $f_{sc}$ ,  $f_1$  through  $f_8$ , and  $f_{oc}$  in Figure 9) define frequencies at which the cumulative combinations of shunt capacitance prescribe the shunted natural frequency of the absorber. First, consider the open-circuit shunt case. The open circuit corresponds to a very small (or zero) shunt capacitance. Thus if the capacitor  $C_1$  in Figure 8 were very small (or removed) and all switches were open, the absorber would be in an approximately open-circuit shunt condition (i.e., the natural frequency of the absorber would equal  $f_{oc}$ ). Next, consider closing the switch  $s_1$  in Figure 8. The net capacitance of the shunt circuit increases to the sum of  $C_1$  and  $C_2$ . Conversely, the natural frequency of the absorber decreases to  $f_8$  (assuming  $C_1$  and  $C_2$  are chosen correctly). Similarly, closing switches  $s_1$  and  $s_2$  will increase the net shunt capacitance to the sum of the  $C_1$ ,  $C_2$  and  $C_3$  and the absorber natural frequency (and thus the frequency of minimum structural response) will decrease to  $f_7$ . Closing all of the switches will increase the net shunt capacitance to the total of all of the capacitors in the ladder circuit. Thus, if  $C_1$ – $C_i$  are chosen correctly, the sum of all the capacitors will be large enough to approximate a short-circuit shunt condition (i.e., the total parallel capacitance will be greater than or equal to  $100 \times C_p^T$ ). The question remains, however, as to how to open and close the switches in the ladder circuit.

The switches in the shunt circuit shown in Figure 9 determine the number of capacitors in parallel with the absorber. Ideally, these switches would operate in response to a prescribed signal from the control system. In doing so, however, the switches should not introduce any additional electrical impedance into the shunt circuit. A relay provides one possible solution to this problem.

The control voltage,  $V_c$ , shown in Figure 9, is used to turn the relays on in succession. Variable resistors wired between each relay driver circuit were adjusted such that for  $V_c = 1$  V, relay #1 would turn "on" while others would remain "off". For  $V_c = 2$  V, relays

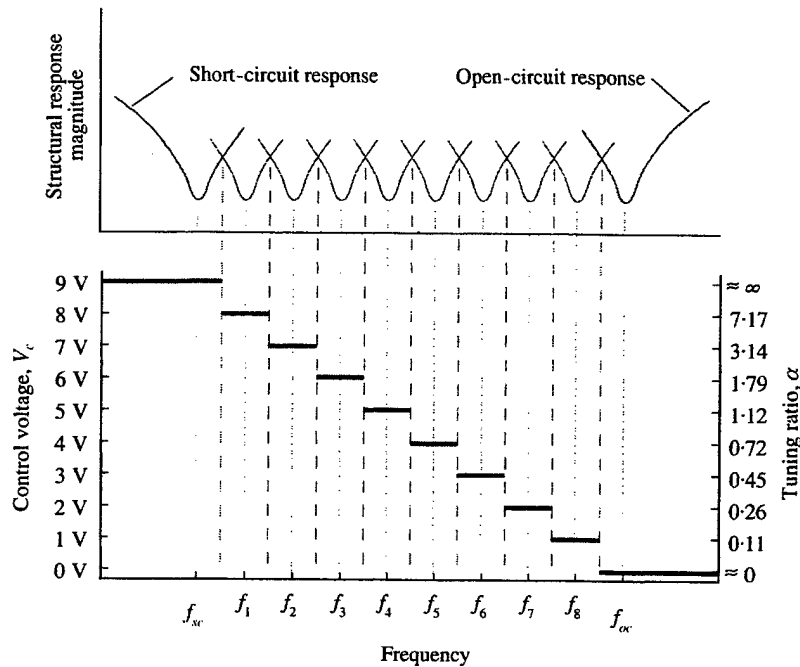


Figure 10. Control voltage to structural response correlation.

#1 and #2 would turn "on" while the other relays would remain "off". Similarly, more relays would turn "on" while the remaining relays remained "off" for increasing integer voltage levels up to and including 9 V. What remained was to program the control logic to output discrete integer voltage levels corresponding to desired shunt capacitance levels. Note that discrete voltage outputs were required to ensure the appropriate relays in the switching circuit were either "on" or "off".

Figure 10 illustrates the correlation between control voltage,  $V_c$ , absorber capacitive tuning ratio,  $\alpha$ , and the frequency of minimum structural response. From Figure 10 it is clear that, for a control voltage of 0 V, no transistors are "on" and thus the absorber is shunted with one capacitor,  $C_1$ . As stated earlier, if  $C_1$  is sufficiently small (say approximately  $0.01 \times C_p^T$ ), the absorber will behave as if it were open circuited. For a control voltage of 1 V, the first transistor turns "on" and the shunt capacitance is increased from  $C_1$  to the sum of  $C_1$  and  $C_2$ . If  $C_2$  equal  $0.1 \times C_p^T$ , the net tuning ratio would be approximately 0.11 and the natural frequency of the absorber and therefore the frequency of minimum structural response would be  $f_8$ .

As shown in Figure 10, varying the control voltage,  $V_c$ , from 0 to 9 V changes the frequency of minimum structural response from approximately the open-circuit natural frequency to approximately the short-circuit natural frequency. Referring to the control system block diagram, in Figure 7, the *estimate control voltage* block contains the code to convert the estimated disturbance frequency to an appropriate control voltage.

#### 4. TUNING CONTROL EXPERIMENTS AND RESULTS

Several experiments were designed to evaluate the effectiveness of the tunable piezoceramic inertial actuator. In the experiments, a representative structure (a

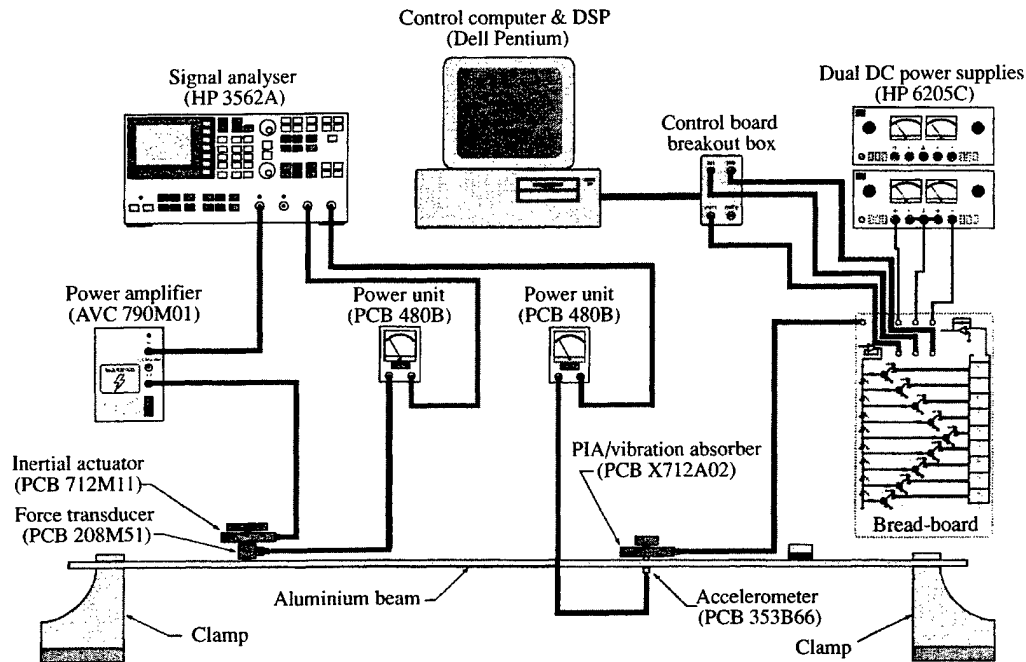


Figure 11. Experimental set-up.

clamped-clamped beam) was driven with a tonal force disturbance. First, structural acceleration measurements were taken both with and without the passive absorber attached to the structure. Measurements in which the absorber was both short and open circuited were used to define the effective tuning bandwidth for the shunt control system. Finally, a sine sweep was used to vary the disturbance frequency from just below the absorber short-circuit natural frequency to just above the absorber open-circuit natural frequency for the short circuit, open circuit, and actively tuned cases.

Figure 11 shows the experimental set-up for the semi-actively tuned vibration absorber experiments. The representative structure was a  $0.913 \times 0.038 \times 0.006$  m aluminum beam rigidly fixed at both ends. An inertial actuator placed 10 cm from the left end of the beam was used to apply a disturbance force to the structure. The drive signal for the actuator was generated by a Hewlett-Packard 3562A signal analyzer and amplified using a PCB/AVC high-power charge amplifier. A dynamic force transducer placed between the actuator and the structure measured the force applied to the structure, while a high-sensitivity accelerometer located 30 cm from the right side of the beam measured the dynamic response of the beam at the absorber location. Both the force transducer and the accelerometer signals were amplified via portable power units and then recorded by the HP signal analyzer. The analyzer was also used to process the force and acceleration signals to calculate acceleration FRFs.

Figure 12 shows the response of the system both with and without the vibration absorber attached to the clamped-clamped beam. The response of the system with no absorber attached has a prominent structural resonance at approximately 318 Hz. Clearly, the passive absorber significantly reduced the structural response in the neighborhood of the original structural resonance, and the frequency at which minimum structural response was obtained varied with the value of the electrical shunt. Also note that, because the absorber itself is lightly damped, the region of low response is bracketed by two regions of relatively

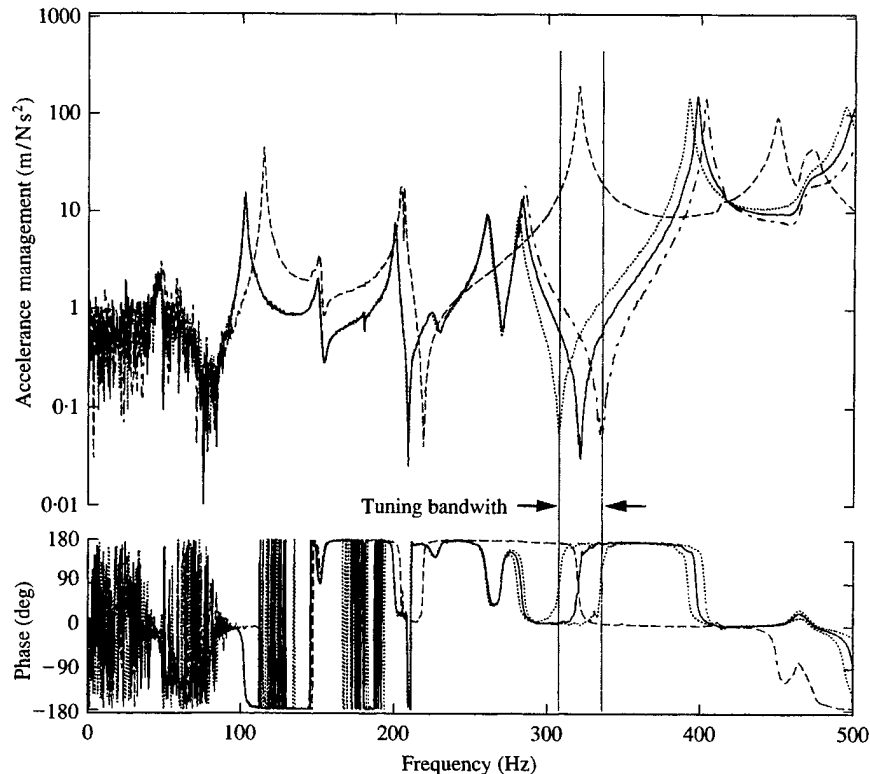


Figure 12. Accelerance for structure with passive tunable absorber. Forcing voltage 12.6 V sweep rate 312.5 Hz/s: —, no absorber; ----, short circuit; ····, matched ( $\alpha = 1$ ); - · - ·, open circuit.

high response. This feature makes a lightly damped tunable vibration absorber most suitable for application to structures driven by variable frequency tonal disturbances.

In addition to the open- and short-circuit measurements (i.e., measurements taken for tuning ratios of 0 and  $\infty$  respectively), the accelerance was also measured for a tuning ratio of 1.0. The response for  $\alpha = 1$  defined the nominal or "control off" condition. In practice, a nominal disturbance frequency would be identified and the mass of the vibration absorber would be selected such that for  $\alpha = 1$ , minimal structural response would occur at the nominal disturbance frequency.

Next, the actuator was connected to the tuning circuit, which was implemented on an electronic breadboard. The breadboard was also connected to the real-time control computer to supply PIA voltage and PIA current estimates and receive shunt control voltages. The op-amps and relays used for the switching circuit were powered with Hewlett-Packard DC power supplies.

The control computer used for the experiments was a 100 MHz Dell Pentium. The Pentium housed a dSPACE DS1102 Floating-Point Controller Board with Texas Instruments TMS320P14 processor chip. The two A/D channels of the controller board had an input voltage range of  $\pm 10$  V and used 16-bit converters. The D/A channel had an output voltage range of  $\pm 10$  V and used a 12-bit converter. MATLAB's Real-Time Workshop was used to translate a SIMULINK block diagram into C-code, then to invoke the TI C-compiler. The compiled C-code was then downloaded to the processor on the controller board. The controller was designed and set to sample at 10 kHz which adequately accommodated the simulation of the analog linear filters.

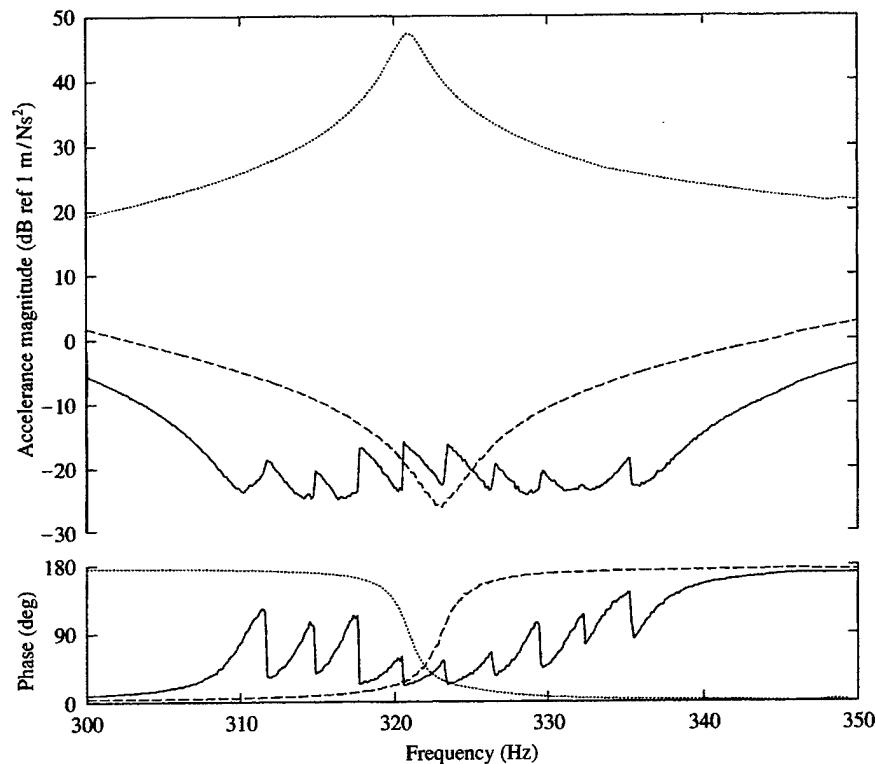


Figure 13. Actively tuned versus passive structural acceleration: - - - -, no absorber; - - -, passive, matched ( $\alpha = 1$ ); —, actively tuned.

To gain a more accurate estimate of the passive and semi-active response of the system, swept sine measurements were made between 300 and 350 Hz. Note that the sweep rate for the measurements was set sufficiently low to ensure that the filters within the controller had time to settle before the analyzer moved to the next frequency in the sweep.

Figure 13 illustrates the effects of using a semi-active piezoceramic vibration absorber on structural acceleration due to a varying-frequency tonal disturbance. The dotted line in Figure 13 is the passive structural acceleration (i.e., structural response with a constant  $\alpha = 1$ ). The solid line is the structural acceleration with the tuning controller turned on (i.e., structural response with a variable  $\alpha$ ). The changing discrete capacitances are evidently effective in increasing minimum acceleration over the previously defined tuning band. In addition, structural acceleration at frequencies below the short-circuit frequency of the absorber and above the open-circuit frequency of the absorber was improved.

Figure 14 shows the difference (in dB) between the passive and active responses. Maximum increases in performance of about 20 dB occurred at both the short- and open-circuit absorber natural frequencies. On average, an approximately 10 dB increase in performance was obtained over the frequency range shown ( $\pm 7\%$  change in frequency from the center frequency of 325 Hz). A slight decrease in performance, however, was observed in a small frequency range in the center of the tuning band. This was attributed to the fact that the discretized shunt capacitance was not quite equal to the absorber capacitance measured at constant stress (i.e.,  $\alpha = 1$ ) at the tuning band center frequency.

Note that the speed of the control system was limited by the speed of the filters used in the control system. The electronics used to adjust the shunt capacitance operated very quickly

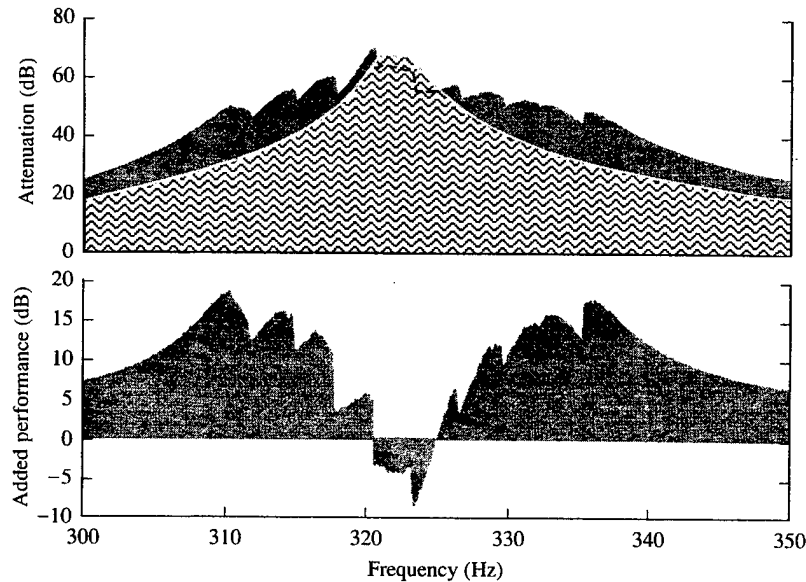


Figure 14. Actively tuned vs. passive structural attenuation performance; ■, actively tuned; ▨, passive.

compared to the filters. Thus, proper tuning was achieved as soon as the filters settled and the proper disturbance frequency was estimated. The rate of re-tuning due to a change in disturbance frequency was limited by the disturbance frequency estimation method. Small changes in disturbance frequency, less than about 11% of the tuning band, were effectively compensated in less than 60 ms. Detecting, then completely switching the absorber from short to open circuit, or *vice versa*, required less than 250 ms. A complete discussion of the effects of control speed as well as variations due to changing forcing amplitudes can be found in reference [11].

## 5. CONCLUSIONS

A solid-state tunable semi-active piezoceramic vibration absorber was developed. Electrically shunting a piezoelectric inertial actuator with a capacitive electrical impedance changed a fraction of the effective net stiffness of the device, thus changing the device's natural frequency. The control system used to tune the absorber monitored the voltage and current produced by the device to estimate a tonal structural vibration frequency and in turn adjust the net discrete shunt capacitance appropriately.

The semi-active vibration absorber had a  $\pm 3.7\%$  tunable frequency band relative to the center frequency. Additional attenuation effects extended beyond  $\pm 7\%$  of the center frequency. Within the tuning band, increases in performance beyond passive performance were as great as 20 dB, and the average increase was over 10 dB.

This combination of tunable vibration absorber and active tuning method has several features that distinguish it from, and give it potential advantages over, others described in the literature. First, it is a piezoelectric-based device. Second, it uses capacitive shunting to accomplish an effective change in stiffness. Third, it is less complex than comparable devices, because it is completely solid state. Fourth, it requires no additional sensors, as the voltage and current signals generated in the piezoelectric elements may be used directly. Fifth, it has relatively low-power consumption relative to other PVA tuning methods; the

electrical power required for shunt-circuit switching is far less than the power required for driving stepper-motors or heating viscoelastic materials. Furthermore, the tuning controller was novel in that it could be implemented as a completely solid-state analog system. Achieving this would require performing the frequency estimation and control voltage calculation in hardware instead of software. Frequency estimation could be accomplished using a phase-locked loop (PLL) circuit [11, 13]. PLLs require little power, react quickly, and are commercially available in compact integrated circuit packages. The output of the PLL is a DC voltage directly proportional to frequency, thus making the control voltage calculation largely a matter of scaling.

#### ACKNOWLEDGMENTS

This work was supported by the Office of Naval Research under MURI Grant N00014-96-1173 (Acoustic Transduction).

#### REFERENCES

1. J. F. UNRUH 1988 *AIAA Journal of Aircraft* **25**, 752-757. Structure-borne noise control for propeller aircraft.
2. C. D. JOHNSON 1995 *Journal of Vibration and Acoustics* **117**, 171-176. Design of passive damping systems.
3. B. G. KORENEV and L. M. REZNIKOV 1993 *Dynamic Vibration Absorbers*, 237-242. New York: Wiley & Sons.
4. E. WATERMAN, D. KAPTEIN and S. SARIN 1983 *Proceedings of the SAE Business Aircraft Meeting & Exposition*, Wichita, KS, SAE Paper No. 830736. Fokker's activities in cabin noise control for propeller aircraft.
5. W. HALVORSEN and U. EMBORG 1989 *Proceedings of the SAE General Aviation Aircraft Meeting & Exposition*, Wichita, KS, SAE Paper No. 891080. Interior noise control of the Saab 340 aircraft.
6. M. LAVITT 1997 *Aviation Week & Space Technology*, 24 February, 68. IPN international product news: active absorbers cancel aircraft engine noise.
7. F. FLORINO 1997 *Aviation Week & Space Technology*, 28 April, 15. Airline outlook: DC-9 noise absorbers.
8. J. DOSCH, G. LESIEUTRE, G. KOOPMANN and C. DAVIS 1995 *Proceedings of the SPIE Smart Structures and Materials Conference*, San Diego, CA, SPIE-2447, 14-25. Inertial piezoceramic actuators for smart structures.
9. D. J. MEAD, *Passive Vibration Control* 1998. Chichester, New York: Wiley & Sons.
10. C. DAVIS, G. LESIEUTRE and J. DOSCH 1997 *Proceedings of the SPIE Smart Structures and Materials Conference*, San Diego, CA, SPIE-3045, 1-2. A tunable electrically shunted piezoceramic vibration absorber.
11. C. DAVIS 1997 *Ph.D. Thesis, Department of Aerospace Engineering, The Pennsylvania State University, University Park, PA*. A tunable piezoceramic vibration absorber.
12. P. HOROWITZ and W. HILL 1994 *The Art of Electronics*, 184. Cambridge: Cambridge University Press, second edition.
13. C. NIEZRECKI and H. CUDNEY 1997 *Journal of Vibration and Acoustics* **119**, 104-109. Structural control using analog phase-locked loops.



# **APPENDIX 78**

# Enhanced Low Frequency Transmission Loss of Light Weight Trim Panels Using PZT Inertial Actuators

WENCHAO HUANG,<sup>1</sup> GARY H. KOOPMANN,<sup>2,\*</sup> STEPHEN J. SHARP<sup>2</sup> AND WEICHENG CHEN<sup>2</sup>

<sup>1</sup>*Aircraft Structure Research Institute, Xi'an, P.R.C*

<sup>2</sup>*Center for Acoustics and Vibration, Penn State University, 157A Hammond Bldg., University Park, PA 16802*

**ABSTRACT:** One method of enhancing the low frequency transmission loss of noise into the cabin of a propeller driven aircraft or helicopter is to replace selected sections of the interior trim with stiff, ultra light panels that are driven with PZT inertial actuators. Given the proper control signals, the panels can be driven by the actuators such that their net volume velocity is minimized. Experiments are described that measure the sound transmission loss for a soft mounted, double layer corrugated aluminum panel driven by four actuators consisting of symmetrically-mounted, cantilevered beams with end masses driven by unimorph piezoelectric elements. A feedback control system is designed by serially connecting three Tow-Thomas biquad filters which are based on a Motorola LF347N integrated circuit design. Using this simple analog controller with the panel's accelerations as an input, experimental results show that the inertial actuators mounted at the center of the panel produce up to 13 dB improvement in both vibration reduction and noise transmission loss of the panel.

## INTRODUCTION

PASSIVE designs to increase the noise transmission loss (TL) of light-weight, aircraft trim panels in the low to mid frequency ranges encounter physical limitations governed by the mass law. Some work has been carried out to improve the acoustic performance of lightweight panels by increasing the thickness of panels, number of stiffeners, etc. [1,2], but few such designs have proved practical enough to be commercially viable. Further, it has been shown that absorption treatments, such as fiber glass, have little effect on the TL at these low frequencies [3]. While honeycomb sandwich panels and corrugation panels have improved TL performance at low frequencies because of their high strength to mass ratio [4,5], this improvement is often offset by structural resonances that occur within the TL band and thus it is difficult to achieve large TL's with these designs using only passive noise control technologies.

If the structural resonances of these types of panels are actively controlled, the resonance problem could be obviated and such a hybrid design could prove to be an effective method for reducing the low frequency noise in cabins of propeller-driven aircraft and helicopters. One method for enhancing the low frequency TL into say, a tiltrotor cabin, would be to replace selected sections of the interior trim panel with ultra-stiff, ultra-light panels that are driven with inertial actuators. Research has demonstrated that inertial shakers embedded in individual trim panels generate the necessary control forces on the panels to minimize the sound

transmission [6]. Given the proper control signals, the panels could be driven by the actuators such that their net volume velocity is minimized [7-9]. For this method to be practical, the trim panels need to be designed such that their structural bending modes occur at frequencies well above the range where the TL is to be enhanced actively. Meeting this requirement insures that the panel motion in the frequency range of control is of the rigid body type that produces well-defined, volume velocity patterns.

## PRELIMINARY COMMENTS

The main goal of this research is to enhance the noise transmission loss of a light-weight trim panel. The panel used in this study is nearly rigid over the frequency range of interest and consequently, the panel vibrates in piston-like and/or rocking motion when acoustically excited. It is well known that at low frequencies, the radiation from a rigid body panel is dominated by the piston-like mode (i.e., the main volume displacing mode). The design goal of the actuator is, therefore, to actively constrain the vibration of the piston-like mode of the trim panel. When the actuator force is exerted at the center of the panel with the requisite magnitude and phase, the net force on the surface of the panel is nearly zero, thus preventing sound transmission through the panel. Therefore, by constraining the panel to vibrate as a rigid body, a reduction in transmission loss is achieved using only structural error sensors, eliminating the need for acoustic information to be included in the control design. This design approach simplifies the control design approach as compared to feedback control strategies based on active struc-

\*Author to whom correspondence should be addressed. E-mail: GHK1@psu.edu

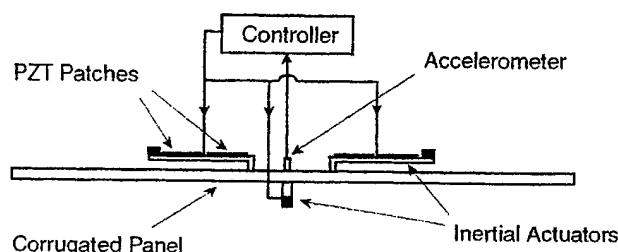


Figure 1. Diagram of active control system concept.

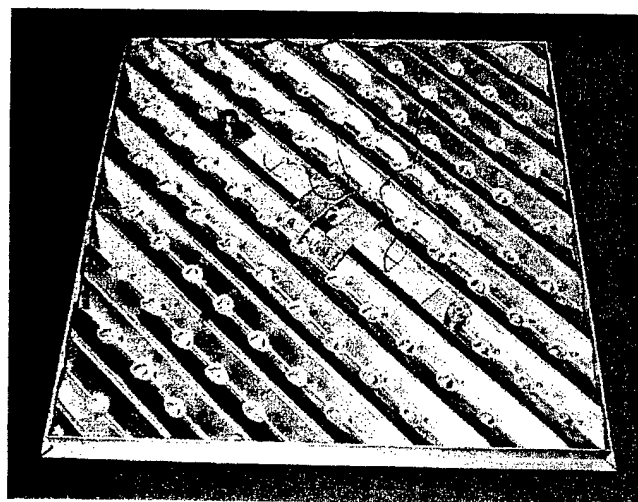


Figure 2. Photograph of corrugated trim panel with PZT inertial actuators.

tural acoustic control [10–13] and radiation modal control [14,15].

Vibration control of the panel is achieved with PZT inertial mass actuators located near the center of the trim panel. The actuators location is chosen to most efficiently control the motion of the piston-like mode. These actuators consist of symmetrically-mounted, cantilevered beams (with end masses) driven by unimorph piezoelectric elements. The feedback controller is designed by serially connecting three Tow-Thomas biquad filters which are based on Motorola LF347N integrated circuit design. The input to the controller is the acceleration response at the trim panel's center (Figure 1). When compared with other active structural acoustic control (ASAC) strategies, which generally require MIMO (distributed control), the one presented in this research is based on SISO (local control) and thus is more economical and easy to use.

For the TL measurements, a transmission loss facility is used which connects a reverberation chamber to an anechoic receiving chamber through a common opening containing the panel. A two-microphone intensity probe is used to measure the total sound power radiated from the panel to the receiving room while incident sound power is measured in the reverberation room in terms of the spatial average of sound pressure level.

## TRIM PANEL AND ACTUATOR DESIGN

The panel used in this research is fabricated from two corrugated aluminum panels attached orthogonally to maximize bending stiffness (Figure 2). The panel is 18 inches per side and weighs approximately 1 lb/ft<sup>2</sup>. The first bending mode occurs above 275 Hz.

The design of the inertial actuator (Figure 2) consists of a mass loaded, cantilevered beam covered with a unimorph piezoelectric patch along its top surface. The inertial actuators are designed such that they have the first and second resonance frequency at 25 Hz and 285 Hz, respectively so that they produce control forces in the enhanced frequency range with flat response characteristics. Each control actuator weighs only 45 g and produces 0.1 N force in the TL frequency range. One pair of actuators is mounted on the front side of the panel (symmetrically to balance their bending moments) with a second pair mounted on the rear side. Each pair is driven with the same feedback control signals but of opposite polarity to sum the control forces in the same direction.

## CONTROLLER DESIGN

The control system is a SISO feedback controller whose error signal is the acceleration at the panel's center. Before designing the feedback control system, a mathematical model of the given plant is generated. For this, experimental data for system identification are obtained by measuring the

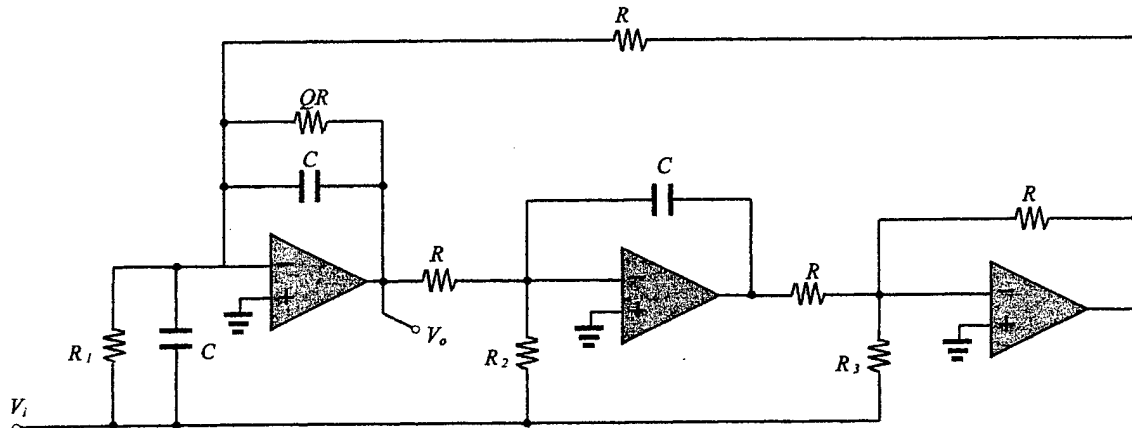


Figure 3. Circuit diagram of Tow-Thomas filter.

transfer function of the secondary plant driven by the four inertial mass actuators. The frequency response data is then curve fitted using a least-squares method. After the plant model is identified, pole and zero representations are used to design the controller.

The feedback controller can be assumed to be a  $n$ th order pole zero model as

$$H_c(s) = \frac{k(s - z_1) \dots (s - z_n)}{(s - p_1) \dots (s - p_n)} \quad (1)$$

The goals of the controller are to generate a very large gain at the specific frequencies for the open loop transfer function, and to make the closed loop gain as low as possible over the controlled frequency range. This can be achieved with the following strategies. First, the poles of the controller are selected close to the imaginary axis on the left half of the  $S$  plane so that the damping ratios of the open loop transfer function are very low. This makes the magnitude of the open loop transfer function become large at the pole frequencies. Second, the zeros of the controller are selected far away from the imaginary axis to make the closed loop poles of the whole system have higher damping ratios as the controller gain  $k$  increases. The value of gain  $k$  may be limited by the stability condition of closed loop system and the saturation bound of the driving signal applicable for the actuator amplifier.

The analog control circuits are conducted by serially connecting three Tow-Thomas biquad filters which are based on a Motorola LF347N integrated circuit design [6]. The Tow-Thomas biquad filter is a second order filter whose mathe-

matical expression and the circuit diagram are shown in Equation (2) and Figure 3, respectively.

$$\frac{V_o}{V_i} = \frac{S^2 + S \frac{1}{C} \left( \frac{1}{R_1} - \frac{1}{R_3} \right) + \frac{1}{C^2 R R_2}}{S^2 + S \frac{1}{QCR} + \frac{1}{C^2 R^2}} \quad (2)$$

The values for resistors and the capacitors which are selected to implement the three biquad filters are listed in Table 1.

## TESTING PROCEDURE AND RESULTS

Initially, the transfer functions of the secondary plant driven by the four inertial actuators are measured. Figure 4 compares the measured results of the transfer function with the curve-fitted model. In the measured results, the first peak occurs at 25 Hz which corresponds exactly to the first resonance frequency of the actuator. For this particular study, the frequency range of interest (i.e., the enhanced TL range) is between 50 Hz and 150 Hz where the first resonance frequency of the panel occurs.

The panel is soft mounted in an opening between a reverberation chamber as the source room and an anechoic chamber as the receiving room. Figure 5 shows the block diagram for the experimental setup of the analog feedback control system. Figure 6 shows the comparison of the vibration magnitudes at the center of the panel with and without feedback control under broad-band acoustic excitation. The results in-

Table 1. Resistor and capacitor values used to implement the Tow-Thomas biquad filters.

	Zeros	Poles	C (nF)	R (k $\Omega$ )	QR (k $\Omega$ )	R <sub>1</sub> (k $\Omega$ )	R <sub>2</sub> (k $\Omega$ )
Section 1	$-800 \pm 600i$	$-250 \pm 1000i$	4.84	200.44	413.22	129.13	212.97
Section 2	$-800 \pm 600i$	$-280 \pm 380i$	4.85	719.59	412.37	128.87	59.08
Section 3	$-400 \pm 600i$	$-250 \pm 140i$	4.86	435.92	367.43	257.20	186.77

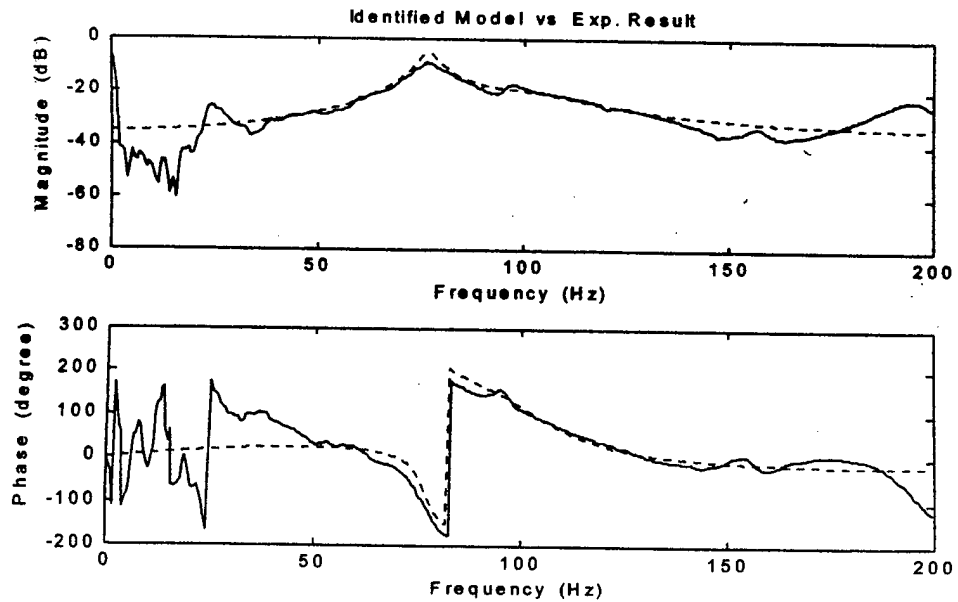


Figure 4. Measured transfer function (solid) and identified model (dashed).

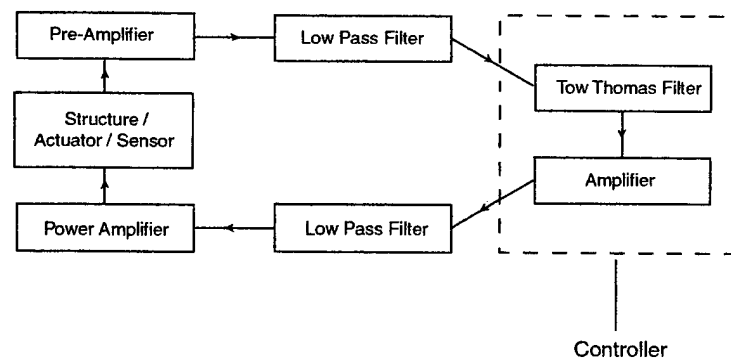


Figure 5. Schematic diagram of the experimental set-up.

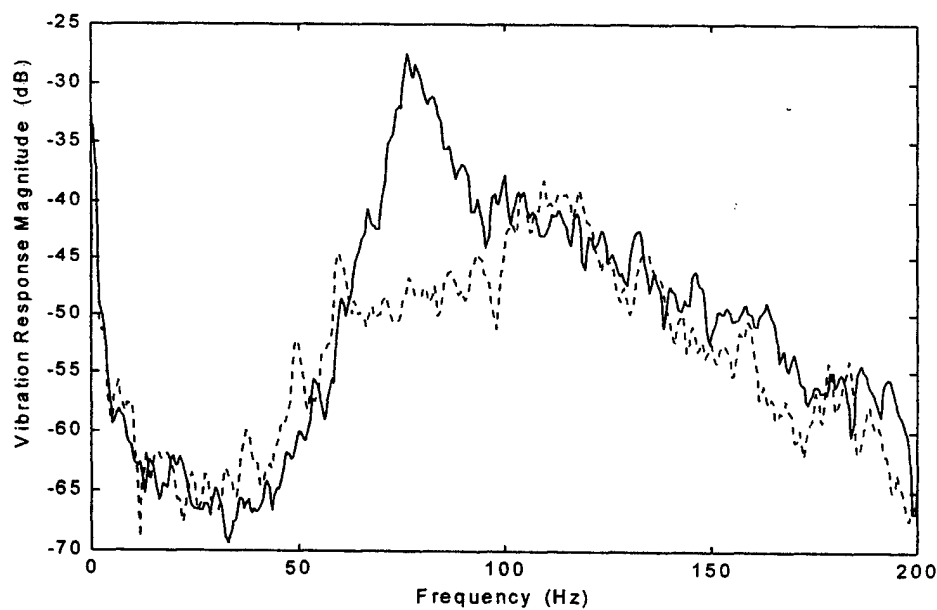


Figure 6. Vibration response with (dashed) and without control (solid).

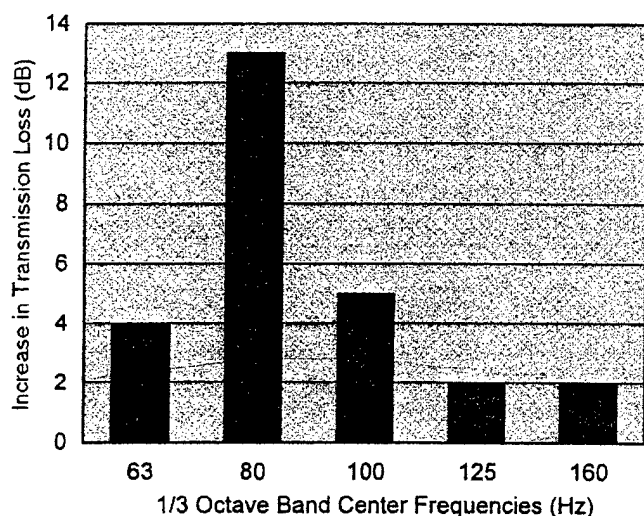


Figure 7. Enhancement of noise transmission loss with control.

indicate that more than 15 dB vibration reduction of acceleration at the resonance frequency of the panel is obtained with four actuators driven by the appropriate feedback control signal. Similarly, Figure 7 shows the comparison of the TL of the panel with and without feedback control under broadband acoustic excitation. The TL measurement indicates that up to 13 dB enhancement is possible in the 80 Hz 1/3 octave band, corresponding to the first resonance frequency of the panel. The noise TL was calculated from Equation (3) using the measurement results of the average sound pressure level in the source room and the sound power level transmitted through the panel to the receiving room and measured near the panel with a scanning acoustic intensity probe.

$$TL = SPL - PWL + 10 \log \left( \frac{S}{4} \right) \quad (3)$$

where  $SPL$  is the spatial average sound pressure level in the reverberation room,  $PWL$  is the sound power transmitted through the panel and  $S$  is the area of the panel.

## CONCLUSIONS

Low frequency enhancement of the transmission loss for an aircraft trim panel specifically designed to be lightweight and ultra-stiff was demonstrated using PZT driven inertial actuators and a simple analog feedback control for broadband acoustic excitation. The analog feedback controller has only one feedback signal of acceleration and drives four actuators with the same output signal. It was designed by serially connecting three Tow-Thomas biquad filters. The trim

panel was fabricated from two orthogonally joined, corrugated aluminum panels, such that the first structural resonance frequency was well above the enhanced TL range. Experimental results show that the inertial actuators mounted at the center of the panel produce up to 13 dB improvement in both vibration reduction and sound transmission loss by controlling the first rigid body resonance frequency of the panel which occurs at approximately 80 Hz.

Further research will be directed to demonstrating the control method with trim panels mounted on sections of an aircraft fuselage to confirm that the locally-controlled trim panels produce global reductions in overall sound power within the cabin.

## REFERENCES

1. Koval, L.R. (1997). Effect of stiffening on sound transmission in a cylindrical shell in flight. *American Institute of Aeronautics and Astronautics Journal*, 15, 899–900.
2. Vaicaitis, R. and Slazak, M. (1980). Noise transmission through stiffened panels. *Journal of Sound and Vibration*, 70(3), 413–426.
3. Lyle, K.H. and Mixson, J.S. (1987). Laboratory study of sidewall noise transmission and treatment for a light aircraft fuselage. *Journal of Aircraft*, 24(9), 660–665.
4. Huang, W.C., and Ng, C.F. (1997). Sound insulation improvement using honeycomb sandwich panels. *Applied Acoustics*, Vol. 53, No. 1–3, pp.163–177.
5. Hansen, C.H. (1993). Sound transmission loss of corrugated panels. *Noise Control Engineering Journal*, Vol. 40, No.2, 187–197.
6. Ho, Y.-R. (1998). Active control of broadband sound transmission through an airplane trim panel using hybrid feedforward and feedback techniques. *Ph.D. Thesis, The Pennsylvania State University*, 1998.
7. Thomas, D.R., Nelson, P.A., Elliott, S.J. and Pinnington, R.J. (1993). An experimental investigation into the active control of sound transmission through stiff light composite panels. *Noise Control Engineering Journal*, Vol. 41, No.1, 273–279.
8. St. Pierre, R.L., Koopmann, G.H. and Chen, W. Volume velocity control of sound transmission through composite panels. *Journal of Sound and Vibration*, 210(4), 441–460.
9. Sharp, S.J., Koopmann, G.H. and Chen W. (1997). Transmission loss characteristics of an active trim panel. *Proceedings of Noise-Con 97*, 149–160.
10. Baumann, W. T., Saunders, W. R. and Robertshaw, H. H. (1991). Active suppression of acoustic radiation from impulsively excited structures. *Journal of the Acoustical Society of America* 90(6), 3202–3208.
11. Baumann, W. T., Ho, F.-S. and Robertshaw, H. H. (1992). Active structural acoustic control of broadband disturbances. *Journal of the Acoustical Society of America* 92(4), Pt.1 1998–2005.
12. Clark, R. L., Saunders, W. R. and Gibbs, G. P. (1998). *Adaptive Structures*. New York, NY: John Wiley & Sons, Inc.
13. Thomas, D. R. and Nelson, P. A. (1995). Feedback control of sound radiation from a plate excited by turbulent boundary layer. *Journal of the Acoustical Society of America* 98(5), 2651–2662.
14. Griffin, S., Hansen C. and Cazzolato, B. (1999). Feedback control of structurally radiated sound into enclosed space using structural sensing. *Journal of the Acoustical Society of America* 106(5), 2621–2628.
15. Gibbs, G. P., Clark, R. L., Cox, D. E. and Viperman, J. S. (2000). Radiation modal expansion: An approach to active structural acoustic control. *Journal of the Acoustical Society of America* 107(1), 332–339.

# **APPENDIX 79**

## Development and evaluation of a surface acoustic intensity probe

Patricia L. Driesch<sup>a)</sup>

*Center for Acoustics and Vibration, Pennsylvania State University, University Park, Pennsylvania 16802*

Hisao Iwata

*Nagoya R&D Center, Mitsubishi Heavy Industries, Ltd., Nagoya, 453-8515, Japan*

Gary H. Koopmann

*Center for Acoustics and Vibration, Pennsylvania State University, University Park, Pennsylvania 16802*

Jeff Dosch

*PCB Piezotronics, Inc., 3425 Walden Avenue, Depew, New York 14043*

(Received 14 April 2000; accepted for publication 28 July 2000)

Commonly, sound power radiated from vibrating machinery is measured either with a two-microphone intensity probe or in a reverberant chamber using a reference source. However, for sound source identification, it is difficult to isolate the sound power radiated from specific areas from the total sound power using these conventional methods. To facilitate this type of measurement, a type of intensity probe has been developed that measures sound intensity directly on the surface of a vibrating structure. It is comprised of an accelerometer and a microphone and requires a straightforward calibration which measures the phase shift in the microphone relative to the accelerometer. This is accomplished with a device that supports the probe on the top of a piezoelectric actuator and encloses both within a small cavity. This method provides a frequency-dependent phase correction for the microphone referenced to the accelerometer. For evaluation at low frequencies where the probe is most applicable, its performance compares favorably (to within 1 dB) with the two-microphone intensity probe measurement for the case of sound radiating from a square, clamped plate. © 2000 American Institute of Physics.

[S0034-6748(00)00811-X]

### I. INTRODUCTION

Sound power is a useful quantity for comparing and rating noise radiated by different machines or machine components. It has the benefit of quantifying a sound source with a single scalar value as opposed to sound pressure or vibration quantities, which are spatially dependent. Several different methods can be used to determine sound power depending on the acoustic environment and nature of the sound source. The method described herein is the surface acoustic intensity method, which computes sound power by a surface integral of acoustic intensity measured over a vibrating surface.<sup>1</sup>

Until the arrival of solid-state devices in the 1970s, accurate measure of the acoustic velocity component (based on pressure gradients) of acoustic intensity was difficult due to instrumentation and transducer limitations.<sup>2</sup> In 1977, independent investigations by Fahy<sup>3</sup> and Chung<sup>4</sup> served as the beginning for modern acoustic intensity methods. They formulated a cross-spectral method for calculating acoustic intensity using two microphones together with the fast Fourier transform analyzer. In that same year, Hodgson<sup>5</sup> successfully demonstrated the surface intensity technique using an accelerometer and a closely located microphone to measure sound power from a large centrifugal chiller. Other pioneering efforts also determined sound radiation from vibrating structures using surface vibration measurements in conjunction

with a microphone.<sup>6-8</sup> Over the last two decades, refinements of acoustic intensity measurements mainly have focused on the two-microphone intensity probe, but surface intensity techniques have also been improved as well. McGary and Crocker,<sup>9</sup> and Wäster and Crocker<sup>10</sup> give excellent overviews of the surface intensity technique, respectively. Surface intensity probes are designed to measure acoustic intensity on vibrating structures such as machine components, automobile engines, aircraft panels, etc. To make such measurements on these types of structures, some knowledge of the structure's modal response is necessary *a priori* to insure that a minimum spatial sampling criterion is met. Satisfying this requirement will be treated in detail later in this article. One advantage of the surface acoustic intensity probe over the two-microphone method is that the probe can measure sound intensity on surfaces that are often inaccessible to the larger, two-microphone probe apparatus. For example, the surface probe is particularly useful for noise ranking analysis in structures that have highly complicated geometry such as found in the engine compartment of an automobile.

The subject of this article is the development and evaluation of a probe that measures the acoustic intensity directly on a vibrating surface. The focus of this study was twofold. First, a practical method was devised to calibrate the probe and then, its performance was evaluated on a complex radiating structure. For this evaluation, the sound power radiating from a square, clamped plate at low frequencies was selected.

<sup>a)</sup>Electronic mail: pld112@psu.edu





FIG. 1. Photograph of surface intensity probe with a dime illustrating its small size.

Acoustic intensity is calculated from sound pressure and surface normal acceleration by simple manipulation of the definition for acoustic intensity. In the frequency domain, the time-averaged acoustic intensity normal to a surface  $I(\omega)$  is defined as one half the real part of the product of sound pressure  $P(\omega)$  and complex conjugate of normal surface velocity  $V^*(\omega)$ :

$$I(\omega) = \frac{1}{2} \text{Re}[P(\omega) \cdot V^*(\omega)]. \quad (1)$$

By substituting the cross spectrum of pressure and acceleration in Eq. (1), the acoustic intensity measured by the accelerometer and the microphone is

$$I(\omega) = -\frac{1}{2 \cdot \omega} \text{Im}[P(\omega) \cdot A^*(\omega)], \quad (2)$$

where  $A^*(\omega)$  is the complex conjugate of normal surface acceleration.

→ Sound power  $W(\omega)$  can be written in terms of the acoustic intensity  $I(\omega)$  and its surface area  $S$  as

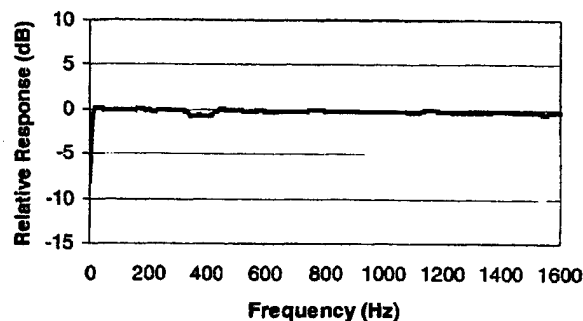
$$W(\omega) = \sum_{i=1}^N I_i(\omega) \cdot S_i, \quad (3)$$

where  $N$  is the number of surface elements.

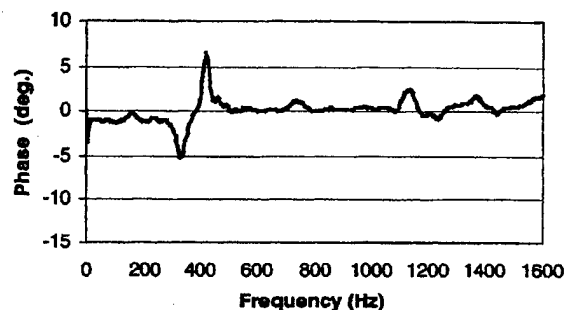
The probe was designed such that the acceleration vector is positive when the surface accelerates outward.

## II. DESIGN OF SURFACE INTENSITY PROBE

The probe design combines a highly sensitive piezoelectric ceramic accelerometer (PCB 352A22, PCB Inc.) and an inexpensive electric condenser microphone (Panasonic WM-62A) within a common titanium housing. The cylindrical housing is 1.46 cm tall and 1.10 cm in diameter, as shown in Fig. 1. The microphone is located beneath a protective titanium grid on the front of the probe. The probe weighs 5 g, minimizing surface loading. The microphone requires a charge amplifier while the accelerometer uses a PCB inductively coupled plasma voltage amplifier. The probe surface mounts by standard adhesives used for accelerometers. The performance of the probe is designed for a frequency range of 50–1600 Hz.



(a)



(b)

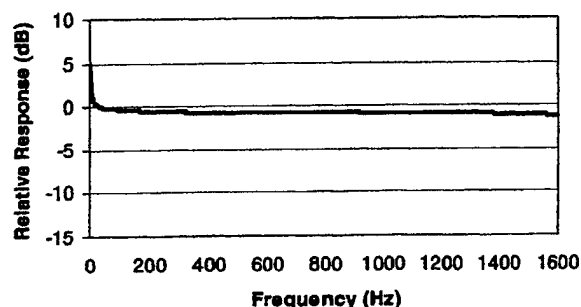
FIG. 2. Frequency response of probe accelerometer relative to PCB353M15 accelerometer: (a) logarithmic magnitude of frequency response and (b) phase of frequency response.

## III. CALIBRATION OF SURFACE INTENSITY PROBE

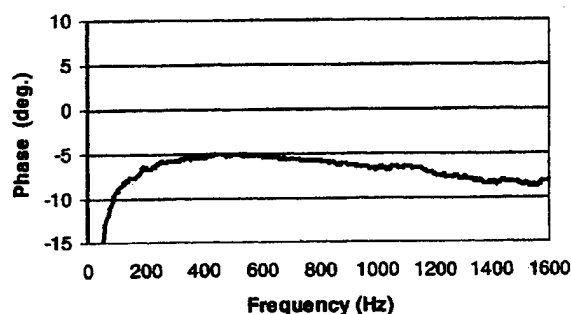
### A. Calibration of sensitivity

For measuring the frequency response of the accelerometer in the probe relative to a calibrated accelerometer (PCB353M15), whose frequency response is flat in frequency up to 1600 Hz, the surface intensity probe and the accelerometer were mounted on a shaker that was driven by white noise. The frequency response [shown in Fig. 2(a)] indicates that the sensitivity of the accelerometer is nearly constant over the 30–1600 Hz frequency range. Consequently, the sensitivity of the probe accelerometer can be measured with conventional methods, such as a hand-held calibrator, e.g., PCB's model 394006 that produces a precise  $9.81 \text{ m/s}^{-2}$  acceleration at 160 Hz. The phase difference between the two accelerometers was negligible [Fig. 2(b)].

For measuring the frequency response of the probe microphone relative to a calibrated microphone (B&K4134), whose frequency response is flat in frequency up to 1600 Hz, the surface intensity probe and the calibration microphone were set side by side in an anechoic chamber. Both microphones measured sound pressure from a loudspeaker located 20 cm in front of the microphones and driven with white noise. The frequency response [shown in Fig. 3(a)] indicated that the sensitivity of the probe microphone is nearly constant over the 30–1600 Hz frequency range. As in the case of the accelerometer, the sensitivity can thus be measured with conventional methods, such as a pistonphone, e.g., B&K's model 4220 that produces a precise 124 dB sound pressure level at 250 Hz. From Fig. 3(b), it is evident that a large



(a)



(b)

FIG. 3. Frequency response of probe microphone relative to B&K4134 microphone: (a) logarithmic magnitude of frequency response and (b) Phase of frequency response.

phase difference between the two microphones occurs below 100 Hz. Consequently, the calibration method described in the next section was developed to measure, and subsequently correct for, the phase shift of the probe microphone relative to the probe accelerometer in this frequency range.

### B. Calibration technique for phase correction between probe microphone and accelerometer

The calibrator design uses a piezoelectric actuator (PCB 712M04) as the excitation source within a sealed air cavity. The actuator's circular plate is driven with a piezoceramic disk bonded to the plate's undersurface. The probe is bonded to the circular plate as shown in Fig. 4. With the enclosure in place and actuator vibrating, the probe's accelerometer mea-

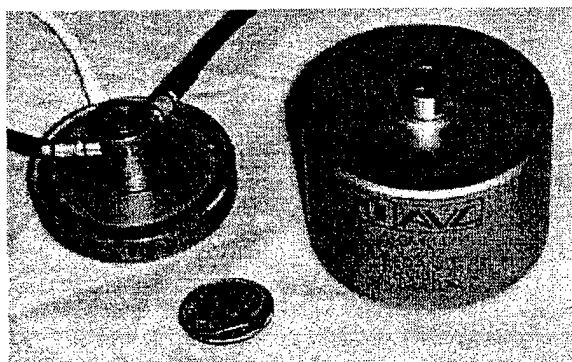


FIG. 4. Photograph of calibrator for phase correction.

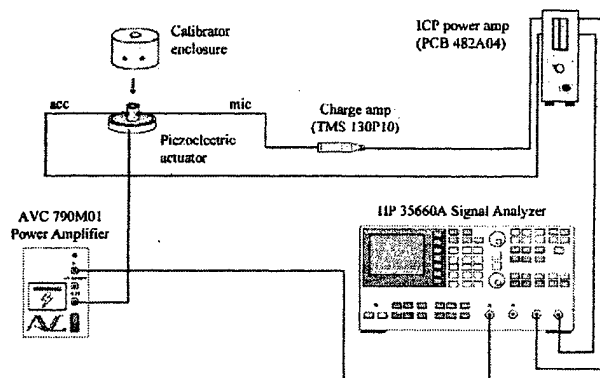


FIG. 5. Experimental setup for phase correction.

sures the motion of the circular plate while the probe's microphone measures the acoustic disturbance due to the volumetric change caused by the actuator.

A photograph of the piezoelectric actuator and calibration enclosure is shown in Fig. 4. The diameter of the actuator face is 3.27 cm. The height of the calibrator cavity is designed to ensure that the first acoustic modal frequencies are well above 1600 Hz.

The frequency-dependent phase shift of the microphone relative to the accelerometer is obtained by measuring their transfer function. To relate this to the geometry, the calibration cavity, and the acoustic pressure within the cavity, the following theory is developed which uses a simple derivation for a pressure field in a small cavity. Volume displacement  $D$  (also referred to as volumetric change in a cavity) is shown in Eq. (4):<sup>11</sup>

$$D \approx -\frac{V}{\rho_0 c^2} P_{\text{cav}}, \quad (4)$$

where  $V$  is the volume of cavity,  $\rho_0$  is the density of air,  $c$  is the speed of sound in air, and  $p_{\text{cav}}$  is the sound pressure in the cavity. The negative sign in Eq. (4) represents a decrease in cavity volume because of a positive displacement. In the cavity, there is zero phase between the volume displacement and the pressure in the frequency range of interest. Therefore, the phase between the volume acceleration and the pressure should be 180° out of phase.

By using a transfer function  $H_{\text{ph}}$  between the probe microphone and the accelerometer in the calibrator, the sound intensity with phase correction  $I_{\text{ph}}(\omega)$  is calculated as

$$I_{\text{ph}}(\omega) = \frac{1}{2\omega} \text{Im} \left[ \frac{P(\omega) A^*(\omega)}{H_{\text{ph}} / |H_{\text{ph}}|} \right]. \quad (5)$$

### C. Experimental setup and results

The experimental setup for measuring the transfer function between the microphone and accelerometer is shown in Fig. 5. For an air-tight seal around the calibrator enclosure, the holes were sealed with clay where electrical leads protrude through the enclosure.

The measured phase of the probe microphone relative to the accelerometer in the cavity of the calibrator is shown in Fig. 6. As a check on this measurement, the phase shift of the

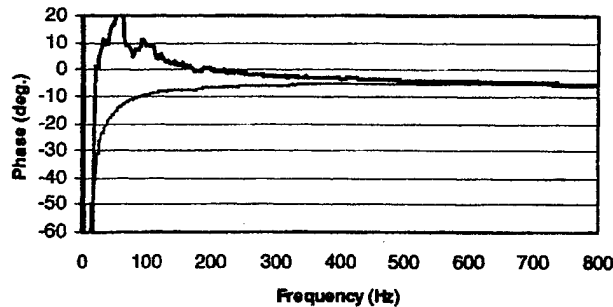


FIG. 6. Phase characteristic between probe microphone and accelerometer. The bold line indicates the phase measured by calibrator and the thin line indicates the phase calculated by the phase shift data shown in Figs. 2(b) and 3(b) and the published phase error of the calibrated B&K microphone.

probe microphone relative to the calibrated B&K microphone [shown in Fig. 3(b)] and the phase shift of the probe accelerometer relative to the calibrated PCB accelerometer [shown in Fig. 2(b)] were applied in the following way. Combining the phase data from Figs. 2(b) and 3(b), and using the published phase error of the calibrated B&K microphone,<sup>12</sup> the phase of the probe microphone relative to the accelerometer was calculated and plotted in Fig. 6. Below 400 Hz, phase measurements using the calibrator were not satisfactory because of the low amplitude of the actuator sound source. However, above 400 Hz, there is good agreement between the phase of the probe and calibration microphone, and thus the validity of the calibration method is demonstrated. The calibration cavity method is straightforward and provides an accurate measure of the phase shift between the probe microphone and accelerometer needed for the acoustic intensity calculation.

#### IV. PERFORMANCE EVALUATION USING A SQUARE, CLAMPED PLATE

To test the accuracy of the surface intensity probe on a distributed radiator, an experiment was designed to quantify the extent of error in a sound power measurement that is introduced by summing discrete intensity measurements over a given surface. A vibrating clamped plate was chosen for this investigation because of its known vibration patterns. As a basis for comparison, the sound power radiated from the plate was measured with both the surface acoustic intensity probe and the two-microphone method.

##### A. Experimental setup

The test specimen was a square 29 cm by 29 cm by 1 mm aluminum plate with highly symmetric mode shapes. The plate is bonded to a stiff frame that provides clamped boundary conditions. A lightweight loudspeaker is attached to the center of the plate via an aluminum push rod for center-point excitation. A schematic of the plate is shown in Fig. 7. The plate was divided into nine equal areas and the probes were attached at the center of these nine areas for symmetrical loading during all measurements. Because of the symmetry in the plate modes, the signal processing can be reduced by rotating only one surface intensity probe to the

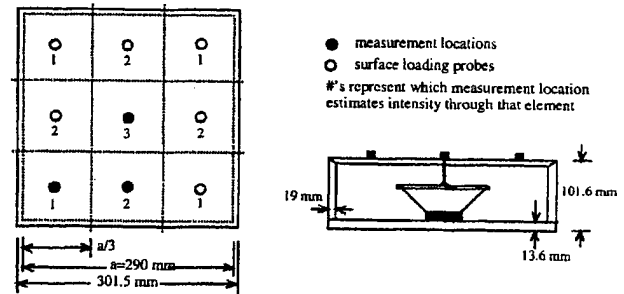


FIG. 7. Schematic diagram of the plate and the discrete nine probes of the plate.

three discrete areas (see Fig. 7). Thus, only one probe sensitivity and phase correction was needed to compute the sound power.

The plate was placed on the floor in semianechoic room and excited at 0–800 Hz of white noise from the signal analyzer (HP35660A). With the surface intensity probe, sound intensity was measured at the three designated elements up to 800 Hz. Using Eq. (3), the sound power  $W(\omega)$  from this specimen can be determined as

$$W(\omega) = (4I_1(\omega) + 4I_2(\omega) + I_3(\omega)) \cdot S_0, \quad (6)$$

where  $I_1$ ,  $I_2$ , and  $I_3$  were surface acoustic intensities measured by the same probe mounted on the surface element corresponding to the notation shown in Fig. 7.  $S_0$  is the area of one element of the specimen.

The sound power was also measured with scanning two microphones over an open cubical frame 86 cm on a side that encloses the test specimen (shown in Fig. 8).

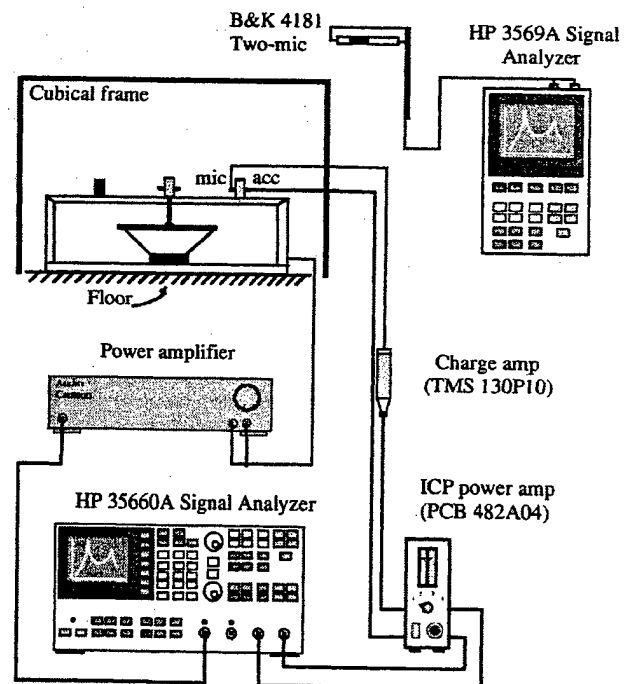


FIG. 8. Experimental setup for both the surface intensity probe and two-microphone probe.

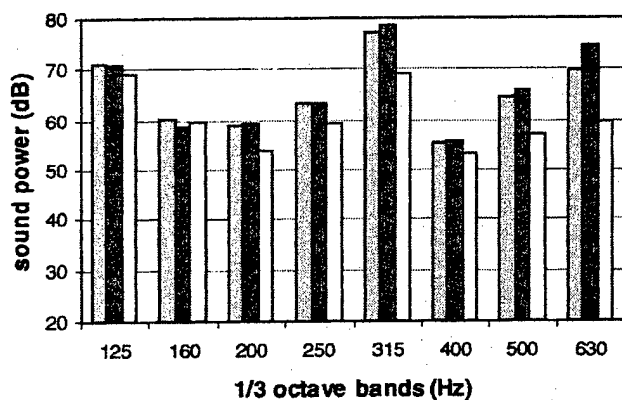


FIG. 12. Comparison of sound power: gray and black bars are measured at 9 and 81 elements (using the B&K microphone and laser vibrometer), respectively. The white bar is measured with the two-microphone probe.

detail, the number of measurement points per structural wavelength at the first, second, and third mode of the plate and their corresponding errors in intensity computations were extracted from the 9 and 81 element measurements (shown in Fig. 13). This graph demonstrates that a minimum number of measurement points per structural wavelength is necessary to measure sound power with the surface intensity method to an accuracy within a few decibels. The experimental data indicate that this number is approximately six points per structural wavelength. Thus, in making surface acoustic intensity measurements, it is important that ad-

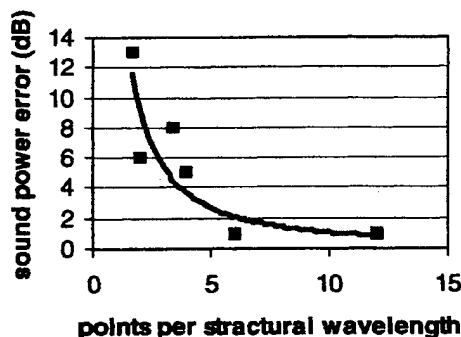


FIG. 13. Relationship between sound power error and measurement points per structural wavelength: dots are experimental data and the solid line is the approximate curve from the experimental data.

equate knowledge of the structure's modal response is available *a priori*.

#### APPENDIX: NOMENCLATURE

$A(\omega)$	normal surface acceleration
$D$	volume displacement in air cavity
$H_{ph}$	transfer function with phase correction between probe microphone and accelerometer
$I(\omega)$	time-averaged acoustic intensity normal to surface
$I_{ph}(\omega)$	time-averaged acoustic intensity normal to surface with phase correction
$N$	number of surface elements
$P(\omega)$	sound pressure
$S$	surface area
$V$	volume of air cavity
$V(\omega)$	normal surface velocity
$W(\omega)$	sound power
$c$	speed of sound in air
$p_{cav}$	sound pressure in air cavity
$\rho_0$	density of air
$\omega$	angular velocity

#### ACKNOWLEDGMENTS

The authors thank the National Science Foundation for their support of this research through a SBIR contract to PCB Piezotronics, Inc. and the Center for Acoustics and Vibration at The Pennsylvania State University. The authors also thank PCB Piezotronics, Inc. for the fabrication and development of the surface intensity probes used in this investigation.

This material is based upon work supported under a National Science Foundation Graduate Fellowship.

<sup>1</sup>N. Kaemmer and M. J. Crocker, J. Acoust. Soc. Am. **73**, 856 (1983).

<sup>2</sup>B. G. Van Zyl and F. Anderson, J. Acoust. Soc. Am. **57**, 682 (1975).

<sup>3</sup>F. J. Fahy, J. Acoust. Soc. Am. **62**, 1057 (1977).

<sup>4</sup>J. Y. Chung, General Motors Research Publication No. GMR-2617 (1977).

<sup>5</sup>T. H. Hodgson, J. Acoust. Soc. Am. **61**, 487 (1977).

<sup>6</sup>M. Arai, Proceedings of the Sixth International Congress on Acoustics, F13-16 (1968) (unpublished).

<sup>7</sup>J. A. Macadam, Appl. Acoust. **9**, 103 (1976).

<sup>8</sup>J. D. Brito, Ph.D. thesis, Massachusetts Institute of Technology (1976).

<sup>9</sup>M. C. McGary and M. J. Crocker, J. Sound Vib. **82**, 275 (1982).

<sup>10</sup>M. P. Waser and M. J. Crocker, Noise Control Eng. **1**, 22, 76 (1984).

<sup>11</sup>G. H. Koopmann and J. B. Fahline, *Designing Quiet Structures: A Sound Power Minimization Approach* (Academic, San Diego, CA, 1997).

<sup>12</sup>Brüel and Kjaer, 17. Instructions and applications: Half-inch condenser microphones 4133/34 (1974).

→ Masaki Arai, vol. 4, pages F13-16  
(report F-1-4)

QC221.I5 annexed

v1-6

Quiet

# **APPENDIX 80**



## Optimally Designed Shell Enclosures with Tuned Absorbers for Minimizing Sound Power

ERIC W. CONSTANS\*, ASHOK D. BELEGUNDU, GARY H. KOOPMANN

*Center for Acoustics and Vibration, The Pennsylvania State University, 157 Hammond Bldg, University Park, PA 16802, USA*

*Received 19, 1999; Revised February 28, 2000*

**Abstract.** This paper presents a design methodology for reducing radiated noise from enclosures using multiple optimized tuned absorbers. The methodology starts from the sound power spectrum of the enclosed noise source and ends with optimally sized/located absorbers on a surrounding thin shell enclosure. The design approach combines a finite element method vibration prediction code, a boundary element method sound power prediction code and a combined stochastic/gradient-based optimization algorithm. A design example has been optimized for a thin shell covering a motor/gearbox. The addition of a small amount of weight (130 g or 1.6% of the weight of the shell) produced substantial reductions in radiated sound power (13 dB in the targeted 1/3 octave band centered at 125 Hz). The design has been validated by experiment.

**Keywords:** vibration absorbers, optimization, noise reduction, sound power

### 1. Introduction

The sound radiating components of most machines, e.g., casings of rotating or reciprocating machines, generally are fabricated from thick metal plates which have high mechanical impedances. Consequently, it is very difficult to modify the acoustic radiation characteristics of these components via addition of mass, stiffness or damping. An alternative approach that can be taken is to enclose such noise sources (e.g. gearboxes) with optimally designed lightweight enclosure to reduced their radiated noise. Thus, we need only to focus on the design of a thin shell structure with low mechanical impedance whose acoustic radiation is highly sensitive to parameters such as mass, stiffness and damping. Here, we show how multiple tuned absorbers may be optimally sized and located on the shell enclosure so as to alter its dynamic response and thus minimize its radiated noise. This approach is also applicable to low impedance shell casings such as on appliances and automobile valve covers.

Work has been done on altering the dynamic response of a vibrating shell by restructuring its mode shapes by use of optimally located point masses (Constans et al., 1998). The efficacy of the approach was also verified experimentally. However, modal tailoring is not always possible—for example, low frequency, large volume displacing modes are difficult to alter with additions of point masses. Further, if the response of the enclosure is a forced

\*Present address: Rowan University, Glassboro, New Jersey, USA.

vibration due to a very high impedance, broadband noise source, modal tailoring via mass or stiffness variations may not be possible. See Christensen et al. (1998) for work on structural optimization in acoustics. For high impedance structures, the approach pursued in this paper is one of attaching tuned absorbers (mathematically, point mass/stiffness/damping) to the vibrating enclosure to minimize its radiated or transmitted sound power.

## **2. Previous work on tuned absorbers**

Tuned absorbers were used as vibration reduction devices since their invention by Frahm at the beginning of this century (Frahm, 1911). The original theory and optimization of a tuned absorber were developed by Ormondroyd and Den Hartog in 1927 (Ormondroyd and Den Hartog, 1927). They studied the simplest case: a single tuned absorber on a single degree-of-freedom system used to control a narrow band of frequencies. More recently, researchers have studied the use of tuned absorbers in reducing vibrations with white noise excitation (Asami et al., 1991), and the use of multiple tuned absorbers for situations where absorber manufacturing errors may render single absorbers ineffective (Abé and Fujino, 1994). Klasztorny (1995) presents a set of optimal design curves for multiple tuned absorbers on a lightly damped structure. A matrix equation is given whereby the dynamic response of a structure with multiple tuned absorbers may be predicted. The designer may use the design curves to optimize each absorber individually, and then use the matrix equation to determine the coupling between absorbers, returning the absorbers as needed. This approach has two major disadvantages: first, coupling between absorbers (which is significant on lightweight structures) is not accounted for in the optimization curves. Second, evaluation of coupling between absorbers requires a full complex eigenvalue analysis.

A more practical method of analysis of structures with several tuned absorbers is given by Hamill and Andrew (1971) and by Kitis et al. (1984). In their method, the analysis of the full structure need only be performed once; the dynamic response as a function of absorber parameters are determined by an efficient re-analysis procedure. This allows optimization, involving iterative analysis, to be carried out in a reasonable amount of time. A modified version of their approach is used in this paper.

## **3. Basic approach for high mechanical impedance structures**

For purposes of illustration, consider a gearbox (the noise source) as shown in figure 1. The gearbox has several enclosing structural elements, e.g., plates, which are usually very thick and thus direct addition of tuned resonators on these plates only affects the acoustic response marginally. As mentioned earlier, our strategy here is to enclose the gearbox in an enclosure which is an air-tight enclosure made of thin sheet metal. Where there is a small gap between the enclosure and the component (such as where the shaft exits the gearbox), an acoustic seal is inserted to retain an airtight enclosure. The idea here is to size and optimally locate tuned absorbers onto the enclosure to minimize transmitted noise as shown in figure 2.

The basic steps in the design approach are given below. Details are presented in the sections that follow.

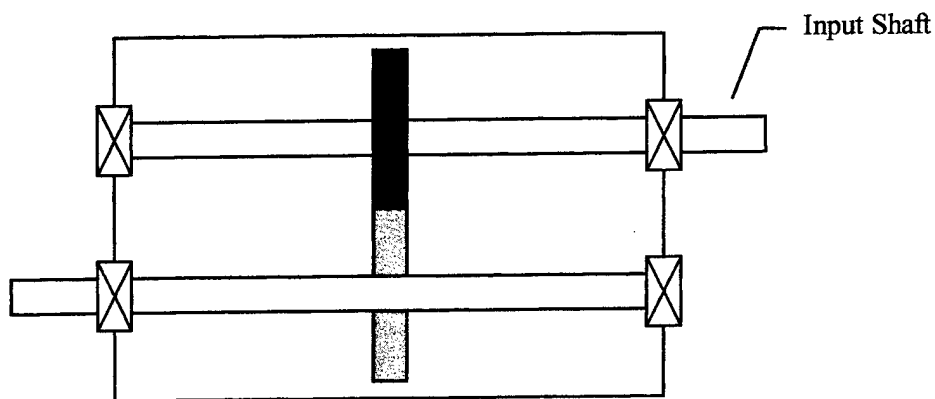


Figure 1. Schematic of a gearbox—the noise source.

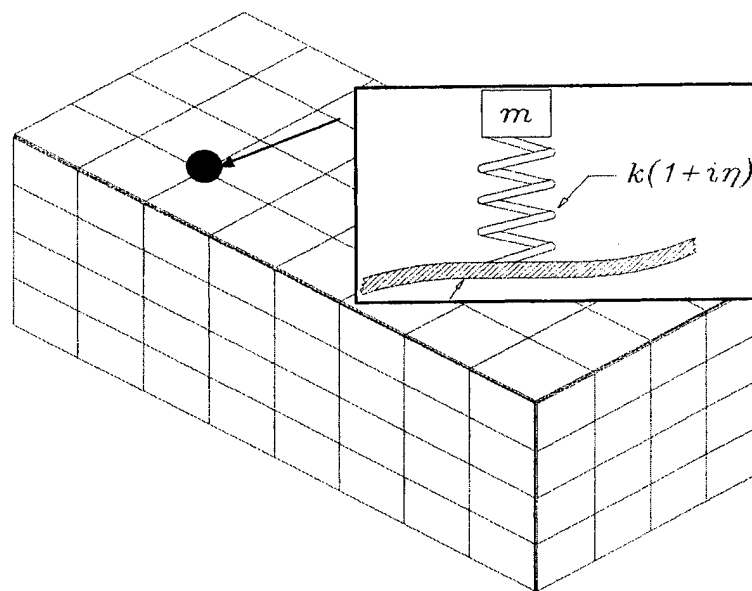


Figure 2. An enclosure around the noise source with tuned absorbers.

*Step 1.* First, the power spectrum of the sound power radiating from the gearbox must be experimentally determined to identify the frequency band within which the sound power levels are high at the operating condition. Within this band, the sound power  $W$  may be discretized as

$$W = \sum_{\omega_{\min}}^{\omega_{\max}} W(\omega_i)$$

$W$  is obtained by summing the total radiated sound power at each frequency or at resonances over the frequency interval.



- Step 2.* Fabricate a lightweight enclosure structure and determine its dynamic response via modal analysis experiments.
- Step 3.* Develop a finite element model of the enclosure, and iterate and ultimately validate the model by comparison with the modal analysis experiments.
- Step 4.* With the enclosed gearbox running at typical operating conditions, measure accelerations at selected points on the enclosure. From this data, back-calculate the forcing function using a generalised inverse method.
- Step 5.* Using surface accelerations computed from the combined numerical and experimental model, validate the acoustical model, by correlating the sound power of the enclosure measured experimentally with that computed via the numerical model.
- Step 6.* Optimize the enclosure design (a shell structure) using tuned absorbers. The objective will be to minimize  $W$  as given above. Design variables will be the locations and values of the absorber parameters. Shape of the enclosure may also be considered at this stage.
- Step 7.* Fabricate the prescribed tuned absorbers with optimum parameters given by the optimization program. This will require experimental testing of the fabricated absorbers.
- Step 8.* For the experimental validation of the method, we proceed in the following way. Once the optimal tuned absorber distribution is achieved with the numerical studies, we then modify the physical system accordingly, e.g., add tuned absorbers in the designated locations as specified by the program, and measure the radiated sound power. This can be achieved with three different methods. On a real system, the sound power can be 1) computed numerically in terms of surface accelerations, 2) measured directly using the two-microphone intensity probe method, and 3) measured directly using the surface intensity probe method. All three of the methods allow for in-situ measurements. Details on sound power measurements and theory are contained in the recent text by Koopmann and Fahline (1997).

The following sections provide the theoretical background for the design strategy outlined above. The major computational components of this design strategy is the computer code POWER, a finite element code which has been developed to provide the dynamic response of a shell structure with tuned absorbers, and a simulated annealing program that is used to determine the optimal distribution and mechanical impedance of tuned absorbers for a minimum power radiation condition.

#### 4. Dynamic response of a shell with tuned absorbers

##### 4A. Dynamic analysis without absorbers

The time-harmonic equation of motion for the shell structure is  $\mathbf{K}\mathbf{x} + \mathbf{C}\dot{\mathbf{x}} + \mathbf{M}\ddot{\mathbf{x}} = \mathbf{F}$ , where  $\mathbf{K}$  is the stiffness matrix of the structure,  $\mathbf{C}$  is a damping matrix,  $\mathbf{M}$  is the mass matrix,  $\mathbf{f}e^{i\omega t}$  is a harmonic driving force vector with frequency  $\omega$ , and  $\mathbf{x}$  is the vector of amplitudes of nodal displacements. Upon substituting  $\mathbf{x}(t) = \mathbf{x}e^{i\omega t}$  and using hysteretic (frequency-independent) damping  $\mathbf{C}\dot{\mathbf{x}} = i\alpha\mathbf{K}\mathbf{x}$ , we get  $[\mathbf{K} + i\alpha\mathbf{K} - \omega^2\mathbf{M}]\mathbf{x} = \mathbf{f}$ . Here,  $\alpha$  is an internal

damping constant. The well-known modal superposition technique is based on

$$\mathbf{x} = \sum_{n=1}^N y_n \phi_n = \Phi \mathbf{y} \quad (1)$$

where  $y_n$  is a modal participation factor. Let  $\mathbf{f}$  = vector of external forces. Denoting the  $n$ th resonance frequency as  $\omega_n$ ,  $\Phi$  as the matrix of eigenvectors and  $\mathbf{y}_0$  as the vector of modal participation factors (of the structure without the absorbers), we obtain the expressions

$$\mathbf{y}_0 = \Lambda \Phi^T \mathbf{f} \quad (2)$$

and  $\dot{\mathbf{x}} = i\omega \Phi \Lambda \Phi^T \mathbf{f} = i\omega \Phi \mathbf{y}_0$ , where  $\Lambda$  is a diagonal matrix whose elements are reciprocals of  $[\omega_n^2(1 + i\alpha) - \omega^2]$ . Further, letting  $\mathbf{Y} = i\omega \Phi \Lambda \Phi^T$ , we have

$$\dot{\mathbf{x}} = \mathbf{Y} \mathbf{f} \quad (3)$$

where  $\mathbf{Y}$  is known as an admittance matrix. Note that  $\mathbf{Y}$  is a function of the real eigenvectors and eigenvalues of the shell structure.

The shell structure is modeled using Discrete Kirchhoff Triangular (DKT) finite elements in conjunction with Constant Strain Triangle (CST) elements. Stiffening ribs or structural frames, which are often found on shell structures, are modeled with three-dimensional beam elements. Commercial codes can be used.

#### 4B. Absorber impedance

A force balance for each absorber, results in the expression

$$\mathbf{e} = \mathbf{Z} \mathbf{v} \quad (4)$$

where  $\mathbf{e}$  = negative of the force exerted by the absorber on the structure,  $\mathbf{v}$  = velocity at the absorber attachment point, and  $\mathbf{Z}$  = a diagonal matrix of absorber impedances. An expression for  $Z_i$  as a function of absorber parameters is now derived. Figure 3 shows a schematic diagram of a tuned absorber attached to a point on the shell. The displacement at the point of attachment on the shell is given by  $z_1$ , and the displacement of the point mass is  $z_2$ . In this analysis we assume a harmonic solution, so that  $\ddot{z} = -\omega^2 z$ . Using a force balance, we may write the equations of motion at the two points as

$$\begin{aligned} k(1 + i\eta)(z_1 - z_2) &= e_s \\ k(1 + i\eta)(z_2 - z_1) - m\omega^2 z_2 &= 0 \end{aligned}$$

where  $e_s$  is the force exerted by the shell on the absorber. Eliminating  $z_2$  from these equations, and noting that  $v_1 = \dot{z}_1 = i\omega z_1$ , is the velocity of the shell at the point of attachment,

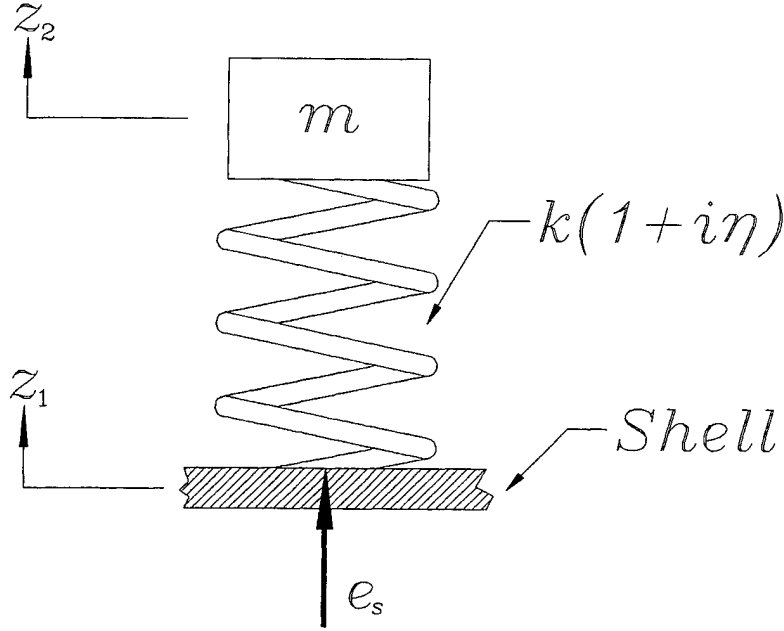


Figure 3. Schematic of tuned absorber with displacements shown.

and denoting the absorber tuned natural frequency by  $\omega_a = \sqrt{k/m}$ , the impedance of an absorber may be written as

$$Z_1 = i\omega \frac{m\omega_a^2(1 + i\eta)}{\omega_a^2(1 + i\eta) - \omega^2}. \quad (5)$$

#### 4C. Force balance

Each tuned absorber  $i$  exerts a dynamic force  $e_i$  on the shell. Also, the shell is excited externally by the driving forces  $f_i$ . In our analysis, we will assume that there are  $p$  absorbers and  $q$  external forces on the shell. If we choose a point  $t$  on the structure, we may write the velocity at that point in terms of the forces (both external and from the absorbers) and the admittances of the shell structure.

$$v_t = (Y_{ta}f_a + Y_{tb}f_b + \cdots + Y_{tq}f_q) - (Y_{t1}e_1 + Y_{t2}e_2 + \cdots + Y_{tp}e_p)$$

where the  $Y_{ij}$  are components of the shell admittance matrix given in Eq. (3). The locations of interest on the structure are the points of attachment of the absorbers, since it is the motion there which we wish to control. The velocity at the point of attachment of absorber  $j$  is then

$$v_j = (Y_{ja}f_a + Y_{jb}f_b + \cdots + Y_{jq}f_q) - (Y_{j1}e_1 + Y_{j2}e_2 + \cdots + Y_{jp}e_p) \quad (6)$$

Let us define the following row vectors

$$\mathbf{c}_j = \{Y_{ja} \ Y_{jb} \ \cdots \ Y_{jq}\} \quad \mathbf{b}_j = \{Y_{j1} \ Y_{j2} \ \cdots \ Y_{jp}\}$$

Then we may rewrite Eq. (6) as

$$v_j = \mathbf{c}_j \mathbf{f} - \mathbf{b}_j \mathbf{e}.$$

Or, if we wish to write the vector of all velocities at the points of attachment of the absorbers, we have

$$\mathbf{v} = \mathbf{C}\mathbf{f} - \mathbf{B}\mathbf{e}. \quad (7)$$

where  $\mathbf{C} = \{\mathbf{c}_1 \ \mathbf{c}_2 \ \cdots \ \mathbf{c}_p\}^T$ ,  $\mathbf{B} = \{\mathbf{b}_1 \ \mathbf{b}_2 \ \cdots \ \mathbf{b}_p\}^T$ . Note that  $\mathbf{C}$  is a  $p \times q$  matrix of admittances relating the external forces to velocities at the absorbers and  $\mathbf{B}$  is a  $p \times p$  matrix relating the absorber forces to the absorber displacements. We refer to the dissertation in Constans (1998) for details of the above computations.

#### 4D. Dynamic analysis with absorbers

Equations (4) and (7) yield an expression from which the velocities can be determined based on the parameters of the absorbers and of the structure:

$$\mathbf{v} = (\mathbf{I} + \mathbf{B}\mathbf{Z})^{-1} \mathbf{C}\mathbf{f} \quad (8)$$

The above equation only involves the inversion of a small ( $p \times p$ ) matrix. Once  $\mathbf{v}$  is determined, then the absorber forces are obtained from  $\mathbf{e} = \mathbf{Z}\mathbf{v}$ . Nodal velocities for the entire structure are obtained by re-defining the modal participation factors as  $\mathbf{y} = \mathbf{\Lambda} \mathbf{\Phi}^T (\mathbf{f} - \mathbf{e})$  or in view of Eq. (2):

$$\mathbf{y} = \mathbf{y}_0 - \mathbf{\Lambda} \mathbf{\Phi}^T \mathbf{e} \quad (9)$$

Given a set of absorbers (as dictated by the optimization algorithm), we determine the structural response from

$$\dot{\mathbf{x}} = i\omega \mathbf{\Phi} \mathbf{y} \quad (10)$$

A critical observation is now made: the expression for  $\mathbf{y}$ , viz.  $\mathbf{y} = \mathbf{y}_0 - \mathbf{\Lambda} \mathbf{\Phi}^T \mathbf{e}$  is independent of the forcing function  $\mathbf{F}$ . This is exploited in the present work by experimentally determining  $\mathbf{y}_0$  and then using the above equation to determine the  $\mathbf{y}$  and hence the velocities in terms of the absorber parameters.

### 5. Calculation of sound power

A full development of the boundary element/wave superposition method used here is given by Fahline and Koopmann (1996, 1997). The method replaces each of the (triangular) elements on a surface with point acoustic monopole and dipole sources. The strength of each of the sources is found through a volume velocity boundary condition:

$$\mathbf{u} = \mathbf{U}\mathbf{s} \quad (11)$$

where  $\mathbf{s}$  is the vector of source strengths (one for each element on the structure),  $\mathbf{U}$  is a matrix relating the source strengths to volume velocities and  $\mathbf{u}$  is the vector of volume velocities. The volume velocity produced by a single element is defined as

$$u_n = \frac{1}{3} A_n (\dot{\mathbf{x}}_{1n} + \dot{\mathbf{x}}_{2n} + \dot{\mathbf{x}}_{3n}) \cdot \mathbf{n}_n \quad (12)$$

where  $A_n$  is the surface area of element  $n$ ,  $\mathbf{n}_n$  is the unit normal to the element, and  $\dot{\mathbf{x}}_{in}$  ( $i = 1, 2, 3$ ) are the nodal velocities at the corners of the triangular element. The nodal velocities are calculated as discussed in the previous section. The acoustic source strengths are found by inverting Eq. (11). We may write Eq. (12) in matrix form, solving for the entire volume velocity vector  $\mathbf{u} = \mathbf{V}\dot{\mathbf{x}}$ , where  $\mathbf{V}$  is a matrix containing element surface areas, unit normals and connectivity information. Writing this in terms of modal participation factors we have  $\mathbf{u} = i\omega\mathbf{V}\Phi\mathbf{y}$  from which

$$\mathbf{s} = i\omega\mathbf{U}^{-1}\mathbf{V}\Phi\mathbf{y} \quad (13)$$

The acoustic power is calculated by pre- and post-multiplying the source strength vector by a coupling matrix  $\mathbf{S}$ :

$$\Pi_{av} = \frac{1}{2} \text{Re}\{\mathbf{s}^H \mathbf{S} \mathbf{s}\} \quad (14)$$

where the  $H$  superscript indicates complex conjugation and transposition. The matrix  $\mathbf{S}$  is not given here for brevity. See Koopmann and Fahline (1997).

Direct use of Eq. (14) above is not as efficient as the following procedure. Substituting Eq. (13) into (14) we have

$$\Pi_{av} = \frac{1}{2} \omega^2 \text{Re}\{\mathbf{y}^H \Phi^T \mathbf{V}^T \mathbf{U}^{-H} \mathbf{S} \mathbf{U}^{-1} \mathbf{V} \Phi \mathbf{y}\}$$

or

$$\Pi_{av} = \frac{1}{2} \omega^2 \text{Re}\{\mathbf{y}^H \mathbf{P} \mathbf{y}\} \quad (15)$$

where

$$\mathbf{P} = \Phi^T \mathbf{V}^T \mathbf{U}^{-H} \mathbf{S} \mathbf{U}^{-1} \mathbf{V} \Phi.$$

Varying the parameters or locations of tuned absorbers on the structure will affect only the modal participation vector  $\mathbf{y}$ , while leaving the  $\mathbf{P}$  matrix unchanged. *The  $\mathbf{P}$  matrix may be calculated and stored before optimization begins*; calculation of sound power involves only the determination of the change in the modal participation vector through Eq. (9), and pre- and post- multiplication of this vector with the  $\mathbf{P}$  matrix at each frequency. This new reanalysis procedure makes feasible the use of the sound power of a structure as an objective function in optimization with tuned absorbers.

## 6. Determination of modal participation factors

Once the eigenvalues and eigenvectors of the structure are known, it is necessary to determine modal participation factors (MPF's) for the structure, either experimentally or through a known forcing function. If the forcing function on the shell is known a priori; we may simply use  $\mathbf{y}_0 = \Lambda \Phi^T \mathbf{F}$  to determine the MPF's. In many cases, however, the forcing function is unknown or is very complicated. In the present context, the forcing function is an acoustic excitation induced by the noise source on the enclosure. In this situation, we may determine the MPF's experimentally as follows.

Examining  $\dot{\mathbf{x}} = i\omega \Phi \Lambda \Phi^T \mathbf{f} = i\omega \Phi \mathbf{y}_0$ , we see that the MPF's are related to the nodal velocities through the matrix of eigenvectors. In theory, we could measure the nodal velocities at all points on the structure and invert the equation to solve for the MPF's. In practice, it is not necessary to measure all points to obtain good estimates of MPF's; only certain critical points (e.g. points located at antinodes of the mode shapes of the structure) need to be measured.

Let us denote the subset of measured velocities with an overbar, in which case we have

$$\bar{\dot{\mathbf{x}}} = i\omega \bar{\Phi} \mathbf{y}_0, \quad (16)$$

where  $\bar{\Phi}$  is the submatrix of eigenvectors associated with the measured nodes. Note that this matrix is generally not square, but will have dimension  $m \times r$  where  $m$  is the number of measured points and  $r$  is the number of known eigenvectors. Premultiplying Eq. (16) by the transpose of the eigenvector matrix, we have

$$\bar{\Phi}^T \bar{\dot{\mathbf{x}}} = i\omega \bar{\Phi}^T \bar{\Phi} \mathbf{y}_0.$$

The matrix preceding the  $\mathbf{y}$  vector is now square, and we can invert this equation to solve for the modal participation factors without tuned absorbers.

$$\mathbf{y}_0 = -\frac{i}{\omega} (\bar{\Phi}^T \bar{\Phi})^{-1} \bar{\Phi}^T \bar{\dot{\mathbf{x}}}. \quad (17)$$

For this method to be successful, the number of measured points must be equal to or greater than the number of modes used in the solution. Obviously, the method increases in accuracy as the number of measured points increases, and the measured points should include the locations of the largest displacements on the structure (modal antinodes).

With tuned absorbers, we simply update the MPF's using Eq. (9) and then substitute this into Eq. (8) to determine the sound power.

## 7. Hybrid optimization algorithm for determining absorber locations and parameters

The objective function to be minimized is the total sound power over the desired frequency range

$$\text{minimize: } F = \sum_{f=f_{\min}}^{f_{\max}} \Pi_f \quad (18)$$

where  $f_{\min}$ ,  $f_{\max}$  are the minimum and maximum frequencies of interest, respectively.

In the optimization problem, we are interested in two major objectives: finding the optimal mass, tuning frequency and damping for each of the tuned absorbers, and finding the optimal absorber locations on the shell for minimum sound power. Thus, we may think of the problem in terms of a local optimization (finding optimal mass, tuning frequency and damping at a given set of absorber locations) and a global optimization (finding optimal locations for the absorbers). The local optimization is performed using a gradient-based algorithm, viz. the ellipsoid algorithm (Urban and Gabriele, 1993), while the global problem is solved using simulated annealing (SA).

The choice of an SA code was motivated by the fact that changes in absorber locations can cause abrupt changes in sound power due to shifting resonances. Thus, the location or global optimization is better achieved using non-gradient methods. This was also noted by Keane (1994). Szykman and Cagan (1995) have demonstrated the use of the simulated-annealing algorithm in highly nonlinear problems, such as three-dimensional routing and component packing. The SA algorithm used here is based on the one presented by Corana et al. (1987). The algorithm has been modified to handle location variables as follows. The 'step size' in the algorithm is interpreted here as defining a three dimensional sphere, which contains a certain number of nodes. To choose a new trial design, the algorithm picks one of these nodes at random and moves there. As the algorithm progresses, the radius of the sphere becomes progressive smaller—a result of the existing strategy that the step be adjusted to balance the number of accepts with the number of rejects. At small enough radius, the range of motion is frozen at the current node. Once all absorbers are frozen, we have convergence. Other aspects of SA are standard and their discussion is omitted.

Note that for each nodal selection, the gradient method is used to optimize absorber parameters and the sound power is then evaluated. In finding optimal tuned absorber locations, the absorbers are constrained to lie on nodal positions of the grid and no two absorbers may lie on the same node. Also, the locations tried out by the SA code are recorded so as to avoid recomputing the objective if the same pattern repeated itself in the SA code. At the optimum, the absorber parameters are used to design "beam-type" absorbers described next.

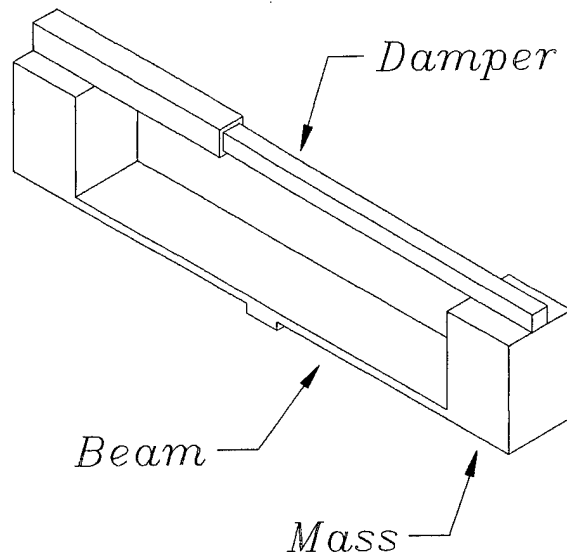


Figure 4. Damping mechanism in the beam absorber.

Gradients of the objective function (sound power) are computed using forward differences with difference parameter  $\varepsilon = 0.01 * x_i$ .

## 8. Design of practical tuned absorbers

The tuned absorbers are modeled as single degree-of-freedom mass/spring/damper systems. For experimental purposes, however, the "beam-type" absorber shown in figure 4 is used. The masses at the ends of the beams serve as the mass element in the absorber, and the bending stiffness of the beams serves as the spring element.

To create damping in the beam absorber, the scheme shown in figure 4 is used. A narrow plastic rod attached to one mass is inserted into a square plastic socket attached to the other mass. Rotational motion of the masses causes the two pieces to slide against one another, creating friction (and damping). Grease is placed inside the socket to create further damping. Overall damping of the beam absorber may be tailored by varying the length of contact between the pieces. A simple FEM model of the beam-type absorber was created to calibrate the beam-type absorber with the theoretical SDOF model.

## 9. Example study: A gearbox enclosure

### 9A. Problem description

Gearboxes are a significant source of noise in many industrial applications. Moreover, the casing containing the gears usually has high impedance, and is itself not amenable to noise



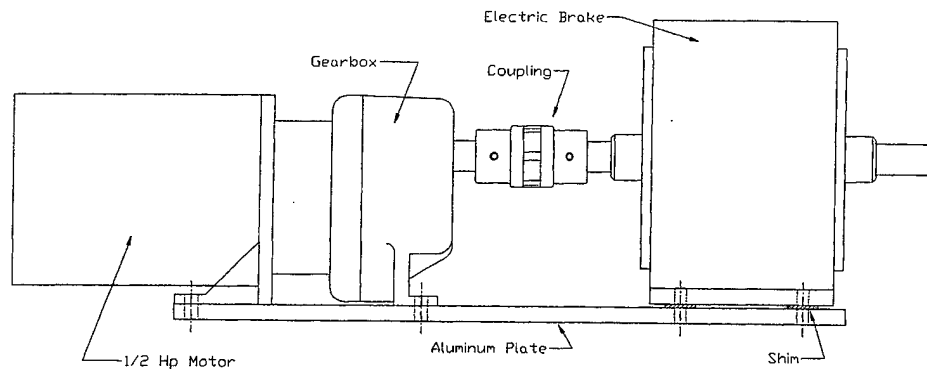


Figure 5. Gearbox/motor assembly.

reduction techniques. To test the optimization strategy presented here, an enclosure was designed to surround a gearbox/motor assembly. The enclosure is a thin shell structure which may be tailored for minimum sound power transmission. Prior to this example, the methodology was applied to minimize radiated noise from an enclosure around a calibrated noise source.

Figure 5 shows the gearbox/motor/brake assembly targeted for noise reduction. The AC motor (manufactured by Dayton) has 0.5 horsepower and rotates at a constant speed of 1725 rpm. The gearbox (also manufactured by Dayton) has a nominal input shaft speed of 1725 rpm and an output speed of 91 rpm. The gearbox output is connected through a coupling to an electric brake, which provides a load on the gearbox and motor. The entire assembly is mounted on a 0.5 inch thick aluminum plate.

To cover the gearbox assembly, an enclosure was constructed from sheet aluminum, such as shown in figure 2. The aluminum is 0.090 inches thick, and is attached with epoxy to a frame. The frame is welded together from 0.5 inch square aluminum stock. The aluminum sheet covers five sides of the box; the bottom side is open, in order that the enclosure may fit over the top of the gearbox assembly.

#### 9B. Sound power spectrum produced by gearbox

The first step in optimizing the enclosure for minimum radiation is to determine the problem noise frequencies of the gearbox itself. The sound power produced by the gearbox was determined with an acoustic intensity probe using the surface scanning technique. During the sound power measurements the electric brake was powered with a DC power supply at a voltage of 15 V and a current of 0.5A. Figure 6 shows the results of the sound power measurements. As can be seen, the sound power has an initial peak in the 125 Hz  $\frac{1}{3}$ -octave band of 69.06 dB, and then drops to around 60 dB until 315 Hz. The largest peak is in the 400 Hz band, with a power of 72.38 dB.

In practice, the higher frequency noise would be reduced with the use of damping material (such as fiberglass) placed inside the enclosure. Low frequency noise, such as that contained in the 125 Hz band, is not absorbed by damping material and must be controlled

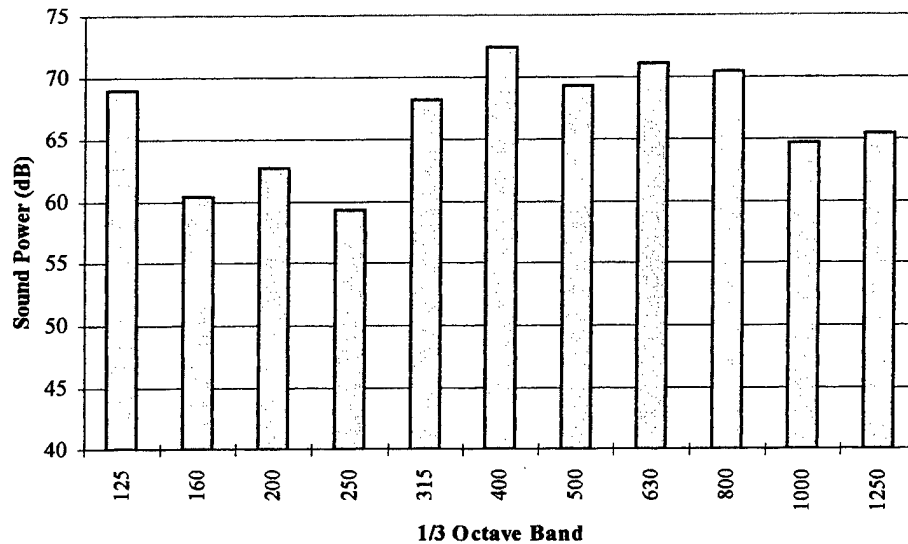


Figure 6. Sound power measurements of gearbox without enclosure (dB reference:  $10^{-12}$  W).

structurally. Therefore, the noise in the 125 Hz band (extending from 111 to 140 Hz) is targeted for reduction.

#### 9C. Finite element model of enclosure

To model the enclosure a finite element mesh was created with 141 nodes and 256 shell elements. The frame was modeled using 64 beam elements. The nodes along the bottom of the enclosure are clamped. Since the gearbox noise targeted for reduction is centered in the 125 Hz  $\frac{1}{3}$ -octave band, only the first fifteen modes were calculated. According to the finite element analysis of the enclosure, these modes occur between 90 and 280 Hz. The results of the eigenvalue/eigenvector analysis are shown in Table 1.

#### 9D. Experimental modal analysis of gearbox enclosure

In order to confirm the eigensolution found by the finite element analysis, an experimental modal analysis was performed on the gearbox enclosure using the STAR modal analysis software package. Table 1 shows the results of the experimental modal analysis, which was carried out over the range of 50–250 Hz. STAR found twelve modes below 250 Hz, corresponding to the first twelve modes predicted by FEM. The results from the experimental modal analysis agree well with the predictions of the FEM code, with a maximum difference in natural frequency of 7%.

#### 9E. Determination of modal participation factors

To calculate modal participation factors for the gearbox enclosure, nodal velocities at certain points on the structure are needed. These were measured with a pair of accelerometers: one

Table 1. Predicted vs. measured natural frequencies of gearbox enclosure.

Mode #	Natural frequencies (Hz)		
	Predicted	Experimental	% Difference
1	93.09	91.84	1.36
2	126.17	130.97	3.66
3	156.16	146.09	6.89
4	157.86	154.08	2.45
5	168.15	179.47	6.31
6	179.42	191.63	6.37
7	182.03	176.68	3.03
8	203.19	201.79	0.69
9	204.19	206.34	1.04
10	220.62	218.01	1.20
11	220.69	218.17	1.16
12	232.53	231.25	0.55
13	254.49	NF	
14	278.27	NF	
15	279.17	NF	

accelerometer remains fixed and is used as a phase reference. The other accelerometer is used to measure the velocities at 31 points on the enclosure. The measurement points are shown in figure 7. Once the participation factors have been calculated, they may be used to predict the sound power of the enclosure before optimization.

The predicted and measured sound power of the gearbox/enclosure system is shown in figure 8. A two-microphone intensity probe was used to measure sound power radiated through a fictitious rectangular grid surrounding the enclosure. General agreement is seen between predicted and measured values, although the sound power prediction code seems to consistently overpredict sound power. This is most likely due to the relatively small number of measurement points on the structure (31 out of a possible 144). More measurement points would have the effect of fixing the values of a greater number of nodes to the measured values, thereby minimizing the effects of measurement error.

Most of the gearbox noise is transmitted to the environment through Mode 3 of the enclosure, which is shown in figure 9. In Mode 3, both of the large sides of the enclosure vibrate in an "umbrella" type mode, that is, all points on each side are in phase.

#### 9F. Optimization

The eigenvalues/eigenvectors for the enclosure and the experimentally-determined modal participation factors were entered into the optimization code, which then found optimal absorber locations and parameters for the cases of one and two absorbers. The constraints

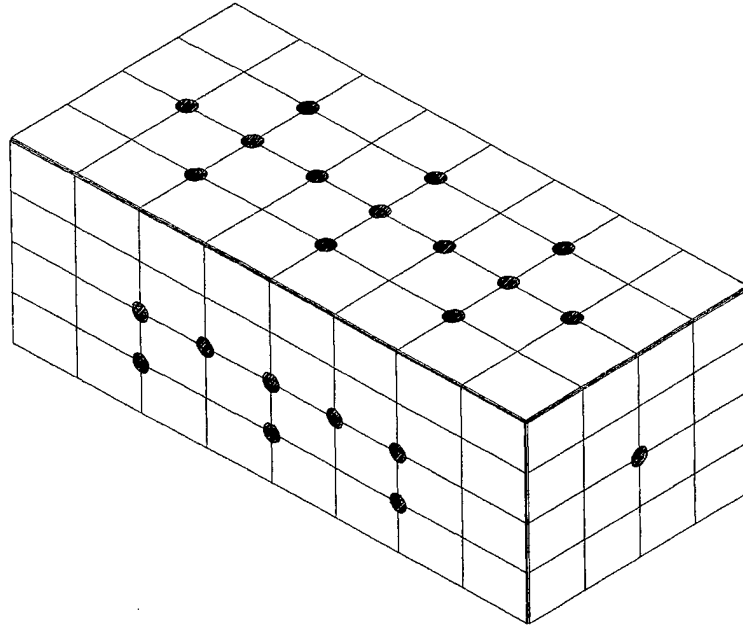


Figure 7. Velocity measurement points on gearbox enclosure.

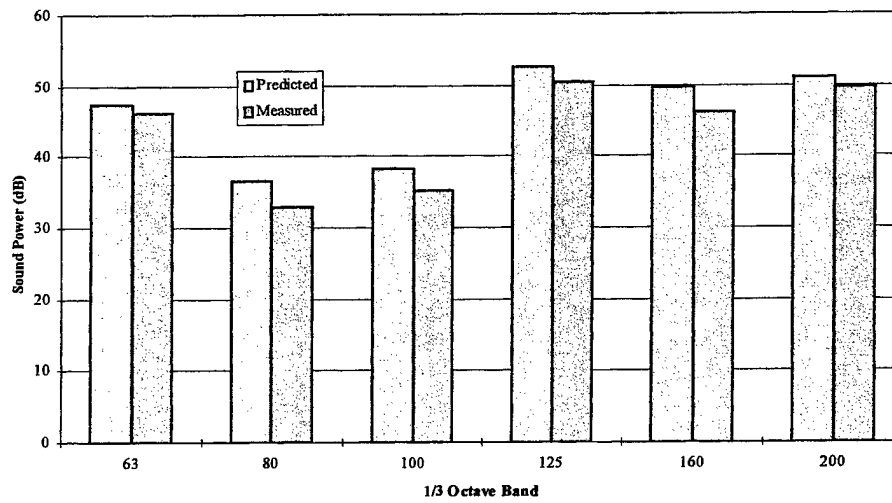


Figure 8. Predicted vs. measured sound power before optimization (dB reference:  $10^{-12}$  W).

Table 2. Lower and upper bounds on absorber parameters (110–140 Hz band).

	Natural frequency (Hz)	Mass (g)	Damping
Lower limit	110.0	10.0	0.02
Upper limit	140.0	50.0	0.10
Initial values	100.5	50.0	0.02

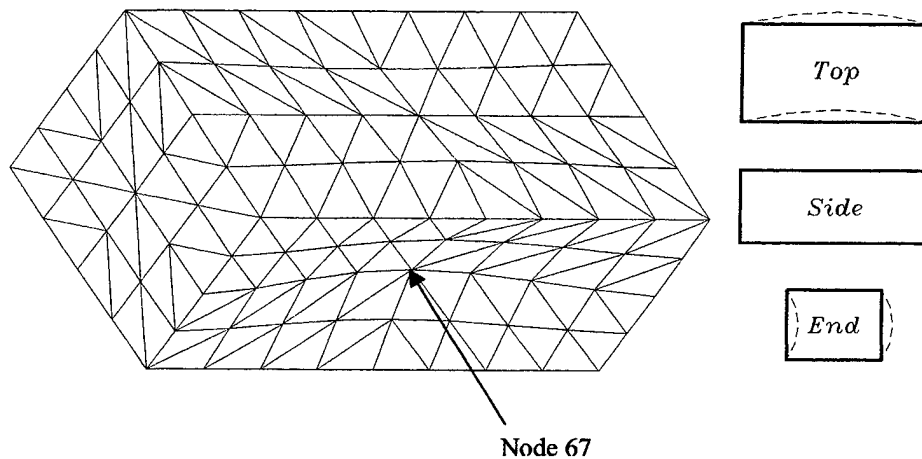


Figure 9. Third mode shape of gearbox enclosure. (Node 75 is located opposite to node 67.)

placed on the absorber parameters can be seen in Table 2. The mass of each absorber was limited to 50 grams, or 0.6% of the total enclosure weight of 8.25 kg. The damping ( $\eta$ ) was limited to a value of 0.1; this value was found through experimentation to be readily achievable with the damping mechanism described earlier. Finally, the natural frequencies of the absorbers are bounded by the upper and lower frequency limits of optimization (110–140 Hz).

Table 3 shows the optimized absorber locations and parameters for the one- and two-absorber cases, as well as the predicted reduction in sound power in the target band. In both

Table 3. Optimal absorber locations and parameters.

Location	Natural frequency (Hz)	Mass (g)	Damping	$\Delta\Pi$ (dB)
Optimization with one absorber				
Node 75	111.00	48.8	0.054	1.7
Optimization with two absorbers				
Node 67	122.83	50.0	0.052	11.6
Node 75	122.46	50.0	0.020	

See figure 9 for location of nodes.

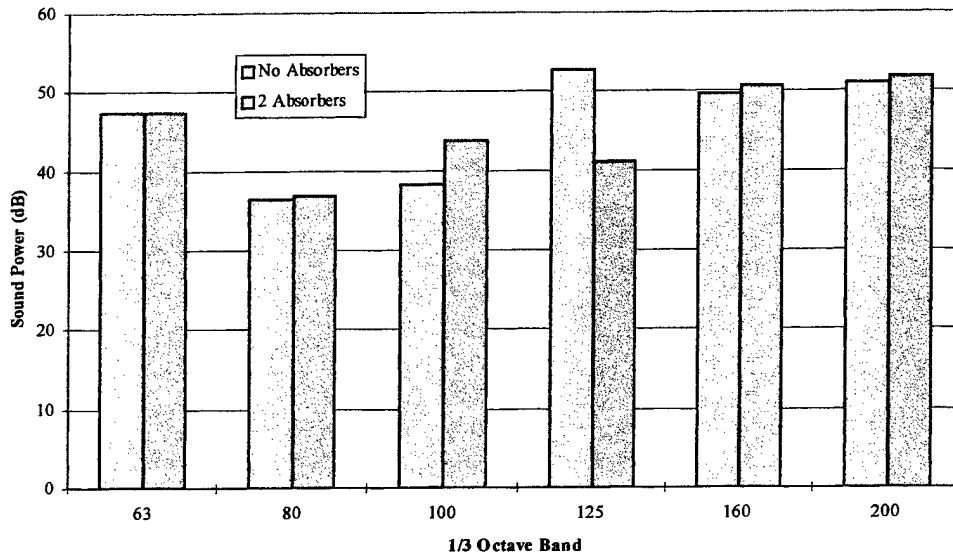


Figure 10. Predicted sound power before & after optimization with two absorbers (dB reference:  $10^{-12}$  W).

cases, the optimized absorbers are located at the centers of the large sides of the enclosure. Only a 1.7 dB reduction in sound power is possible with a single absorber. Since both sides of the enclosure are vibrating with large amplitude, the effect of reducing the vibration of only one side is negligible. In contrast, figure 10 shows that a significant reduction (11.6 dB) in sound power can be achieved with two optimized absorbers. These two cases demonstrates the utility of a design methodology which can optimize multiple absorbers simultaneously.

#### 9G. Experimental verification

To confirm the optimization results experimentally, two absorbers having the parameters shown in Table 3 were constructed. Both absorbers are made of brass. The end masses are made from  $0.5 \times 0.5$  inch bar stock and  $0.75 \times 0.0625$  inch bar stock was used to build the beams. Four  $0.5 \times 0.125$  inch notches have been removed from the ends of the beams to make the absorber more closely approximate the FEM model. Figure 11 and Table 4 shows the dimensions of the experimental absorbers, as well as the total measured weight of the absorbers including the damping mechanism.

Table 4. Critical dimensions of beam absorbers.

Absorber node	Mass height $H$ (mm)	Beam length $L$ (mm)	Total mass (g)
67	13.1	125.2	66.5
75	13.0	125.6	65.3

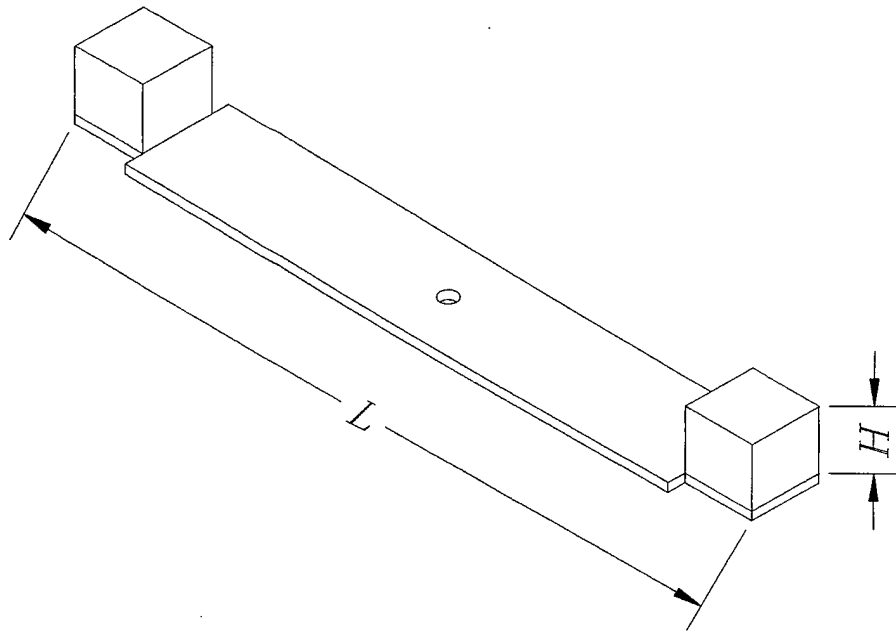


Figure 11. Schematic or experimental tuned absorber (Shown without damping mechanism).

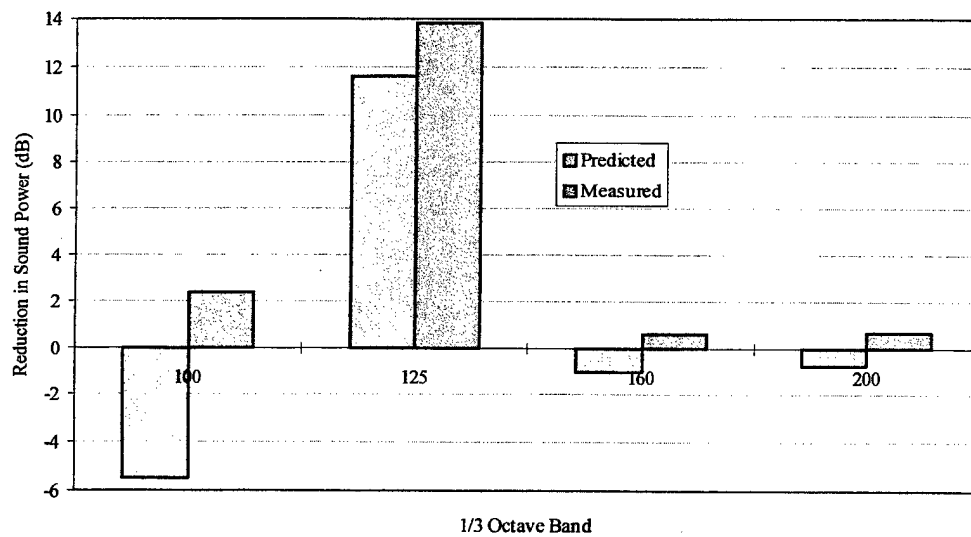


Figure 12. Predicted vs. measured sound power reduction with two absorbers.

After the absorbers were tuned, they were placed in their optimized locations and the sound power was measured. Figure 12 shows the predicted and measured sound power reduction achieved through the absorbers. An 11.6 dB reduction in sound power was predicted, and a 13.8 dB reduction was measured. In the 100 Hz band, the code predicts a 5 dB increase in sound power while a 2 dB decrease was measured. The discrepancy occurs because the static mass of the absorbers is not accounted for in the model (the static mass is the difference between the measured mass and the dynamic mass of 50 g). Overall, however, the agreement between predicted and measured results is quite good. A 13.8 dB reduction in sound power has been achieved through the addition of only 131.8 g of mass (1.6% of the enclosure weight).

## 10. Conclusions

The preceding case study has shown that significant noise reduction can be obtained through the use of optimized tuned absorbers. A reduction in sound power of 13 dB was achieved in the target band through the addition of only 1.6% of the weight of the enclosure. The reduction was obtained despite the relatively high modal density of the enclosure.

The design methodology presented here is relatively insensitive to slight errors in the manufacturing of the absorbers. While tuning the absorbers, deviations of approximately 5% in tuning frequency and 10% in damping values were noted. This had only a small effect on the measured sound power of the enclosure. To conclude, the use of thin shell enclosures with optimally tuned absorbers offers the possibility of significant noise reduction through the addition of very small amounts of weight. Future work will address problems where several modes are dominant in the noise spectrum and numerical challenges when several tuned absorbers need to be optimally sized and located.

## Acknowledgment

We thank the National Science Foundation under Grant DMI-9800050 for their support.

## References

- M. Abé and Y. Fujino, "Dynamic characterization of multiple tuned mass dampers and some design formulas," *Earthquake Engineering and Structural Dynamics* vol. 23, pp. 813–835, 1994.
- T. Asami, T. Wakasono, K. Kameoka, M. Hasegawa, and H. Sekiguchi, "Optimum design of dynamic absorbers for a system subjected to random excitation," *JSME International Journal, Series III* vol. 34, no. 2, pp. 218–226, 1991.
- S. T. Christensen, S. V. Sorokin, and N. Olhoff, "On analysis and optimization in structural acoustics—Parts I & II: Problem formulation and solution techniques," *Structural Optimization* vol. 16, no. 2–3, 1998.
- E. W. Constans, "Minimizing radiated sound power from vibrating shell structures: Theory and experiment," Ph.D. Thesis, The Pennsylvania State University, University Park, PA, May 1998.
- E. W. Constans, A. D. Belegundu, and G. H. Koopmann, "Design approach for minimizing sound power from vibrating shell structures," *AIAA Journal* vol. 36, no. 2, pp. 134–139, 1998.



- A. Corana, M. Marchesi, C. Martini, and S. Ridella, "Minimizing multimodal functions of continuous variables with the "simulated annealing" algorithm," *ACM Transactions on Mathematical Software* vol. 13, no. 3, pp. 262–280, 1987.
- J. B. Fahnlne and G. H. Koopmann, "A lumped parameter model for the acoustic power output from a vibrating structure," *Journal of the Acoustical Society of America* vol. 100, no. 6, pp. 3539–3547, 1996.
- J. B. Fahnlne and G. H. Koopmann, "Numerical implementation of the lumped parameter model for the acoustic power output from a vibrating structure," *Journal of the Acoustical Society of America* vol. 102, no. 1, pp. 179–192, 1997.
- H. Frahm, U.S. Patent No. 989, 958 (1911), 3576 Device for Damping Vibrations of Bodies, 1911.
- W. J. Hammill and C. Andrew, "Receptances of lumped-parameter systems containing discrete damping sources," *Journal of Mechanical Engineering Science* vol. 13, no. 4, pp. 296–301, 1971.
- A. J. Keane, "Experiences with optimizers in structural design," *Adaptive Computing in Engineering Design and Control*, Plymouth, U.K., pp. 14–27, September 1994.
- L. Kitis, W. D. Pilkey, and B. P. Wang, "Optimal frequency response shaping by appendant structures," *Journal of Sound and Vibration* vol. 95, no. 2, pp. 161–175, 1984.
- M. Kiasztorny, "Reduction of steady-state forced vibrations of structures with dynamic absorbers," *Earthquake Engineering and Structural Dynamics* vol. 24, pp. 1155–1172, 1995.
- G. H. Koopmann and J. B. Fahnlne, *Designing Quiet Structures: A Sound Power Minimization Approach*, Academic Press, 1997.
- J. Ormondroyd and J. P. Den Hartog, "The theory of the dynamic vibration absorber," *Transactions of the ASME, Journal of Applied Mechanics* vol. 50, no. 7, p. 9, 1927.
- S. Szykman and J. Cagan, "A simulated annealing-based approach to three-dimensional component packing," *ASME Journal of Mechanical Design* vol. 117, pp. 308–314, 1995.
- C. T. Urban and G. A. Gabriele, "Optimal heat sink design and component placement using the ellipsoid algorithm," *ASME DE Advances in Design Automation* vol. 65, no. 2, pp. 605–614, 1993.